Effects of Metallurgical Chemistry and Service Conditions on the Oxidation Limited Life Time of FeCrAl-based Components

Dmytro Naumenko, Willem J. Quadakkers*

** Dissertation*

Berichte des Forschungszentrums Jülich ; 3948
ISSN 0944-2952
Institut für Werkstoffe und Verfahren der Energietechnik
IWV 2: Werkstoffstruktur und -eigenschaften Jül-3948
D 82 (Diss., Aachen, RWTH, 2002)

Zu beziehen durch: Forschungszentrum Jülich GmbH · Zentralbibliothek
52425 Jülich · Bundesrepublik Deutschland
☎ 02461/61-5220 · Telefax: 02461/61-6103 · e-mail: zb-publikation@fz-juelich.de

Abstract

FeCrAl alloys are high temperature structural materials with ever increasing technological importance, because in the temperature range of 900-1300°C their resistance against environmental attack exceeds that of other metallic materials. This is due to the formation of a protective alumina scale on the surface of FeCrAl-alloys during high temperature service.

During exposure at elevated temperatures, the major life limiting factor for FeCrAl alloys is the depletion of the alloy Al-content. In the present work a number of commercial and model alloys have been studied with respect to the lifetime oxidation behaviour. The experimentally determined lifetimes were compared with those calculated based on the available lifetime prediction model. Analytical studies were performed on oxidised alloys using a range of surface analysis techniques to elucidate the oxidation mechanisms as a function of exposure time and temperature.

The results demonstrate the importance of the minor alloying chemistry for scale growth rate and adherence and consequently for the service life of FeCrAl-based components. The observed differences in oxidation rates between the studied commercial materials and even between different batches of one commercial alloy have been found to originate from the interaction of typical minor alloying additions of the reactive elements, such as Y, La, Ti, Zr and Hf with typical alloy impurities of carbon and nitrogen. A major finding was that for this reason, the optimum oxidation resistance can not be achieved by one reactive element addition, but rather by a combination of the latter. The exact amounts, type and distribution of the reactive elements must be carefully selected depending on the particular alloy application.

Table of contents

1. Introduction and problem definition

World-wide efforts for achieving increased efficiencies in the power generation-conversion processes as well as transportation lead to an increasing demand for metallic materials, which can be used in high temperature aggressive environments. If the components are subjected to long term service at temperatures well above 1000°C, the only metallic material, which possesses sufficient resistance against environmental attack are alloys of the type FeCrAl. These materials are being used under arduous conditions including temperatures up to 1300°C because they are able to form very protective alumina based surface oxide scales. This allows application of FeCrAl alloys as construction materials in a large variety of industrial and domestic facilities, where operating temperatures of 900 to 1300°C prevail [1].

Examples of domestic use range from heating element foils and thin wires in cooking plates, radiation devices, toasters, microwave equipment, heaters in boilers and washing machines to glow plugs and precision resistors in cars. In industrial environments the FeCrAl-based heating elements are being applied in furnaces for heat treatments and drying in e.g. paper-, aluminium-, semiconductor- and coating industries. Additionally the alloys are commonly used in heat exchangers, including newer designs of energy efficient, low emission, single ended recuperators (SER, Figure 1.1). In such applications, especially if a high creep strength of the material at elevated temperatures is required, the alloys strengthened by oxide dispersions (ODS alloys) and manufactured by powder metallurgical methods are being used [2].

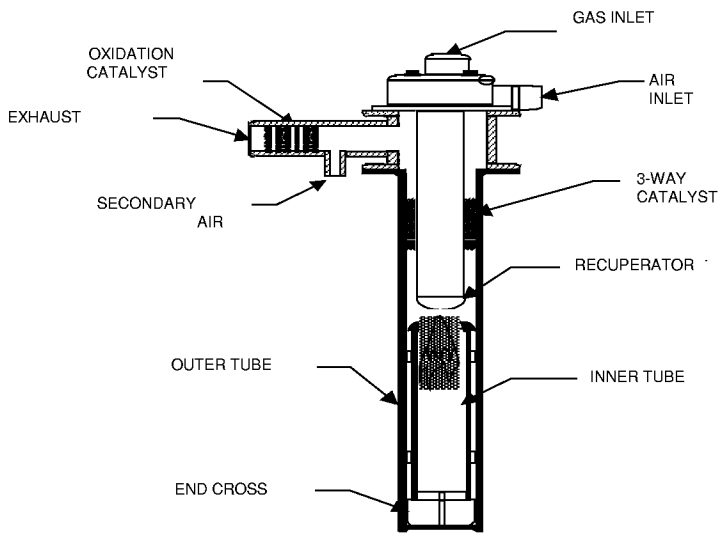

(courtesy of B.Jönsson, KANTAL AB)

Figure 1.1: Advanced single ended recuperative system "Kanthal GAS" with FeCrAl materials used for radiant tubes and metallic catalyst supports

More recently the FeCrAl alloys have been introduced or are being considered as construction materials in a number of new applications. The latter include car catalyst carriers (Table 1.1 and Figure 1.2), fibre based domestic and

industrial burners (Figure 1.3) as well as hot gas filtering systems for removing particulate emission in diesel engines exhausts and in flue gases of power plants.

Depending on the actual component design the FeCrAl alloys are manufactured in a large variety of semifinished products ranging from fibres and foils of 20-100µm thickness to wires, plates and tubes with a thickness up to few millimetres.

Table 1.1: Annual Production of FeCrAl alloys for car catalyst supports
(Tonnage: Metric Tonnes/year, Value – Million EURO/year) [Courtesy of Krupp VDM]

1988		1992		2000		2005	
Tonnage	Value	Tonnage	Value	Tonnage	Value	Tonnage	Value
600	8	300-5000	34-56	10000–20000	71-140	30000-40000	200-300

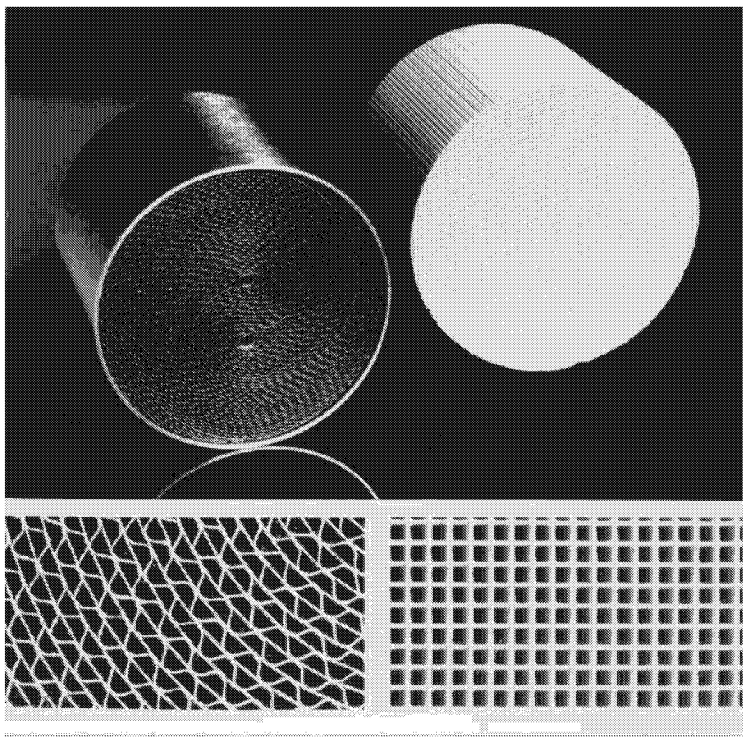

Figure 1.2: Catalyst support systems (left) FeCrAl based and (right) ceramic based
[Courtesy of EMITEC GmbH]

In spite of the excellent protective properties of the alumina scale resulting from its high thermodynamic stability and low growth rate, maximum operating temperatures for FeCrAl steel components have to be selected with great care. This is because in the envisaged temperature range of application (900 – 1300°C) a sudden, unannounced component breakdown can occur during long term service after the scale forming element, aluminium, has been depleted from the alloy [2]. The depletion process originates from the scale growth

and is especially fast in thin walled components with small Al-reservoir. In addition, the Al-depletion is enhanced in case of a repeated spallation of the alumina scale, which is a common event under temperature cycling conditions, thus consuming the Al for scale re-healing [2,3,4].

If due to scale growth and spallation the Al is depleted beneath a certain critical level, a continuous protective alumina layer can no longer be established [2,3,4]. It follows then that Fe-based oxides are formed, fast growing at temperatures of around 1000°C, leading to a rapid "breakaway" oxidation of the whole alloy matrix and failure of the component. Breakaway corrosion is a sudden phenomenon and for real components it can not be predicted from regular plant inspections. Typical values of the alumina scale thickness at the commencement of breakaway for 1 to 2 mm thick components are of the order of 20 to 50 µm. Hence, the oxidation limited life of FeCrAl components is determined by a sudden chemical failure and not by a continuous loss of the component wall thickness, as is e.g. the case for Cr-alloyed steels and NiCr-based alloys [5].

Expected requirements and legislations, which dictate saving of raw material and primary energy sources as well as recycling costs will in the medium and long time future require lifetime extension of the FeCrAl-based components. Additionally, the request for more efficient energy conversion and reduction of hazardous emissions, will cause the FeCrAl alloys to operate at ever higher temperatures and in new designs, which often require a decreased component wall thickness. Under such critical operating conditions the depletion of the aluminium reservoir will be significantly faster than in the present applications. This can be illustrated using the following examples:

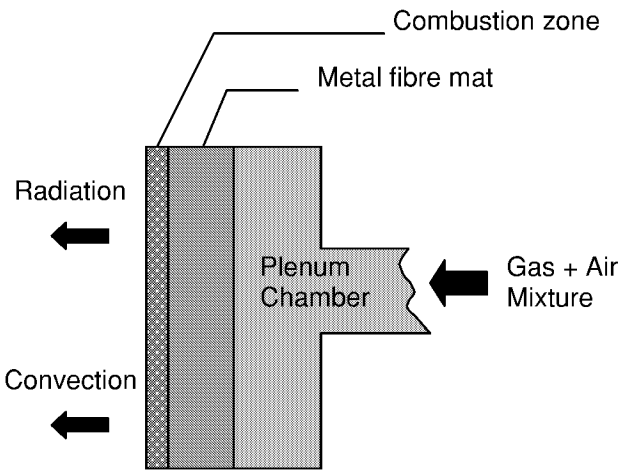

Figure 1.3: Design of Surface Combustion Burner

- An increasing demand exists for domestic and industrial application of FeCrAl-fibre based, low NO_X burners, operating at temperatures over 1000°C for achieving higher burner efficiencies. Under such arduous conditions, the very thin (20 to 50µm diameter)

fibre components can have an extremely short service life (e.g. at 1100°C only a few hundred hours).

- Car catalysts fabricated of FeCrAl alloys, which are gradually replacing the ceramic devices (Figure 1.2) commonly used in the last 30 years, will have to operate at higher temperatures (1000-1100°C) and will have to be fabricated from ultra-thin foils (20 instead of presently 50μm) to fulfil the new, ultra low emission regulations, which have to be met in the years beyond 2005 [1].

- Metallic hot gas filters, which are of crucial importance for reduction of particulate emission in engines and large-scale combustion systems, especially in future biomass fired power plants, will posses extremely short lives due to the extremely thin metal fibres used. The high operating temperature of 800 to 900°C, in combination with deposit assisted, accelerated corrosion will lead to extremely rapid exhaustion of the alloy aluminium reservoir.

- New types of the Single Ended Recuperative (SER, Figure 1.1) heat exchangers allow energy conversion with very high thermal efficiencies (>80%), better controllability and up to 70% reduced NO_X and CO emissions compared to the presently used industrial open heating systems. In spite of the relatively large tube wall thickness (1-2 mm), the service temperatures needed to obtain the required optimum efficiency are extremely high, i.e. up to 1250°C. This has a consequence that the anticipated economically viable service lives of these devices of around 100 000 hours appear to be challenging to achieve.

Due to the arduous service conditions for the above components, ceramics would theoretically be alternative construction materials for the FeCrAl alloys because of their good high temperature capabilities. However, in all the domestic and industrial applications mentioned above, ceramics are unsuitable because:

- they cannot easily be manufactured in very thin walled semifinished products (wire, foil, fibre) required in many of the components mentioned,

- they are much more difficult to join as FeCrAl alloys, which can be welded and brazed using conventional methods,

- they are brittle and thus susceptible to fracture induced by thermal stresses, thermal shock and mechanical impact damage,

- they do not have a suitable electrical conductivity, which is required in some applications, such as the resistance heating elements.

Considering the above mentioned facts it can be concluded that there is a need to extend the oxidation limited lifetime of the FeCrAl alloys, which can primarily be achieved by slowing down the exhaustion of the aluminium reservoir.

The current work deals with the aluminium depletion and breakaway failure of FeCrAl materials emphasising the role of alloy chemistry as well as aspects related to the component design and operating conditions. Based on the knowledge of oxidation mechanisms, methods for a reliable prediction of component life will be discussed. Additionally a number of possibilities for lifetime extension of the FeCrAl-based components will be derived.

2. Literature Review

2.1 Oxidation of FeCrAl alloys: thermodynamic and kinetic background

The overall chemical reaction for the formation of a metal oxide can be written, as [5]:

$$x \cdot M + \frac{y}{2} \cdot O_2 = M_x O_y \tag{2.1}$$

The driving force for this reaction is the Gibbs free energy minimisation, namely:

$$\Delta G = \Delta G_0 + RT \cdot \ln K\,, \tag{2.2}$$

where

ΔG - Gibbs free energy; ΔG_0 - Standard Gibbs free energy

R - Gas constant; T - Temperature; K - Equilibrium constant.

In thermodynamic equilibrium ΔG=0 and consequently it follows that:

$$\Delta G_0 = -RT \cdot \ln K \tag{2.3}$$

The thermodynamic stability of different oxides can be compared by plotting the standard Gibbs free energy of their formation as a function of temperature (i.e. in the form of an Ellingham diagram, Figure 2.1). The oxide having the lower free energy of formation possesses the higher thermodynamic stability.

In an FeCrAl alloy between the major alloying elements (Figure 2.1) it is the aluminium oxide, which is the most stable with ΔG_0 at 1000°C being around 900 kjoules / mole oxygen.

For the reaction

$$2Al + \frac{3}{2}O_2 = Al_2O_3 \tag{2.4}$$

the equilibrium constant is given by:

$$K = \frac{a_{Al_2O_3}}{a_{Al}^2 \cdot p_{O_2}^{3/2}} \tag{2.5}$$

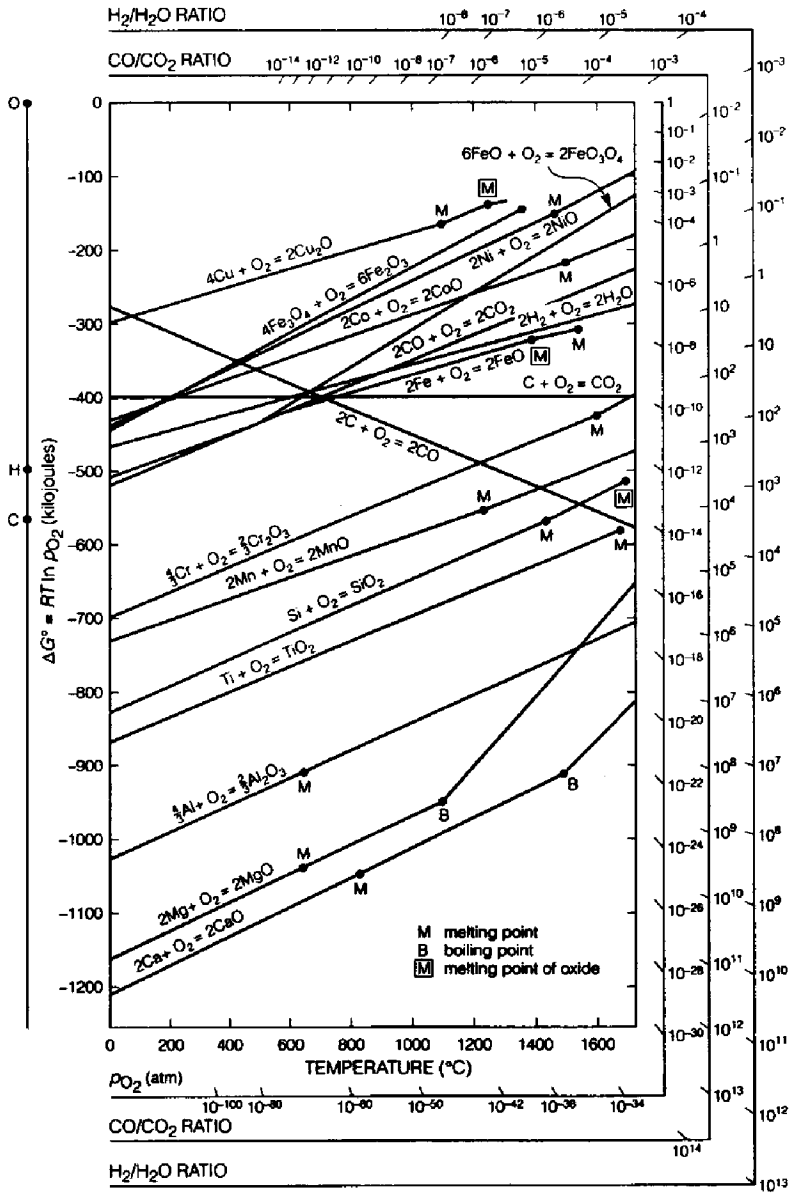

Figure 2.1: Temperature dependence of standard free energy of formation for selected metal oxides

From eq-ns (2.3) and (2.5) the oxygen partial pressure at the scale/metal interface, which equals the dissociation pressure of alumina, is given as:

$$p_{O_2} = \frac{a^{2/3}_{Al_2O_3}}{a^{4/3}_{Al}} \exp\left[\frac{2\Delta G_0}{3RT}\right] \tag{2.6}$$

If depletion of the scale forming element, i.e. Al, occurs during oxidation then its activity decreases with exposure time. It can be seen from eq-n (2.6) that the decrease in Al-activity leads to an increase in oxygen partial pressure at the scale/metal interface. After a critical Al-depletion, the oxygen partial pressure can reach a value, which is sufficiently high for the next stable oxide (chromia) to form. In reality, however, the depleted alloy often becomes exposed to the oxidant due to the scale cracking or spalling. Then, because of kinetic reasons,

mixed Fe/Cr oxides are formed. At temperatures of around 1000°C the growth rates of $(Fe,Cr)_2O_3$-type oxides are orders of magnitude higher than that of alumina. Such rapid oxidation results in complete destruction of the alloy matrix within tens of hours. This event is called "breakaway corrosion" [4].

After the formation of a dense oxide layer diffusion of the reactants (metal and/or oxygen) through the scale is determining the oxide growth. For a number of metal oxides the scale growth occurs via bulk diffusion of either metal cations or oxygen anions or both [6]. This situation is illustrated in Figure 2.2. As a result, gradients in metal activity and oxygen partial pressure are established across the scale. The scale thickness is generally proportional to the square root of exposure time, which can be justified by the following considerations:

If an oxide scale grows by ionic flux j_i, then in terms of the Fick's first law [6]:

$$j_i = \frac{D_i}{RT} \cdot \left(\frac{\delta \mu}{\delta x} \right), \tag{2.7}$$

where

D_i - ionic diffusion coefficient;

R - gas constant;

T - temperature;

$\frac{\delta \mu}{\delta x}$ - gradient of chemical potential across the scale of thickness x.

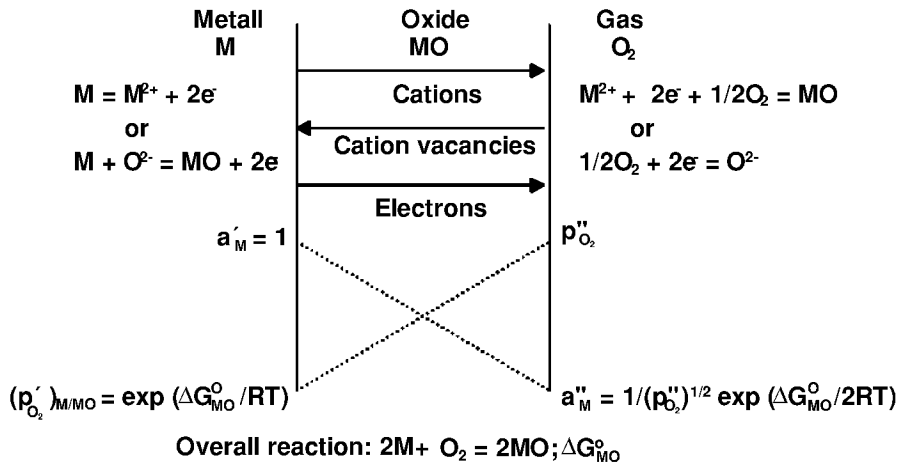

Figure 2.2: Schematic of oxidation process controlled by ionic diffusion

If thermodynamic equilibrium is established at both the scale-metal and scale-gas interfaces, the values of chemical potentials μ_i' and μ_i'' at these places are constant and it follows that:

$$j_i = const \cdot \frac{dx}{dt} = D_i \frac{\mu_i' - \mu_i''}{x} \tag{2.8}$$

The value of the chemical potential of a species is defined by its activity:

$$\mu_i = RT ln(a_i), \tag{2.9}$$

where a_i – activity of the i-species; in case of oxygen – its partial pressure $P(O_2)$;

Integrating eq-n (2.8) leads to the parabolic rate law:

$$x = k_P \cdot t^{1/2} \tag{2.10}$$

$$\text{where } k_P = \left[2D_i \frac{\mu_i' - \mu_i''}{const} \right]^{1/2} \text{ is the parabolic rate constant} \tag{2.11}$$

A more extensive mathematical treatment of the oxide growth process, which is controlled by cation lattice diffusion is given in reference [7].

For commercial FeCrAl alloys the experimentally determined oxide growth [8] (see also Figure 2.3) at temperatures above 1000°C frequently shows a sub-parabolic time dependence i.e.:

$$x = k \cdot t^n, \tag{2.12}$$

where the value of n was often found to be around 0.35 [8]. The reason for such sub-parabolic oxidation kinetics will be discussed in Chapter 2.3.

During the oxidation testing of high temperature materials a common way of determining the scaling kinetics is measuring the specimen mass change (which equals the oxygen uptake) as a function of exposure time. The scale thickness on an FeCrAl alloy, assuming a uniform, dense and gas tight alumina layer has formed, can be easily obtained from the specific mass change data. Hence, 1 mg/cm^2 mass change corresponds to a scale thickness of ca 5.3 micrometers [9]. Typical mass change data for the lifetime cyclic oxidation of a 2 mm thick

FeCrAl alloy specimen is presented in Figure 2.3. In the beginning of the test an increase in the specimen mass is observed, which is due to oxygen uptake caused by the growth of the alumina scale. During this stage, the alloy Al reservoir is consumed only for the scale formation. After some time the alumina scale starts to spall [10, 11], which is indicated by decrease of the specimen mass. Since there is still sufficient Al in the alloy, the protective alumina scale is successfully re-healed. This process of spalling/re-healing, which significantly contributes to the consumption of the alloy Al-reservoir, continues until the Al is depleted beneath a critical level. If this critical level has been reached breakaway oxidation occurs characterised by a rapid specimen mass increase (Figure 2.3).

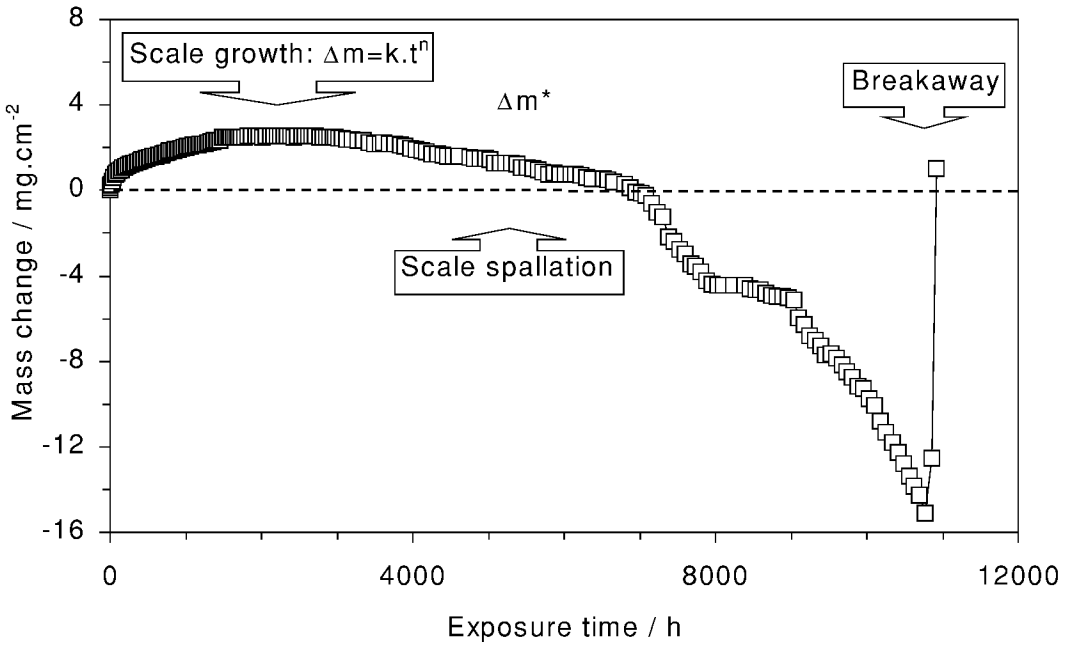

Figure 2.3: Typical mass change data obtained during lifetime cyclic oxidation of a 2 mm thick commercial FeCrAl alloy at 1200°C in air [11]

If the aluminium reservoir and the oxidation kinetics (i.e. rate of Al-depletion) are known, it is possible to quantitatively predict the lifetime of FeCrAl-components.

2.2 Lifetime prediction for FeCrAl components

In a recently developed model [11] a flat specimen of thickness d (in cm) and infinite length and width was considered. The oxygen uptake (in mg/cm^2) by the specimen surface A due to the oxide growth is given by:

$$\frac{\Delta m(O)}{A} = k \cdot t^n, \tag{2.13}$$

where t is the oxidation time in hours, k the oxidation rate constant and n the oxidation rate exponent [8, 11].

Assuming that the surface oxide consists completely of Al_2O_3 (i.e. the Al/O mass ratio is equal to 1.124), the amount of aluminium per unit area of the scale $\frac{\Delta m(Al)}{A}$ (in mg/cm^2):

$$\frac{\Delta m(Al)}{A} = 1.124 \cdot k \cdot t^n \tag{2.14}$$

The total amount of aluminium $\Delta m(Al)^{ox}$ (in mg) in the oxide scale on the surface of the specimen is given by:

$$\Delta m(Al)^{ox} = 1.124 \cdot A \cdot k \cdot t^n \tag{2.15}$$

Considering the volume of the specimen to be $\frac{1}{2} A \cdot d$ (in cm^3), the total amount of aluminium (in mg) depleted from the alloy due to oxide formation after a certain time t is

$$\Delta m(Al)^{depl} = \frac{C_0 - C_t}{100} \cdot \rho \cdot \frac{1}{2} A \cdot d\,, \tag{2.16}$$

where ρ is the alloy density in mg.cm^{-3}, C_o the initial alloy Al content in mass% and C_t the remaining Al content at time t. The amount of Al depleted from the alloy will be equal to that tied up in the oxide, i.e. after a certain oxidation time, the following equation will be valid:

$$1.124 \cdot A \cdot k \cdot t^n = \frac{C_0 - C_t}{100} \cdot \rho \cdot \frac{1}{2} A \cdot d \tag{2.17}$$

Re-arranging this equation reveals the time, which is required to deplete the initial aluminium content C_0 to a certain, i.e. lower aluminium content in the alloy matrix after time t. If we define C_B as the critical Al content, at which breakaway oxidation starts, the time for the occurrence of this event (assuming no scale spallation has occurred) is given by [11]:

$$t_B = \left[4.4 \cdot 10^{-3} (C_0 - C_B) \frac{\rho \cdot d}{k} \right]^{\frac{1}{n}} \tag{2.18}$$

As explained in references [10, 11] and Figure 2.3, the alumina scales on the FeCrAl-based alloys become prone to spallation after long term exposure. Assuming that this spallation starts after the oxide reaches a critical thickness x^*, corresponding to a critical mass change Δm^* (Figure 2.3), the time to breakaway for a flat specimen of infinite size is given by (compare equation 2.18):

$$t_B = 4.4 \cdot 10^{-3} (C_0 - C_B) \cdot \rho \cdot d \cdot k^{-\frac{1}{n}} \cdot (\Delta m^*)^{\frac{1}{n}-1} \qquad (2.19)$$

Equations (2.18) and (2.19) appear to be not only useful tools for the prediction of the time to breakaway, but also as an illustration of how different factors can affect the service lives of the FeCrAl components. These factors will be discussed in details in the remaining of the literature review.

2.3 Al-Reservoir

For an FeCrAl-component the Al-reservoir can be defined as the amount of aluminium available for the formation of an external continuous alumina layer. This amount is determined (see eq-n 2.18) by the initial Al content C_0, the critical Al-content for occurrence of breakaway C_B and the component thickness d.

Most of the commercial FeCrAl alloys contain 4 to 6 mass percent aluminium. From eq-n 2.18 it can be concluded that a significant lifetime extension can be achieved by increasing the initial aluminium content C_0. However, in practice this amount can not exceed approximately 7% because of deterioration of the alloy mechanical properties, especially ductility and formability [12].

The exact value of the critical aluminium content for the occurrence of breakaway (C_B) is still a point of debate. Theoretically, the transition from a protective continuous flat oxide layer to non-protective internal oxidation of a scale forming element was described by Wagner [13]. According to Wagner [5,13], the transition from external to internal oxidation of Al in FeCrAl alloy is expected to occur when:

$$C_{Al} = C_B < \left[\frac{\pi g^*}{2\nu} C_{O_2} \frac{D_O V_m}{D_{Al} V_{ox}} \right], \qquad (2.20)$$

where:
D_O and D_{Al} are the diffusion coefficients of oxygen and aluminium in the alloy matrix;

C_{O2} is the oxygen concentration at the scale/metal interface;
C_{Al} is the transitional concentration of Al in the alloy matrix, i.e. C_B;
V_m and V_{ox} are the molar volumes of the metal and oxide respectively;
ν is the number of moles oxygen per mole oxide;
g^* is a critical value for transition from external to internal oxidation of the parameter $g=f(V_{ox}/V_m)$.

A direct application of the Wagner's treatment for the calculation of C_B for real components is, however, difficult. This is because, the breakaway normally starts locally after scale cracking or spalling at the specimen/component corners or edges, i.e. far from the equilibrium conditions of an infinite flat surface considered in [13]. Experimental determination of C_B can be performed either from the mass change measurements during oxidation tests or, more accurately, by measuring the residual Al-content in the breakaway specimens e.g. using Electron Probe MicroAnalysis (EPMA). Only few literature references [10, 11] give the measured values of C_B depending on the alloy composition and experimental conditions. Bennett et.al. reported a C_B-value of around 2.5 mass% for the commercial ODS alloy MA956 oxidised in air at 1300°C [10]. The authors in reference [11] give for the commercial ODS alloy ODM 751 during air oxidation at 1200°C an EPMA measured value of C_B =1.2 mass%. It must be noted that the point EPMA-measurements of C_B may sometimes provide values, lower than the real ones. This has been attributed to nitridation of Al within the alloy matrix, often observed after commencement of breakaway during air exposures [12].

The second parameter determining the component Al-reservoir is its wall thickness (d in eq-n 2.18 and 2.19). Increasing the wall thickness obviously results in an extended lifetime of the component. It was shown [4] that under the same experimental conditions, thicker specimens due to the higher volume to surface ratio fail after much longer exposure times than the thinner ones. In practice, however, it is often not possible to substantially increase the component wall thickness due to design restrictions.

2.4 Growth rates of alumina scales

From eq-ns (2.18) and (2.19) it is easy to derive that the oxide growth rate constants k and especially n have a significant effect on the alloy lifetime. The main parameters determining the kinetics of scale growth on FeCrAl alloys have been subjected to extensive studies. The most valuable findings starting from as early as 1937 [14] refer to the minor alloying of the base FeCrAl composition with elements from Groups IIIA to IVA, such as Y, La, Zr etc, which significantly alter the protective properties of the alumina scales. The most important

observations with the above Reactive Elements (RE) are summarised in a number of review papers [15, 16, 17]

It is generally accepted that minor additions of the reactive elements change the transport phenomena on the grain boundaries of alumina scales. It is doubtful, whether the RE-additions can influence the diffusion through the bulk α-Al_2O_3, e.g. by acting as donors and/or acceptors, thereby changing the defect concentrations in the oxide. The recent studies of tracer distribution and electrical conductivity of RE-doped alumina single-crystals have shown only minor, if any, effect on the diffusion [18,19]. In addition it must be said, that the diffusion coefficients of aluminium and oxygen determined experimentally in bulk alumina are significantly lower than those on the grain boundaries of polycrystalline oxides [20,21].

RE-effects on the properties of the alumina grain boundaries have been verified in recent experiments using oxygen-18 isotopes [22,23,24]. The alumina scales on FeCrAl alloys without any RE-additions were found to grow by both inward oxygen and outward aluminium transport. The RE-alloying additions apparently suppress the outward transport of aluminium cations [22]. The latter results in a lower scale growth rate, however a number of other effects seem to be of importance, e.g. an improvement of the scale adhesion, which is to be discussed in the following Chapter 2.4. Using high resolution TEM/EDX analyses, presence of the reactive elements at the scale grain boundaries and sometimes at the scale/metal interface was observed [25,26,27]. Besides decorating the scale grain boundaries, the reactive element yttrium has been found to diffuse through the alumina scale to the scale/gas interface and to form there precipitates such as $Y_3Al_5O_{12}$. These precipitates were found to grow with time, indicating a continuous diffusion process of yttrium through the scale [28].

One of the consequences of the reactive element effect in slowing down the scaling kinetics is that the latter changes from parabolic to sub-parabolic [8,29]. These alterations may well be associated with the observed changes in the scale structure, as was explained in reference [8]. It was assumed that the growth rate of the alumina scale is controlled by inward oxygen diffusion via the scale grain boundaries. In order to account for this, in eq-n 2.11 the parabolic rate constant k_P instead of D_i becomes proportional to the oxygen diffusion coefficient along the scale grain boundaries D_o^{gb} and a ratio of the grain boundary width δ to the grain size r:

$$k_P \sim D_o^{gb} \frac{2\delta}{r} \cdot \frac{\Delta\mu}{RT} \qquad (2.21)$$

The experimentally observed structure of the alumina scales grown on RE-doped alloys features small equiaxed grains at the scale/gas interface and large columnar grains at the scale/metal interface. The formation of the fresh oxide occurs at the scale/metal interface, contributing to increase of the size of the columnar grains, i.e. in terms of the scale thickness:

$$r(x) = a \cdot x\,, \tag{2.22}$$

where x – scale thickness and a is a proportionality factor [30]. Combining eq-ns (2.9), (2.21) and (2.22) leads to the sub-parabolic oxidation kinetics given in eq-n (2.12).

The exact way, in which the reactive elements block the cation transport on the alumina grain boundaries is far from being completely understood. Several alternative mechanisms have been proposed in literature in order to explain the effect.

The first one suggests that a segregation of the large, massive ions of the reactive elements occurs to the alumina grain boundaries, suppressing the boundary transport in several different routes [8,22,25,31]:

1) It may simply reduce the number of ionic sites, available for diffusion of Al cations;
2) It may change the boundary structure and/or energy;
3) It may alter the electrostatic potential associated with the boundary; etc.

The driving force for the segregation has been claimed to be the misfit energy of the large RE-ions in the bulk alumina. This mechanism, however, can not easily explain some other important effects of the reactive elements, e.g. their interaction with sulphur (to be discussed in Chapter 2.4).

The second proposed mechanism of the reactive element effect is the "poisoned interface" model of Pieraggi and Rapp [32], which treats the experimental observations in terms of the segregation of RE-ions to the scale/metal interface. The model (which originally referred to chromia scales) stresses the importance of the scale/metal interfacial reactions. In undoped systems Al-cations are being constantly produced at the scale/metal interface, which necessitates consumption of Al-vacancies. The authors [32] postulate that this reaction can only proceed if a constant removal of these vacancies by the climb of misfit dislocation into the alloy matrix occurs. The role of the RE-ions is then to pin the misfit dislocations at the

scale/metal interface, which effectively stops the formation of Al-cations. Although elegant, this model lacks the experimental verification as well as it is in contradiction with the oxidation studies of the Y-implanted FeCrAl alloys [33]. The latter experiments found only minor short term beneficial effect of low dose Y-implantation and even adverse effect on the scale morphology and growth rate occurred with increasing the yttrium surface concentration.

An attempt has been made recently by Pint [34] to relate the RE-effects to experimental STEM data of RE-ions segregation to the scale boundaries and to the scale/metal interface. The proposed "dynamic segregation theory" states that the RE-ions first segregate to the scale/metal interface and then, driven by the oxygen chemical potential gradient, diffuse outwards through the scale. In course of this outward diffusion the RE-ions segregate also to the scale grain boundaries. Slowly outward diffusing, large RE-cations compete with light Al-cations, and when a critical amount of the RE-dopant on the grain boundary is reached, the Al-diffusion is essentially blocked. The weak point of the dynamic segregation theory (as well as of the first two models) is that it contains many assumptions, which at the present time are difficult to check experimentally.

So far, no theory has been established, which fully explains and quantitatively describes the reactive element effect on the scale growth kinetics. The experimental data are often controversial and a lot of those important are lacking. More research work must be undertaken in order to get a better understanding of the phenomena.

2.5 Resistance of the oxide scale to spalling

2.5.1. General remarks

A parameter, which is of vital significance for the oxidation limited lifetime of an FeCrAl component is the resistance of the formed alumina scale against spalling. A simple prediction based on eq-n 2.19, assuming a sub-parabolic scale growth gives a factor of four in lifetime increase if the critical thickness for spallation is increased by just a factor of two. The scale resistance to spalling is determined by a number of factors. The most noteworthy are the effects related to alloy impurities, such as sulphur, the reactive elements and the effects induced by temperature cycling.

2.5.2. Intrinsic scale adhesion: effects of sulphur impurity and reactive elements

The deleterious effect of sulphur on the scale adhesion has been known for around two decades [35,36]. The presence of sulphur at the scale/metal interface of undoped FeCrAl alloys was experimentally verified by AES studies after different oxidation times [36] and associated with interfacial voids [37]. However, it is still a point of debate whether the sulphur segregates to the intrinsically strong oxide/metal interface [37] or enhances the growth of existing voids at this interface [38]. Alloys containing high sulphur and no reactive elements are prone to early and severe scale spallation. Both hydrogen annealing and doping of the FeCrAl alloys with the reactive elements result in improvement of the scale adherence, but the RE-additions seem to be more beneficial [36]. It has been suggested [35] as well as proven by high resolution TEM analysis of an alumina forming alloy [39], that the reactive elements form stable sulphides in the alloy matrix, thus preventing it from segregating to the oxide/metal interface. The alloy manufacturers are well aware of the S-effect and the sulphur content in commercial FeCrAl materials is therefore normally kept below 20ppm.

The RE-effects with respect to the scale adherence are multiplex and they are generally no less complicated issue then the oxide growth. In addition to sulphur gettering, some other mechanisms, in which the reactive elements may positively influence the scale adhesion, are the vacancy sink model, mechanical pegging and enhanced chemical bonding [15].

The provision of vacancy sinks by the RE-oxide particles in the FeCrAl ODS alloys, which is claimed to effectively prevent their condensation into voids at the scale/metal interface, was a common idea to explain the RE-effect in the beginning of the 1980's [15]. However, since later it was shown that the alumina scales on RE-containing alloys grow by inward oxygen diffusion [22], this assumption appears to be hardly plausible [40].

The formation of RE-containing oxide protrusions (pegs) into the metal substrate was often observed on a number of wrought alumina forming alloys [40]. These pegs could contribute to the improvement of oxide adhesion, by "anchoring" the scale to the substrate. Unfortunately, this mechanism cannot explain why a good adherence is often observed for very flat and uniform alumina scales.

It has been shown by theoretical considerations [41] that the presence of RE-atoms or ions can decrease the free energy of the alumina/metal interface, thus enhancing the chemical bonding. However, on FeCrAl ODS alloys the scale adherence is greatly improved, although the

reactive element is present in the form of stable oxide particles. Hence, it should be clarified, how these particles "dissolve" and the reactive element becomes homogeneously distributed at the scale/metal interface, which makes this theory much more complex.

The improved scale adherence on RE-doped alloys can also be related to the change in the scale growth mechanism [8]. The scale adherence should indeed benefit from a decrease in the oxide thickening rate and prevention of convoluted scale morphologies, due to lower oxide stresses in comparison to those in the undoped scale after the same exposure time [8].

2.5.3. Oxide adhesion during temperature cycling

During the operation of FeCrAl components in practice, it is often not the intrinsic adhesion and/or oxide growth stress, but the stresses arising due to temperature cycling, which make the protective scales to fail. These thermal stresses are generated because of a mismatch in thermal expansion coefficients between the alloy and the alumina scale. Numerous literature exists on the failure of the alumina scales under temperature cycling conditions. This includes excellent reviews in references [42,43]. Among other factors, the stress generation and relaxation were found to depend on the scale structure and thickness, mechanical properties of oxide and metal, heating and cooling rates etc. In the present work, the effects of thermal stress will be discussed in detail in Chapter 5.3.4., when comparing the oxidation results of the commercial FeCrAl alloys.

3. Aim of the present investigation

The oxidation of FeCrAl alloys at elevated temperatures has been studied extensively for more than three decades. These studies have necessitated from both scientific understanding of the observed physical phenomena and from constantly growing technological importance of this class of high temperature materials.

Up to now, no comprehensive theory exists, that can explain the important effects of reactive elements on the scale growth rate and adherence, thus allowing optimisation of alloy chemical composition and microstructure for particular applications. Most of the scientific understanding of the above phenomena is based on short term oxidation data and its relevance to the long term operation of FeCrAl components is frequently doubtful. Moreover, little is known about interactive effects of minor alloying additions in commercial materials, which often contain a combination of reactive elements and a number of unavoidable or unintentionally added impurities.

At the same time, the industrial application of the FeCrAl alloys require their reliable operation at ever increasing temperatures often combined with a reduction in the component wall thickness. Under such critical operating conditions, the limited alloy Al-reservoir can rapidly run into short supply, resulting in a sudden breakaway oxidation of the component.

Therefore, it is of great importance to gain a better understanding of the lifetime oxidation behaviour of the commercial alloys and reveal the factors, affecting the depletion of the Al-reservoir. These studies should be combined with the long term oxidation experiments on model alloy systems, looking specifically at the interaction of the reactive elements with each other as well as with the frequently encountered alloy impurities.

In the current study the results of lifetime oxidation tests are presented carried out on a number of commercial and model alloys including wrought, powder metallurgical and ODS materials of thickness ranging from 0.05 to 2 mm. The test temperatures vary from 900 to 1300°C with accumulated exposure times up to 15 000 h. The experimentally determined lifetimes are compared with those, calculated from the available lifetime prediction model taking into account metallurgical aspects as well as component and service related parameters. In order to get a detailed insight into oxidation mechanisms as a function of exposure time

and temperature, shorter time oxidation tests are performed with subsequent characterisation of the formed oxide scales using a variety of surface analyses techniques. The latter include optical metallography, X-ray diffraction (XRD), scanning electron and transmission electron microscopy (SEM and TEM) coupled with energy dispersive x-ray analysis (EDXA), secondary ion mass spectrometry (SIMS) and Rutherford backscattered electron spectrometry (RBS).

In the following sections the current report will first describe and discuss experimental results concerning the lifetime of commercial FeCrAl alloys. The results will be compared with existing lifetime prediction model, described in Section 2.2. Subsequently, mechanistic studies will be presented to explain the encountered differences in oxidation behaviour of the commercial materials and variations between different batches of one material. The studies of batch to batch variations will relate to ODS as well as wrought alloys. For obtaining a better mechanistic insight into the above mentioned differences, studies on high purity model alloys with systematic variation in minor alloying additions will be presented. In a separate section effects of different metallurgical and testing parameters on the oxidation kinetics of FeCrAl alloys will be summarised. Finally, the existing lifetime model will be looked at on the basis of the obtained experimental data and proposals for developing more reliable lifetime prediction will be made. In general the results will be discussed in terms of alloy chemical composition and microstructure, however a number of other important issues, such as alloy or component creep strength and imposed mechanical constraints are taken into account, when considering the overall materials behaviour.

4. Experimental Procedure

4.1 Materials

The studied commercial and model FeCrAl alloys can be divided into three groups with respect to production methods and thus to a number of important properties including alloy microstructure, type and distribution of the reactive elements, mechanical strength etc.:

I) Wrought alloys, produced by conventional metallurgical methods (casting, followed by hot and cold rolling), namely: Aluchrom YHf, Kanthal AF, Model alloys;

II) A powder metallurgical alloy manufactured by spraying of the FeCrAl melt into powder, compacting by Hot Isostatic Pressing (HIP), hot and cold rolling: Kanthal APM;

III) Oxide Dispersion Strengthened (ODS) alloys, produced by mechanical alloying of FeCrAl powders with an yttrium oxide dispersion followed by HIP and/or hot and cold rolling: PM2000, MA956 and Model ODS alloys.

Most of the alloys prevailed as cold-rolled sheets with a thickness varying from 0.05 to 2 mm. Some of the ODS materials were delivered as hot extruded bars of 6 mm in diameter. The batch designation, sheet thickness and chemical composition analysed by Atomic Absorption Spectrometry (AAS) for each of the studied commercial and model alloys are listed in Tables 1 to 3 in Appendices.

4.2 Specimen preparation

Coupons of 20×10 mm size or 6 to 12 mm diameter discs were machined from the as-delivered materials. Depending on the requirements of the experimental set-up, in some of the specimens a 2mm hole close to the specimen edge was drilled. The 0.05 mm thick foils of the wrought alloys were oxidised in the as-received (cold-rolled) state. The 0.1 mm thick foils of the ODS alloy PM 2000 and 0.5 to 2.0 mm thick sheets were ground to 1200 grit surface finish using SiC-paper. Some of the specimens, intended for subsequent investigation of the oxide scales with sensitive surface analysis techniques, were polished with 1µm diamond paste. All specimens were ultrasonically degreased in a detergent before oxidation.

4.3 Oxidation testing

Cyclic lifetime oxidation tests were performed in resistance heated furnaces in laboratory air at temperatures varying between 900 and 1200°C. The 0.05 to 0.10 thick specimens (foils) were normally exposed in a vertical cyclic oxidation rig (Figure 4.1). The specimens hung freely on platinum hooks mounted on a carousel-type silica specimen holder. The specimen holder on a lifting stage was inserted in and removed out of the hot zone of the furnace at regular time intervals. The oxidation kinetics during the cyclic exposures were determined by weighing of the specimens after cooling to room temperature. The cyclic conditions for the foils were normally 20 h cycles i.e. 20 h heating at the oxidation temperature / 2 h cooling at room temperature. The heating/cooling rates were in the order of 600 K/min.

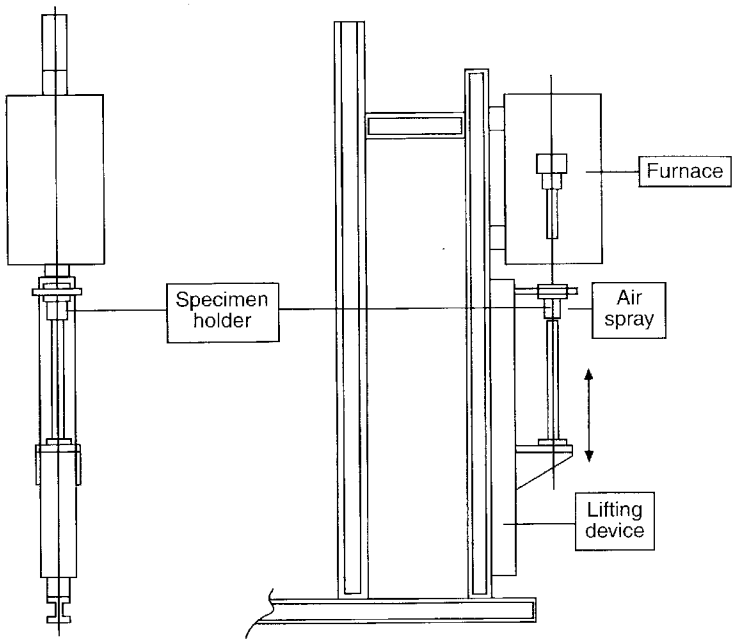

Figure 4.1: Schematic of cyclic oxidation rig used in this study

The 0.5 mm - 2 mm thick coupons were normally oxidised till breakaway in a tube furnace using 100 h cycles, i.e. 100 h at the oxidation temperature and 2 h at room temperature with heating / cooling rates of ca. 90 K/min. These specimens were put into small alumina crucibles that enabled oxide spall collection during testing. Three parameters of the oxidation kinetics during 100 h cycles exposures were determined from the mass change measurements. The first one was the gross mass change i.e. the mass change of the crucible with the specimen, which effectively represents the total oxygen uptake including the adherent and the spalled oxide. The second parameter was the specimen mass change, characterising the oxygen uptake by the adherent scale. Finally, the difference between the gross and specimen mass changes gave the mass of the spalled oxide.

In order to determine isothermal oxidation kinetics, thermogravimetric (TG) experiments up to 200h at temperatures between 900°C and 1300°C were carried out in synthetic air using a SETARAM® microbalance. The heating / cooling rates were 90 K/min.

4.4 Characterisation of oxidised specimens

The oxidised specimens were analysed using a variety of techniques, commonly used in materials science. These included optical metallography, X-Ray Diffraction (XRD), Scanning Electron Microscopy (SEM) with Energy Dispersive X-Ray Analysis (EDX), Electron Probe MicroAnalysis (EPMA), Transmission Electron Microscopy (TEM), Secondary Ion Mass Spectrometry (SIMS), Atomic Force Microscopy (AFM). The application of the above methods for studying thermally grown oxide scales have been described elsewhere [44]. Procedures used for quantification of the SIMS depth profiles of oxide scales have been given in reference [45]. Before preparation of the mounted cross sections the oxidised specimens were first sputtered with a thin gold layer and subsequently electrochemically Ni-coated in a $NiSO_4$-bath. This procedure was necessary to protect the scales during mounting and polishing steps as well as to achieve a better optical contrast during metallographic studies.

5. Lifetime of Commercial Alloys

5.1 Oxidation of commercial FeCrAl foil materials

5.1.1 Lifetime of commercial foils during isothermal and cyclic oxidation

The chemical composition of the studied foil materials can be found in Table 1 in Appendices. It is worth noting that the concentrations of the major elements, i.e. Fe, Cr and Al in all foils are very similar. In the given composition range of Fe, Cr and Al at high oxidation temperatures all the alloys are expected initially to form continuous alumina scales [16].

Comparison of the mass change data during isothermal and 20 h cycles oxidation for three commercial FeCrAl foils at 1200°C is presented in Figures 5.1 to 5.3 respectively. No significant difference in mass gain between cyclic and isothermal oxidation for a given alloy batch was observed until breakaway.

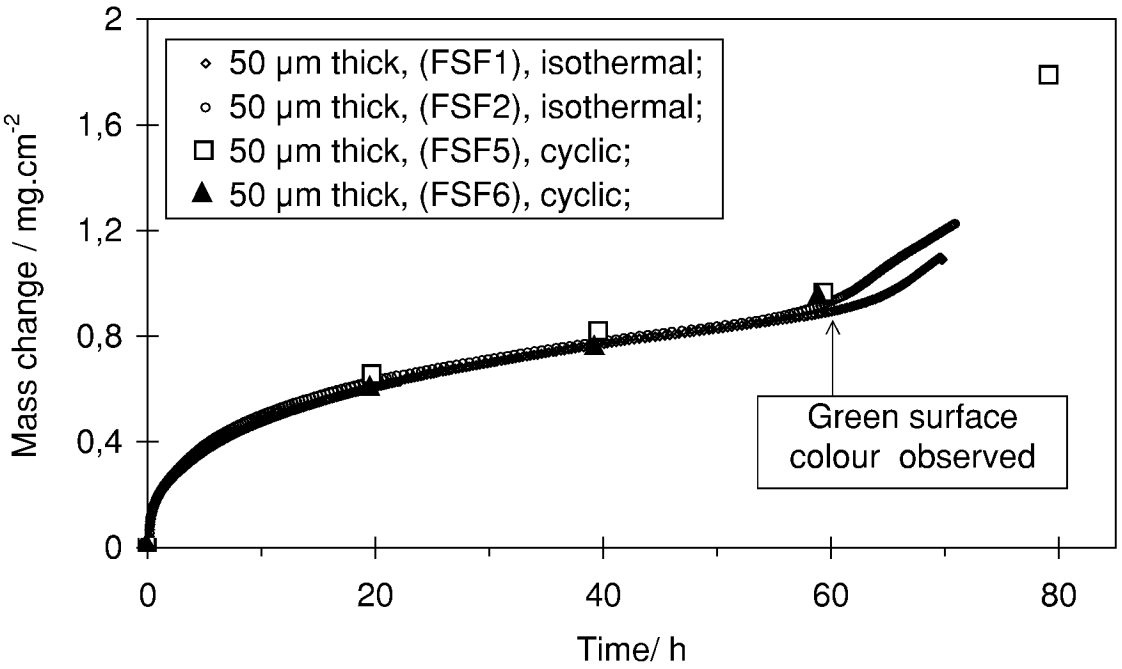

Figure 5.1: Mass change data for 50 µm thick foils of Kanthal AF during isothermal and 20h cycles exposures at 1200°C in air

An important observation made during cyclic tests was that the foils of the wrought alloys Aluchrom YHf and Kanthal AF showed greenish surface colouring at least one cycle before the real breakaway apparent by the presence of black Fe-rich oxides. The greenish colour was attributed to chromia formation. Contrary to the wrought foils, the ODS foils of PM2000 did not show this chromia formation prior to breakaway.

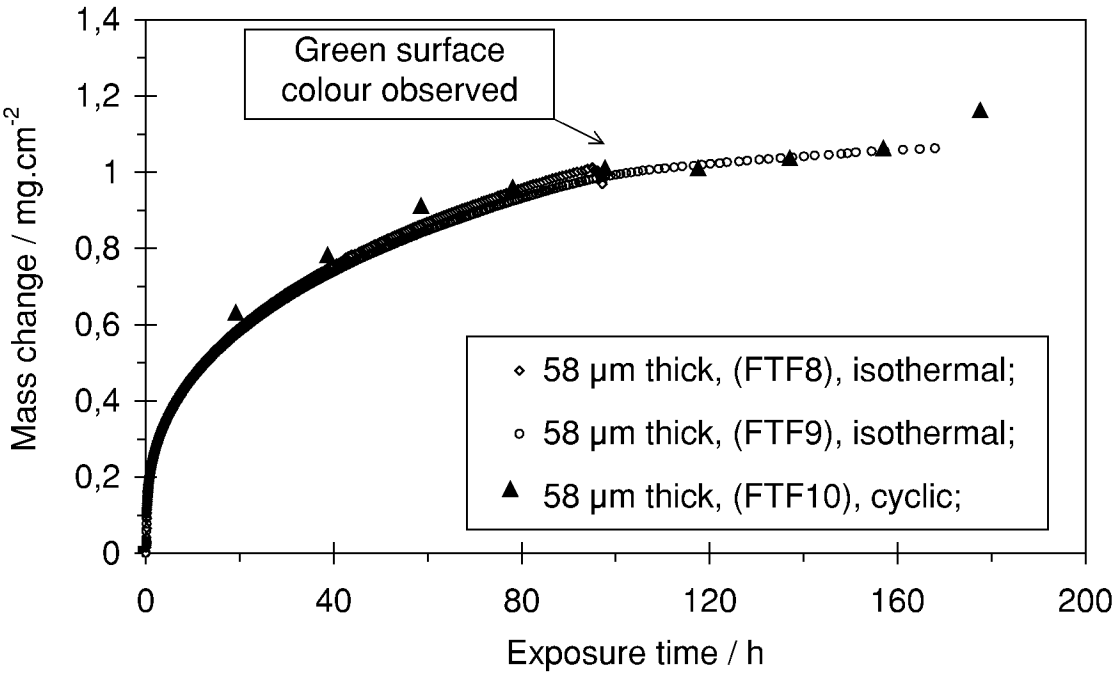

Figure 5.2: Mass change data for 58 µm thick foils of Aluchrom YHf during isothermal and 20h cycles exposures at 1200°C in air

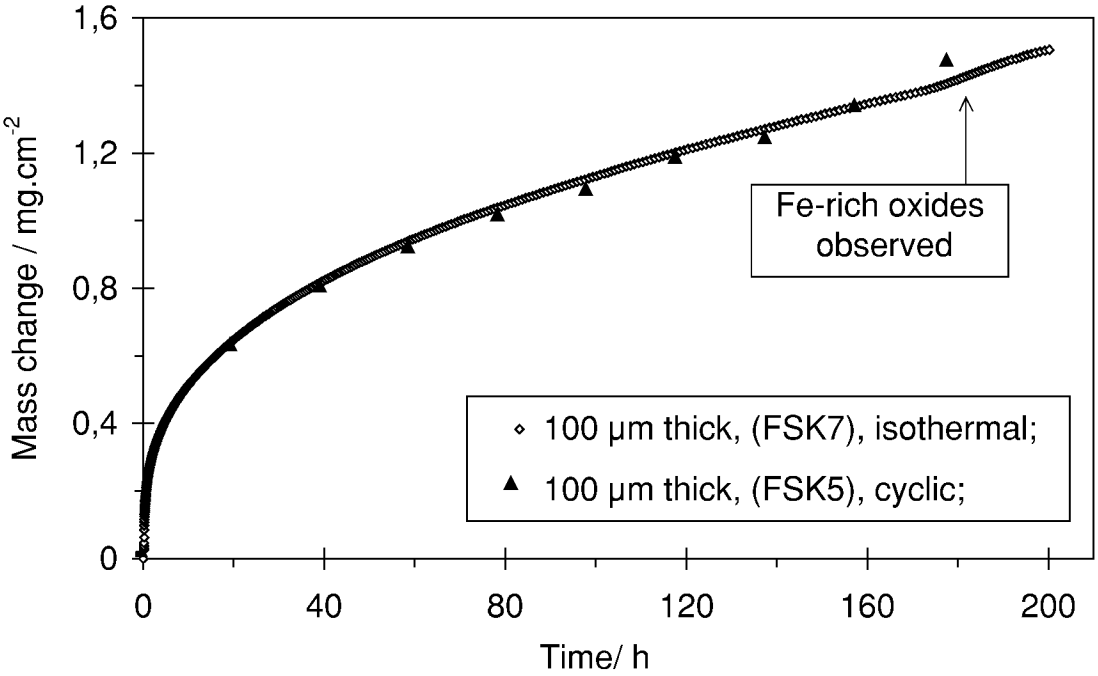

Figure 5.3: Mass change data for 100 µm thick foils of PM 2000 during isothermal and 20h cycles exposures at 1200°C in air

The thermogravimetrical data obtained in the microbalance during isothermal oxidation of the three commercial foils at 1200°C are shown in Figure 5.4.

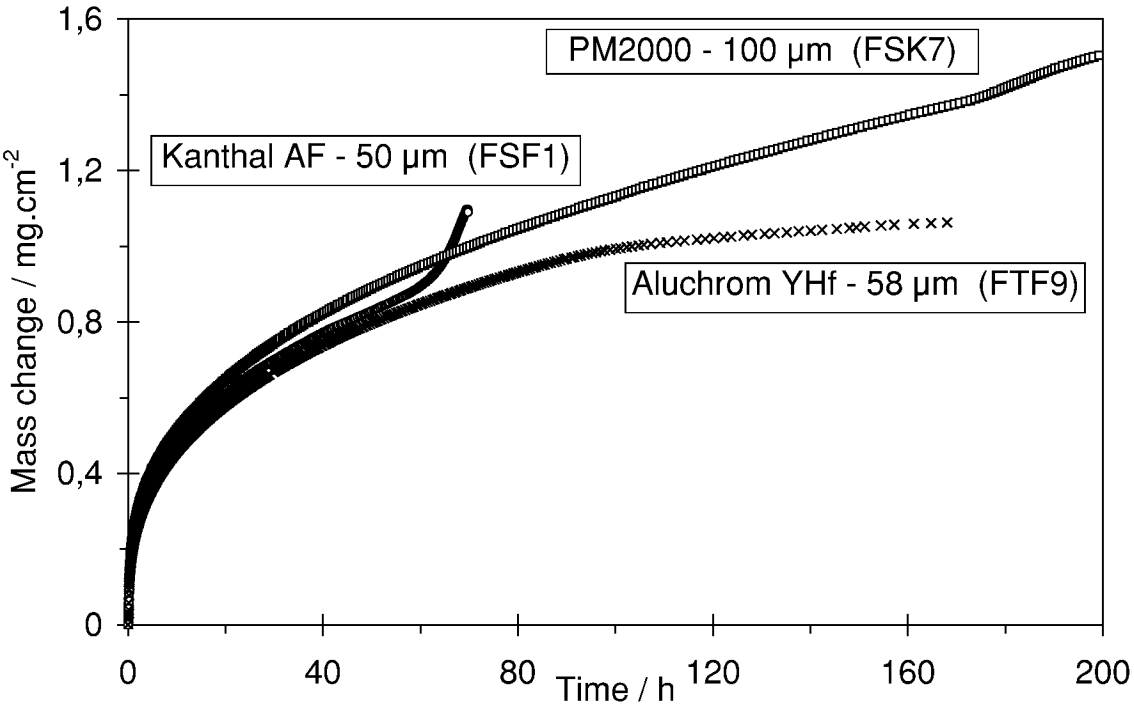

Figure 5.4: Comparison of mass change data for studied foils of commercial alloys during isothermal oxidation at 1200°C in synthetic air

The results of the TG experiments were used for two purposes. First, the oxide growth rate constants ***k*** and ***n*** (compare eq-n 2.12) were determined using a double logarithmic plot of the mass change data. An example of the latter is presented for the 58 µm thick foil of Aluchrom YHf in Figure 5.5.

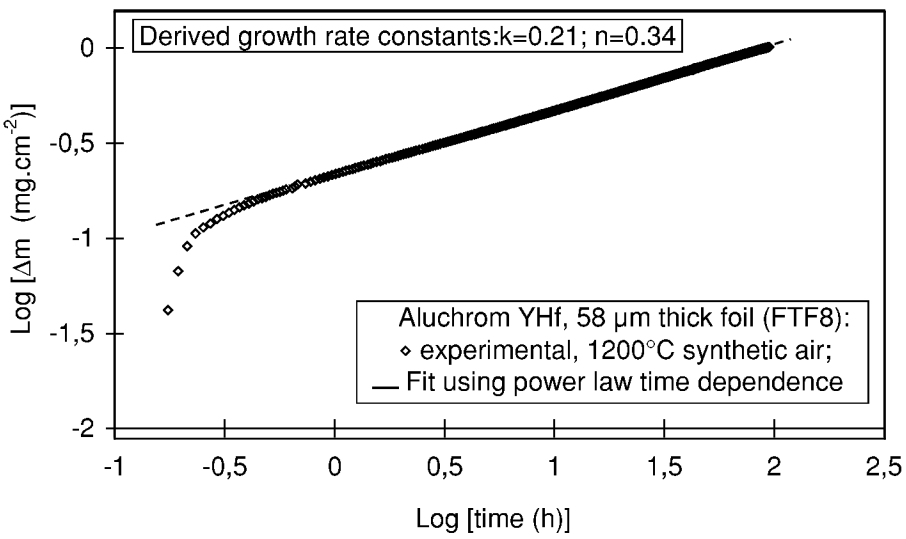

Figure 5.5: Double logarithmic plot of mass change data for 58 µm thick Aluchrom YHf foil during isothermal oxidation at 1200°C in synthetic air and fitting of data using power law time dependence

The values of ***k*** and ***n*** for the studied foil materials are shown in Table 5.1. The lowest growth rates were found for the 58 µm specimens of Aluchrom YHf and the highest for the 100 µm thick specimens of PM2000.

Table 5.1: Values of power law constants k and n describing oxidation kinetics of studied foils during isothermal oxidation at 1200°C (k and n defined after eq-n (2.12) as $\Delta m=k.t^n$, where Δm is the mass change in mg/cm^2 and t is the exposure time in hours)

Material	Thickness	k	n
Aluchrom YHf	58 µm	0,21	0,34
Kanthal AF	50 µm	0,20	0,38
PM2000	100 µm	0,24	0,34

The second important reason for carrying out the thermogravimetric measurements was for a very accurate determination of the foil lifetime by calculating the time dependence of the parabolic rate parameter k_P. Based on eq-n 2.10 k_P can be defined as:

$$k_P = \frac{\Delta m^2}{t} \tag{5.1}$$

If the scale growth satisfies the parabolic law in eq-n (2.10), k_P has a constant value independent of time, which is effectively a tangent of the linear function $\Delta m^2 = f(t)$. However, since the scale growth on the studied alloys is sub-parabolic, eq-n 5.1 can be re-written for a definite oxidation time to give an instantaneous parabolic rate parameter, which is time dependent:

$$k_P(t) = \frac{d(\Delta m^2)}{d(t)} \tag{5.2}$$

Plotting k_P versus time allows pin-pointing of very small changes in the scale growth rate, which are not apparent from the original mass change data [46].

The $k_P(t)$-plots for the three foil materials are given in Figures 5.6 – 5.8. During the first 40h oxidation of the 50 µm Kanthal AF foil (Figure 5.6) k_P slowly decreases with time, which is typical for alumina forming alloys exhibiting sub-parabolic oxidation rates [47]. However, after approximately 43-44 h exposure k_P exhibits a slow increase. At this stage apparently the chromium-rich oxide starts to form. The dominating formation of Fe-rich oxides leading to a rapid increase of k_P occurs apparently after around 57 h. In the case of the 58 µm Aluchrom foil after about 95 h isothermal oxidation at 1200°C even a decrease in k_P was found (Figure 5.7), which continued up to 160 h without any indication of breakaway (compare with Figure 5.6). This decrease was related to the chromia formation and confirmed by the specimens

oxidised at 20 h cycles which showed greenish surface colouring after the fifth cycle i.e. 100 h exposure.

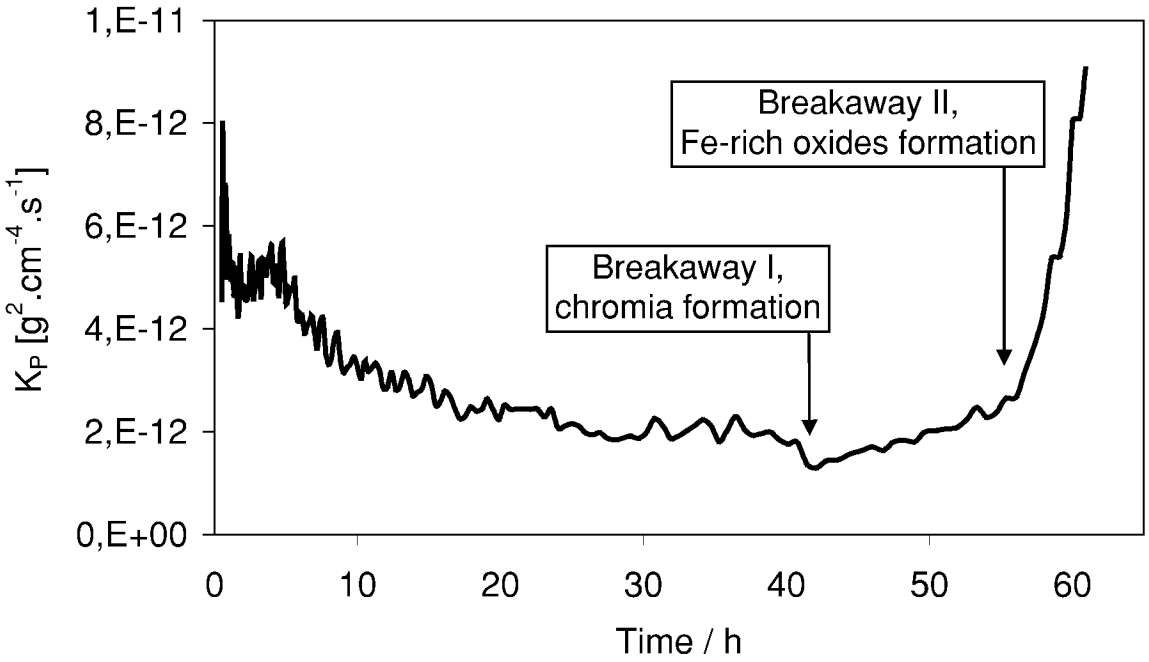

Figure 5.6: Instantaneous parabolic rate parameter vs time for isothermal oxidation at 1200°C in synthetic air of 50 µm thick wrought foil of Kanthal AF

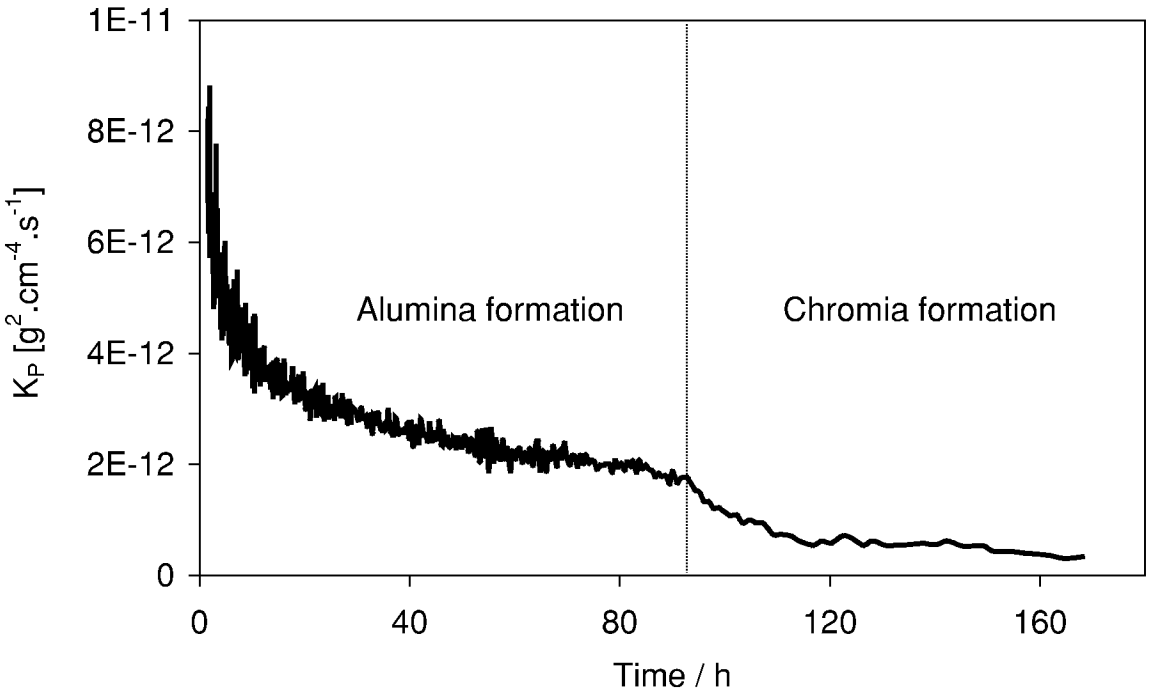

Figure 5.7: Instantaneous parabolic rate parameter vs time for isothermal oxidation at 1200°C in synthetic air of 58 µm thick wrought foil of Aluchrom YHf

In contrast to the wrought foils, the $k_P(t)$ plot for the 100 µm thick ODS foil of PM 2000 did not show any changes in the scale growth rate due to the chromia formation prior to "classical" breakaway, which occurred apparently after around 170 h exposure (Figure 5.8).

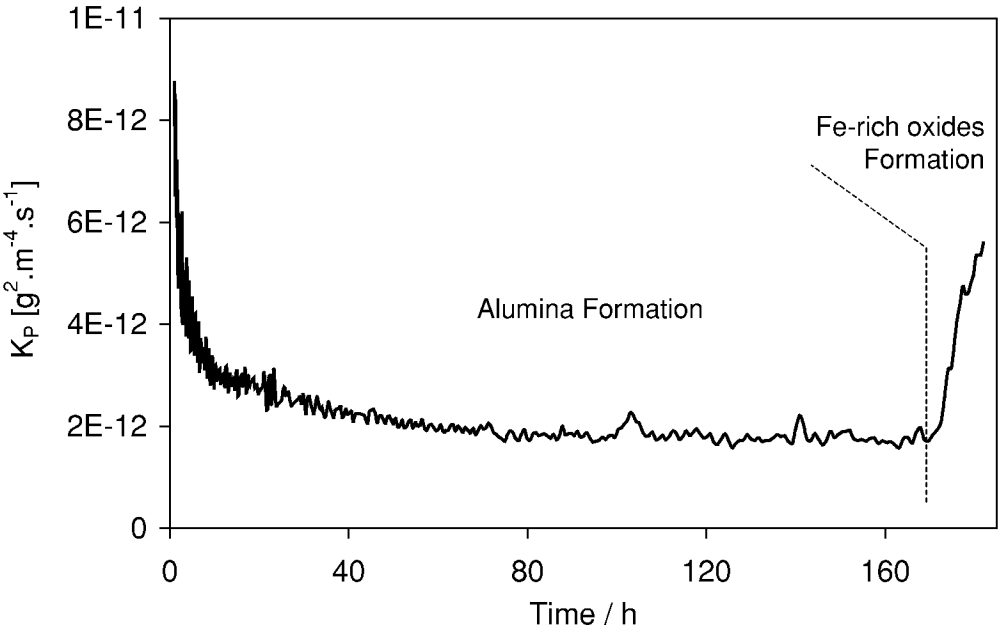

Figure 5.8: Instantaneous parabolic rate parameter vs time during isothermal oxidation at 1200°C in synthetic air of 100 µm thick ODS foil of PM 2000

5.1.2 Metallographic studies of oxidised commercial foils

The ODS foils clearly showed a type of breakaway oxidation which is different from that of the wrought alloy foils (Figures 5.9-5.11). For the ODS material the breakaway front macroscopically starts at the specimen corner propagating towards the centre (Figure 5.9-a). Metallographic cross-section (Figure 5.10) shows the typical appearance of commencement and progress of breakaway as previously described in literature for thick ODS coupons [3,4]. The breakaway front is preceded by a region of internal oxidation (Figure 5.10) and further away from the front, by TiN precipitates within the alloy matrix. In case of the wrought alloy foils breakaway is accompanied by changes in surface colour and deformation of the specimen (Figure 5.9-b). The metallographic cross-sections reveal that this is caused by formation of chromium-rich oxide beneath the alumina scale (Figure 5.11). This double-layered scale, which is macroscopically apparent by a greenish colouring, covers practically the whole surface of the foil before rapidly growing Fe-rich oxides start to form. After longer exposure time severe scale and substrate deformation occur and frequently the formation of large rectangular pores is observed (Figure 5.12).

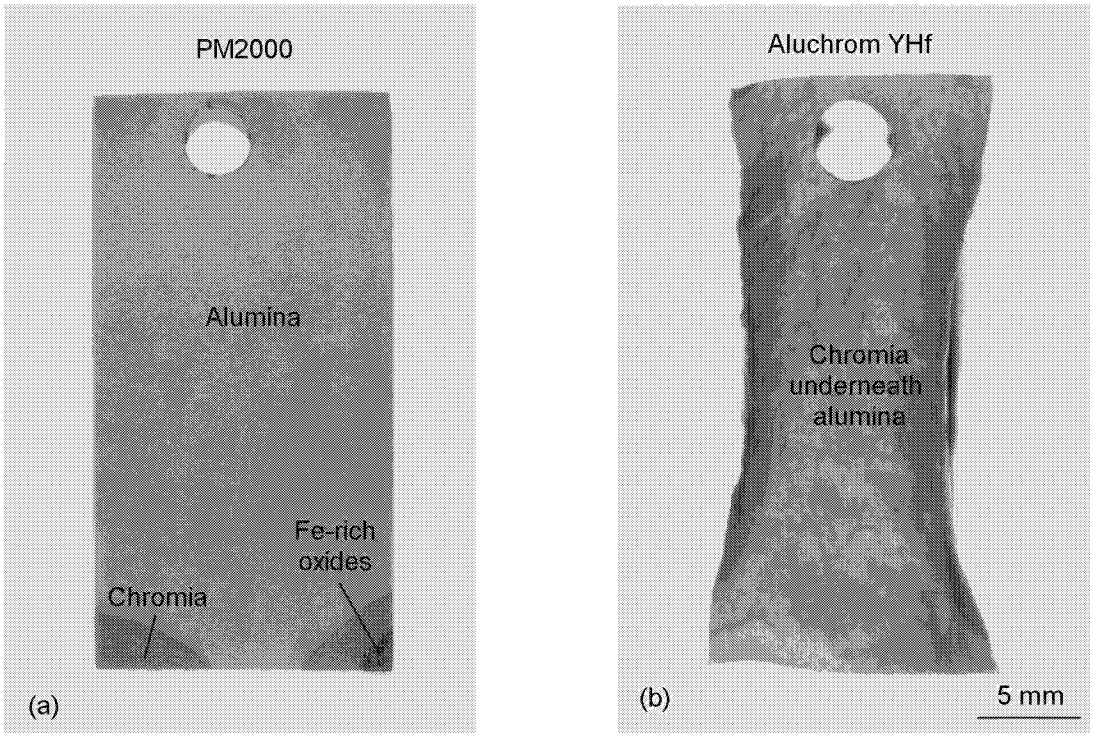

Figure 5.9: Macrographs of breakaway features for commercial FeCrAl foils after isothermal oxidation at 1200°C in synthetic air: (a) ODS alloy PM2000 100 µm thick foil after 200h exposure; (b) wrought alloy Aluchrom YHf 58 µm thick foil after 170 h exposure.

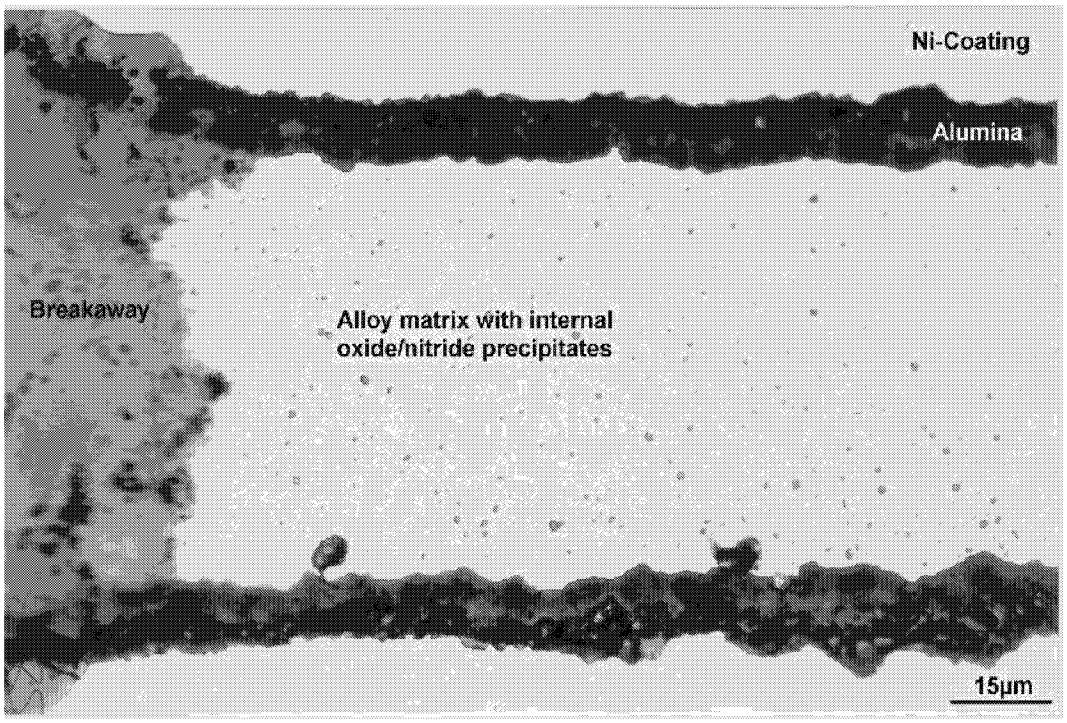

Figure 5.10: Metallographic cross-section of 100 µm thick ODS foil after 200 h isothermal oxidation test till breakaway at 1200°C in synthetic air.

The residual aluminium content (C_B) in the matrices of the studied foils was determined by window EDX analysis. It is important to stress that point EDX or EPMA analyses may not always give relevant values of $\boldsymbol{C_B}$ due to the internal precipitation of aluminium nitrides

and/or oxides, resulting in extremely low matrix Al concentration [12,46]. Far from the breakaway front in the matrix of the ODS PM2000 foil an aluminium content of 1.2 to 1.5 mass% was measured. This is in agreement with literature data for thick ODS coupons [11,12]. The EDX measurements in the region of internal oxidation next to the breakaway front showed, however, much lower values i.e. less than 0.5 mass%. Contrary to PM2000, only less than 0.3 mass% of aluminium were determined by EDX in the Kanthal AF and Aluchrom YHf foils. This leads to the conclusion that in case of the wrought materials almost all aluminium had been consumed before the formation of a chromia sub-scale, started.

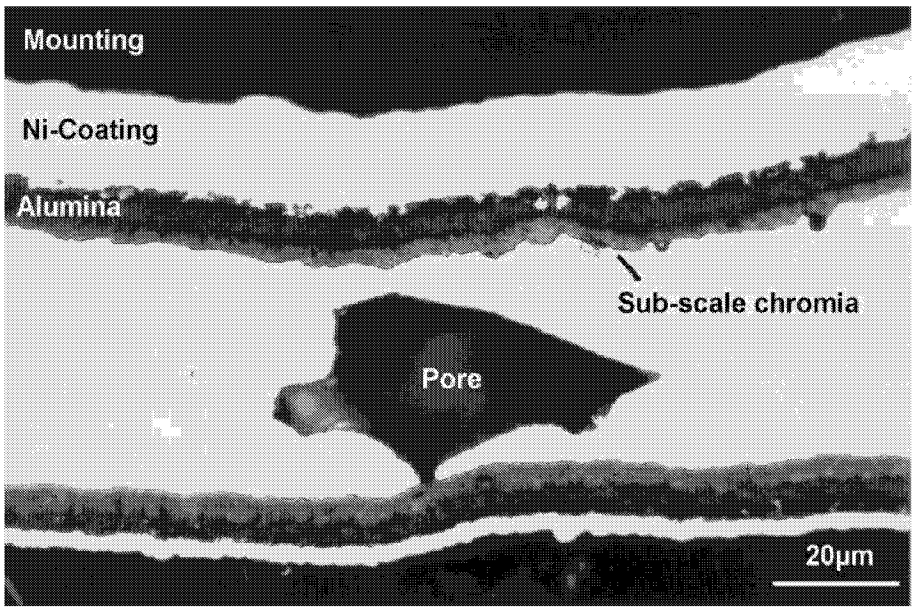

Figure 5.11: Metallographic cross section of 58 µm thick wrought Aluchrom YHf foil after 170 h isothermal oxidation at 1200°C in synthetic air

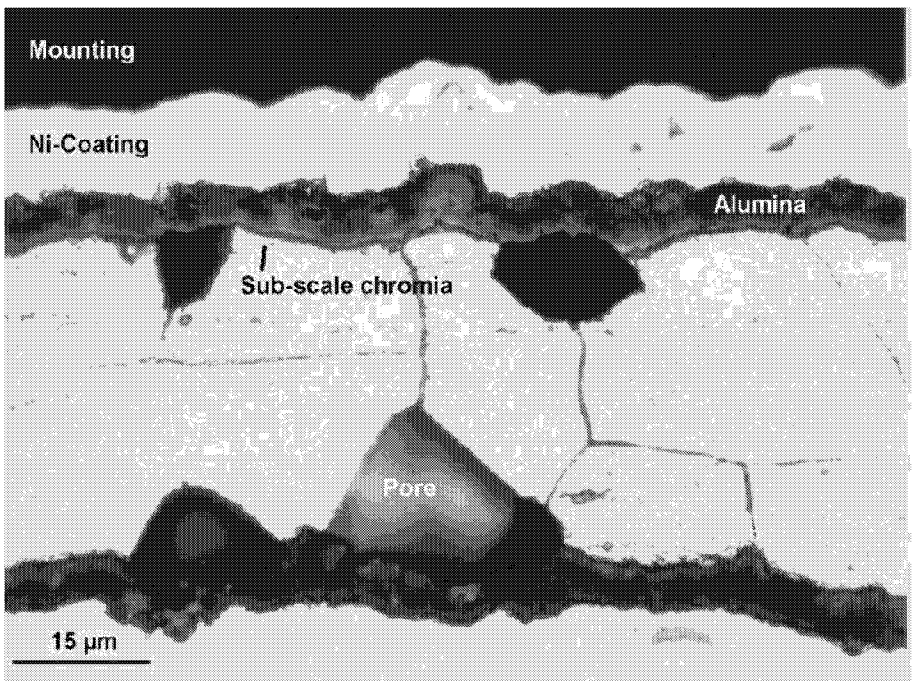

Figure 5.12: Metallographic cross-section of 50 µm thick wrought Kanthal AF foil after 60 h isothermal oxidation till breakaway at 1200°C in synthetic air

5.1.3 Lifetime of commercial foils: prediction and experimental observations

Times to breakaway of the foil materials assuming that no scale spalling occurred, were calculated using the equation (2.18). C_B values of 1.3 mass% for the ODS foils and 0.3 mass% for the foils of the wrought alloys respectively were used. The oxidation rate parameters k and n determined from the isothermal oxidation testing were taken from Table 5.1. The calculated values of t_B are plotted together with the experimental data in Figure 5.13 showing good agreement between prediction and measurements.

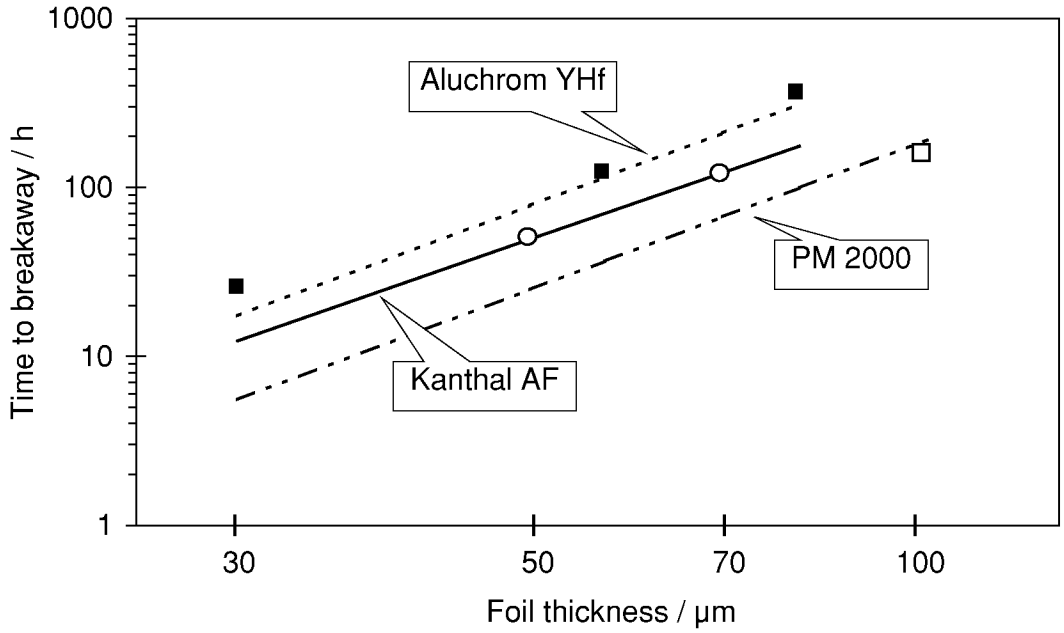

Figure 5.13: Time to breakaway vs thickness plot for studied commercial foils. Lines represent calculated lives derived from eq-n 2.18 and points are for experimental data.

The presented results indicate that for thin foils of the wrought FeCrAl alloys, as was also reported elsewhere [48,49,50], three stages of oxidation can be distinguished: 1- alumina formation; 2 - sub-scale chromia formation and 3 - formation of iron-based oxides.

The duration of each stage is alloy dependent and seemingly depends on the foil thickness. The results also confirm that for thin foils the time at which sub-scale chromia formation occurs can actually be considered as t_B because this event is accompanied by significant deformation of the foil (Figure 5.9 and reference [48]). A possible explanation for the latter effect are the stresses induced by the chromia growth. It is well established that both aluminium and chromium oxides on Fe-based RE-doped alloys grow mainly by inward oxygen diffusion [22,23]. In this case compressive growth stresses within the scale can be related to the larger volume of the formed oxide compared to that of the metal consumed, i.e. the so called Pilling-Bedworth Ratio (PBR) [51]. The PBRs for alumina on a Fe20Cr5Al alloy and chromia on the Al-depleted Fe20Cr alloy were calculated to be 1.8 and 2.1 respectively.

Thus, higher compressive growth stresses are expected in sub-scale Cr_2O_3 than those in the initially formed Al_2O_3. The compressive stresses in the scale result in tensile stresses and plastic deformation in the thin, mechanically weak substrate especially at the oxidation temperature of 1200°C.

The significant deformation of the foils because of the growth stresses and perhaps the thermally induced stresses on cooling can also justify the observed porosity in the alloy matrix (Figure 5.12). Thin section foils have a high surface to volume ratio. This means that even a relatively small increase of length and width should result in a large decrease in the section thickness with relatively high deformation rates [50]. At temperatures as high as 0.85 T_{melt}, assuming that no high oxide growth stresses have developed, the deformation is most probably to occur by diffusional creep flow [42]. In the deformed substrate the plastic flow is obviously not uniform. It follows then that locally within the alloy substrate the vacancy concentration can be high enough for pore nucleation and subsequent growth. The nucleation and growth of pores take place at alloy inhomogenities, e.g. at the alloy grain boundaries, as confirmed by metallography in Figure 5.12. An additional factor, namely coalescence of vacancies left by Al and Cr atoms within the alloy matrix, may also contribute to the observed porosity.

The 58 µm thick Aluchrom YHf foils behaved in a slightly different manner upon the occurrence of chromia formation as Kanthal AF. For Aluchrom YHf the second stage of oxidation is very extended and the instantaneous k_P values are even lower than during the first stage (Figure 5.7). Similar observations by Ishii et al. [48] were explained by the fact that the growth of chromia is limited by the oxygen transport through the initially formed Al_2O_3. Another reason for this drop in oxidation rate may be chromium loss due to evaporation of volatile CrO_3 and/or $CrO_2(OH)_2$ species at the high oxidation temperature [5].

In contrast to the wrought alloys the mechanism of breakaway oxidation for PM2000 foils (see Figures. 5.8-5.9) is very similar to that of 1-2 mm thick ODS specimens previously described in references [11,12]. Fe-rich oxides formation starts at the corner of the specimen progressing towards the centre. As can be concluded from the macrograph in Figure 5.9. and the parabolic parameter plot in Figure 5.8., the second oxidation stage, accompanied by sub-scale chromia formation for the ODS foil is extremely short. Assuming C_B=1.3 mass%, the time to breakaway was calculated with eq-n 2.18 for 100 µm PM2000 foil to be around 170 h, which is in excellent agreement with the experimental data (Figure 5.3). A large region in the

alloy matrix is affected by breakaway: an internal oxidation zone appears and further from the breakaway front an area with TiN precipitates is visible. These nitride precipitates have formed apparently by the reaction of titanium with nitrogen diffusing through the breakaway area into the alloy [12]. The TiN precipitates do not exist in the region of internal oxidation probably because of the high local oxygen activity. The zone of TiN precipitates and the area totally unaffected by breakaway can lead to the conclusion that the Al activity in these places is still high enough to maintain the protective alumina scale.

The above results indicate that the oxidation behaviour of the wrought materials and that of the ODS materials are different. Because of a thicker specimen section the studied ODS foils prior to exposure had a larger Al-reservoir than the thinner wrought foils. However, as can be seen from the plot in Figure 5.13, when comparing the same wall thickness, the time to breakaway for the ODS material is much shorter, than those of Kanthal AF and especially Aluchrom YHf. Such a lifetime reduction of PM2000 can be attributed on one hand to the higher scale growth rates (Figure 5.3 and Table 5.1). On the other hand the shorter life of the ODS material is due to the higher value of C_B. The difference in critical concentration for the formation of a continuous alumina layer is surprising for alloys with very similar major element contents. Simple thermodynamic calculations show that, if the alumina scale is dense and adherent, the aluminium must be depleted practically to zero before chromium oxide becomes more stable than alumina.

The reasons for the higher C_B of the ODS alloy can be related to the nature of the ODS material, i.e. to the presence of yttria dispersion in the alloy matrix. First, there is a possibility that the yttria dispersion has a different effect on the selective oxidation of aluminium, than the metallic yttrium. It might be that the incorporation mechanism and mobility of yttrium in the alumina are different for the ODS alloys and the wrought materials. For chromia formers, in which a very similar reactive element effect is shown by yttria it was found recently [52], that the oxidation rates of a chromium based ODS alloy strongly depended on the distribution of the oxide dispersoid within the alloy matrix. Thus the local yttria deficiencies due to its inhomogeneous distribution may result in a failure of establishing a continuous alumina layer by the Al-depleted alloy. It might also be that the tiny (10 to 20 nm) yttria particles serve as nucleation sites for internal oxidation of aluminium, as described elsewhere [5].

The second assumption, which seems to the author to be more plausible is based on the fact that yttria dispersion greatly increases the alloy creep strength at elevated temperatures by the

dislocation pinning mechanism [53]. The importance of alloy creep for the relaxation of the oxidation induced stresses has been shown in reference [42] and verified experimentally elsewhere [54]. The stresses due to the scale growth and temperature cycling can not be relaxed by the alloy creep of the ODS substrates as easy as in case of wrought alloy substrates. Thus, the relaxation of the stresses within the oxide is most probably to occur by scale cracking and /or spalling [42]. This imparts that locally in the vicinity of a crack or a spalled region, high oxygen activities close to those in the atmosphere can be reached. According to the Wagners' treatment of internal oxidation [13] an increase in oxygen activity can lead to internal oxidation of Al, which is in a short supply in the Al-depleted matrix, or in other words should result in an increase of C_B. If, however, the surface scale remains gas tight and well adherent to the substrate, which is apparently the case of the wrought alloys, than the Al can be depleted to a much lower practically zero level before breakaway. Figure 5.14 schematically illustrates the effects of protective properties of the alumina scale on C_B [50].

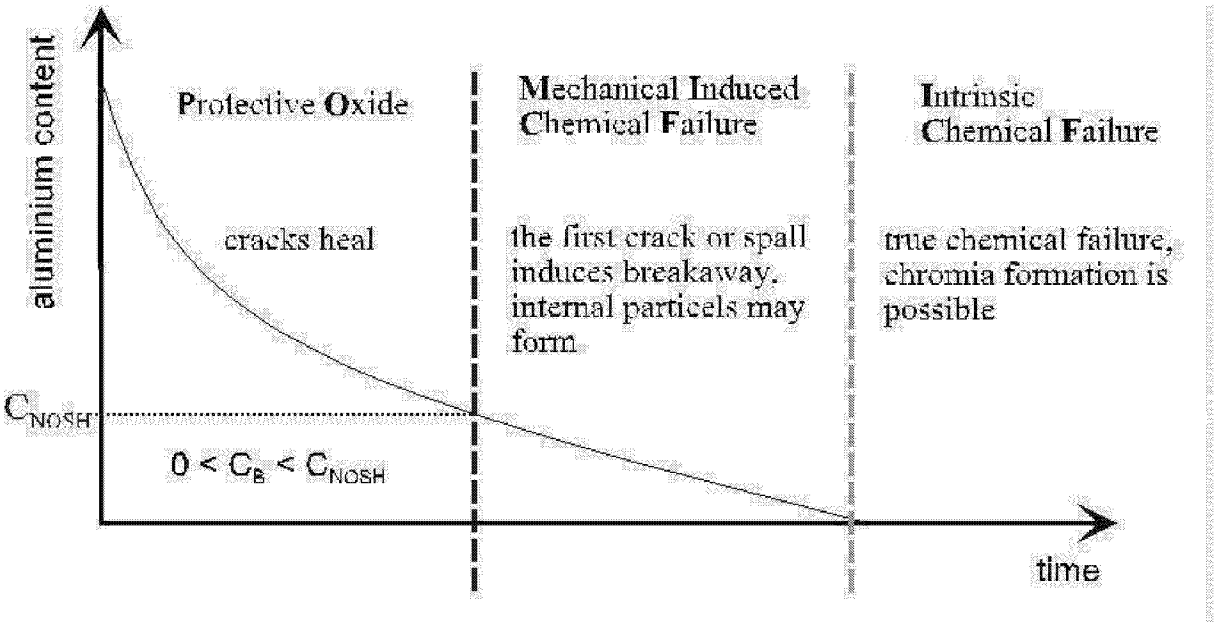

Figure 5.14: Effect of protective properties of alumina scale on critical Al-content for occurrence of breakaway oxidation; after reference [50]

5.2 Effect of mechanical constraints on life of FeCrAl-foil based components

The results presented and discussed in the previous section consider the oxidation of free hanging foils. The oxidation behaviour of real components (e.g. a car catalyst substrate) can be different from that of free hanging foils due to a more complicated geometry, which can impose mechanical constraints and enable crevice corrosion in joints. Figure 5.15 shows that the scales formed on a free hanging foil at 1100°C exhibit slower oxidation kinetics than those formed on the mechanically constrained ring and model catalyst specimens, which were manufactured from the same foil sheet. The macrophotograph of the model catalyst after the testing (Figure 5.16) clearly shows that on part of the specimen chromia has formed and this chromia formation is accompanied by macroscopically visible scale cracking.

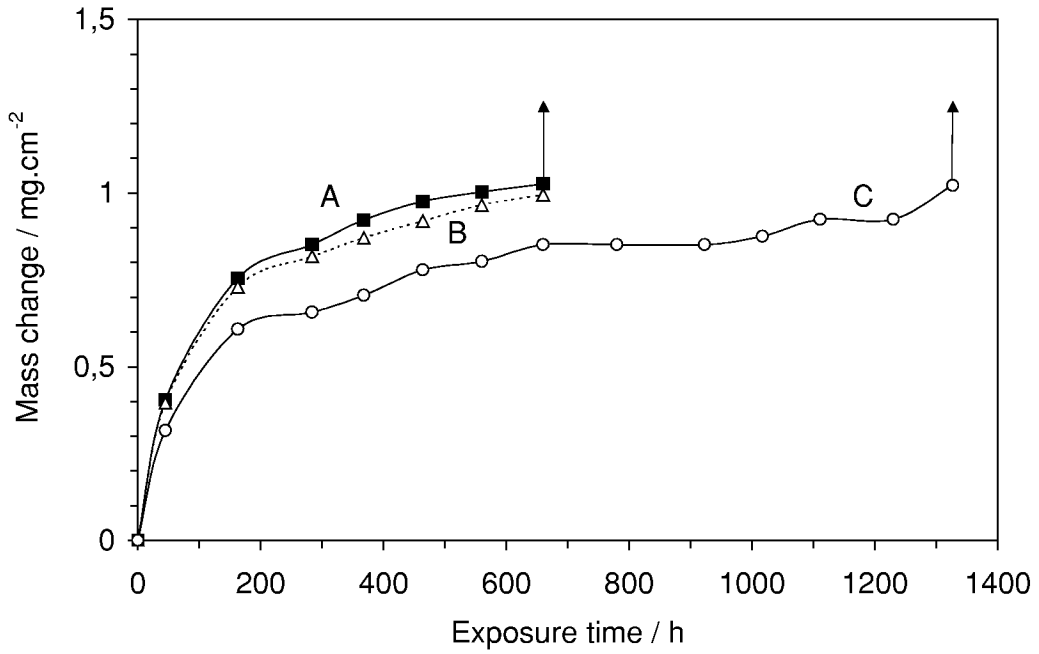

Figure 5.15: Mass change data for Aluchrom YHf foil-based components during 100 h cycles oxidation at 1100°C in air: A-Model car catalyst; B-Ring specimen; C-free hanging foil coupon. Tests were interrupted upon visual observation of chromium oxide (indicated by arrows)

As it was claimed in the previous chapter, the oxidation induced stresses can be relaxed either by the plastic deformation of the substrate or by scale cracking. For free hanging, wrought foils the first relaxation mechanism will prevail.

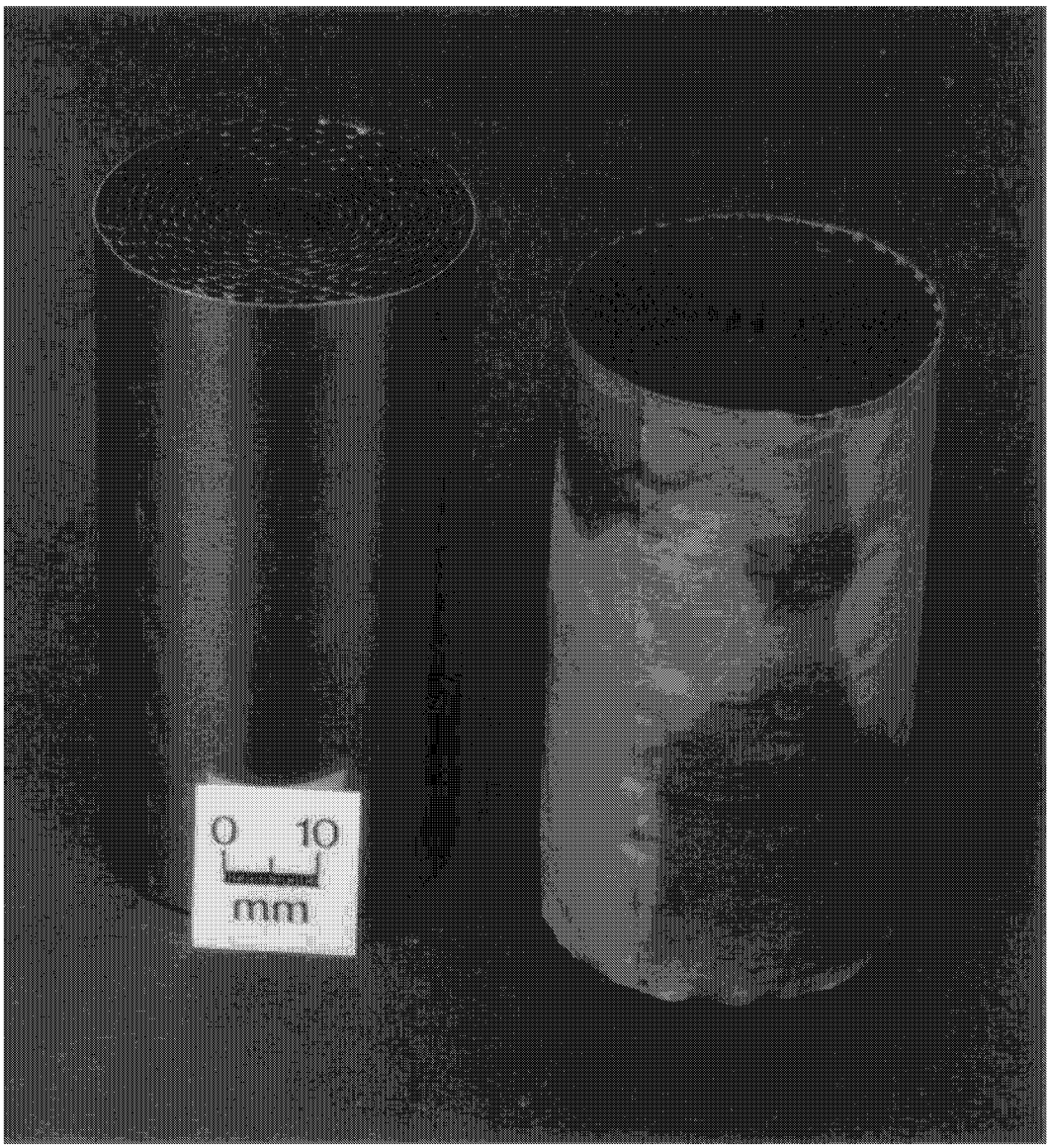

Figure 5.16. Macroscopic pictures of FeCrAl-foil based model car catalyst prior to exposure (left) and after 670 h oxidation at 1100°C in air (right, compare mass change data for specimen A in Figure 5.15)

The reason for the accelerated oxide growth on the ring and model catalyst specimens can be an inability of the constrained substrate to relax the oxidation induced stresses by deformation. It is important to note that no macroscopically visible cracks had been seen on the constrained ring and model catalyst specimens until the formation of chromia was observed. Hence, in the case of the constrained specimens, relaxation of the oxide stress most probably occurs by the scale microcracking mechanism described elsewhere [43]. Consequently, fast molecular oxygen transport through the microcracks results in accelerated scaling kinetics.

5.3 Oxidation behaviour of 0.5 to 2 mm thick sheets of commercial alloys

5.3.1. Kinetics of oxide growth and spalling during long term oxidation

The cyclic oxidation performance of 0.5 to 2 mm thick plates of the commercial FeCrAl alloys was tested at 100 h cycles. The results of the tests are presented in Figures 5.17-5.19. The first plot for each set of materials shows the total oxygen uptake, i.e. the sum of the specimen mass change due to the scale growth plus the mass change of the spalled oxide. The second plot for each set of the sheet materials presents the mass change of the spalled oxide as a function of time.

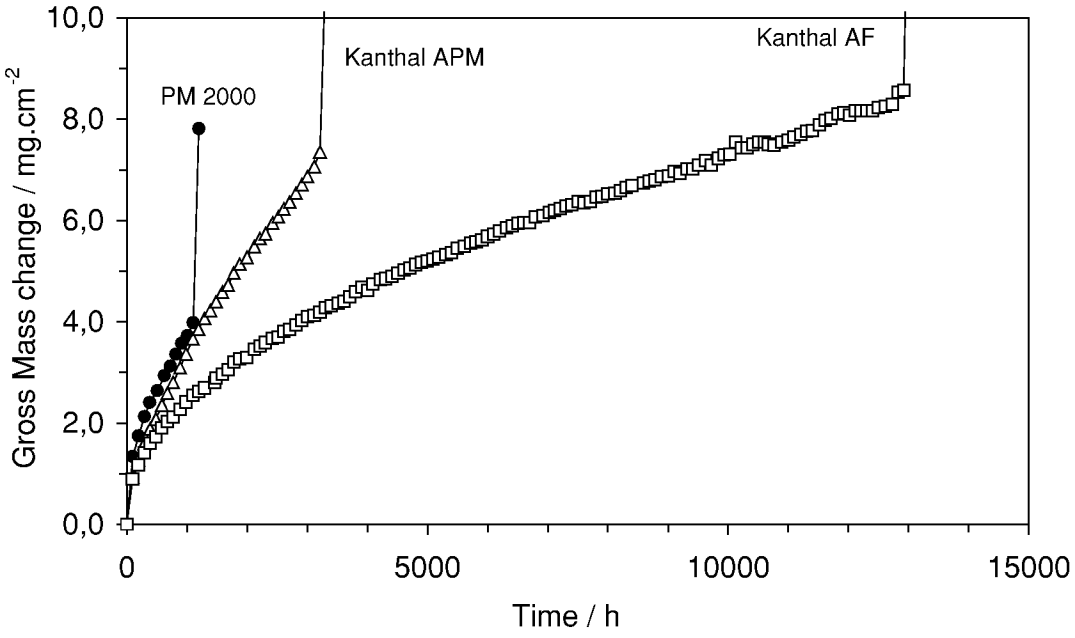

(a)

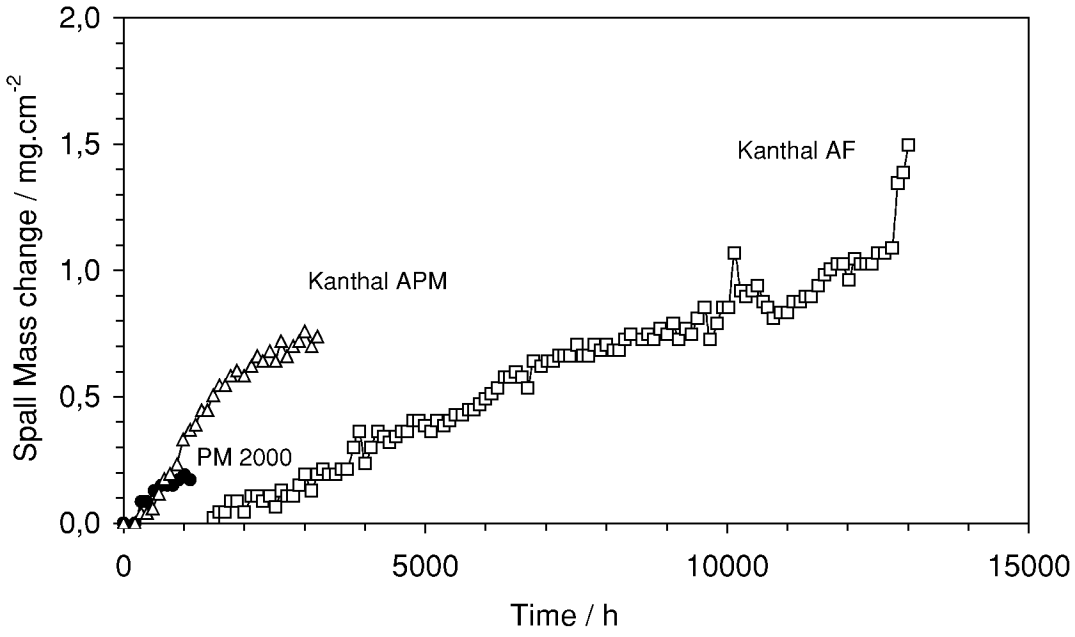

(b)

Figure 5.17: Mass change data for 0.5 mm thick sheets of commercial alloys during 100 h cycles lifetime oxidation testing at 1200°C in air: (a) Gross mass change (oxygen uptake due to scale growth plus spalled oxide); (b) Mass change of spalled oxide

Between the 0.5 mm thick plates, the ODS alloy PM2000 possessed the shortest time to breakaway of 1,200 h (Figure 5.17-a). A good scale adherence and low scale growth rate of the 0.5 mm thick Kanthal AF (Figure 5.17-a, b) can explain an extremely long lifetime of 13,000 h. Rather low weights of spalls for 0.5 mm thick sheets (Figure 5.17-b) indicate that for these materials similar to the observations made with 0.05 to 0.12 mm foils in Section 5.1, the main Al-consuming factor appeared to be the scale growth, whereas the spalling was only to a limited extend responsible for Al-consumption.

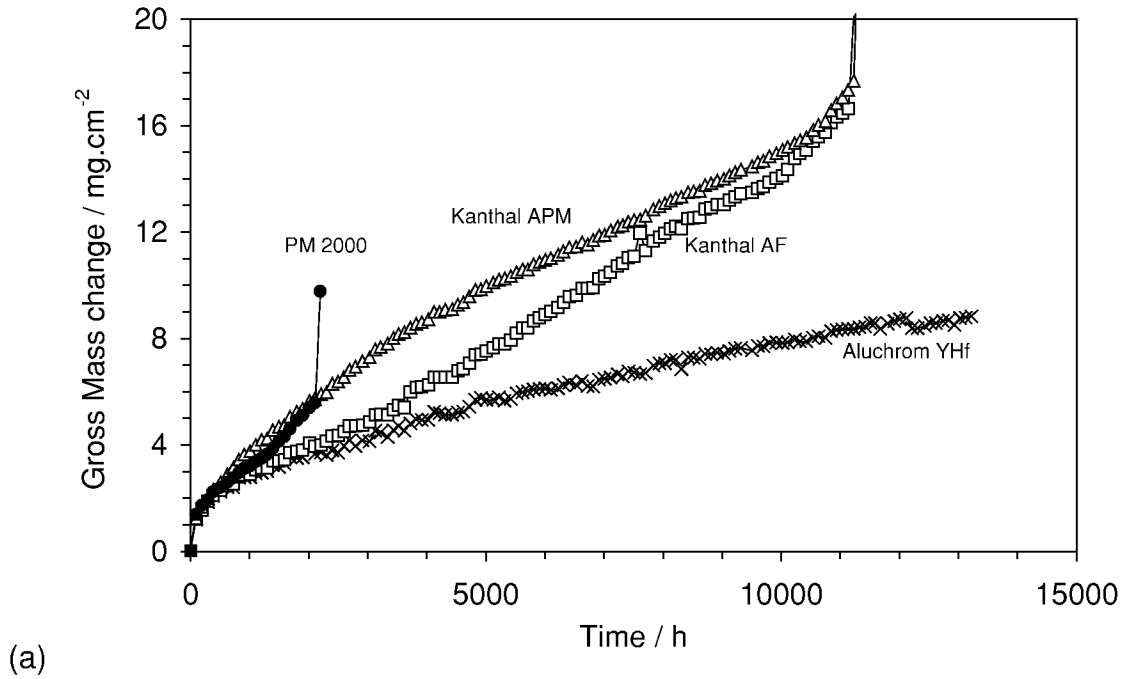

(a)

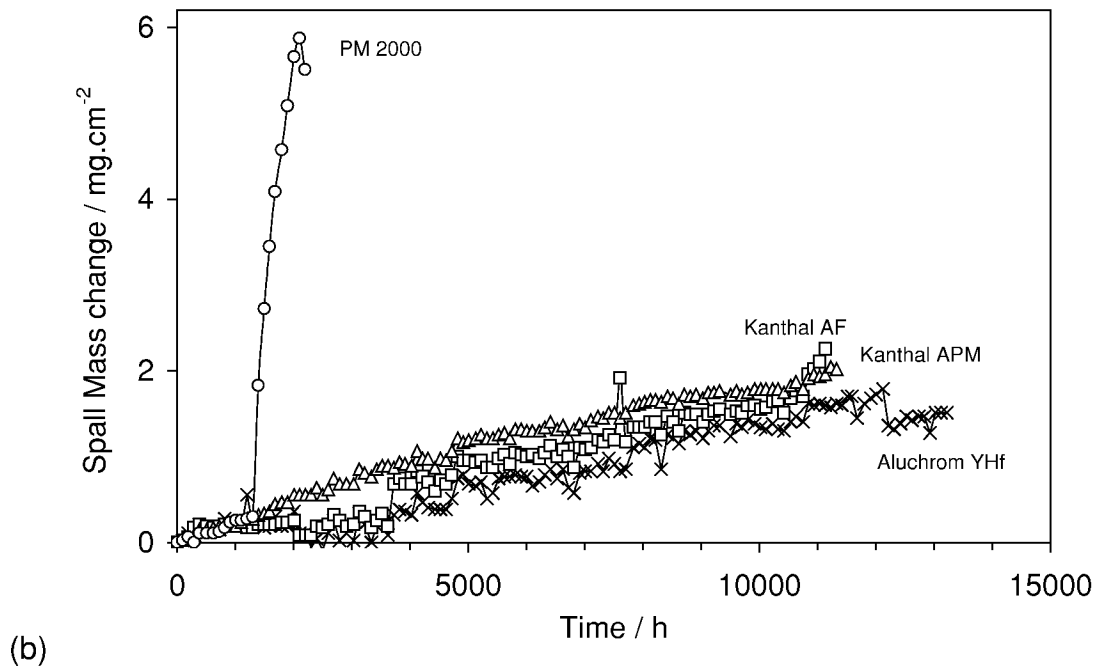

(b)

Figure 5.18: Mass change data for 1 mm thick sheets of commercial alloys during 100 h cycles lifetime oxidation testing at 1200°C in air: (a) Gross mass change; (b) Mass change of spalled oxide

The 1 mm sheet commercial materials up to 500 h oxidation showed almost identical oxidation rates (Figure 5.18-a). However, after longer exposure times a higher oxidation rate was measured for the alloy Kanthal APM. Massive scale spallation was observed on the PM2000 1 mm plate (Batch HEP) after approximately 1,100 h exposure, which led to an unexpectedly early failure of the material shortly after 2,000 h. The wrought alloys Aluchrom YHf and Kanthal AF showed the lowest rates of scale growth and spallation.

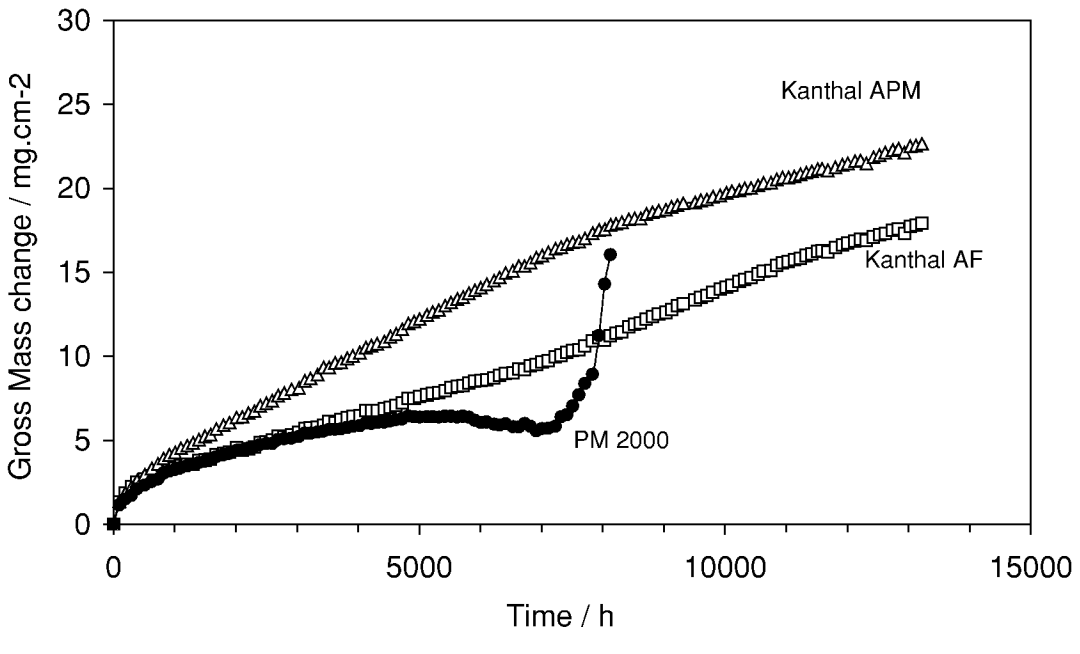

(a)

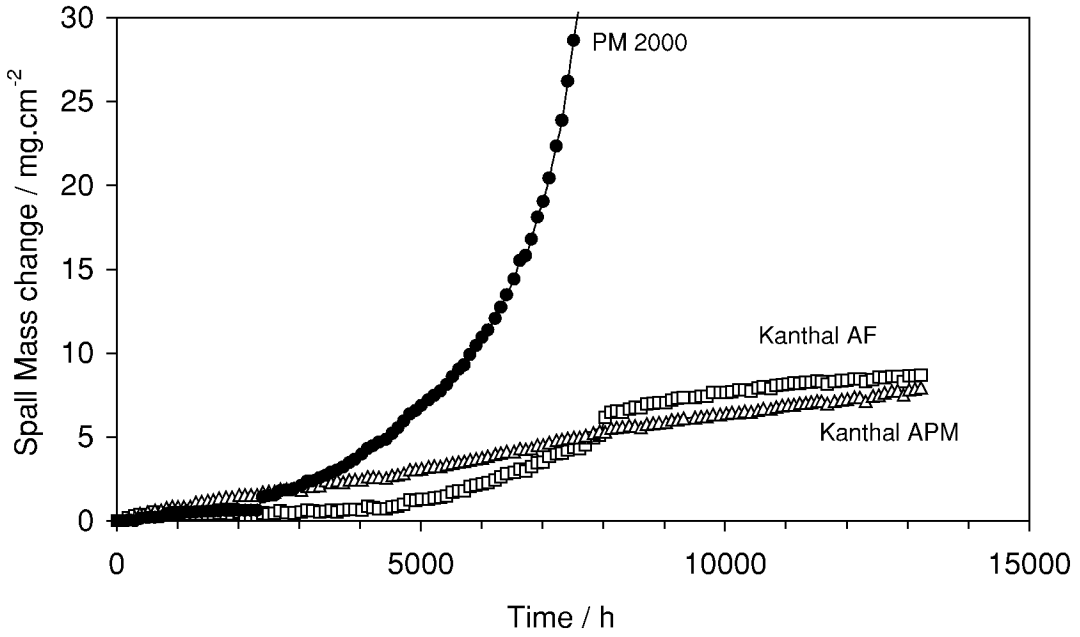

(b)

Figure 5.19: Mass change data for 2 mm thick sheets of commercial alloys during 100 h cycles lifetime oxidation testing at 1200°C in air: (a) Gross mass change; (b) Mass change of spalled oxide

Also the oxidation behaviour of the 2 mm thick sheets (Figure 5.19) during the first 500 h exposure was characterised by very similar rates of oxide growth and spalling. After longer exposure times the best resistance against cyclic oxidation was shown by the wrought alloy Kanthal AF. The powder metallurgical alloy Kanthal APM exhibited the highest growth rate and a moderate spallation rate. The alumina scale formed on the alloy PM2000 started to spall intensively after 2200 h exposure. The Al-depletion induced by scale spallation was the primary reason for the breakaway failure of this material after 8000 h, i.e. much shorter time than those of the two other alloys.

The isothermal oxidation kinetics up to 100 h exposure at 1200°C for 1 mm thick plates of the commercial alloys were determined in a microbalance. The growth rate exponent ***n*** (eq-n 2.12) calculated from the mass change data was found to vary between 0.33 for Aluchrom YHf to 0.41 for PM 2000 (Figure 5.20).

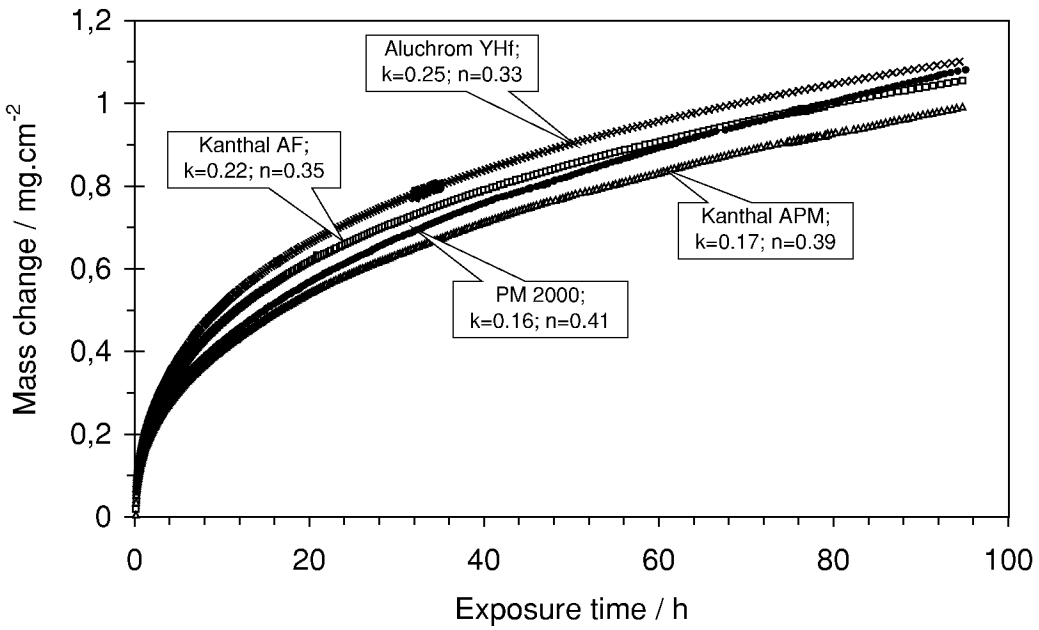

Figure 5.20: Thermogravimetric data of 1 mm thick commercial sheets during isothermal oxidation at 1200°C in synthetic air. Scale growth rate parameters k and n are plotted in Figure (k and n defined after eq-n (2.18) as $\Delta m=k.t^n$ where Δm is the mass change in mg/cm^2 and t is the exposure time in hours)

5.3.2. Differences in oxide scale features of commercial alloys

The macrographs of the specimens taken in course of the oxidation tests present an overview of the scale growth and degradation (Figure 5.21-22). After 100h isothermal oxidation at 1200°C (Figure 5.21) all the alloys have formed flat and adherent alumina scales. The alloy Kanthal APM exhibited some local scale decohesion without spalling after cooling to room temperature. The scale decohesion becomes visually apparent by a white colour of the

specimen surface [55]. Figure 5.22 shows the specimens oxidised for 1000 h. The three types of FeCrAl materials i.e. wrought, PM and ODS alloys of 0.5, 1 and 2 mm thickness are compared. As can be seen, the scale and specimen features vary between the alloys and also between sheets of different thickness of the same alloy. The visual observations with the specimens are summarised in Table 5.2.

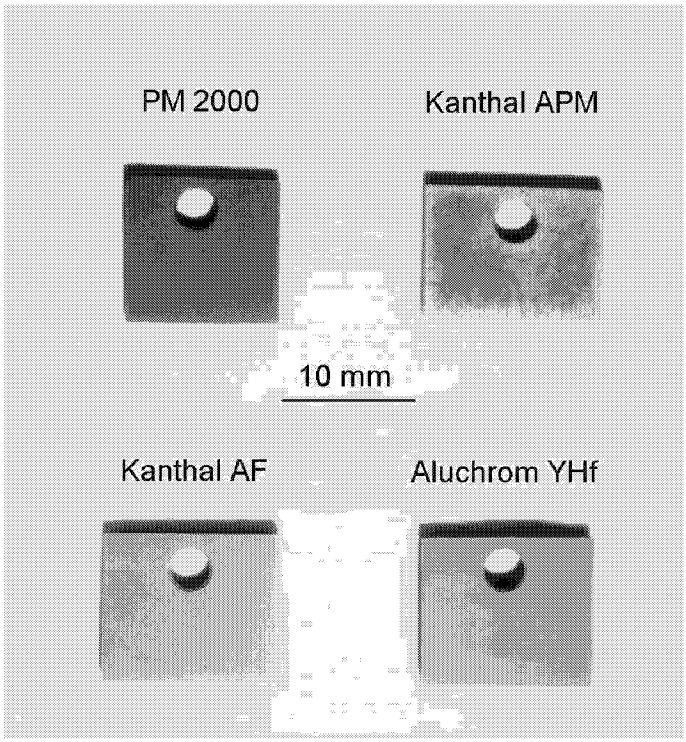

Figure 5.21: Macrophotographs of 1 mm sheets of commercial alloys after 100h isothermal oxidation at 1200°C in synthetic air

After 4000 h cyclic oxidation all the specimens, which had not gone into breakaway, i.e. 1 and 2 mm thick sheets, exhibited scale cracking and/or spalling (Figure 5.23). On the wrought alloy Aluchrom YHf first a network of cracks through the oxide scale appeared (Figure 5.23-a). The scale decohesion and spalling took then place along these cracks. Cracking of the scale was also observed on Kanthal APM. However, in contrast to Aluchrom YHf, the scale spalling was related to the small spot areas where the scale lost its adhesion to the substrate alloy (Figure 5.23-b). On the ODS alloy PM2000 essentially 1 to 2 mm large patches of the oxide scale spalled off but no scale failure in other areas could be found (Figure 5.23-c).

SEM studies of the surface oxide morphologies were performed on the plates of Aluchrom YHf and PM2000 oxidised for 1000h at 1200°C. The scale on PM2000 was flat, while that on Aluchrom YHf was convoluted (Figure 5.24).

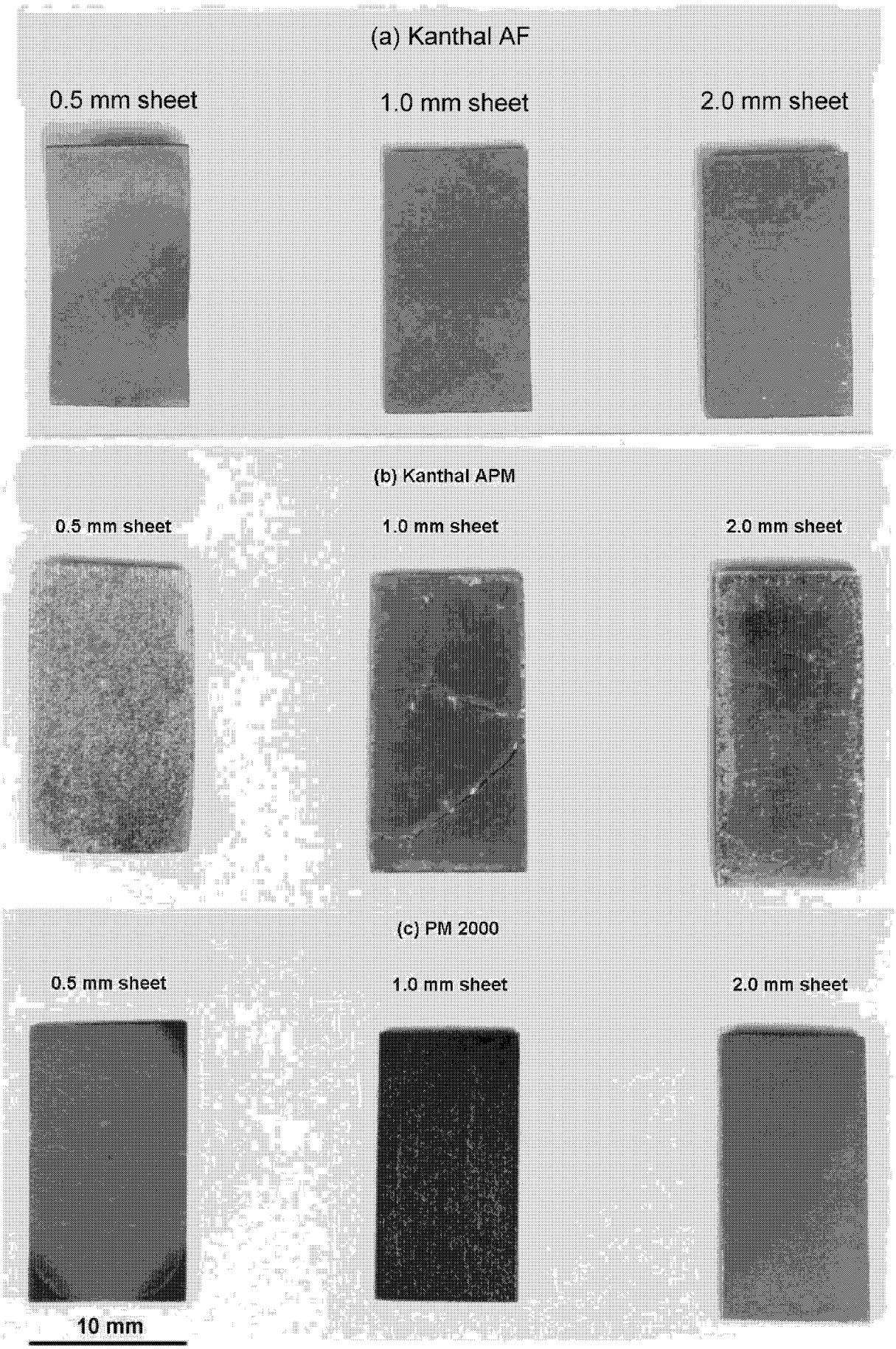

Figure 5.22: Macrophotographs of 0.5 to 2mm thick commercial sheets after 1000 h exposure at 100h cycles at 1200°C in air: (a) Kanthal AF; (b) Kanthal APM; (c) PM 2000

Additional information on the morphology and structure of the scales formed on the commercial alloys after 1000 h exposure was provided by the metallographic cross-sections. The scales on the wrought alloys and Kanthal APM were found to be not very uniform in thickness, but convoluted and buckled (Figure 5.25-a,b). The scale on the ODS alloy PM2000 appeared to be flat and its thickness was fairly constant (Figure 5.25-c).

Table 5.2: Visual observations made with 0.5, 1 and 2 mm thick sheet specimens of commercial FeCrAl alloys after 1000 h cyclic oxidation (100 h cycles) at 1200°C in air

Alloy	0.5 mm sheet	1.0 mm sheet	2.0 mm sheet
Kanthal AF (wrought)	Deformation (bending) of specimen; Adherent scale; No cracks	No deformation of specimen; Adherent scale; No cracks	No deformation of specimen; Adherent scale; No cracks
Kanthal APM (powder metallurgical)	Deformation (bending) of specimen; Local 0.5 mm spot scale decohesion observed everywhere; No scale cracking.	No deformation of specimen; Through scale cracking; Local scale decohesion along cracks.	No deformation of specimen; Local scale decohesion especially at edges; Small cracks at edges and/or corners.
PM2000 (ODS)	No deformation of specimen; Adherent scale; No scale cracking; Darkish oxides formed at corners;	No deformation of specimen; Local scale decohesion; No through scale cracking;	No deformation of specimen; Adherent scale, some local spallation at edges; No scale cracking;

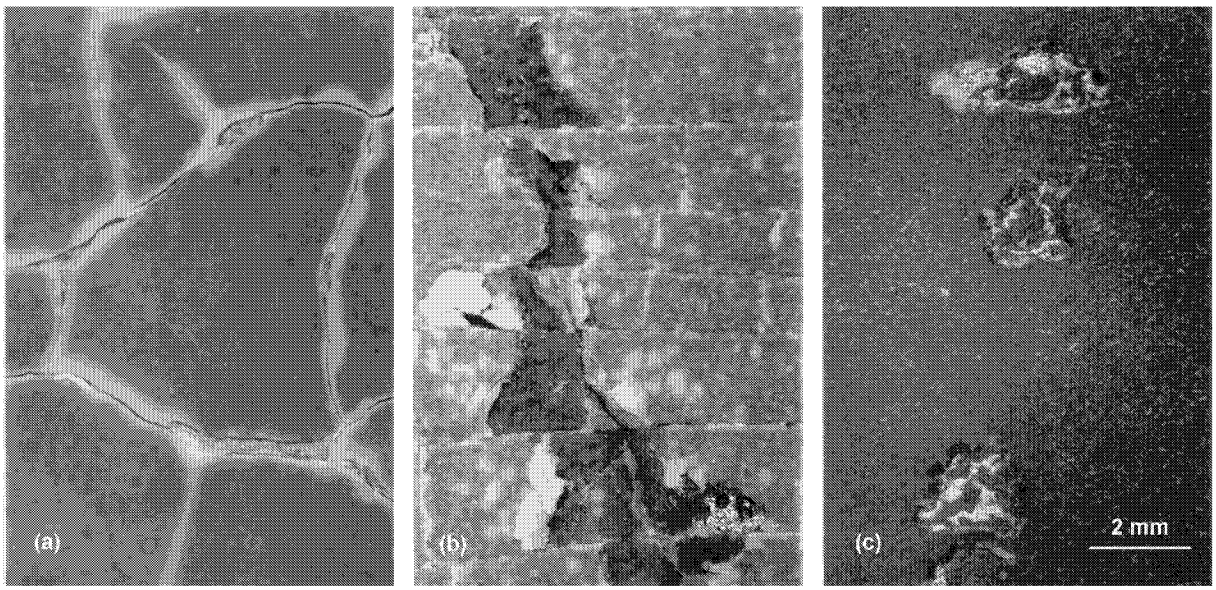

Figure 5.23: Macroscopic features of oxide scales formed on commercial FeCrAl alloy sheets after 4000 h oxidation (100 h cycles) at 1200°C in air: (a) 1 mm thick Aluchrom YHf; (b) 1 mm thick Kanthal APM; (c) 2 mm thick PM 2000

It is important to mention that one of the batches of the ODS alloy PM2000 (1 mm sheet; Batch HEP) exhibited very untypical scale features after longer exposure time. The scale on

Batch HEP after only 1000 h cyclic oxidation was found to be porous and buckled, with significant spallation at the buckle crests (Figure 5.26). This morphology could be well correlated with the mass change data in Figure 5.18, which shows rapid increase of oxide spalling for HEP after ca. 1000 h exposure.

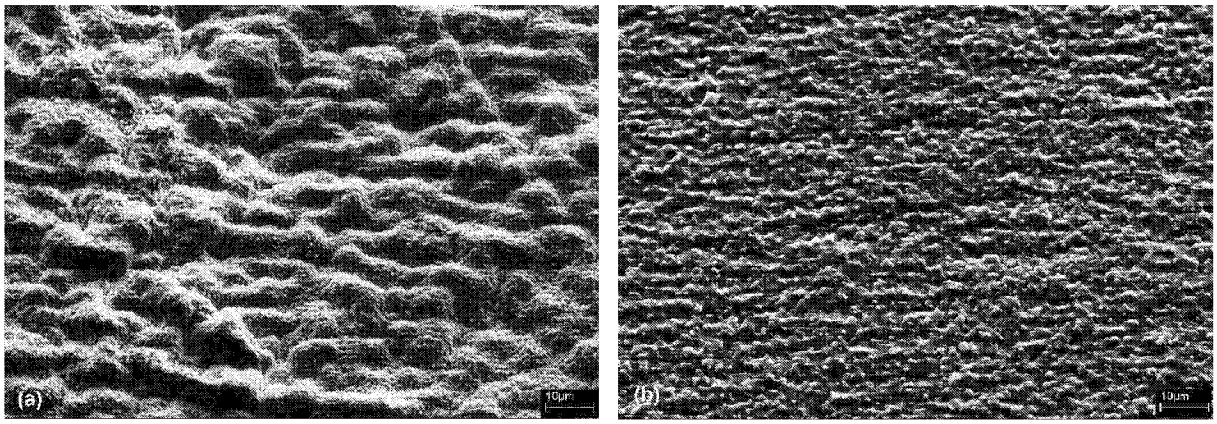

Figure 5.24: SEM images of surface scales formed after 1000 h oxidation (100h cycles) at 1200°C in air on: (a) Aluchrom YHf; (b) PM 2000

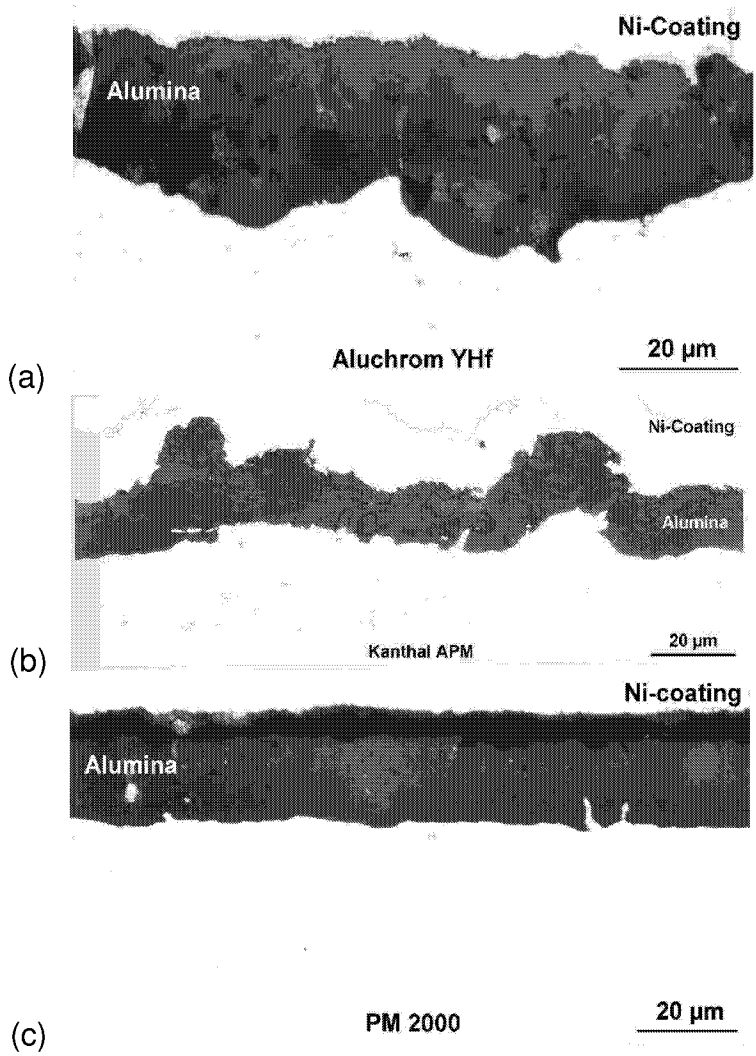

Figure 5.25: Metallographic cross-sections of oxidised commercial alloys (1000 h oxidation at 100 h cycles at 1200°C in air): (a) 1 mm thick sheet of Aluchrom YHf; (b) 2 mm thick sheet of Kanthal APM; (c) 2 mm thick sheet of PM 2000

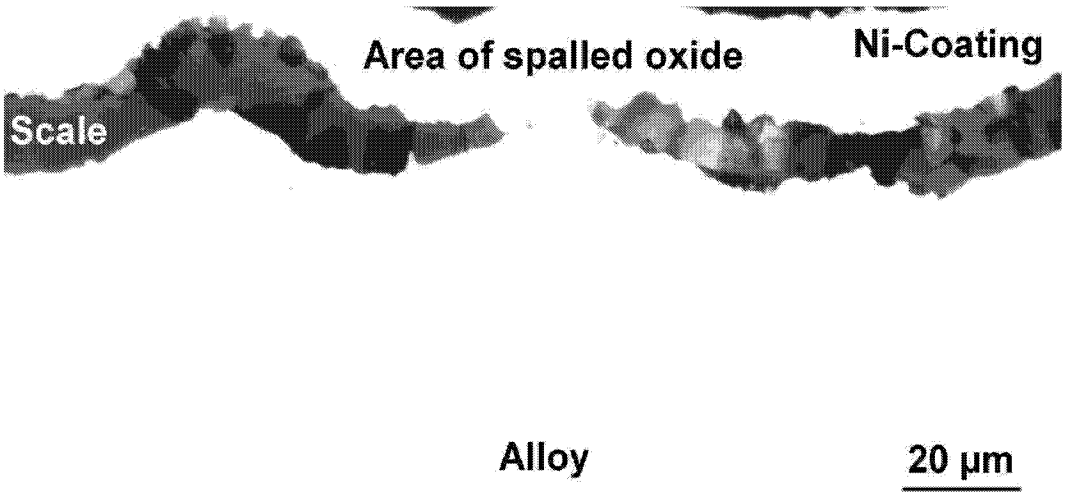

Figure 5.26: Metallographic cross section of 1mm thick sheet of PM 2000 (Batch HEP) after 1000 h oxidation (100h cycles) at 1200°C in air

5.3.3. Internal porosity in alloys produced by powder metallurgical routes

A frequently observed feature of the oxidised alloys produced by powder metallurgical (PM) methods, i.e. Kanthal APM and PM2000, was internal porosity (Figure 5.27-5.28). The latter effect is most probably related to the fact that the concentration of defects (vacancies, dislocations and micropores) in the PM products is much higher than that in the wrought alloys. During exposure at temperatures as high as $0.8\text{-}0.9T_{MELT}$ recrystallisation of the defective structure occurs. This process is accompanied by vacancy coalescence into pores.

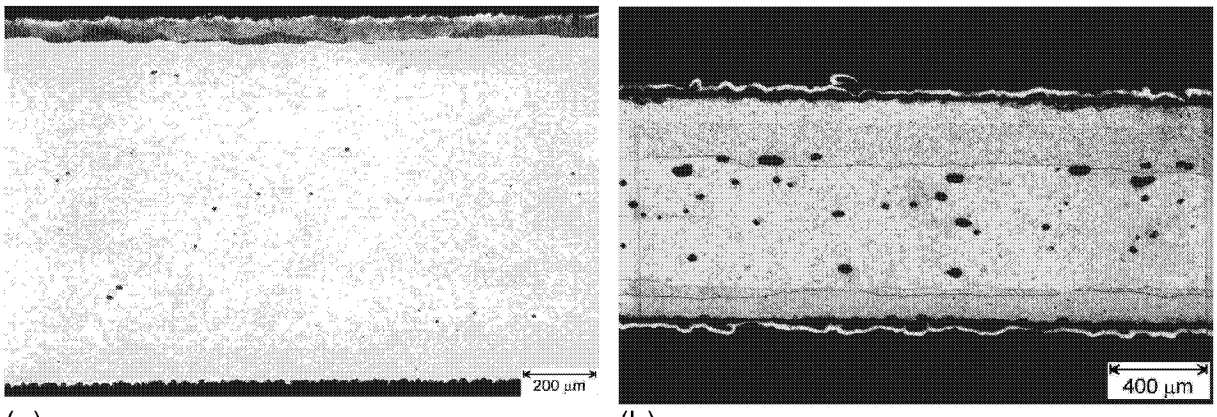

Figure 5.27: Etched metallographic cross-sections of 1 mm thick sheet of PM 2000: (a) in as-received condition; (b) after 1000 h exposure at 1200°C in air

The general trend to decrease the free energy of the system will lead to dissolution of the small pores, possessing a high surface energy. The small pores become then vacancy sources and their dissolution occurs by vacancy diffusion towards vacancy sinks. For the pores close to the original metal surface, the scale/metal interface will be the largest vacancy sink. It may especially be true because the growth of the alumina scale occurs by inward oxygen diffusion and the opposite flux of vacancies is a necessary condition for the scale growth to happen. For

pores in the middle of the alloy, however, the diffusion path towards the scale/metal interface is too long and the larger pores there are expected to grow at the expense of the smaller ones. At the final stage (Figure 5.27), a pore free zone under the scale/metal interface will form and pores as big as 0.5 mm in size in the middle of the alloy may appear. The thickness of the pore free zone ξ as a function of time t can be described in terms of Lifshitz-Sliozov theory [56] as:

$$\xi = const(D_o t)^{1/3}, \tag{5.1}$$

where D_0 is the self diffusion coefficient for vacancies in the alloy matrix. Schematically the process of vacancy coalescence into large internal pores is illustrated in Figure 5.28.

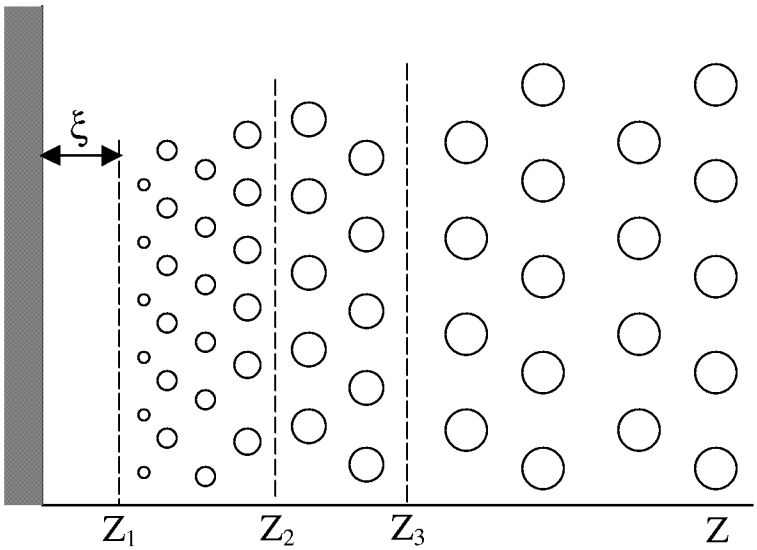

Figure 5.28: Development of porosity from crystallographic defects in alloys produced by powder metallurgical routes, after [56]

5.3.4. Effects of temperature cycling and alloy creep strength on oxide scale adherence

During 100 h cycles oxidation at 1200°C the 0.5 to 2 mm thick sheets of the commercial alloys failed generally after much longer times than thin foils of the same alloys. Comparing times to failure of the studied sheet materials it is easy to find significant variations for the specimens with very similar aluminium reservoirs. The data is summarised in Table 5.3.

Indeed, for 0.5 mm sheets the lifetime varies between 1,200 h for PM2000 and 13,000 h for Kanthal AF, which is a factor of 10 difference. Another peculiar result was that 0.5 mm sheet of Kanthal AF failed after longer time, than the 1.0 mm sheet of the same material. The 1.0 mm sheet of Aluchrom YHf exhibited excellent oxidation resistance and after 18,000 h exposure still maintained a protective alumina scale. These variations can be partly explained by the differences in the initial Al-content and actual specimen thickness after grinding. For

example, the chemical analyses data in Table 3.1 reveal that the 0.5 mm sheet of PM2000 (Batch FSK) contains only around 4 mass% Al. This is about 80% of the amount of Al in corresponding 0.5 mm sheets of Kanthal APM and Kanthal AF. Still, for the latter two materials, which have comparable Al-contents and thickness, the discrepancy is a factor of six. So there should be other reasons for the differences in lifetime.

Table 5.3. Times to breakaway for 0.5, 1.0 and 2.0 mm thick sheets of commercial FeCrAl alloys oxidised at 100h cycles at 1200°C in air

Material	Specimen Number	Thickness (nominal) mm	Thickness after grinding mm	Time to breakaway, hours
Kanthal AF	FVJ4	0.5	0.36	13 100
	FVJ2	1.0	0.89	11 100
	FVJ3	2.0	1.78	18 000; no Breakaway
Kanthal APM	FSG1	0.5	0.36	2 200
	FSG2	1.0	0.94	11 300
	FSG3	2.0	1.80	16 000; no Breakaway
PM2000	FSK1	0.5	0.42	1 200
	FSK2	1.0	0.85	2 700
	FSK3	2.0	1.80	8 300
Aluchrom YHf	FVK1	1.0	0.90	18 000; no Breakaway

One of the explanations may lie in the fact that, contrary to the thin foils, the long term oxidation behaviour of the 0.5 to 2 mm sheet specimens appeared to be much more affected by temperature cycling. If the response of the materials to cyclic oxidation is not the same, this would account for the observed discrepancies in the lifetimes.

The primary adverse effects of temperature cycling on the protective alumina scales have been found their decohesion and spalling [10,11,42,54]. These detrimental effects have been attributed to the stresses generated in the scale/alloy composite due to the differences in thermal expansion coefficients of the oxide scale and the metal substrate [42,43]. In the simplest case of an oxidised infinite flat metal plate, the stresses generated in the oxide scale after cooling can be formulated as [42]:

$$\sigma_{ox} = -\frac{E_{ox}\Delta T(\alpha_m - \alpha_{ox})}{(1-\nu)}, \tag{5.2}$$

where σ_{ox} is the average stress in the oxide; E_{ox} is the oxide Young's modulus;
α_m and α_{ox} the thermal expansion coefficients for metal and oxide respectively;
ν - Poisson ratio (in this example assumed to be the same for both phases).

The value of σ_{ox} calculated using eq-n (5.2) is in the order of 4 GPa [43], i.e. high enough to initiate scale damage. The exact damage mechanism depends on a number of parameters, including scale thickness and structure, alloy properties as well as heating/cooling rates.

If a defect of a critical size exists in the scale, than oxide fracture can occur, which is confirmed by the literature data on bulk alumina ceramics [57]. It has been shown that the scale thickening during oxidation results in an increase of the number and size of scale defects, such as pores and microcracks [58]. Thus, after reaching a critical scale thickness (x^* in eq-n (2.19)) the alumina scales on the FeCrAl alloys are expected to crack and consequently spall. This approach appeared to describe well the scale spallation on 1 to 2 mm thick coupons of the ODS alloys, with the value of x^* varying between 15 and 20 µm [11]. However, in some cases, e.g. when the scale adherence is intrinsically deteriorated, the assumption of a critical scale thickness can not easily be applied for description of the oxide spallation. It has been found recently that spallation of the alumina scales on alloy Kanthal A1 occurred after only 25h oxidation at 1200°C and mild cooling to room temperature [59]. In the present study scale decohesion on Kanthal APM was observed after 100h isothermal oxidation at 1200°C. Another example could be the abnormal scale spallation on 1 mm sheets of PM2000 which started suddenly after 1000 h oxidation at 1200°C (Figures 5.18, 5.26). These results clearly demonstrate the complexity of the scale adherence issues, which makes the modelling of scale spallation and alloy lifetime prediction a complicated problem.

Two principle modes of scale failure under compression, namely wedging and buckling, have been proposed recently in [42] (Figure 5.29). If the scale is relatively defect free but the adhesive strength of the scale/metal interface is low, the compressive stress in the oxide results in its decohesion from the metal substrate. Such a decohesion under constant compressive stress leads to the formation of buckles. Cracking of the scale occurs then at the buckle crest leading to oxide spallation (Figure 5.29). An example of the scale failure by the buckling mode on Aluchrom YHf is given in Figure 5.23-a. It can be seen that indeed the alumina scale spalls along the cracks and there is a crack precursor in the form of a decohesion band. It must be noted that the buckles observed on Aluchrom YHf in this work are not classical instances of the round buckles which occur under uniform biaxial compression [42]. This means that the scale stress distribution and/or scale adhesion to the metal substrate are not uniform along the oxide/metal interface.

For scales with a large number of defects but good scale adherence, compressive shear cracks develop first in the oxide layer. Then a wedge crack driven by the thermal expansion mismatch, grows between the shear cracks leading to spall of the oxide piece (Figure 5.29-a). This situation seems to occur in this study on the 2mm thick sheet of PM2000, which is illustrated in Figure 5.23-c.

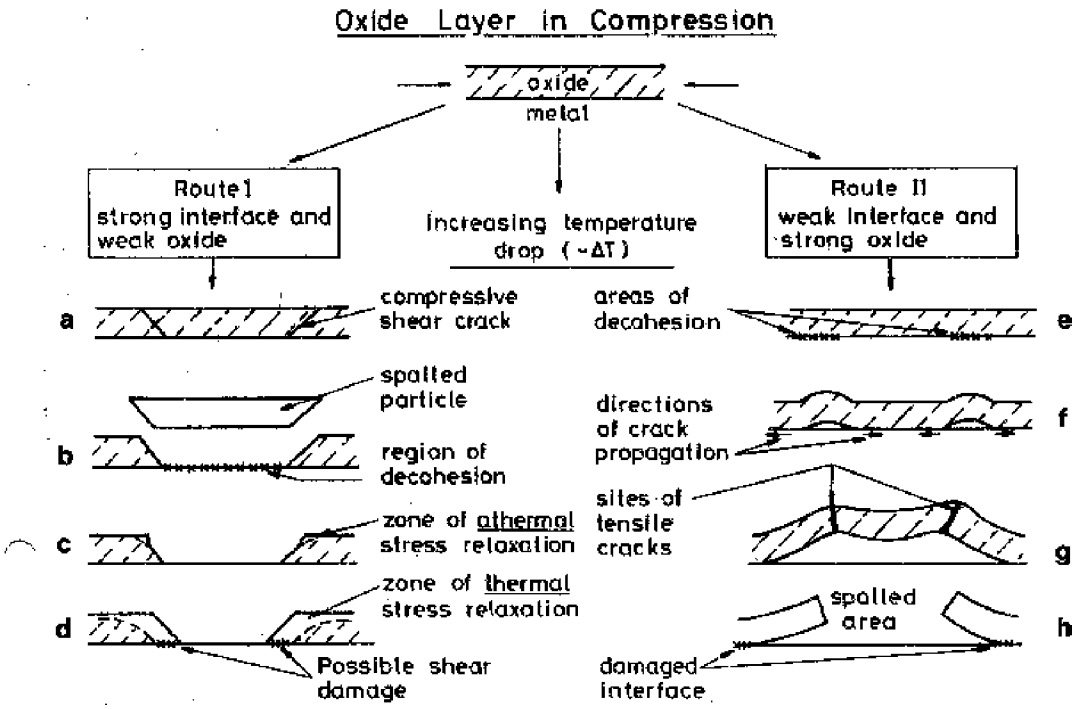

Figure 5.29 Cracking and spallation caused by compressive stresses: (a) shear cracks develop; (b) wedge crack grows between shear cracks; (c) local athermal stress relaxation; (d) thermal stress relaxation; (e,f) localised decohesion can lead to buckling; (f) buckles may spread laterally and coalesce; (g,h) tensile cracks develop in regions of tensile stress leading to spallation [42]

The value of the compressive stress calculated directly from eq-n 5.2 for alumina on an FeCrAl substrate is often much larger than the values measured experimentally and reported in literature [59]. Thus one must take into account possible stress relaxation during cooling. A number of relaxation mechanisms have been proposed in order to justify the lower residual stresses [42]. These include scale microcracking as well as plastic deformation of the scale [43]. Another important phenomenon pointed out elsewhere [42, 54] was the relaxation of the oxide stresses by the plastic deformation of the alloy substrate.

The latter relaxation mechanism was found in this study to prevail for the wrought FeCrAl alloys during mild cooling to room temperature. This is because the alloy substrate is oxidised at the high temperature fraction of the alloy melting point of 1450°C. The actual extent of stress relaxation depends on the intrinsic creep strength of the alloy as well as on the section

thickness [42,54]. Generally, for cooling from the same oxidation temperature more relaxation occurs on thin substrates and for the alloys with a low creep strength. Qualitatively between materials in this study the intrinsic alloy creep strength increases in the following way [54]:

Aluchrom YHf / Kanthal AF → Kanthal APM → PM2000

From the mass of the spalled oxide as a function of exposure time (Figure 5.18-5.19), it can be seen that significant spalling starts on the PM2000 specimens at lower gross mass changes, corresponding to thinner scales than on the "weaker" alloys Kanthal AF, Aluchrom YHf and Kanthal APM. The alloy plastic relaxation is apparently responsible for an extremely long life of the 0.5 mm thick sheet of Kanthal AF (13000 h at 1200°C). This by far exceeds e.g. the 8000 hour life of the "stronger" 2 mm sheet of PM2000, in spite of the fact that the latter specimen had, prior to exposure, a four times larger Al-reservoir. The lifetime extension in case of Kanthal AF occurs not only due to significantly smaller losses of the spalled oxide, but also apparently due to the lower value of C_B. As has been discussed in Section 5.1 for thin foil specimens the C_B value of 1.2% for PM2000 is much higher than those of the wrought alloys (less than 0.3%) because of the absence of the molecular oxygen access towards the Al-depleted metal in the latter case. Although giving not very accurate values of C_B, the residual Al-contents can be calculated from the total mass change measurements using eq-n 2.18. This gave 0.1% for Kanthal AF and around 2% for PM2000.

Considering the alloy plastic relaxation of the oxidation induced stresses discussed above, the lifetime variations between the "strong" and "weak" alloys can be explained. The plot in Figure 5.30 gives the lifetimes, predicted by equations 2.18 and 2.19 compared with those determined during the oxidation tests. A good agreement between the predicted and experimental data is observed, when taking into account the effects of alloy plastic relaxation (i.e. the lower values of C_B and higher x^*) for the weaker substrates.

Although the resistance to scale spalling has been manifested to have a significant influence on the oxidation limited life of thick walled FeCrAl components, it alone can not explain all the experimentally found lifetime variations. For example, the 1 mm thick wrought alloys Kanthal AF and Aluchrom YHf with very similar mechanical properties exhibited big differences in the growth rates after around 2000 h oxidation (Figure 5.18-a). This effect is apparently not related to the scale adherence since both alloys show very similar spallation

rates (Figure 5.18-b). During cyclic oxidation at 1200°C these variations emerged only after several thousands of hours oxidation. As will be shown in the next section, the effects, which do not become apparent during short term oxidation tests seem to be the main problem for reliable lifetime prediction of the FeCrAl based components.

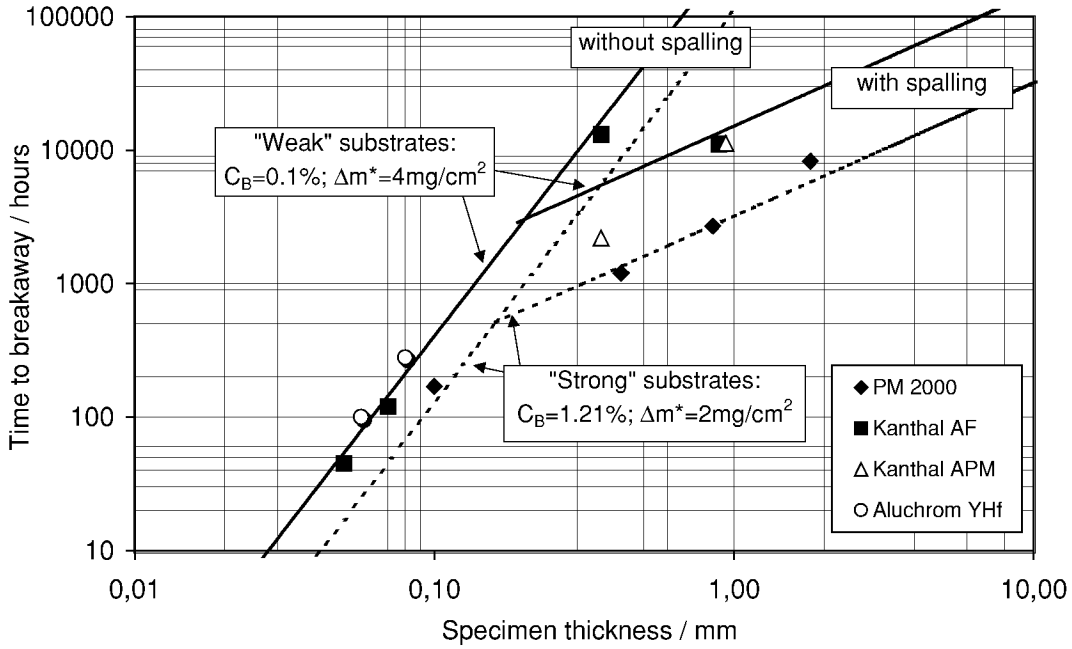

Figure 5.30: Oxidation diagram for studied commercial alloys at 1200°C, showing effect of substrate creep strength on time to breakaway. Dashed and solid lines represent predicted from eq-ns (2.18 and 2.19) values for "strong" and "weak" substrates respectively. "Strong" means that relaxation of oxidation induced stresses occurs mainly by scale cracking and spalling. "Weak" means that substrate creep deformation contributes to relaxation. Predicted data are compared with experimental results (symbols)

5.4 Lifetime variations in commercial FeCrAl alloy systems

As explained in Section 2.2, eq-ns (2.18) and (2.19) allow a simple lifetime prediction for FeCrAl-components, which is in reasonable agreement with the experimental results (Sections 5.1 and 5.2). Based on eq-ns (2.18) and (2.19) oxidation diagrams can be constructed [11], which predict lifetime for a given FeCrAl alloy as a function of component wall thickness and oxidation temperature (Figure 5.31).

However, in some cases prediction can be complicated by changes in the oxidation rates and/or spallation kinetics, which occur after relatively long exposure times. These changes lead to significant lifetime variations between the alloys, which have virtually identical mechanical properties. Hence, these variations cannot be explained only in terms of relaxation of the oxidation induced stresses by alloy creep (Section 5.2), but are more probably related to other alloy parameters, e.g. chemical composition and microstructure. On the other hand, the

manufacturers of FeCrAl alloys and components are extremely interested in a reliable lifetime assessment of their products, without performing expensive and time consuming life tests. Therefore, in order to find out extends of and reasons for the life variations and establish the limits of components safe operation it is necessary to compare alloys with very similar compositions, microstructure and mechanical properties, e.g. different batches of the same commercial alloy.

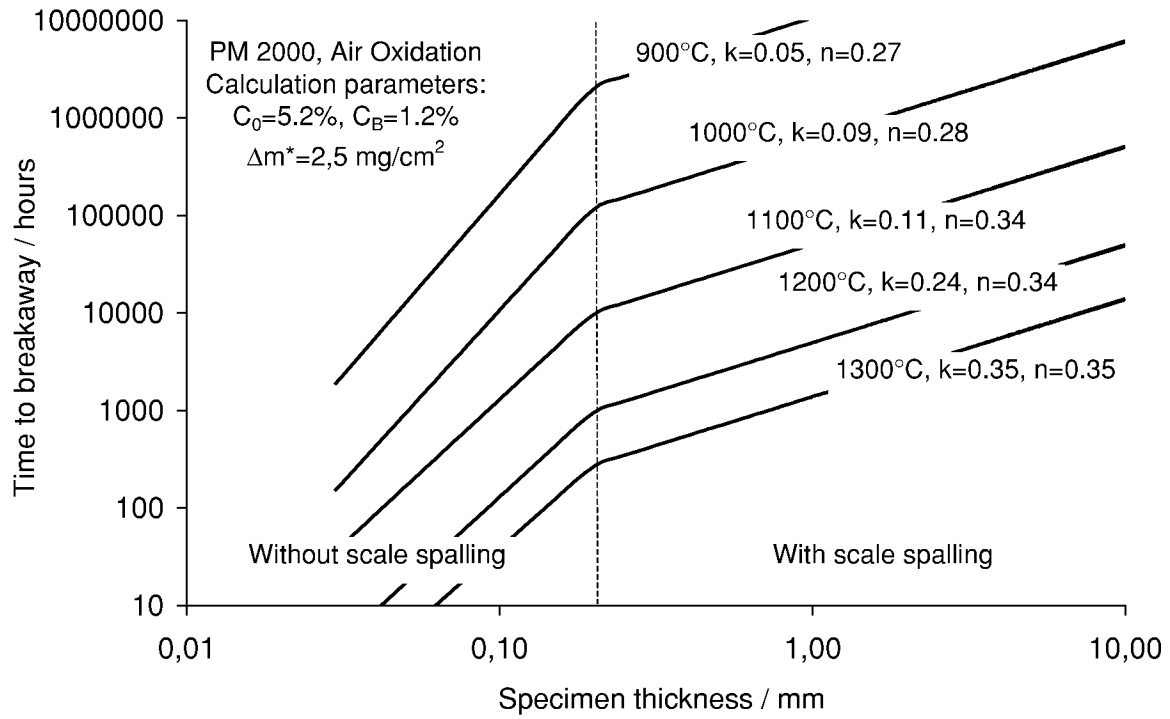

Figure 5.31: Oxidation diagram showing calculated temperature dependence of lifetime for PM 2000. Indicated growth rate parameters k and n used in eq-ns 2.18 and 2.19 for lifetime calculation are those typically obtained for PM 2000 during short term thermogravimetrical tests.

Figure 5.32 presents the mass change data obtained during cyclic oxidation at 1200°C with 1 mm thick specimens of different batches of the commercial ODS alloy PM2000. The data clearly illustrates that even for the same commercial alloy and specimen thickness big differences in the oxide growth rates, the commencement and rate of scale spalling and consequently lifetime variations occurred.

The oxidation diagram in Figure 5.33 compares the experimentally determined lifetimes during cyclic oxidation tests at 1200°C for different batches and specimen thickness of PM2000 with the values calculated from eq-ns 2.18 and 2.19. For calculations, the values of the growth rate parameters k and n were used, which are typically obtained for PM 2000 during short term thermogravimetrical tests (see Table 5.1).

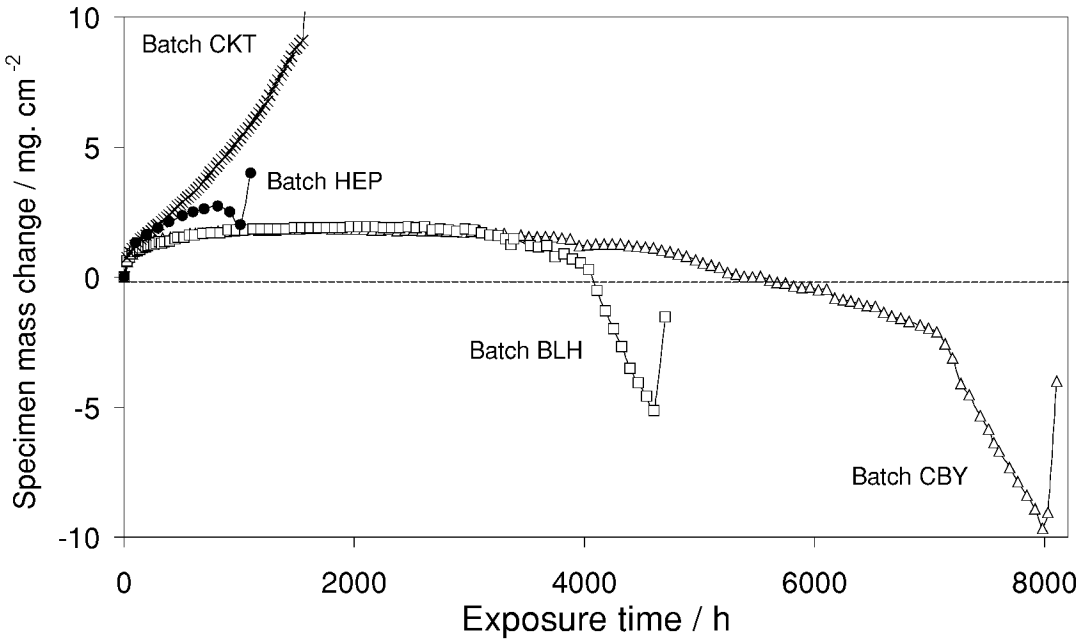

Figure 5.32: Mass change data obtained with different batches of alloy PM 2000 (1 mm thick specimens) during lifetime cyclic oxidation at 1200°C in air

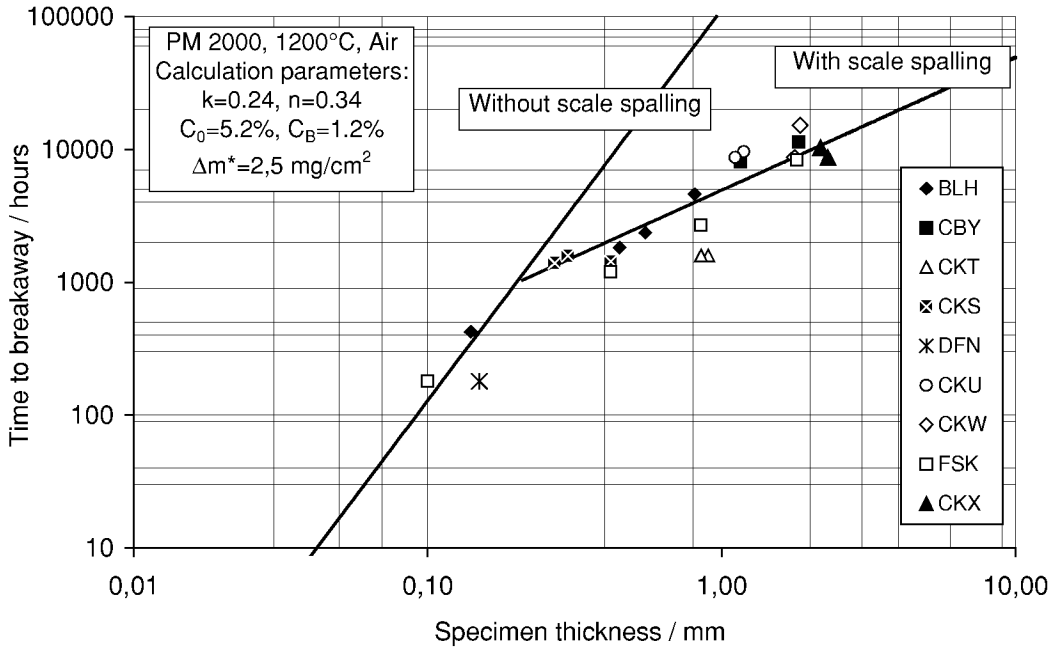

Figure 5.33: Oxidation diagram, showing extend of lifetime variations between different batches of PM 2000 (symbols) during cyclic oxidation at 1200°C. Predicted lifetimes (lines) are calculated from eq-ns 2.18 and 2.19. Growth rate parameters k and n given in plot are those typically obtained during short term thermogravimetrical tests of PM2000.

In Figure 5.33 it can be seen that the life prediction based on the short term oxidation kinetics gives values, which are generally in a reasonable agreement with the experiments. However, for several batches, such as DFN and CKT, the experimentally determined lifetimes are much

shorter than the predicted ones apparently due to increased scale growth rate of these batches after longer exposure times (Figure 5.32).

The batch to batch variations were found in this study not to be a unique feature of PM2000, as can be suggested from the cyclic oxidation data for three batches of Aluchrom YHf at 1200°C (Figure 5.34). Batch HDX exhibits clearly higher oxidation rates, than the two other batches. The calculated oxidation diagram in Figure 5.35 indicates, that the difference in the scale growth rate should lead to a substantial difference in lifetime.

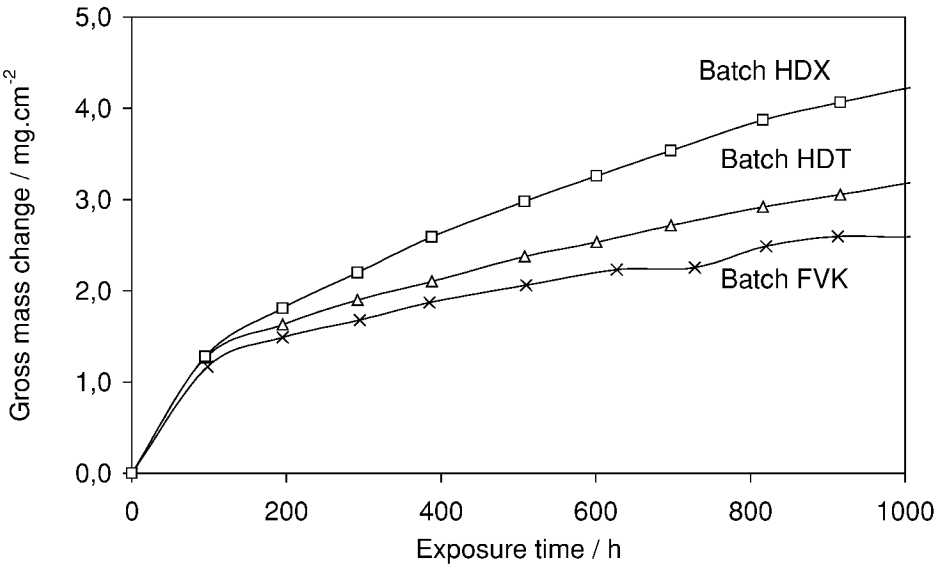

Figure 5.34: Mass change data for different batches of Aluchrom YHf showing significant variations in scale growth rate during 1000 h cyclic oxidation at 1200°C

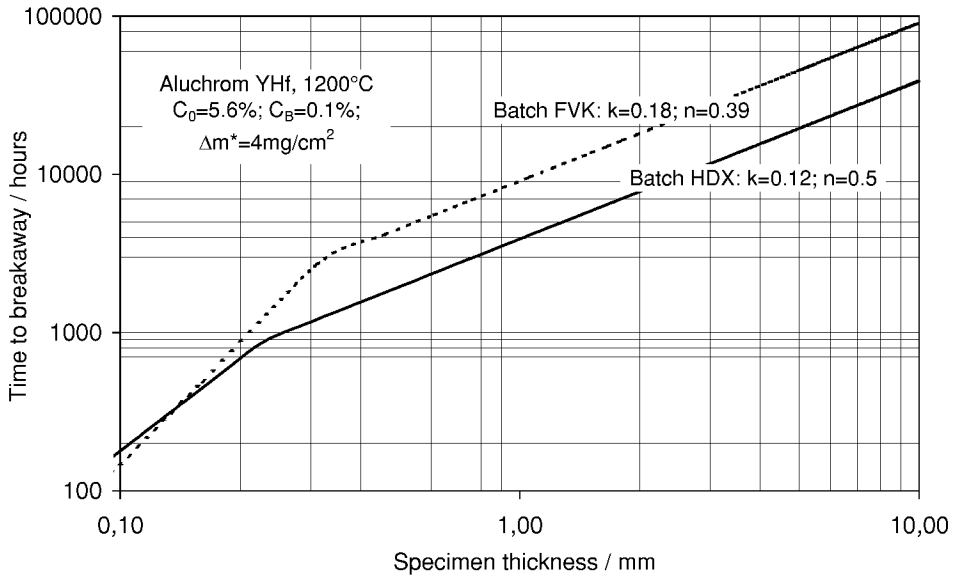

Figure 5.35. Oxidation diagram showing predicted from eq-ns 2.18 and 2.19 lifetimes for two batches of commercial wrought alloy Aluchrom YHf. Calculation parameters given in plot are derived from mass change data in Figure 5.34.

Based on the above oxidation data, the encountered lifetime variations between different batches of one commercial alloy under the same experimental conditions can be as large as a factor of four (Figure 5.32). These variations are apparently related to differences in the oxidation kinetics and/or scale spallation rates. Detailed studying of the phenomena responsible for these variations are of great technological importance to get a reliable lifetime prediction and for establishing possible ways for a lifetime extension.

Therefore, the following two sections are devoted to analytical studies on the batches of commercial alloys, which showed the largest deviations during the lifetime oxidation tests. The oxidation behaviour of ODS alloys (PM 2000 in Section 6.1) and wrought alloys (Aluchrom YHf in Section 7.1) is considered. Each study on the commercial alloys is followed by experiments with model alloys (Sections 6.2 and 7.2 respectively) carried out for a detailed investigation of the involved oxidation mechanisms.

6. Batch to batch variations in the oxidation behaviour of commercial FeCrAl ODS alloys

6.1 Comparative studies on two batches of ODS alloy PM2000

6.1.1 Lifetime oxidation testing of two ODS batches

Two batches of the commercial ODS alloy PM 2000 were delivered by PLANSEE GmbH as sheets of nominal thickness of 0.5mm for CKS and 1.0 mm for CKT. The microstructure of the as-received batches in light optical micrographs in Figure 6.1, shows that both materials possessed a recrystallised, large grained structure typical for ODS materials [53].

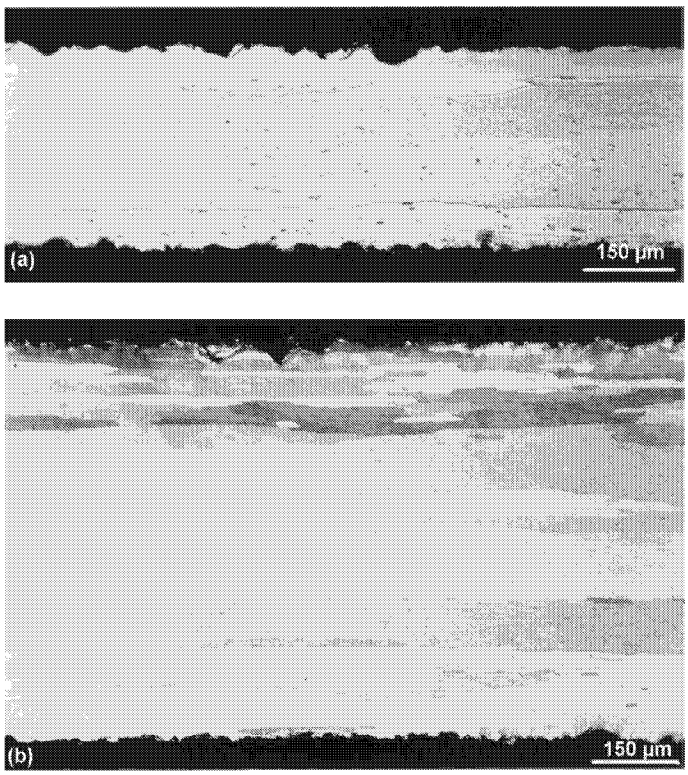

Figure 6.1: Metallographic etched cross-sections of (a) Batch CKS and (b) Batch CKT of alloy PM 2000 in as-received condition

Figures 6.2 presents mass change data obtained during cyclic oxidation experiments. The oxide scale growth rates of the two batches at 1200°C appeared to be very similar until an accumulated exposure time of around 300 h (Figure 6.2a). However, after longer times batch CKT exhibited clearly higher mass gains than batch CKS. For both materials no indications of significant scale spalling were found. Due to its subsequent high scale growth rate, the CKT specimen went into breakaway after a similar exposure time as CKS, in spite of having the double thickness (i.e. around a factor of two larger aluminium reservoir).

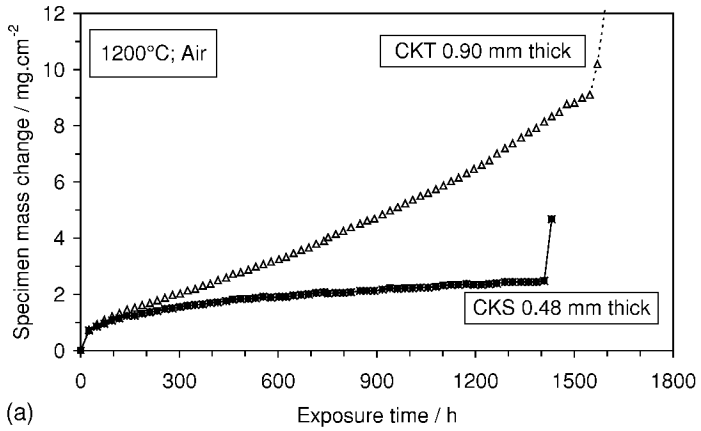

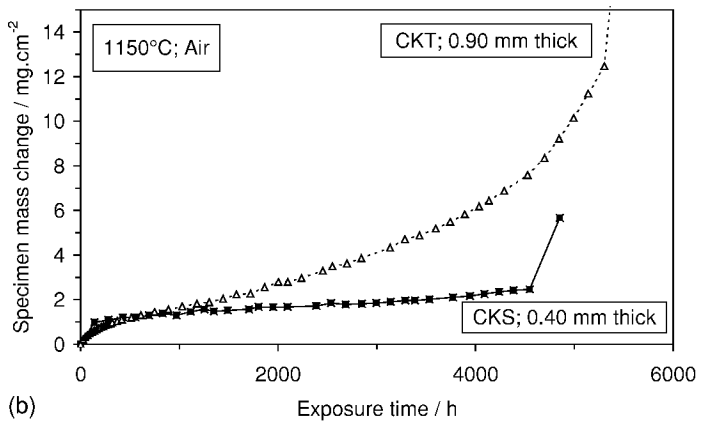

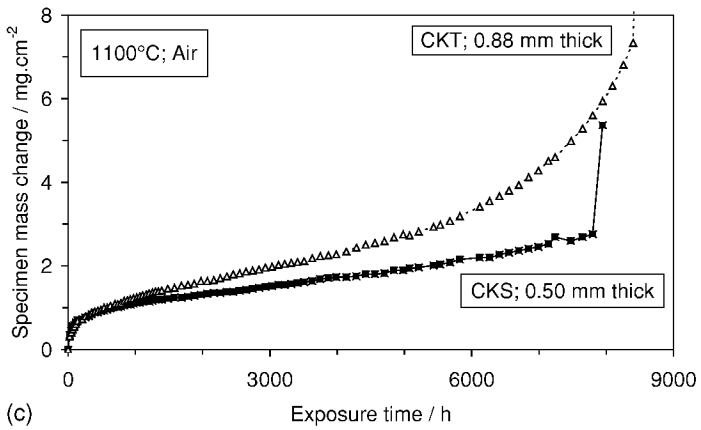

Figure 6.2: Mass change data of two studied batches (CKS and CKT) of alloy PM2000 obtained during cyclic oxidation till breakaway at (a) 1200°C; (b) 1150°C; (c) 1100°C

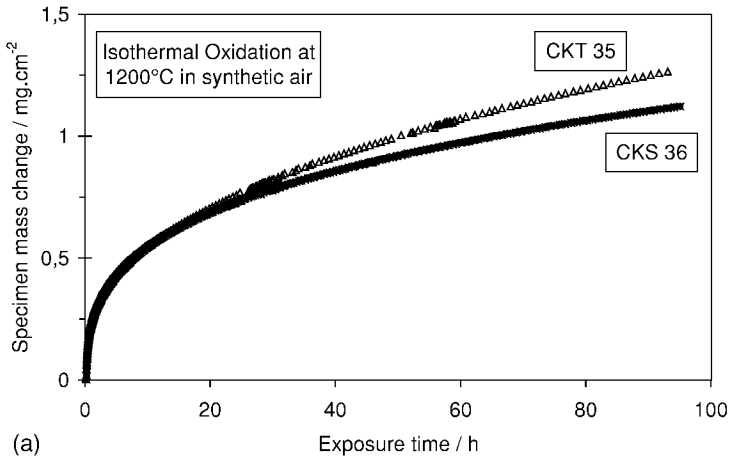

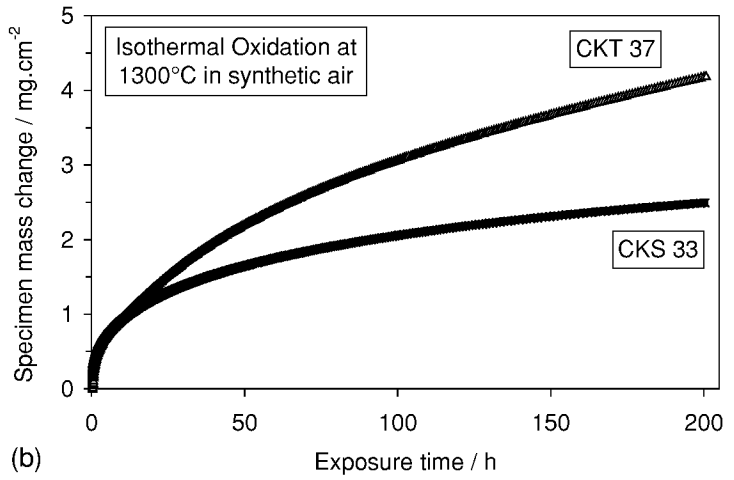

Figure 6.3: Mass change data of two studied batches (CKS and CKT) of PM2000 obtained during isothermal oxidation at (a) 1200°C and (b) 1300°C (compare Figure 6.2)

An interesting observation was made during the cyclic oxidation tests after long exposure times. The scale on batch CKT acquired a yellowish colour, whereas that on batch CKS retained the silver grey colour, typical for dense, adherent alumina. Similar observations with respect to scale growth rate and scale appearance were made during oxidation at 1150 and 1100°C (Figure 6.2 b, c), however, at these lower temperatures the differences in behaviour of the two batches became apparent after much longer times, i.e. several thousands of hours. During isothermal oxidation up to 100 hours at 1200°C (Figure 6.3a) only minor differences in growth rate between CKS and CKT could be found after 100 h exposure, in agreement with the cyclic data in Figure 6.2a. However, during isothermal exposure at 1300°C a clear difference in oxidation behaviour was found already after around 30 h (Figure 6.3b), which

was confirmed by the plot of the instanteneous parabolic growth rate parameter k_P as a function of time in Figure 6.4. The results obtained at various oxidation temperatures indicate that the differences in alumina growth rate on the two batches appeared at a mass gain of 1 to 1.5 mg/cm^2, i.e. when the scales reached a thickness of around 6.5 to 7.5 µm.

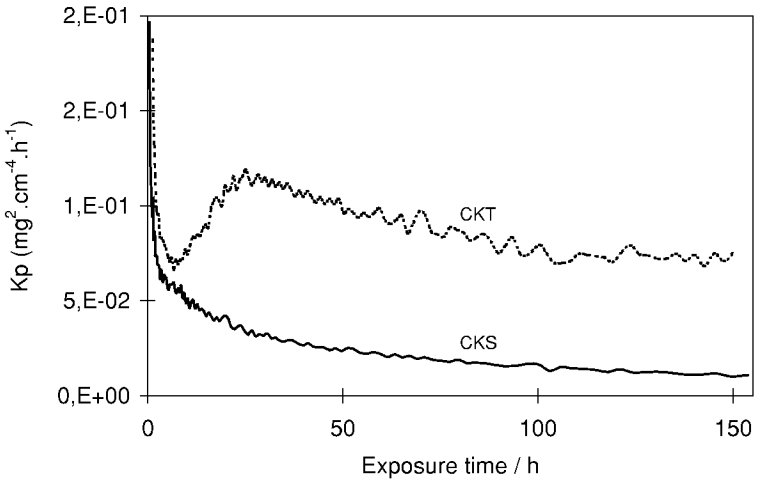

Figure 6.4: Parabolic rate constant plotted as a function of time for isothermal oxidation at 1300°C of two studied batches of PM2000 (calculated from data in Figure 6.3-b)

6.1.2 Analytical studies of oxide scales formed on two ODS batches of PM 2000

The XRD results in Figure 6.5 show that a practically pure α-Al_2O_3 scale was formed on both studied batches. Additionally some weak lines were found on both alloys, which were attributed to the presence of $Y_2Ti_2O_7$ and minor amounts of different Y/Al oxides. The main deviant feature of the XRD pattern taken from the CKT specimen was the presence of titanium in the scale as TiO_2, which was not found in the case of batch CKS.

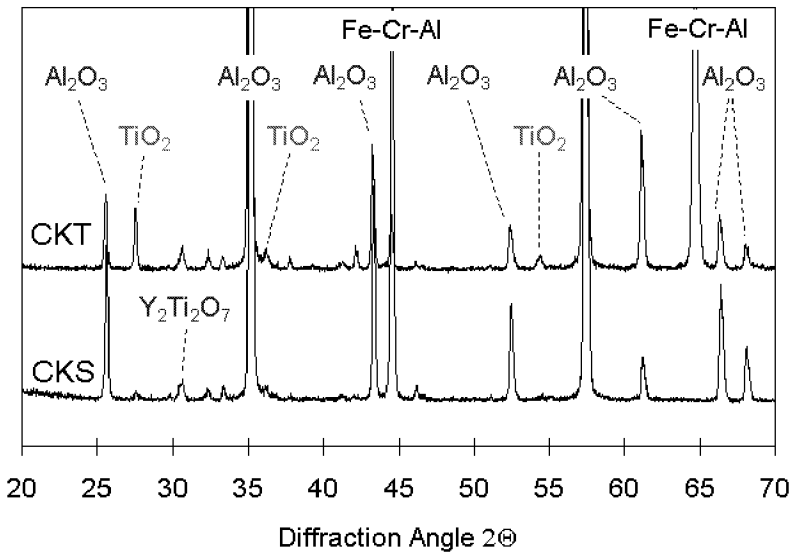

Figure 6.5: XRD patterns taken from surfaces of batches CKS and CKT (alloy PM 2000) oxidised for 600 h at 1200°C in air

Metallographic cross sections of the oxide scales formed on the studied alloys after long term oxidation at 1200°C are shown in Figure 6.6. In agreement with the gravimetric data, the scale on batch CKT (Figure 6.6-b) appeared to be much thicker than that on batch CKS (Figure 6.6-a). It exhibited significant porosity and a substantial amount of Ti-rich inclusions. The largest voids in the scale seemed to be associated with these inclusions (Figure 6.6-c).

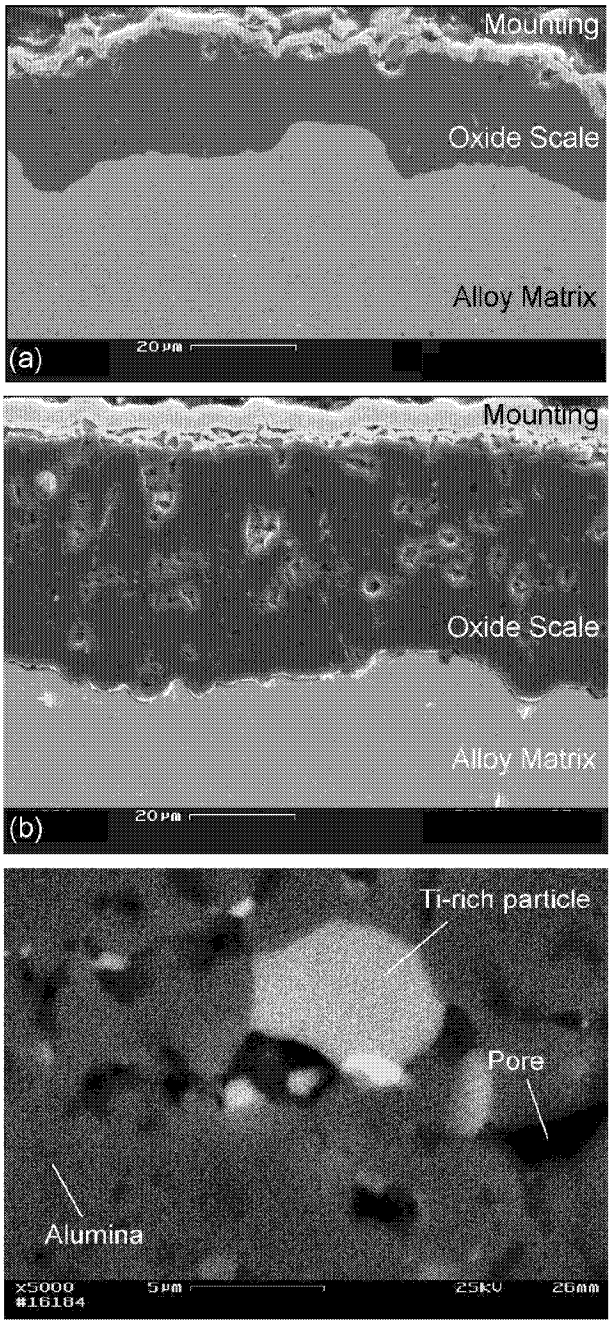

Figure 6.6: SEM cross sections of the oxide scales formed on two batches of PM 2000: (a) Batch CKS and (b, c) Batch CKT after 1000 h cyclic oxidation at 1200°C in air

Oxide fracture surfaces revealed that initially the scale microstructure on both batches did not differ significantly (Figure 6.7), showing a columnar scale morphology, which had been previously found typical for alumina scales growing by oxygen grain boundary diffusion

[8,29]. After longer times, batch CKS still maintained a columnar oxide grain structure (Figure 6.8-a), whereas batch CKT exhibited small equiaxed oxide grains with an increased amount of pores and microcracks (Figure 6.8-b). The latter observation can in fact explain the enhanced oxide growth rate for batch CKT after long term exposures in Figure 6.2, considering that fast molecular oxygen transport occurs through the pores and micro-cracks.

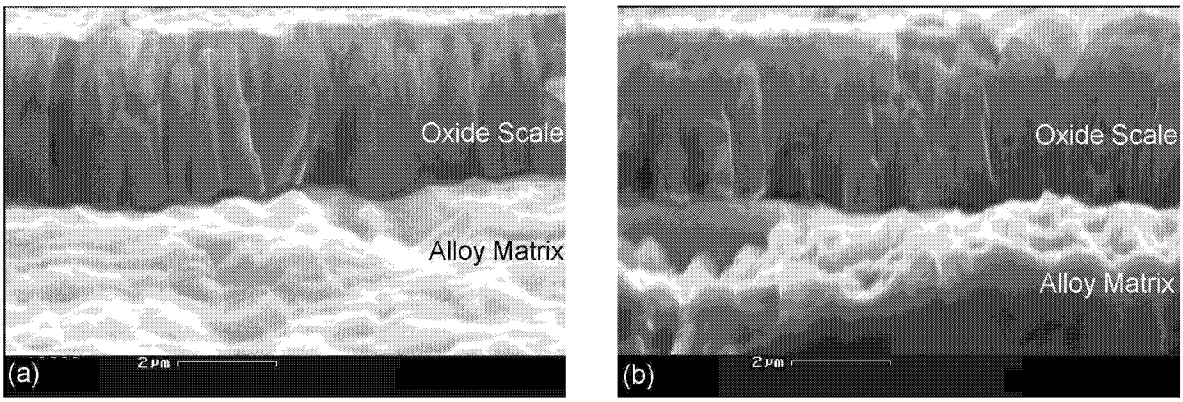

Figure 6.7: Fracture surfaces of oxide scales formed during 100 h isothermal oxidation of PM2000 at 1200°C in air: (a) Batch CKS; (b) Batch CKT

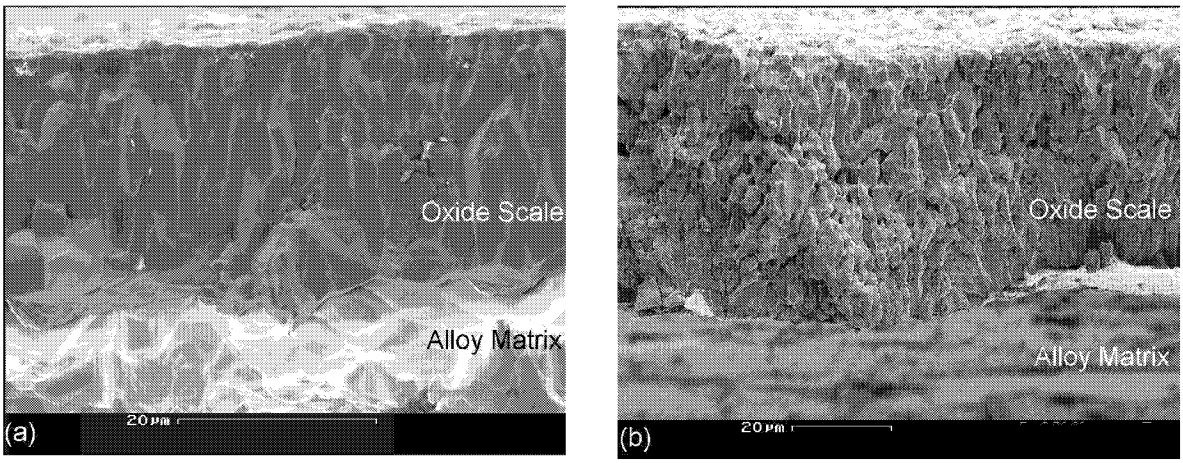

Figure 6.8: Fracture surfaces of oxide scales formed during 1000 h cyclic oxidation of PM 2000 at 1200°C in air: (a) Batch CKS; (b) Batch CKT

Figure 6.9 shows MCs^+-SIMS depth profiles of the oxide scales on the two batches after short time oxidation at 1200°C. The scales consisted of alumina with only small amounts of Fe, Cr, Ti and Y. An increase in the iron concentration followed by a relative maximum in the Cr concentration close to the oxide/gas interface was found. These Fe and Cr depth distributions appeared to be similar to those described earlier in reference [23], and related to the initial stages of oxidation. Both Ti and Y showed a tendency of enrichment at the oxide/gas interface. Yttrium seemed to exhibit a depletion area within the oxide, immediately beneath its zone of maximum enrichment at the oxide surface. The above mentioned features

were found for both batches whereby in the inner part of the scale on batch CKS (Figure 6.9-a), the Ti content was much lower than that in the scale on CKT (Figure 6.9-b).

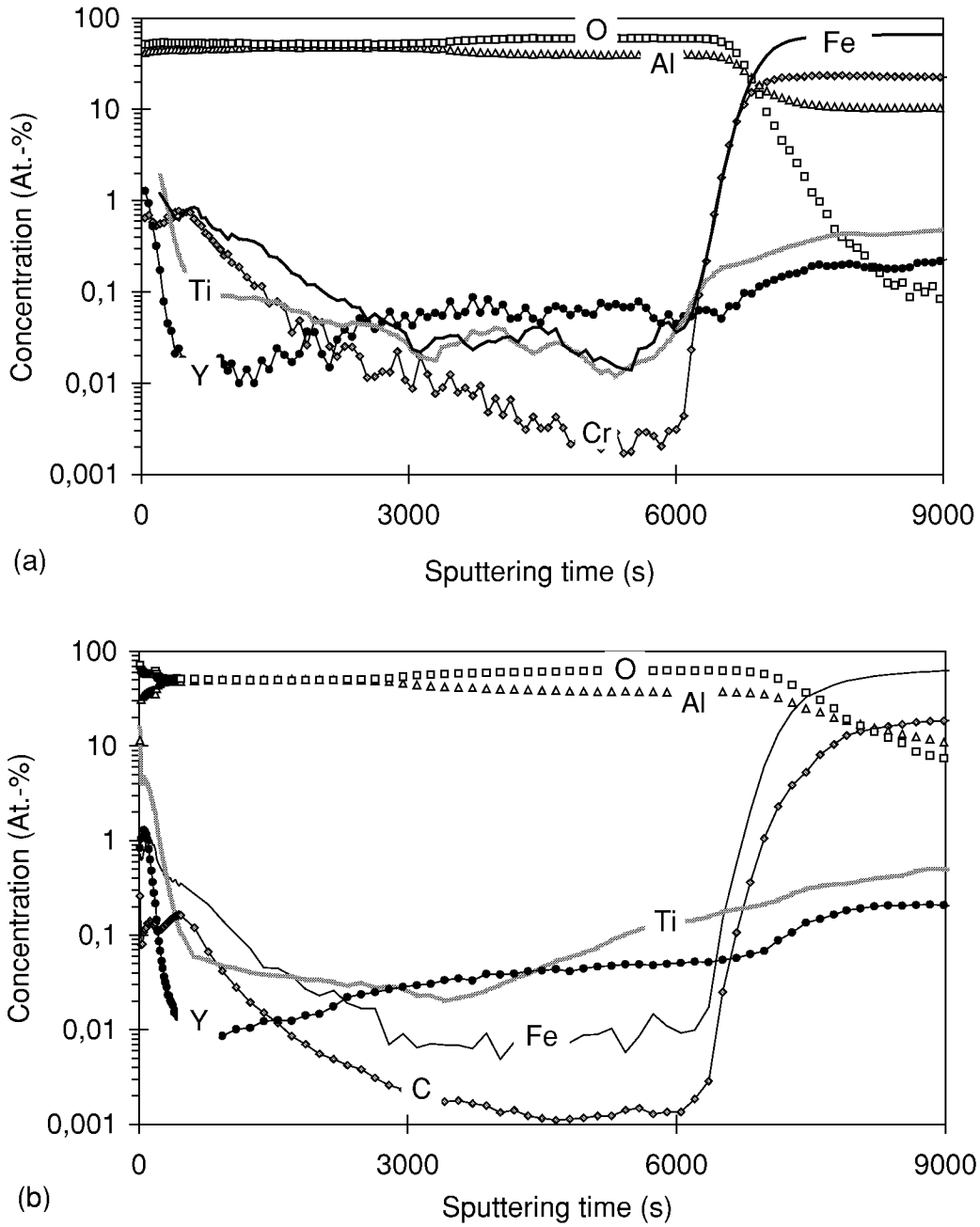

Figure 6.9: MCs^+-SIMS depth profiles of oxide scales formed on PM 2000 after 100h isothermal oxidation at 1200°C in air: (a) Batch CKS and (b) Batch CKT

Ti is commonly found in oxide scales formed on the FeCrAl-based ODS alloys [25,27]. It forms Y-Ti oxide precipitates at the scale grain boundaries and it is known to become enriched at the oxide surface [8,9,25,27]. Considering the correlation between Y and Ti in the alumina scale it is likely to assume, that both elements are transported to the scale/gas interface via the same paths i.e. oxide grain boundaries [25]. Similar observations of TiO_2 particles within the alumina scale were made recently when studying the long term oxidation

behaviour of the commercial ODS alloy MA956 at 1100°C and 1200°C [60,61,62]. The scales on the studied batches of MA956 showed similar features as observed here for batch CKT, i.e. the scales were porous and exhibited accelerated growth kinetics during long term oxidation [61,62].

The unusual oxidation behaviour of batch CKT can be explained taking into account the following observations: The enhanced oxide growth rate occurs after the scale reached a thickness of 6.5 to 7.5 µm, independent of the oxidation temperature. The increase in the growth rate proceeds together with adoption of a yellowish scale coloration. This yellowish colour is due to the presence of the titania particles embedded into optically transparent alumina scale. These rutile particles seem to correlate with the scale macrodefects, such as voids and microcracks. All these observations strongly indicate that the differences in oxidation rates for the two batches of PM 2000 are related to differences in Ti incorporation into the growing oxide scale.

Considering the bulk alloy chemical composition (Table 2 in Appendices), there appears to be no obvious reason why Ti-incorporation into the scale should differ for the two studied batches, because their Ti contents are virtually identical. For checking a possible correlation between oxidation behaviour and alloy microstructures, TEM studies were carried out to characterise the time dependence of the alloy microstructural features. Figure 6.10 and Table 6.1 summarise the microstructural characteristics of both studied batches in the as-received state and after 1000 h exposure at 1200°C. Both materials contained the common [26] yttrium-rich oxide dispersions with a size of around 10 to 20 nm. In addition, large particles ($d \approx 260$ nm) were found in the bulk of batch CKT. These large particles were identified as titanium carbonitrides. In batch CKS this type of precipitates was not observed. A small number of large particles in the bulk of CKS ($d \approx 270$ nm) were found to consist of aluminium oxide.

In low-C/N alloys Ti can be assumed to be dissolved in the alloy matrix and to get incorporated into the scale via normal diffusion processes [8]. Since the nitrogen content in batch CKT is significantly higher than that in batch CKS (Table 4.1) the Ti in the first mentioned batch is partly tied up in the bulk alloy as stable TiN and/or Ti(C,N) precipitates. Therefore, the process of normal Ti incorporation in the scale is expected to be hampered. However, initially this difference between the CKS and CKT materials has apparently no significant effect on the alumina growth rate (Figure 6.2).

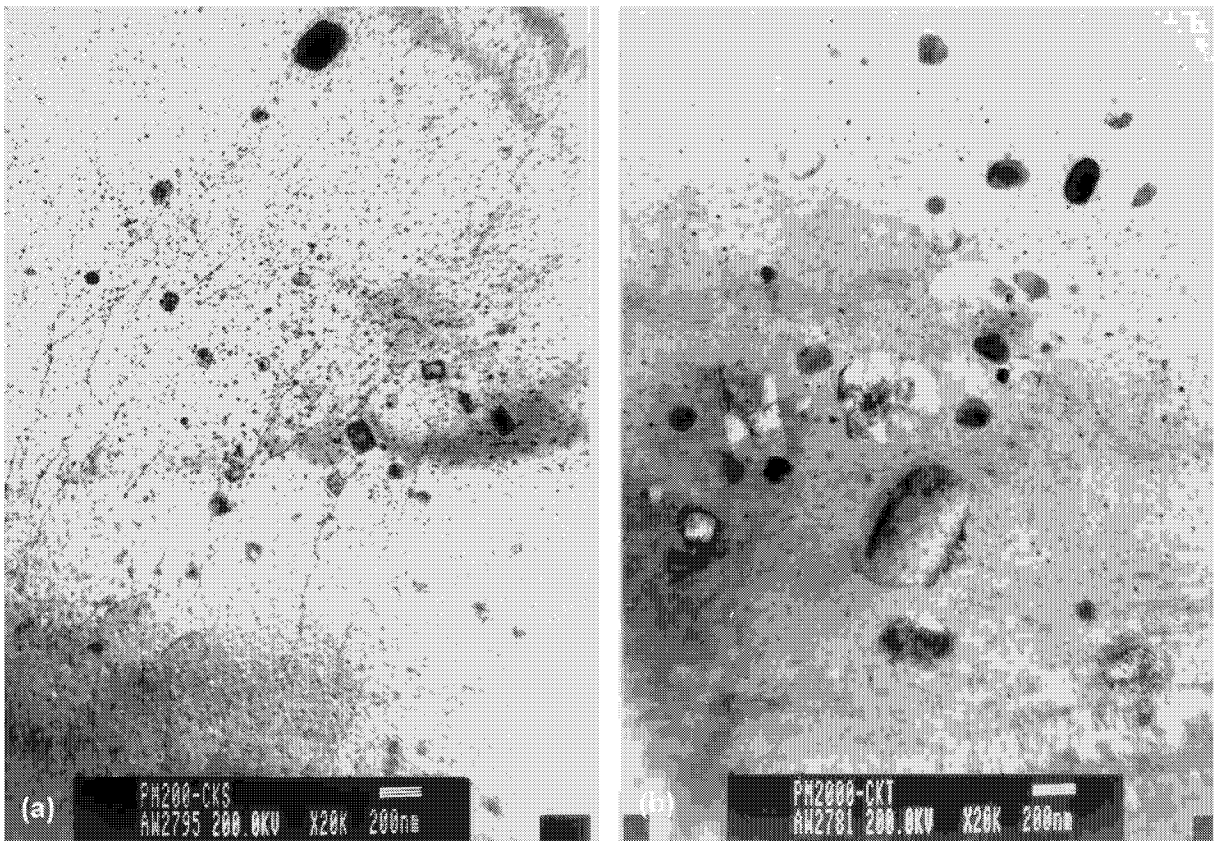

Figure 6.10: TEM images (double extraction replica) showing precipitates in alloy bulk of PM 2000 in as-received condition: (a) Batch CKS; (b) Batch CKT

Table 6.1: Quantitative analyses of bulk alloy precipitates in batches CKS and CKT of PM2000 identified in TEM-studies by Energy Dispersive X-Ray Spectroscopy (EDS) and Selected Area Diffraction Pattern (SADP)

CKS as received		CKS after 1000h at 1200°C	
$Y_3Al_5O_{12}$ d = 12 nm	Al-rich particles d = 115 nm	$YAlO_3$ d = 17 nm	Al_2O_3 D = 267 nm
CKT as received		CKT after 1000h at 1200°C	
$Y_4Al_2O_9$ d = 22 nm	Ti-rich particles d = 221 nm	$Y_4Al_2O_9$ + $YalO_3$ d = 21 nm	TiN D = 258 nm

6.1.3 Mechanistic understanding of batch to batch variations in ODS alloys

In addition to the discussed above mechanism a second process of titanium incorporation into the scale is observed for batch CKT. TEM cross sections of the oxide scales (Figure 6.11a) and the element maps in Figure 6.11-c clearly showed that, as the alumina scale grows inward via grain boundary oxygen diffusion [8,34], the titanium (carbo)nitrides from the bulk material become incorporated and subsequently embedded into the scale. Due to the low oxygen partial pressure near the scale/metal interface the embedded nitrides initially remain thermodynamically stable (Figure 6.11-b,c).

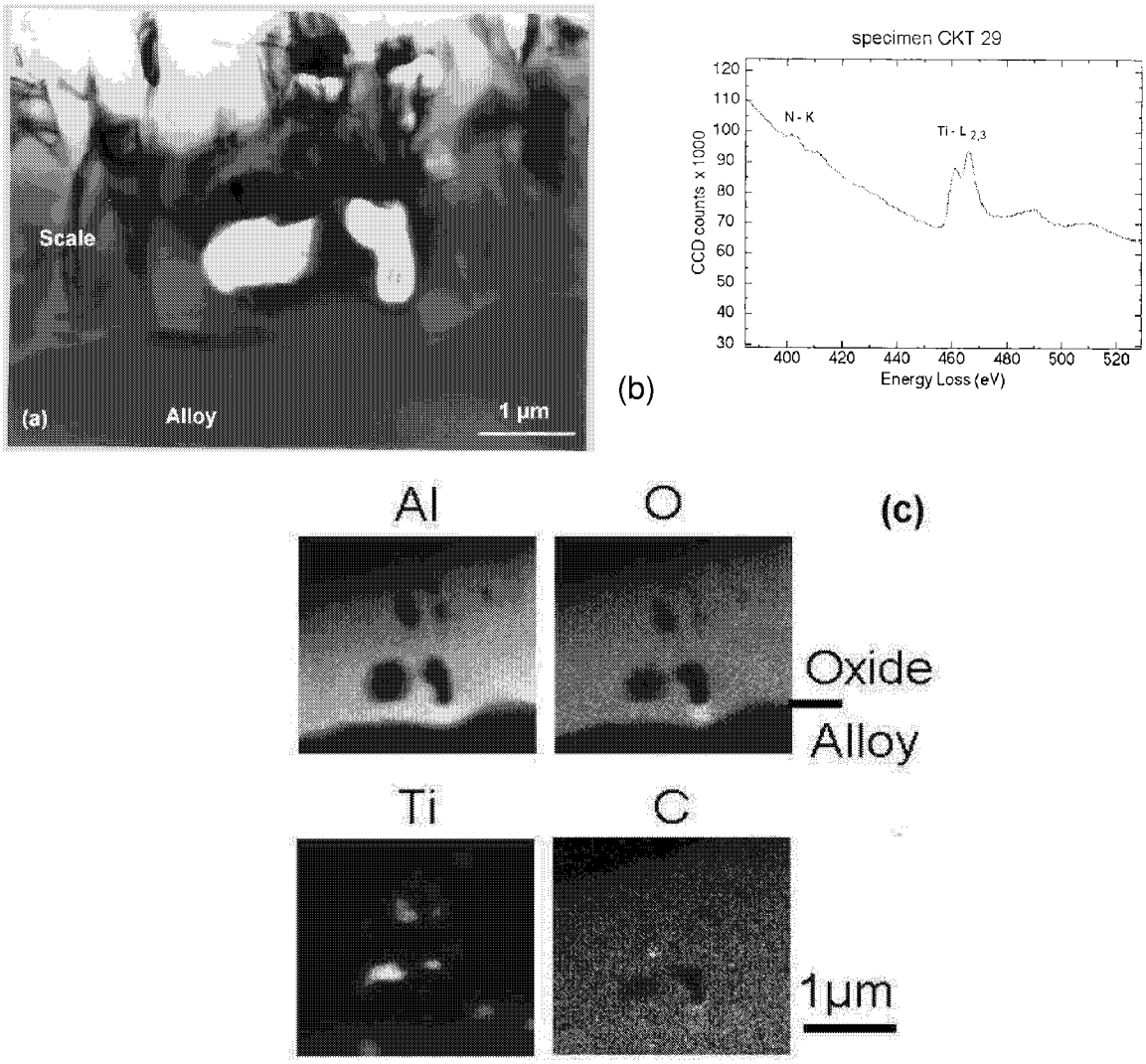

Figure 6.11: Oxide scale formed on batch CKT during oxidation for 20h at 1200°C in air:
(a) TEM cross section image;
(b) EELS analysis of Ti-rich inclusion in (a);
(c) Element mapping of oxide scale cross section in (a)

If the inward scale growth proceeds, the nitride particles in the scale will approach the area where the oxygen partial pressure is sufficiently high for the nitrides to be oxidised (Figures 6.12 and 6.13) according e.g. to the chemical reaction:

$$2TiN + 2O_2 \rightarrow 2TiO_2 + N_2^{\uparrow} \qquad (6.1)$$

During the transformation of the nitride into oxide one mole of titania (V_{mol}^{TiO2}=18.88 cm^3/mole) is produced from one mole of TiN (V_{mol}^{TiN}=11.39 cm^3/mole), i.e. a factor of 1.7 volume increase is expected. This volume change is believed to be responsible for the formation of micro-cracks and pores in the scale. Possibly the pore and crack formation is enhanced by the release of high pressure nitrogen gas resulting from reaction (6.1) (Figure 6.12).

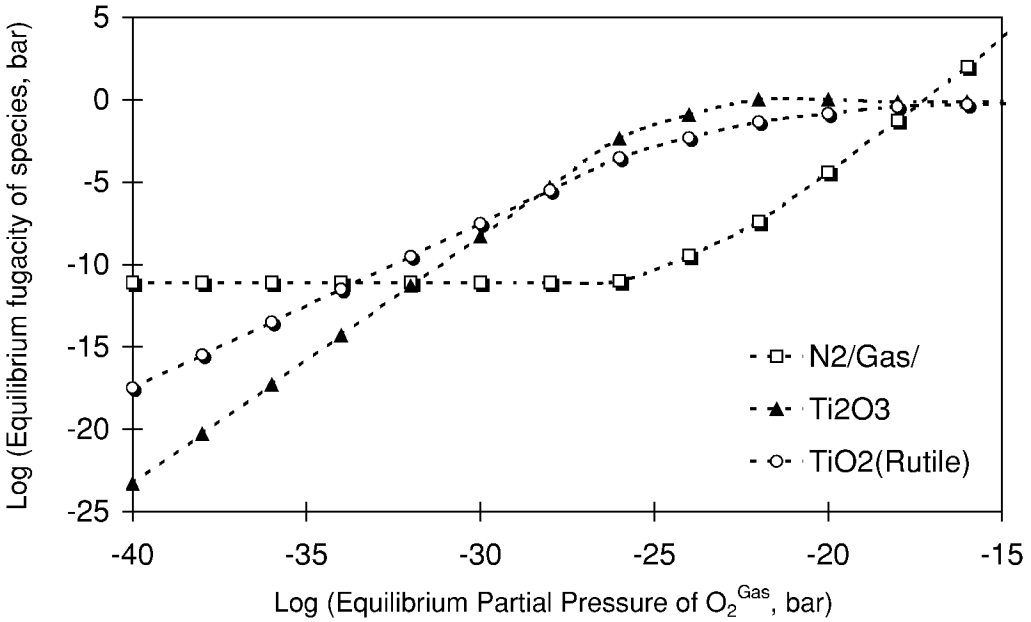

Figure 6.12: Calculated dependence of partial pressures of different species for oxidation of titanium nitride (compare equation 6.1.) as a function of oxygen partial pressure

Only few literature data exists on the presence of titanium nitrides in the alumina scales. TiN particles were found recently in scales formed on the commercial ODS alloy MA956 during short time oxidation (25h) at 1400°C in air [63]. The presence of the nitrides was also related to the alloy microstructure, due to the fact that the production of MA956 includes mechanical alloying of FeCrAl powders in air. However, no specific TEM studies on the alloy microstructure were made and no transformation of the particles into oxides was observed. Like in the present study, no significant spallation of the alumina scale was found, although microcracking of the scale in the vicinity of the TiN particles upon cooling was reported [63].

The proposed mechanism of Ti(C,N) particles incorporation into the alumina scale can fully explain the main experimental observations concerning the differences in oxidation behaviour of the two batches of PM 2000, i.e:

- the detrimental effect of the (carbo)nitride particles embedded into the scale does not appear during short term exposures. It can only be observed and becomes pronounced after longer exposure times, i.e. after the (carbo)nitrides are transformed into oxides. The time, which is necessary for the (carbo)nitrides to become oxidised depends on the scale thickening rate i.e. it decreases with increasing temperature (Figure 6.2 and 6.3);
- the yellowish colour of the scale on the PM 2000 batch CKT only occurs after relatively long exposure times. It is caused by the titania particles formed after oxidation of (carbo)nitrides within the alumina scale which is transparent for visible light.

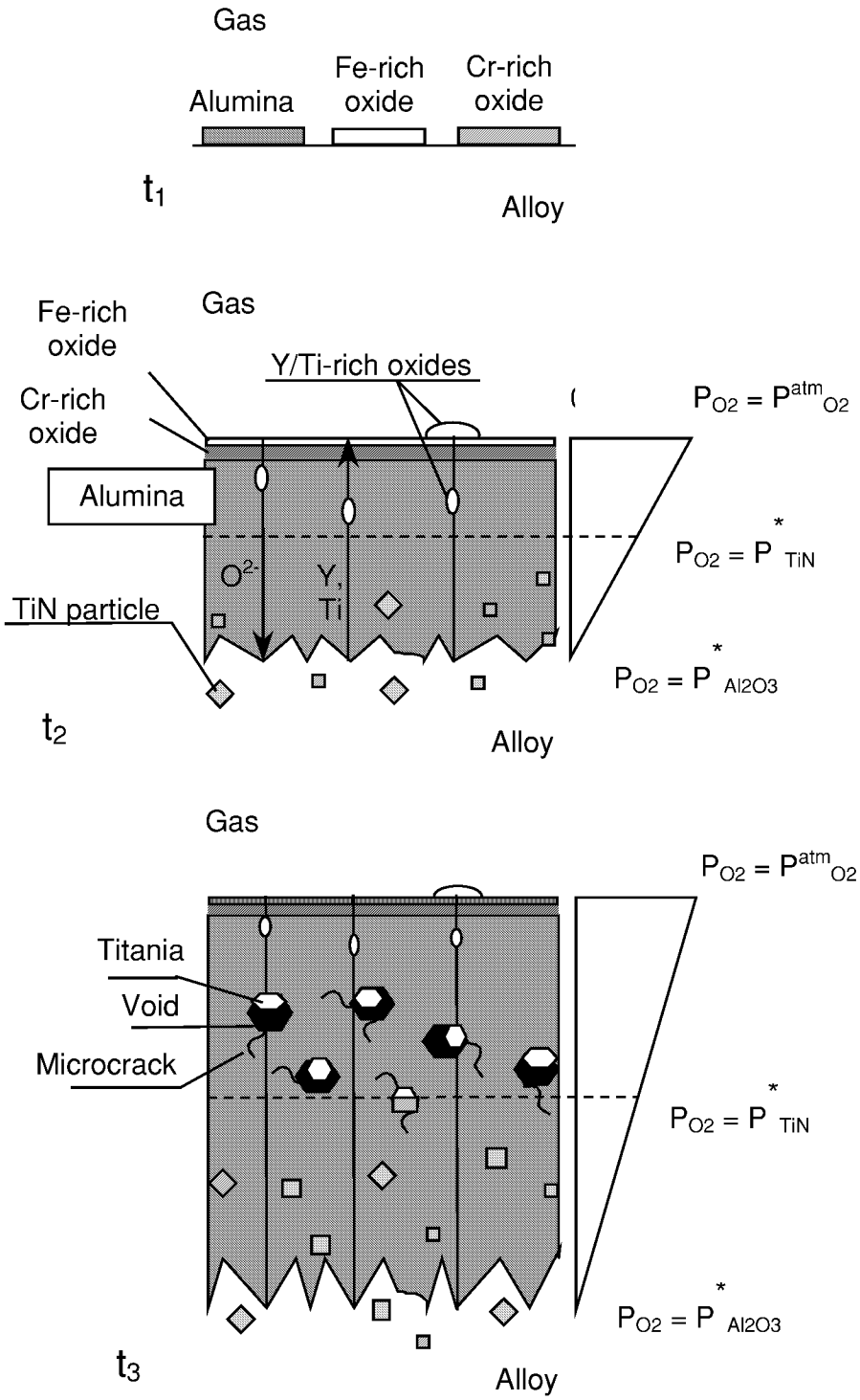

Figure 6.13: Schematic of (carbo)nitrides incorporation in inward growing oxide scale and subsequent oxidation to Ti-rich oxides:
P^*_{Al2O3} - oxygen partial pressure at scale/metal interface;
P^*_{TiN} - oxygen partial pressure required to oxidise TiN.

An important observation made during the cyclic oxidation tests was the excellent scale adherence on batch CKT in spite of a very large scale thickness of 50µm. The latter value is far above the typical reported scale thickness for spall initiation of 15-20 µm [11]. The good adherence is even more surprising considering a number of large size defects (pores and

cracks, Figure 6.6-c) in the alumina scale on batch CKT. The combination of the two above mentioned factors, i.e. large scale thickness and numerous macro-defects, could lead to scale cracking and spalling upon cooling [42]. However, in ceramics science it is well known that porous refractory oxides generally possess a better resistance against thermal shock than the dense ones [57]. This is because the porous ceramics have a much lower Young's Modulus, than the compact specimens [57]. Hence, under the same cyclic conditions the same cooling oxide strain leads to a much lower oxide stress in a porous oxide than in a dense one. It must be noted that the beneficial effect of porosity on oxide adherence is expected to occur when the former is large, i.e. in the order of 10 % [57].

It was found that Ti doping of the FeCrAl wrought alloys, which already contained yttrium, led to an increase of the oxide growth rate [64]. In this study it has been shown that an adverse effect on oxide growth rate can occur if most of the Ti is tied up in the bulk alloy as Ti(C/N) particles due to high C and/or N contents of the actual alloy or alloy batch.

On the other hand in the commercial FeCrAl ODS materials, such as PM 2000, MA956 and ODM 751, Ti is not an impurity, but a typical minor alloying element, added for modification of the alloy mechanical properties. The results presented in this section clearly show, that the intentionally added Ti can have a substantial effect on oxidation of FeCrAl ODS alloys. Therefore, in the following section, the oxidation behaviour of a Ti-containing and Ti-free model ODS alloys are compared, to get more mechanistic insight into the effects of the minor alloying addition of titanium.

6.2 Significance of Ti-additions for oxidation performance of FeCrAl ODS alloys

6.2.1. Effect of Ti on scale adherence during cyclic oxidation of ODS alloys

During cyclic oxidation at 1200°C the Ti-free material DAG exhibited significant scale spallation as shown in Figure 6.14-a. Just after two cycles, i.e. 200 h exposure the mass of the spalled oxide on DAG overtook that due to the scale growth, which is indicated by a decrease in specimen mass. In contrast, on the Ti-doped model alloy the scale spallation occurred at a mass change of 2.5 to 3.5%, i.e. when the alumina scale reached a thickness of ca 20 µm. This behaviour of the Ti-containing model alloy is similar to that of the commercial ODS alloys, which normally have a 0.5% Ti addition [46] (the chemical compositions of the model and commercial alloys are given in Tables 2 and 3 in Appendices). The difference in spallation resistance resulted in a significant lifetime variation between the two model alloys, which appeared to be around a factor of two (Figure 6.14-b).

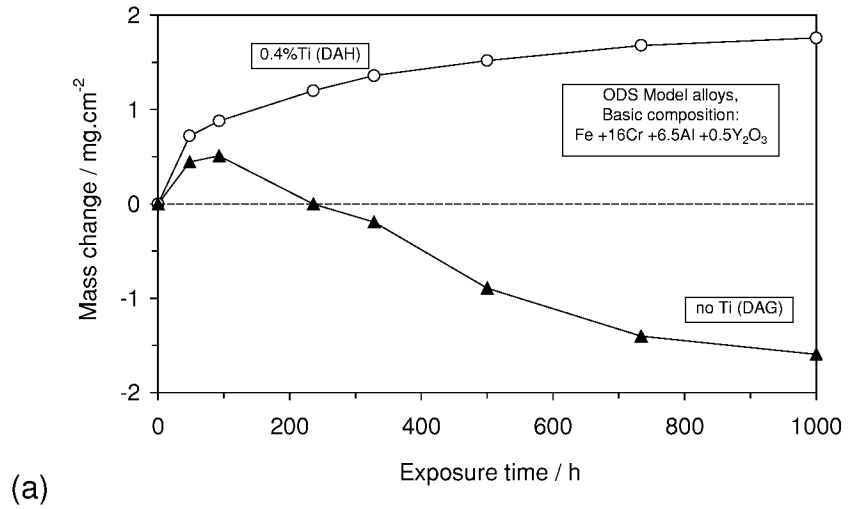

(a)

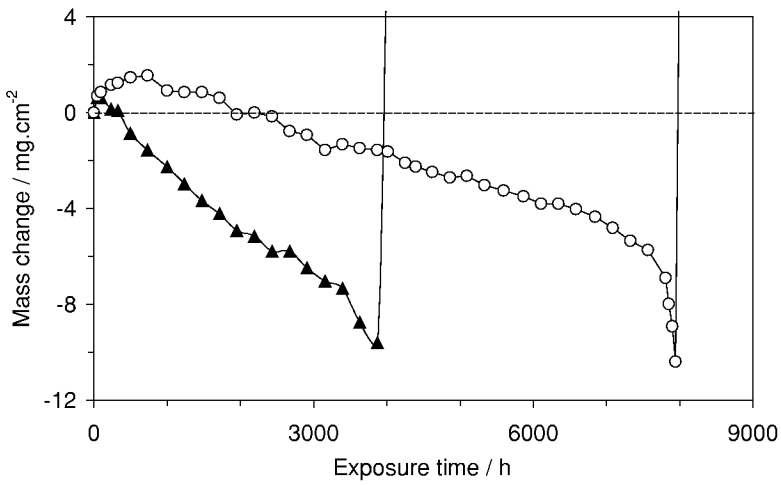

(b)

Figure 6.14: Mass change data for 2 mm thick model ODS alloys with Ti (Batch DAH) and without Ti (Batch DAG) during cyclic oxidation (50 h cycles) at 1200°C in air:
(a) 1000 h exposure; (b) lifetime oxidation test till breakaway

The isothermal oxidation data at 1200°C for the model ODS alloys are presented in Figure 6.15. The mass changes after 100 h exposure seem to be very similar. After cooling down to room temperature substantial scale spallation was observed on the specimens of the Ti-free model alloy DAG (Figure 6.16).

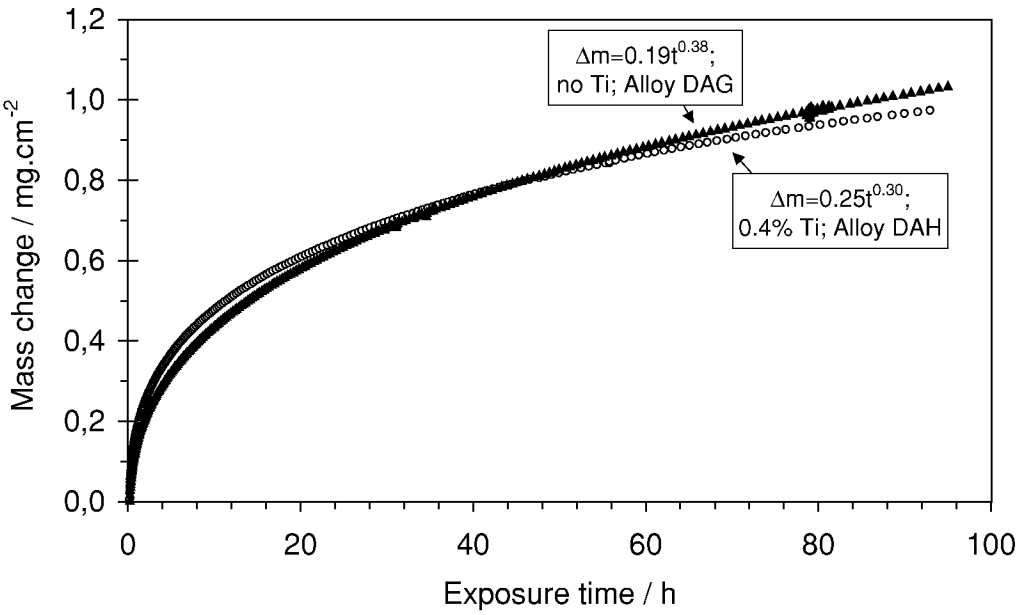

Figure 6.15: Mass change data for model ODS alloys with Ti (DAH) and without Ti (DAG) during isothermal oxidation at 1200°C in synthetic air. Scale growth kinetics, calculated from mass change data, assuming power law time dependence (eq-n 2.12) are given in plot

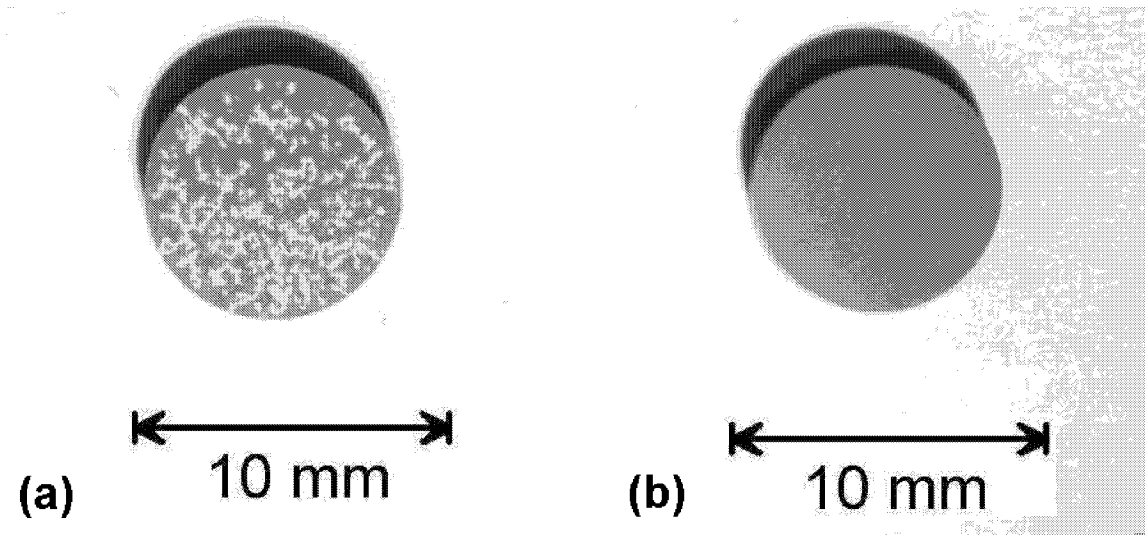

Figure 6.16: Macrographs of model ODS coupons after 300 h cyclic oxidation (100 h cycles) at 1200°C in air: (a) Ti-free alloy DAG; (b) 0.4%Ti-containing alloy DAH

6.2.2. Effect of Ti on structure and morphology of protective alumina scale

The XRD patterns obtained from the specimens oxidised for 300 h at 1200°C are presented in Figure 6.17. The highest peaks belong to Al_2O_3 and the FeCrAl matrix. The ratio of the alumina /matrix peak intensities is lower for the Ti-free alloy because a significant amount of

the oxide has spalled off. On the pattern for the Ti-counting alloy in addition to the above mentioned phases some small peaks appeared, which were identified as those of $Ti_2Y_2O_7$.

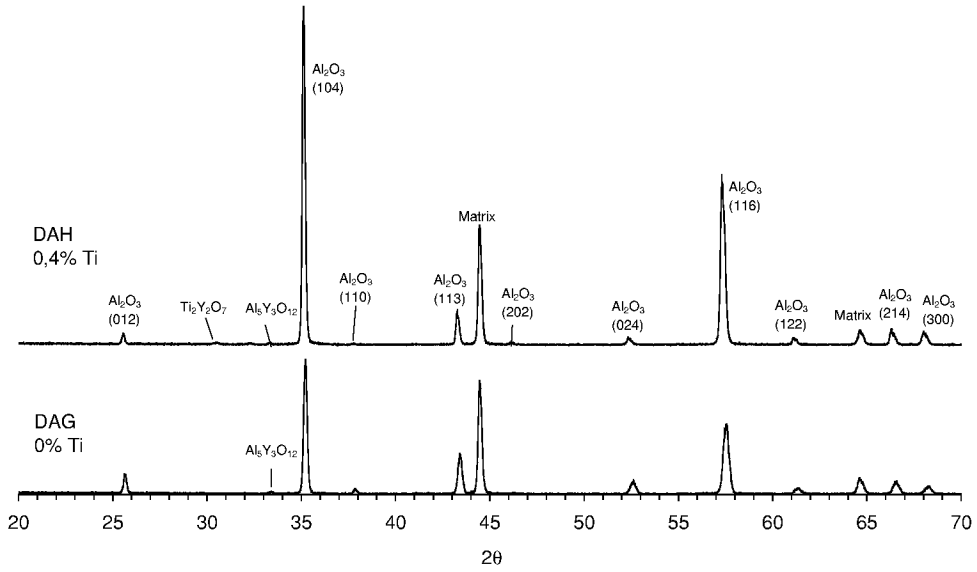

Figure 6.17: XRD patterns taken from specimens of model ODS alloys with Ti (DAH) and without Ti (DAG) after 300 h cyclic oxidation at 1200°C in air

The morphologies of the surface scales were studied by SEM after short 2 h isothermal oxidation and 300 h cyclic oxidation at 1200°C (Figure 6.18 to 6.21). After 2 h oxidation, the surface of the Ti-free alloy appeared to have convolutions with a size of ca 20µm (Figure 6.18-a). In case of the Ti-doped alloy DAH the scale was flat (Figure 6.19-a). It is noteworthy that after 2h exposure the scale thickness on both alloys is identical, which can be concluded from the mass changes in Figure 6.15. The detailed SEM-pictures of the scales in backscattered electrons revealed on the Ti-free alloy small ≤0.1µm and random particles of an Y-rich oxide (Figure 6.18b). In contrast on the Ti-containing alloy, 0.5 µm large Y-rich oxide particles were detected (Figure 6.19-b). After 300 h cyclic oxidation large parts of the scale spalled off on the Ti-free alloy DAG (Figure 6.20-a). At the same time the scale on DAH remained flat and well adherent to the substrate (Figure 6.21-a). In the places on DAG, where the scale was still intact, small 0.3 µm large alumina grains and randomly distributed Y-rich oxide particles could be observed (Figure 6.20-b). On alloy DAH, 1 to 2 µm large alumina grains and a number of evenly distributed Y- and Y/Ti-rich oxide particles of similar size were found (Figure 6.21-b). Figure 6.22 shows in detail a spalled region on the Ti-free alloy DAG. It gives an indication for the scale failure mechanism, namely that the scale cracking occurred first at the crest of a convolution. The wedge crack then propagated along the scale/metal interface leading to spalling of a scale piece.

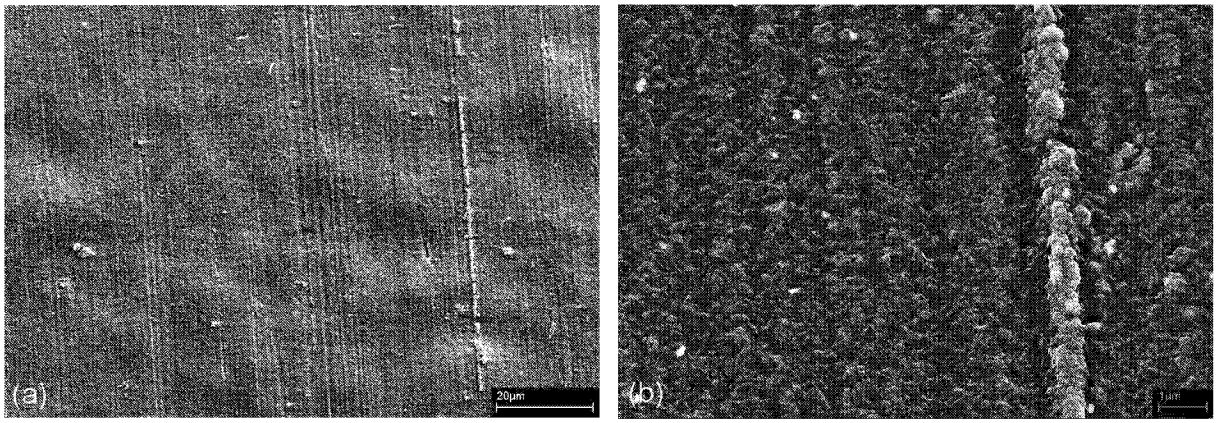

Figure 6.18: Surface scales on Ti-free model ODS alloy DAG after 2h isothermal oxidation at 1200°C in air: (a) secondary electron image; (b) high resolution backscattered electron image

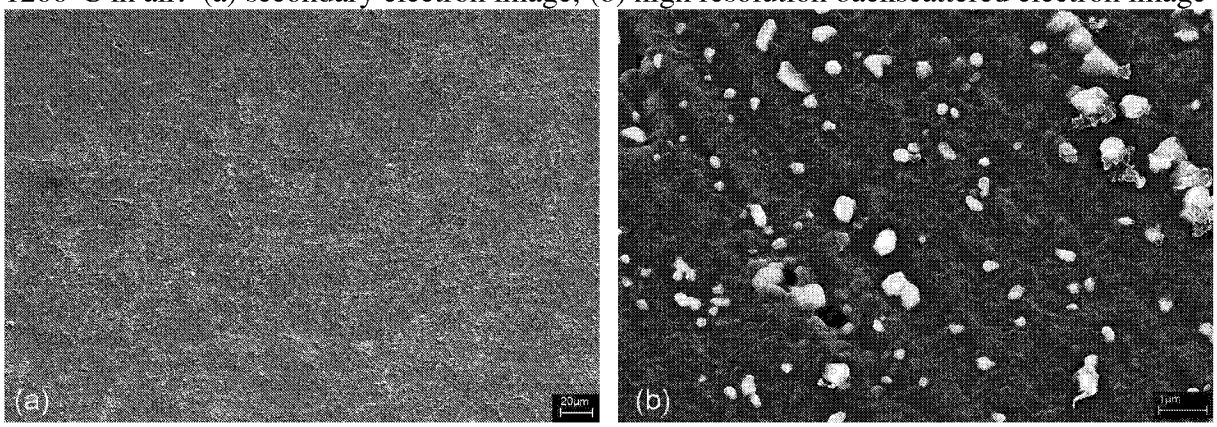

Figure 6.19: Same as Figure 6.18 for Ti-containing model ODS alloy DAH

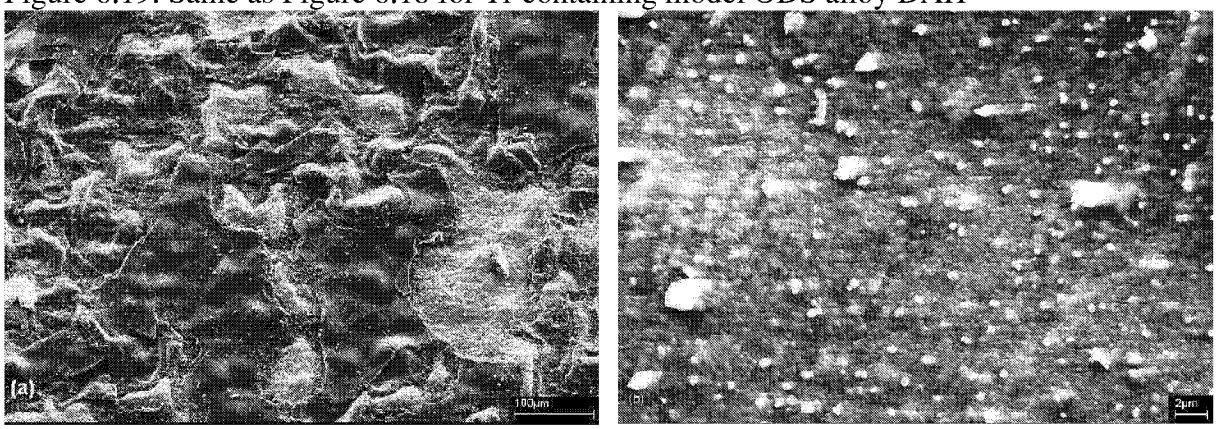

Figure 6.20: Surface scales on Ti-free model ODS alloy DAG after 300h cyclic oxidation at 1200°C in air: (a) secondary electron image; (b) high resolution backscattered electron image

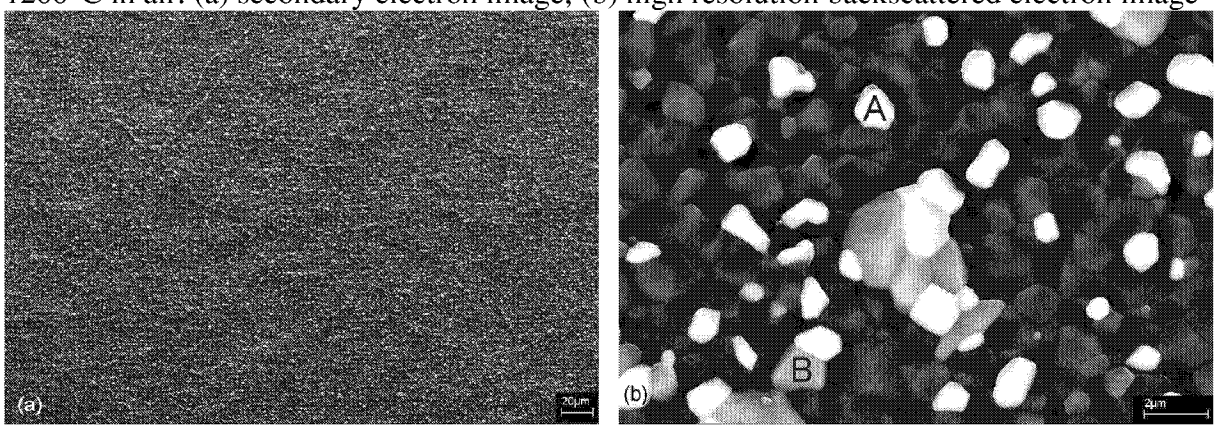

Figure 6.21: Same as Figure 6.20. for Ti-containing model ODS alloy DAH: Particle A – Y/Al-rich oxide phase; Particle B – Y/Ti-rich oxide phase

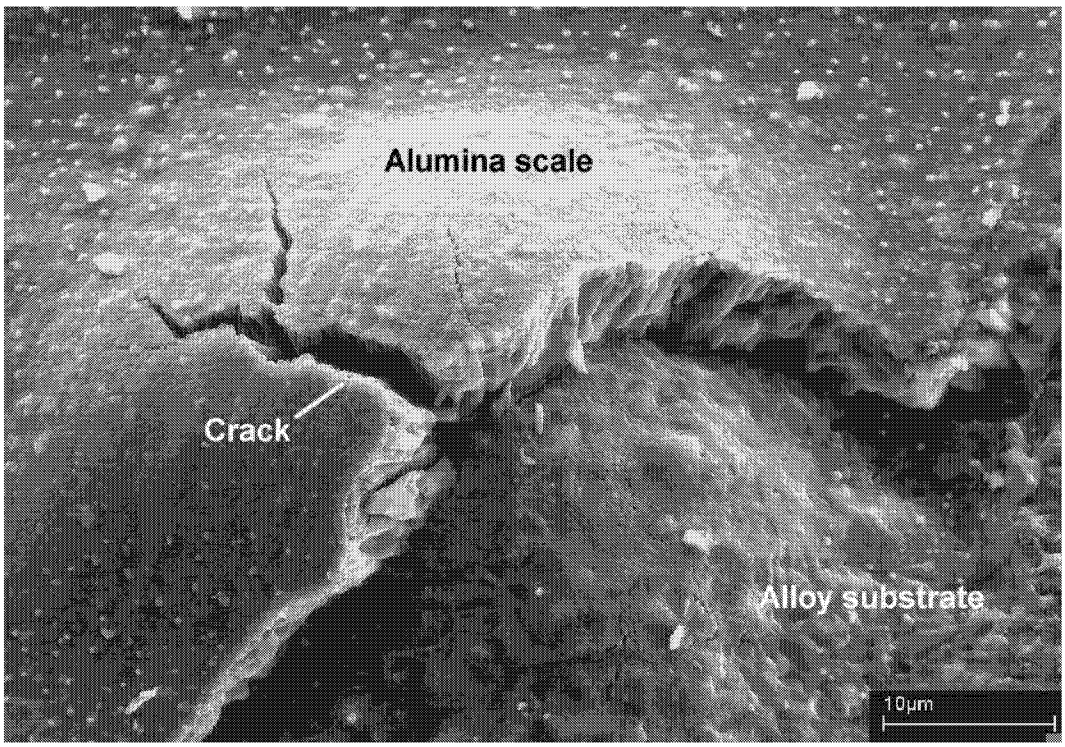

Figure 6.22: Spalled area of oxide scale formed on Ti-free model ODS alloy DAG after 300 h cyclic oxidation (100 h cycles) at 1200°C in air

Additional information on surface morphologies of the scales on the two alloys was provided by atomic force microscopy (AFM). The studied specimens had been polished to a mirror-like surface prior to exposure and subsequently oxidised for 2 h at 1200°C in air, so that no scale spallation occurred on batch DAG. Comparison of the two AFM images in Figure 6.23 shows that after 2h oxidation on alloy DAG local scale buckles emerged with an extremely high (close to unit) height to lateral size ratio. Although the effect of local scale buckling on the originally flat surface was also present on alloy DAH (Figure 6.23-b), it was not as obvious as on DAG and apparently diminished after longer exposure times not leading to scale spallation.

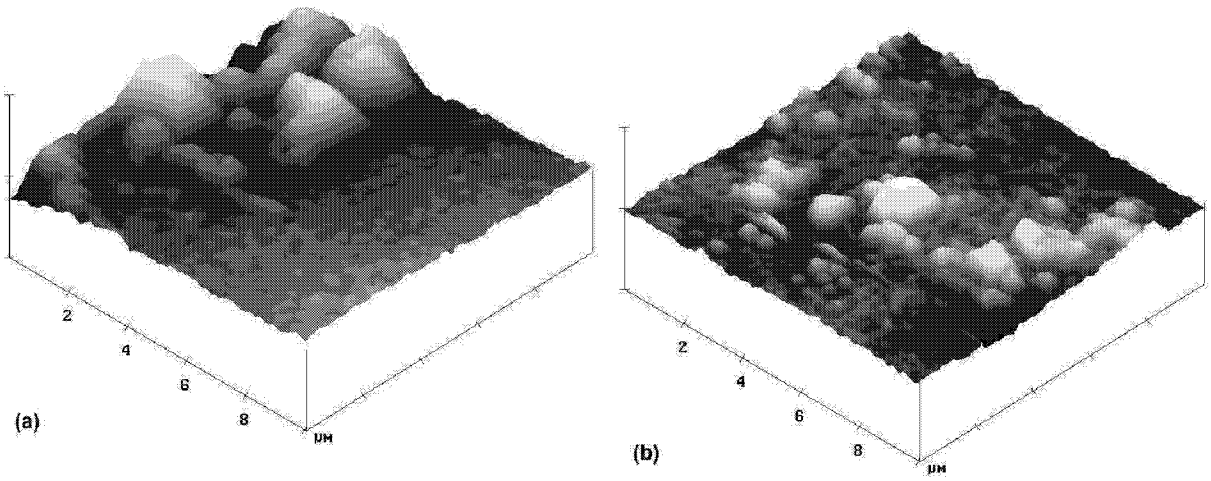

Figure 6.23: AFM images of scale topographies after 2 h oxidation of polished surfaces of two model ODS alloys: (a) Ti-free alloy DAG; (b) 0.4%Ti-containing alloy DAH

The metallographic cross-sections of the oxidised specimens shown in Figure 6.24 supported the SEM-observations on the scale surface. The oxide/metal interface of the Ti-free alloy DAG is severely convoluted; it can be clearly seen, that the scale spallation takes place at the convolution crests and the scale adherence at the valleys is still maintained (Figure 6.24-a). A flat scale, which is uniform in thickness on the DAH specimen demonstrates a scale morphology typical for the Ti-containing commercial ODS alloys (Figure 6.24-b).

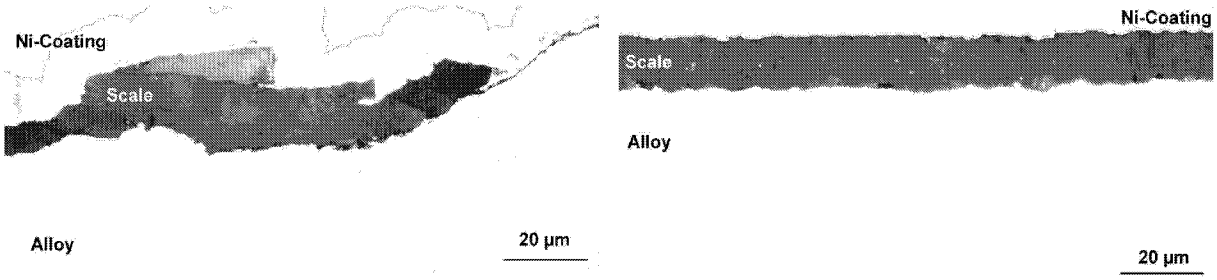

(a) (b)

Figure 6.24: Metallographic cross sections of oxide scales formed on two model ODS alloys after 300 h cyclic oxidation at 1200°C in air: (a) Ti-free alloy DAG; (b) 0.4%Ti doped DAH

The model alloys microstructure was characterised by metallography after acid etching of the alloy cross-sections (Figure 6.25). In the as-received condition (Figure 6.25-a, 6.26-a) the model ODS alloys showed a typical grain structure after hot isostatic pressing (HIP) of the metal powders. After exposure at 1200°C for 300 h and 600 h the grain boundaries became more apparent, however no significant grain growth occurred (Figure 6.25-b,c / 6.26-b,c). The latter observation contrasts to these made with the commercial FeCrAl ODS alloy PM2000 where the coarse grained structure was present in the as-received, i.e. recrystallised state (Figure 6.1). This is most probably related to the fact that the deformation rate after the HIP treatment of the model ODS alloys was not sufficient for subsequent recrystallisation to occur at 1200°C [64].

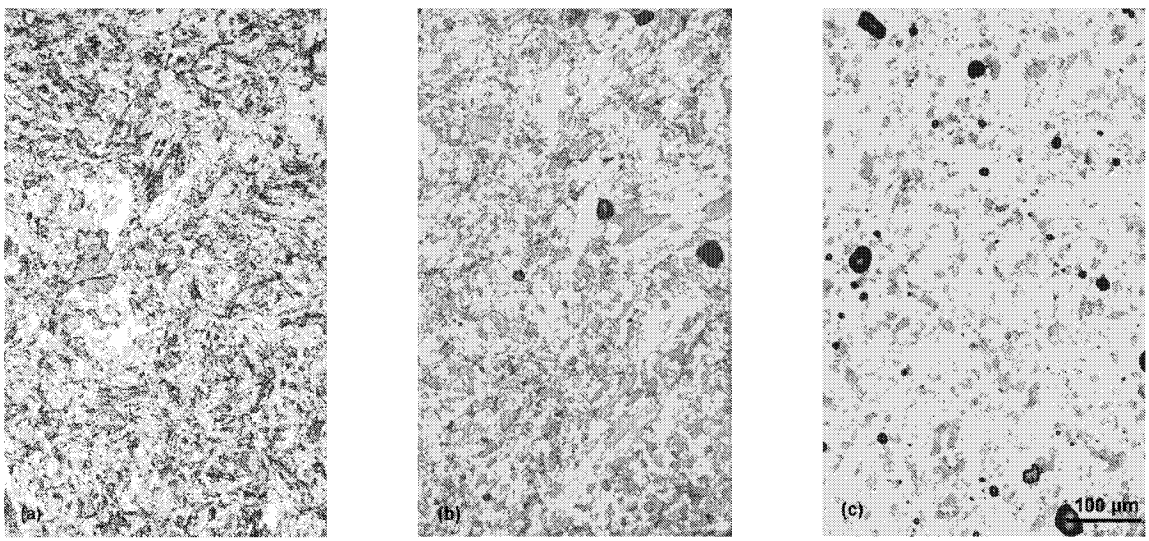

Figure 6.25: Etched cross sections of model ODS Ti free alloy DAG: (a) as received state; (b) after 300 h oxidation at 1200°C; (c) after 600 h oxidation at 1200°C

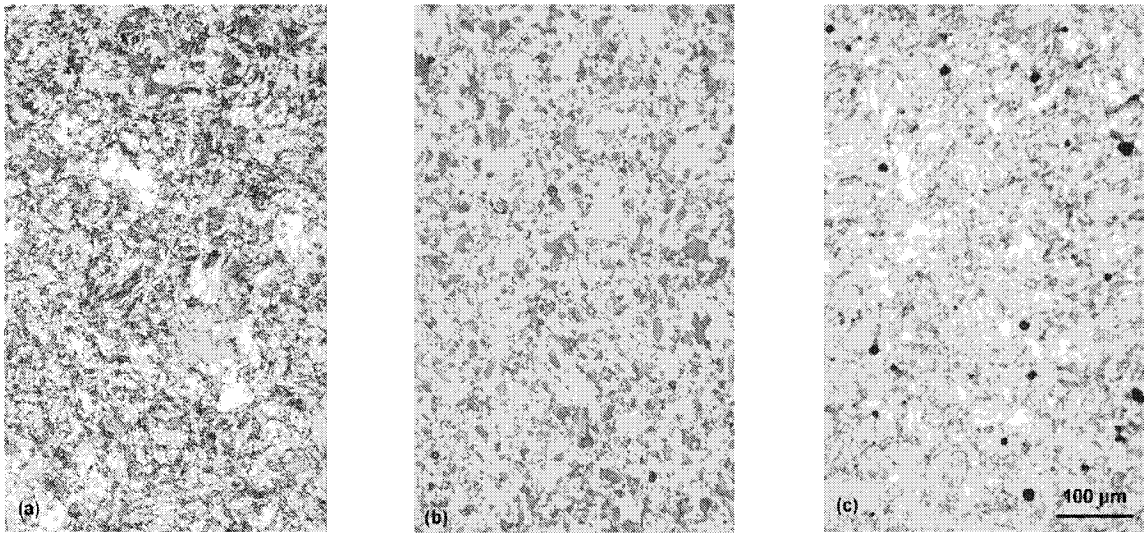

Figure 6.26: Etched cross sections of model ODS 0.4 %Ti-containing alloy DAH:
(a) as received state; (b) after 300 h oxidation at 1200°C; (c) after 600 h oxidation at 1200°C

The SEM studies of the cross-sectioned specimens after 300 h cyclic oxidation further stress the differences, related to the Ti effect. The scale formed on the Ti-free alloy, where still adherent, appeared to contain a number of defects, such as pores and microcracks (Figure 6.27-a). A complementary proof for the deteriorated scale adherence on the Ti-free material was that in the places, where the scale had not spalled after cooling, frequently a gap between the scale and the metal was observed, which might have occurred during the specimen preparation.

Precipitates of internal aluminium oxides and nitrides can be clearly seen in the matrix of alloy DAG (Figure 6.27-a). The scale on the Ti-doped alloy DAH appeared to be much less defective and perfectly adherent (Figure 6.27-b).

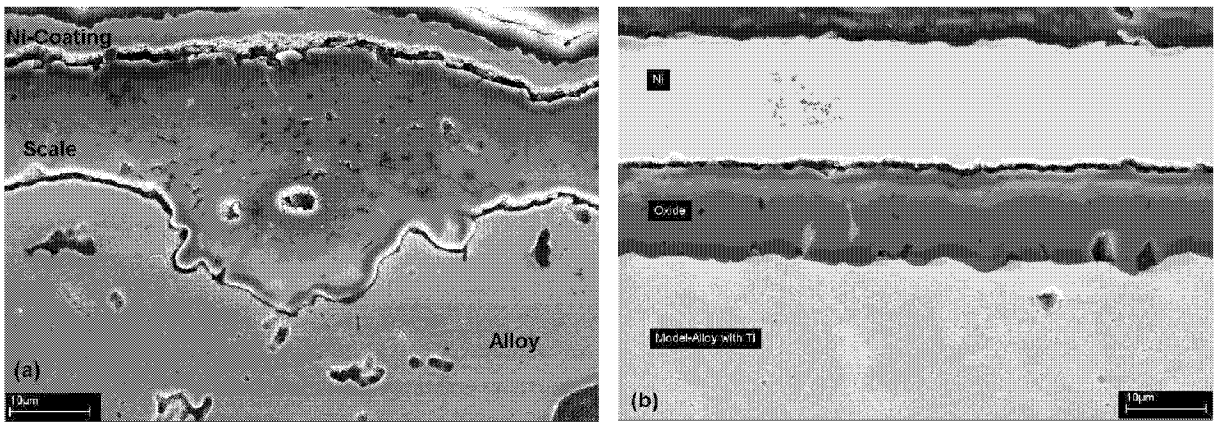

Figure 6.27: SEM images of cross-sectioned scales formed on model ODS alloys after 300 h cyclic oxidation at 1200°C in air: (a) Ti-free alloy DAG; (b) 0.4%Ti-containing alloy DAH

The element mapping in Figure 6.28 shows that the scales on both alloys mainly consisted of alumina. In alumina layers on both studied alloys, Y-rich oxide particles within the scale were

found, which are apparently $Y_3Al_5O_{12}$, as can be suggested from the XRD data in Figure 6.17. In addition, Al-nitride particles seemingly originating from the alloy matrix can be seen to become incorporated into the growing alumina scale. The scale on alloy DAH appeared to have more incorporated yttrium which was not only present as precipitates within the scale but also apparently enriched at the scale/metal and scale/gas interfaces.

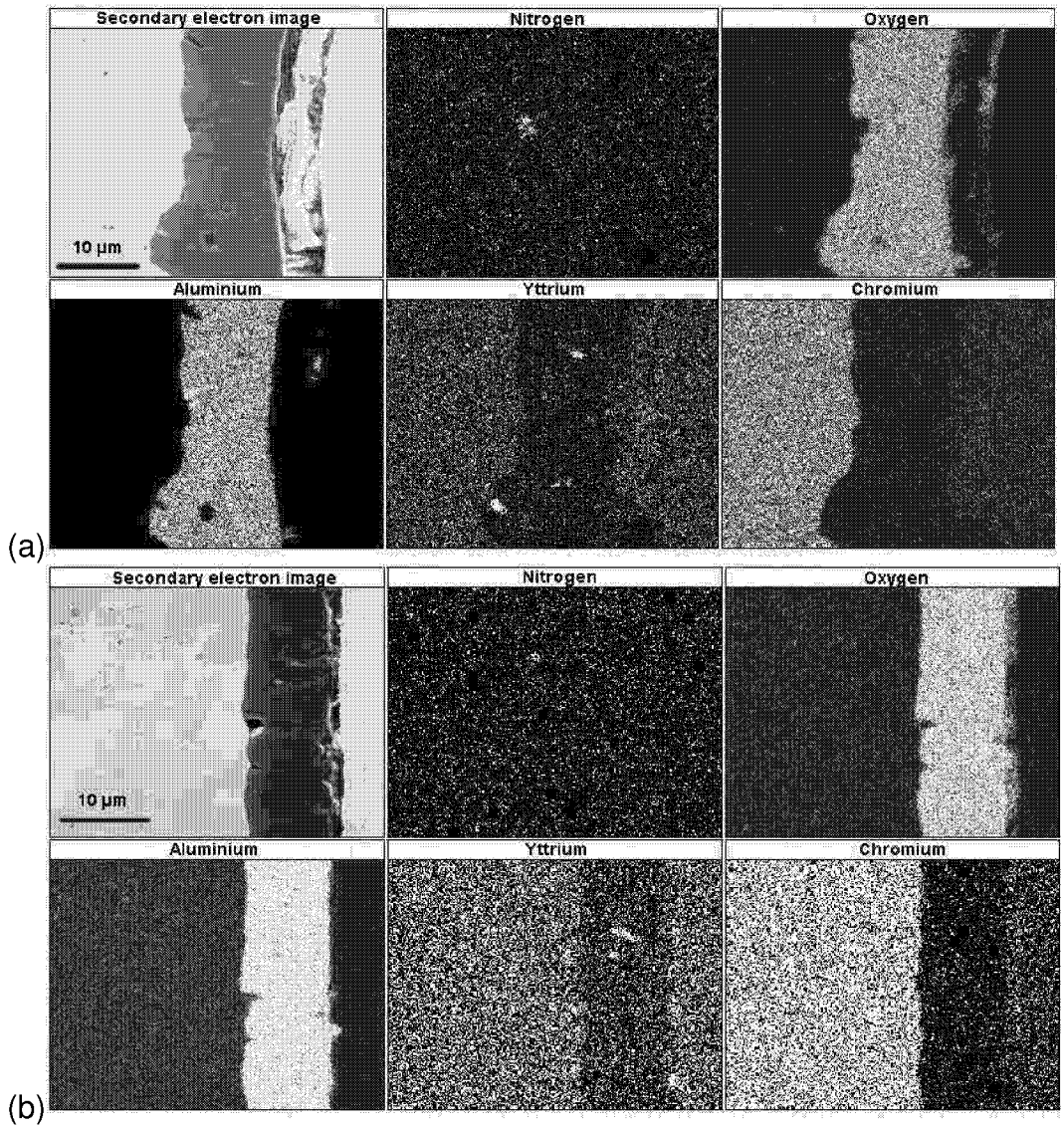

Figure 6.28: EDX element mapping of scales formed on two model ODS alloys after 300 h cyclic oxidation at 1200°C in air: (a) Ti-free alloy DAG; (b) 0.4%Ti-doped alloy DAH

6.2.3. Effect of titanium on yttrium mobility in alumina scale

In order to get more information on the composition of the scales on DAG and DAH two sensitive surface analysis techniques were applied, namely RBS and MCs^+-SIMS. The results of the RBS measurements in Figure 6.29 indicate that the 0.4% Ti addition to ODS alloy DAH promoted yttrium enrichment in the outer part of the alumina scale. Due to the method limitations the data on Y-enrichment could only be collected down to 0.1µm from the scale

top. The second difficulty was that due to overlapping of the characteristic energies for Fe, Cr and Ti, so it was not possible to measure the presence of Ti in the oxide layer.

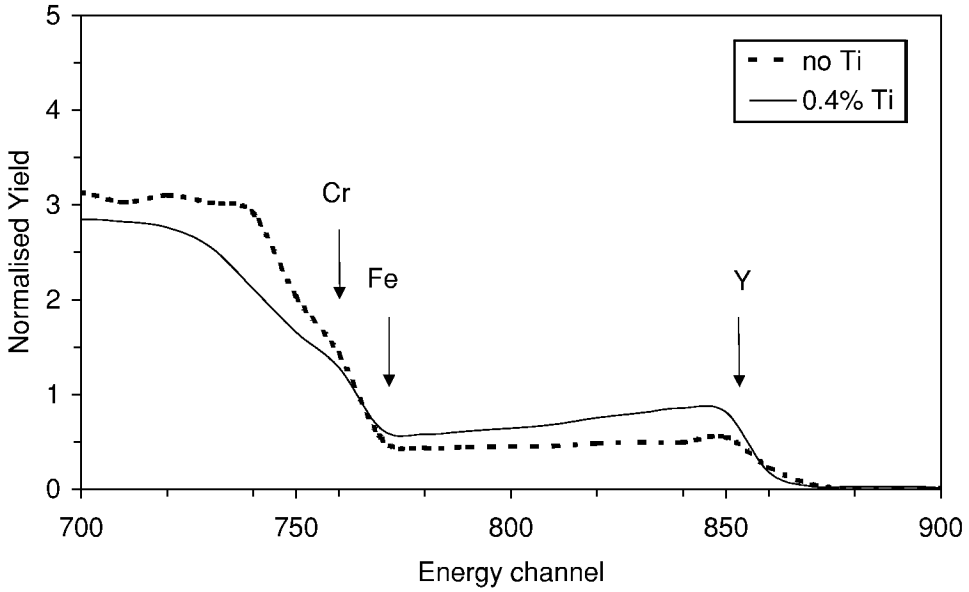

Figure 6.29: RBS-Spectra taken from the surfaces of model ODS alloys with and without Ti after 2 h oxidation at 1200°C in air. High energy edges for Cr, Fe and Y are indicated in plot, showing higher Y-signal intensity for the Ti-doped alloy

The SIMS depth profiles (Figure 6.30) helped partly to solve the above mentioned problems. After 2h oxidation at 1200°C both scales consisted mainly of alumina. The increase in Fe and Cr contents in the outer part of the oxide layers are due to the initial stages of oxidation as has been explained in reference [22]. On both alloys Y-enrichment at the scale/gas interface was detected. However, for the scale on the Ti-containing alloy DAH this effect is more obvious. In the outer part of the scale on alloy DAH a Ti-enrichment was found corresponding well to the Y-enrichment (Figure 6.29-b).

An interesting observation was that in the inner part of the scale on alloy DAH the Ti-profile exhibited a decrease, which was observed in the Y-profile. The most apparent difference in the composition of the two scales was the nitrogen distribution. A very high nitrogen concentration in the scale on alloy DAG could neither be easily correlated with the profiles of elements with high N-affinity nor with the data obtained using the other analyses techniques.

Based on the experimental data and contrary to the expectations after studying the two batches of the commercial alloy PM2000 in Chapter 6.1, Ti appeared to have a clear positive effect on the scale adherence on the yttria-doped FeCrAl ODS alloys. The most obvious

physical effect of titanium revealed in this study is enhancement of the yttrium incorporation and mobility in the alumina scales (Figure 6.19 and 6.21).

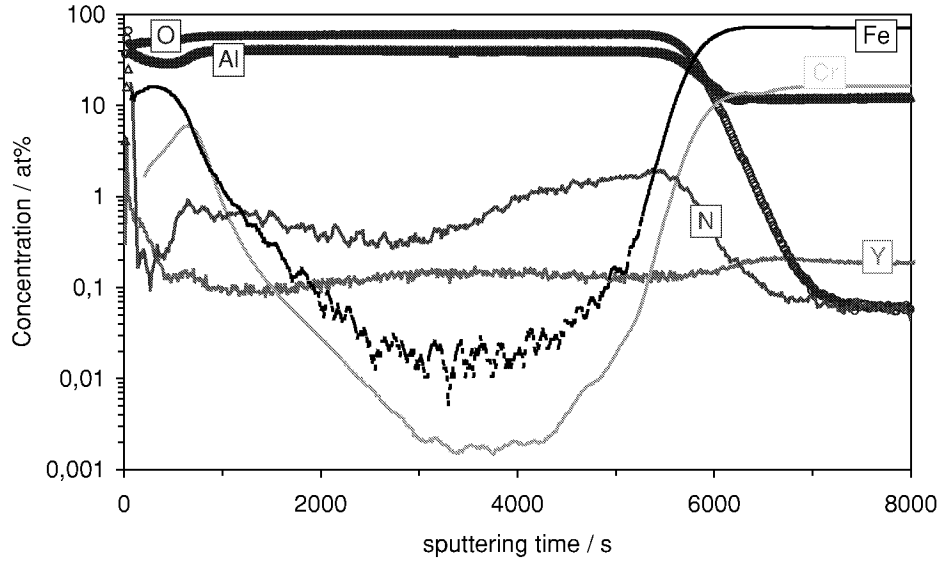

(a)

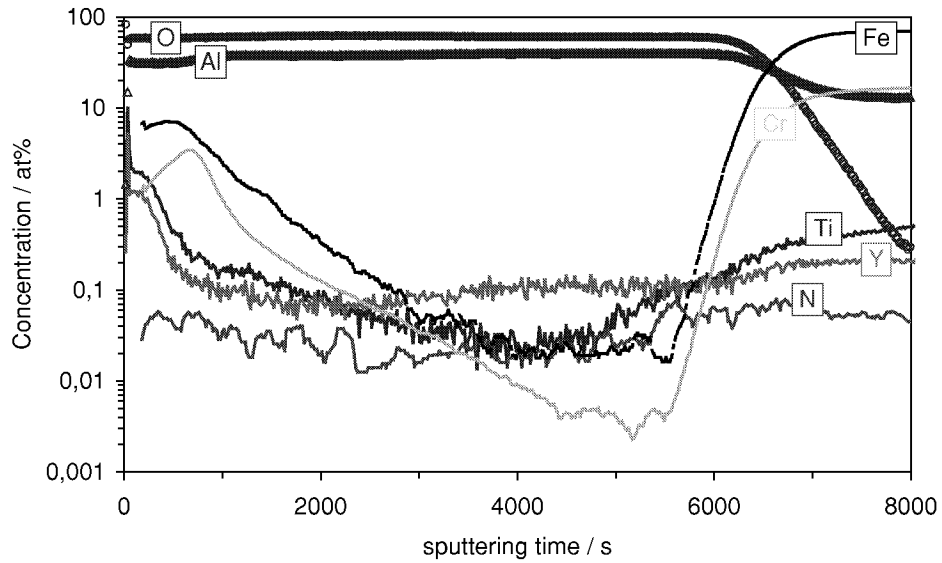

(b)

Figure 6.30: MCs^+-SIMS depth profiles of oxide scales formed on two model ODS alloys after 2h isothermal oxidation at 1200°C: (a) Ti-free alloy DAG; (b) 0.4%Ti-doped alloy DAH

The SEM studies after 2h oxidation at 1200°C show that there is almost no yttrium present on the top of ca 0.5µm thick scale on the Ti-free alloy (Figure 6.18). Since the amount and distribution of the yttrium oxide particles in both alloys are virtually the same it is clear that the outward transport of yttrium is slow if there is no Ti present within the alumina scale. In contrast on the Ti-containing alloy the Y- and Ti-rich oxide particles are 0.2 to 0.5 µm in size (Figure 6.19), i.e. much larger than the dispersoids in the bulk alloy. This leads to the

conclusion that Ti somehow facilitates the yttrium diffusion through the alumina scale towards the scale/gas interface.

The exact mechanism of the Ti-effect in FeCrAl ODS alloys is, however, far from being clear. Based on the present experiments and literature data [25,31] it is believed that Ti forms with yttrium a mixed oxide phase e.g. of the type $Y_2Ti_2O_7$ on the alumina grain boundaries. It might be that diffusion of yttrium through the bulk of or alternatively the yttrium surface diffusion on such a compound are significantly higher than those in pure alumina. A detailed characterisation of the scale by TEM and comprehensive data on diffusivity of the reactive elements in different oxide phases are necessary in order to get better understanding of the phenomena involved. The problem in achieving this goal is that the amounts of the grain boundary segregants are rather low and sometimes it is even difficult to discern between ionic or atomic segregation and the formation of mixed oxide compounds [31].

6.2.4. Mechanisms responsible for improved scale integrity on Ti-doped ODS alloys

The consequences of the enhanced yttrium mobility on the alumina grain boundaries on the Ti containing alloy are multiplex. One clear observation is the absence of the macroscopic scale convolutions on the 0.4%Ti alloy. In fact, the scale morphology observed in this work on the Ti-free alloy is rather similar to those described in literature for FeCrAl alloys without any RE additions [40]. On the RE-free FeCrAl alloys the scale convolutions have been attributed to growth stresses generation and relaxation processes [40, 66]. The common concept is that on undoped wrought FeCrAl alloys new oxide is formed within the scale due to the counterdiffusion of oxygen and aluminium [22, 23]. As a result, large and obviously non-evenly distributed oxide strains occur, which lead to a non-uniform deformation, i.e. convolution of the scale together with the underlying metal. This deformation seems to be a means of relaxation of the scale growth stresses, which is confirmed by the experimental measurements [66, 68, 69]. In contrast, on the RE-doped FeCrAl alloys the main growth mechanism was manifested to be the oxygen inward diffusion [22, 23]. Hence, the formation of new oxide occurs at the scale/metal interface. In spite of the high measured scale growth stresses on the RE-doped FeCrAl [66, 68, 69], the oxide/metal composite remains flat, apparently, because of the low strains. The latter effect can be explained due to an increase in creep strength of the RE-doped alumina [69], although it might also be related to the scale growth mechanism. Indeed, since on the RE-doped alloys the new oxide is formed at the scale/metal interface, a more uniform oxide stress and strain distributions are expected.

Returning to the studied model ODS alloys it can be claimed that if in the scale on the Ti-free alloy the yttrium mobility is low, then the scale will behave in a similar manner to the undoped scales, i.e. it will convolute. Convoluted scales have been found to be susceptible to spalling because on the convex surface of a convolution, significant stresses can be generated upon cooling [43, 67]. Although the average oxide stress is still expected to be compressive, the normal stress at the scale/metal interface will be tensile, which may lead to scale decohesion [43]. The scale spalling, however, is expected to occur during cooling, since the values of the thermal stresses are normally one to two orders of magnitude higher than those of the growth stresses [67, 69].

Another possible explanation of the excellent scale adherence on the 0.4%Ti alloy can be considered, based on the following. The growth stress calculated from the Cr^{3+}-fluorescence spectra taken from FeCrAl-0.3%Y (no Ti) single crystals oxidised for 100 h at 1000°C revealed the values of 500 to 700 MPa [66]. These values are in good agreement with the in-situ XRD measurements reported in reference [68], which gives for an FeCrAl-0.07%Y alloy during oxidation at 1000°C, similar growth stresses of 500 to 700 MPa. However, significantly lower oxide growth stresses were measured by M. Groß [69] for the Ti-doped ODS alloy PM2000. Moreover, according to in-situ XRD-measurements in [69], the oxide growth stress for PM2000 was found to drop from ca 350 MPa after 5h oxidation at 1000°C down to ca 50 MPa after around 30h exposure, remaining fairly constant at longer exposure times. This is surprising, taking into account the high creep strength of the substrate material PM2000 at 1000°C [53, 66]. Although a comparison of the stresses generated on the different alloy substrates is not straightforward, the apparent presence of Y/Ti-rich oxide phases on the scale grain boundaries of PM2000 might have an influence on the stress relaxation mechanism at temperature, e.g. by facilitating oxide grain sliding.

6.2.5. Effect of titanium on oxidation of ODS alloys as a complex issue

Considering the results obtained when studying the batch to batch variations and the model ODS alloys with and without Ti, some suggestions can be made to explain the "strange" behaviour of 1 mm thick PM2000 sheet HEP. The convolutions of the alumina scale observed on HEP (Figure 5.26) and somewhat large but inhomogeneously distributed Y/Ti-rich particles on the scale top may lead to the conclusion that the Ti distribution within the alloy is not uniform. The chemical analysis data (Table 2 Appendices) shows a very high carbon content in batch HEP. If similar to the PM2000 batch CKT, the Ti addition in HEP is tied up in bulky carbide precipitates than a local deficiency of Ti in some scale areas and local

abundance of titanium carbides in the other areas may emerge. Different areas of the scale may consequently either become undoped with Ti or contain incorporated TiC-particles. The exact Ti-distribution within the scale will of course depend on the exact carbide size and distribution in the alloy, which were not specifically investigated in this study. As shown above in this Section, both incorporation of Ti-carbonitrides and Ti-deficiency in the alumina scale may result in a scale damage by the respective mechanisms discussed above.

Several recent publications have stated that, irrespectively of the type of the added reactive element, i.e. a metallic addition or an oxide dispersion the effects related to the scale growth and adhesion are fairly similar [34]. Based on this assumption, attempts have been made in creating universal theories, which pretend on a complete description of the reactive element effect [32,34]. However, considering the present results it can be argued that a mere presence of a reactive oxide dispersion, e.g. yttria in the FeCrAl alloys is a necessary, but not the only requirement for obtaining the optimised oxidation resistance and thus component life.

Minor alloying addition of Ti is definitely involved in the growth process of the alumina scales. Although Ti alone failed to improve substantially the oxidation resistance of the FeCrAl alloys either as the metallic addition or as an oxide dispersion [71,72], this element seems to be of vital importance in the yttria containing ODS alloys for maintaining good scale adherence.

Due to the production route, wrought alloys have different microstructural properties than those of the ODS alloys. Also the amounts of the added reactive elements are normally significantly lower in wrought alloys, than in the ODS materials. Hence, it is not clear whether the observed batch to batch variations in wrought alloys have the same reasons as those found in the ODS alloy systems and described in Section 6.1. The next two sections discuss the oxidation behaviour of FeCrAl wrought alloys with respect to batch to batch variations and effects of minor alloying additions and impurities. First, in Section 7.1. studies on five batches of the commercial wrought alloy Aluchrom YHf are presented. Based on the outcome of these studies, in Section 7.2 the oxidation of high purity model alloys with systematic variation of different minor additions will be investigated. The selection of the minor additions will be derived from the batch to batch variation studies in Section 7.1.

7. Batch to batch variations in oxidation of wrought FeCrAl alloys

7.1 Oxidation of five batches of commercial wrought alloy Aluchrom YHf

7.1.1. Differences in oxidation kinetics during isothermal and cyclic exposures

All the studied batches of Aluchrom YHf (supplied by Krupp/VDM) in the as-received condition possessed a typical microstructure after cold rolling. The grains are deformed along the rolling direction, as shown in the etched cross section in Figure 7.1-a. Exposure at 1200°C, which is around 0.85 of the alloy melting point, resulted in fast recrystallisation (Figure 7.1-b). This process is practically finished already after 100 h exposure since no obvious microstructural changes occurred after longer times e.g. 1000 h (Figure 7.1-c). As in case of the two batches CKS and CKT of the ODS alloy PM2000, described in Section 6.1, comparison of the chemical analysis data of the studied Aluchrom YHf batches does not reveal any principle differences (Table 2 in Appendices).

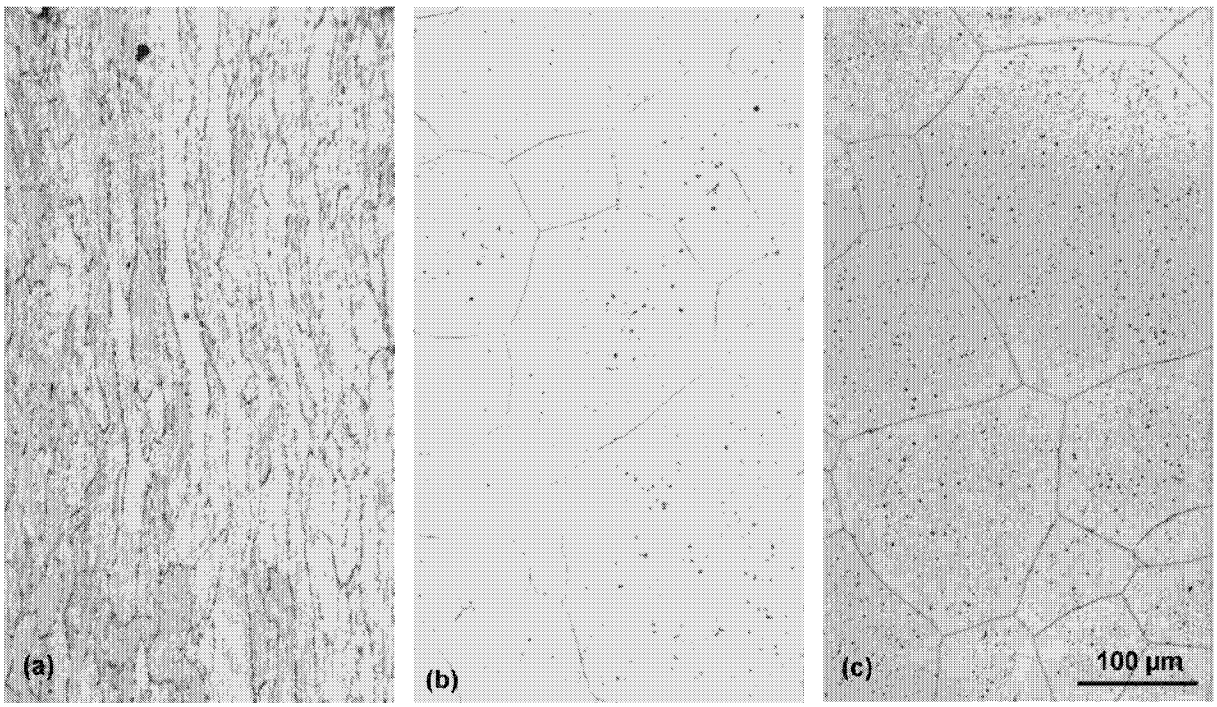

Figure 7.1: Etched cross sections of studied 2 mm thick sheet of Aluchrom YHf (Batch HDT): (a) as received condition; (b) after exposure at 1200°C for 100 h; (c) for 1000 h

Thermogravimetric analyses of the five studied batches at 1200°C appeared after 100 h oxidation to show only minor differences in oxidation kinetics (Figure 7.2). However, during cyclic oxidation for 1000h at the same temperature (Figure 7.3), one of the batches, HDX demonstrated a clearly higher mass gain than the others.

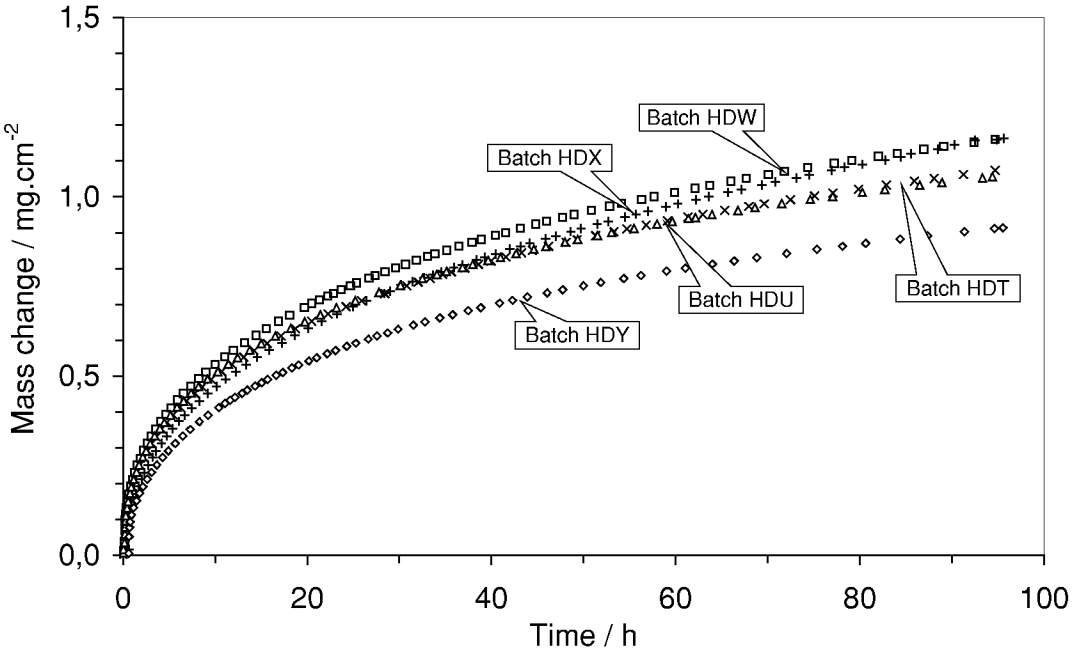

Figure 7.2: Mass change data for five studied batches of Aluchrom YHf during isothermal oxidation at 1200°C in synthetic air

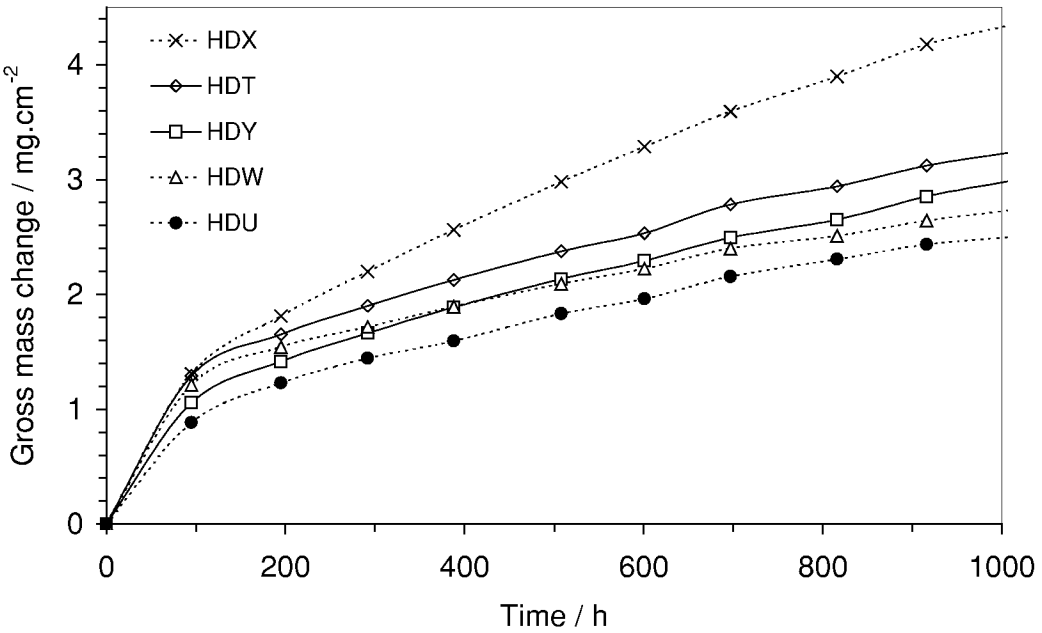

Figure 7.3: Mass change data for five studied batches of Aluchrom YHf during cyclic oxidation (100 h cycles) at 1200°C in synthetic air

7.1.2. Analytical characterisation of oxidised wrought alloy batches

No macroscopically visible features were found which could distinguish batch HDX from the rest of the oxidised specimens (Figure 7.4).

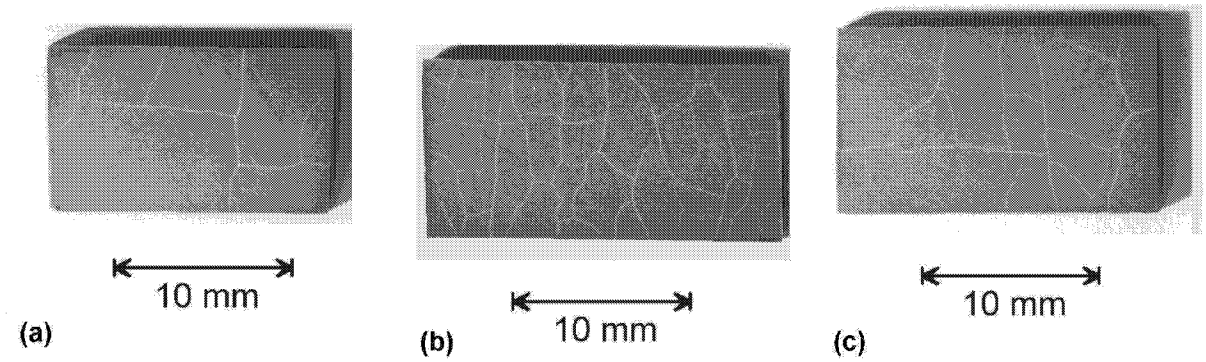

Figure 7.4: Macrographs of different batches of Aluchrom YHf specimens after 1000 h cyclic oxidation at 1200°C in air: (a) Batch HDX; (b) Batch HDW; (c) Batch HDU

Also x-ray diffractometry of the specimens after oxidation showed the aluminium oxide and FeCrAl matrix to be dominating phases in all batches (Figure 7.5). In contrast to the studied ODS alloys, in the XRD patterns of all oxidised Aluchrom YHf batches some additional smaller peaks corresponding to a M_3O_4-type spinel phase (presumably $MgAl_2O_4$) were found.

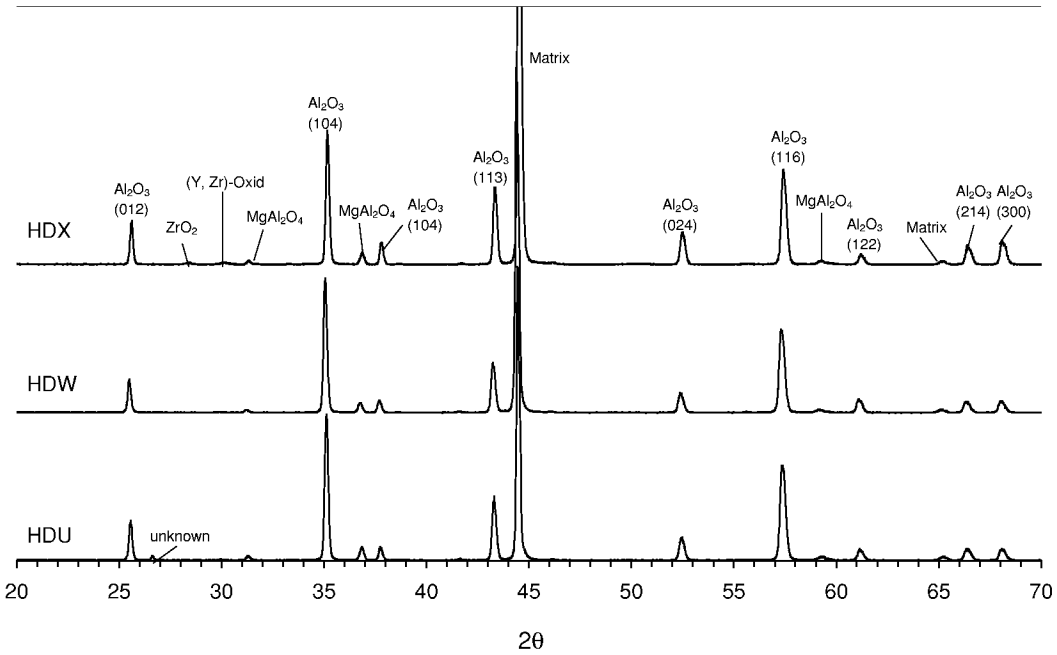

Figure 7.5: XRD-patterns taken form surfaces of three specimens (Batches HDX, HDW and HDU) of Aluchrom YHf after 1000 h cyclic oxidation at 1200°C in air

First indications of the reasons for the higher oxidation rate of batch HDX were found by SEM morphological studies of the surface scales formed after 1000 h exposure. Apparent scale buckling in a preferential direction on batch HDX (Figure 7.6-a) did not prevail in case of the other batches (Figure 7.6-b).

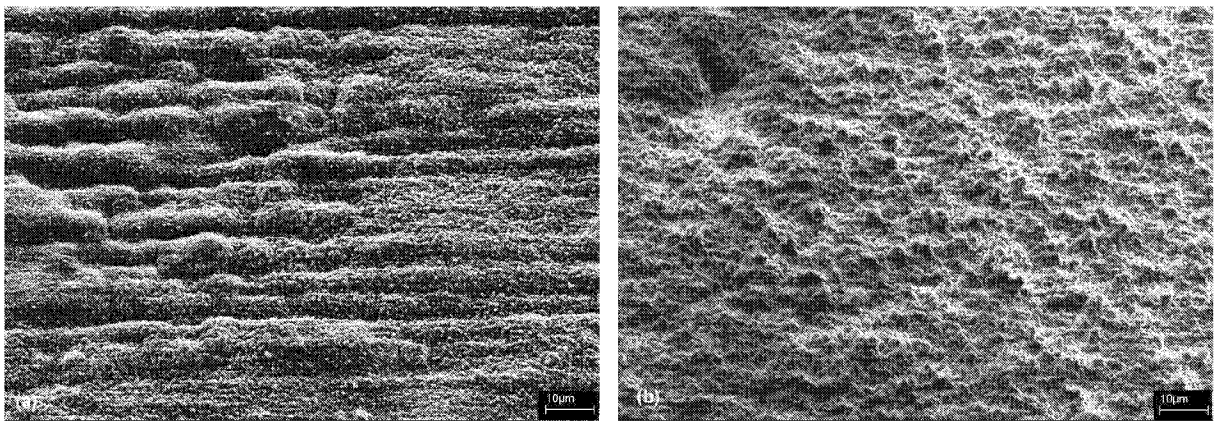

Figure 7.6: SEM images of surface scales formed during 1000 h cyclic oxidation of Aluchrom YHf at 1200°C in air: (a) Batch HDX; (b) Batch HDW

The scale cross sections after 100 h and 1000 h oxidation (Figures 7.7 and 7.8) revealed for all studied Aluchrom YHf batches some common morphological features. These contrasted with the typical scale morphologies described for the ODS alloys (compare Figure 5.25-c in Section 5.3). First, in contrast to the ODS material, which formed flat and even scales, wrinkling of the alumina scales occurred on the wrought alloy Aluchrom YHf. Second, inward growing alumina intrusions, apparently associated with the alloy grain boundaries, were observed. Third, the somewhat convoluted outer scale/gas interface (Figure 7.7) indicated a certain contribution of outward scale growth to the overall scaling process. The metallographic results for the Aluchrom YHf batches clearly showed that the scale on batch HDX was clearly thicker and more porous, than on the other batches (Figure 7.7-a, 7.8-a). Such defectiveness of the oxide scale on this batch apparently led to an accelerated growth kinetics shown in Figure 7.5.

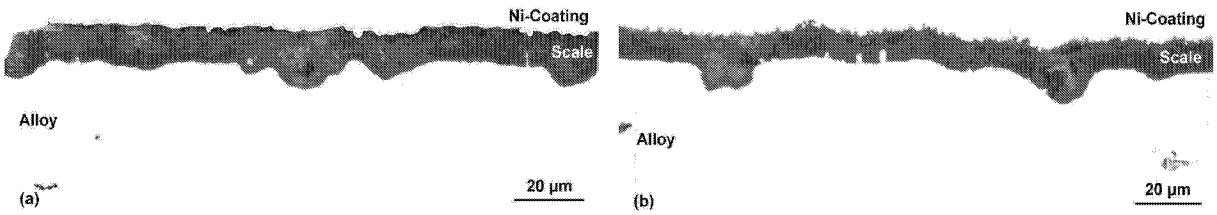

Figure 7.7: Metallographic cross sections of alloy Aluchrom YHf after 100 h isothermal oxidation at 1200°C in air: (a) Batch HDX; (b) Batch HDU

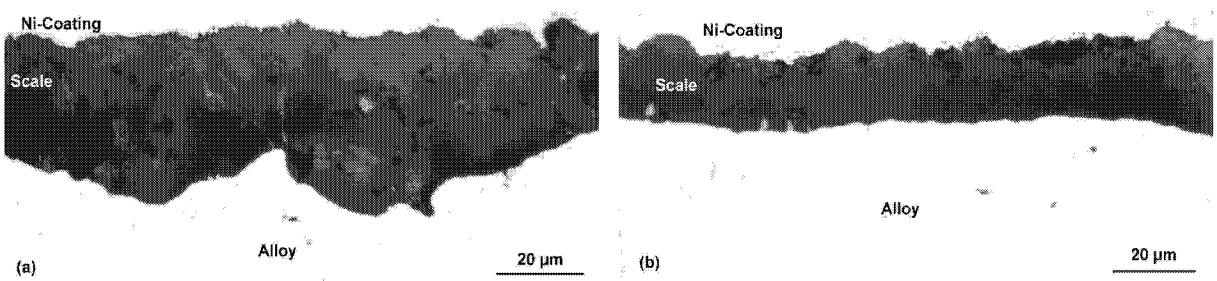

Figure 7.8: Metallographic cross sections of Aluchrom YHf after 1000 h cyclic oxidation at 1200°C in air: (a) Batch HDX; (b) Batch HDU

The SEM studies of the oxide scale fractures of the Aluchrom YHf batches revealed columnar grain structures typical for RE-doped FeCrAl alloys ([8], Figure 7.9-a). Randomly presence of RE-rich inclusions incorporated into the alumina scale was observed, which were often found in the vicinity of pores, cavities and microcracks (Figure 7.9-b,c). Batch HDX appeared to be the most susceptible to the inclusions associated porosity, which for this material was a common feature (Figure 7.10-a) The EDX analysis of the inclusions indicate that these are originally zirconium/hafnium-rich carbides (spectrum A in Figure 7.11). Closer to the scale/gas interface a transformation of the carbide into oxide occurs (spectrum B in Figure 7.11) and initiation of a pore can be seen (Figure 7.10-b). These observations are very similar to those made for the nitrogen contaminated ODS material CKT (Section 6.1). It appears that the mechanism of deterioration of the scale protective properties is in both studied cases related to the incorporation of non-oxide precipitates into the inward growing alumina scale. The EDX mapping of the cross section in Figure 7.12 confirms that this effect of Zr-rich carbides incorporation into the alumina scale does not occur locally, but is rather a typical phenomenon. Besides Y and Zr incorporation, the EDX mapping in Figure 7.12 clearly shows Mg-enrichment in the outer part of the scale.

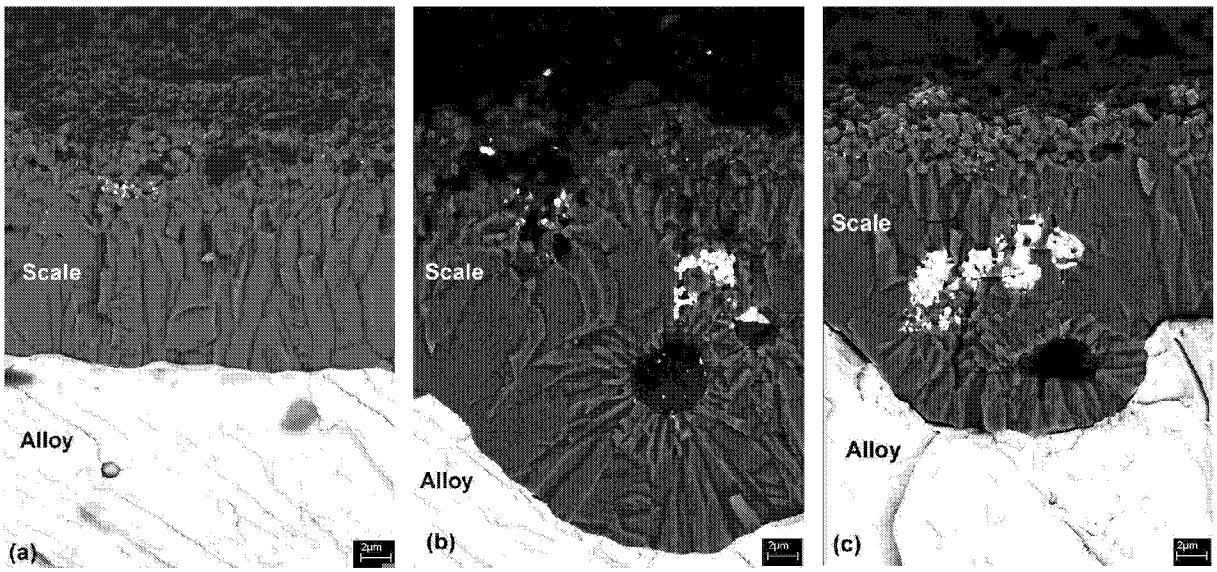

Figure 7.9. Fracture surfaces (SEM backscattered electrons images) of oxide scales formed on Aluchrom YHf during 1000 h cyclic oxidation at 1200°C in air: (a) Batch HDT; (b) Batch HDU; (c) Batch HDW

The latter finding of the outer Mg-rich oxide layer seems to be in good agreement with the XRD data in Figure 7.5, showing presence of a spinel phase and the morphologies of the scale/gas interface, typical for outward growth, as observed in Figures 7.6 and 7.7. Hence, in addition to the main process of the inward alumina scale growth typical for all commercial FeCrAl alloys [22,23], on Aluchrom YHf formation of the spinel $MgAl_2O_4$ occurs by the

outward transport of Mg ions. It is worth noting that the Mg-content in Aluchrom YHf (see Table 2 in Appendices) is extremely low i.e. ca 100 ppm mass. This means that the Mg-enrichment in the outer scale apparently occurred by diffusion of Mg from the bulk alloy.

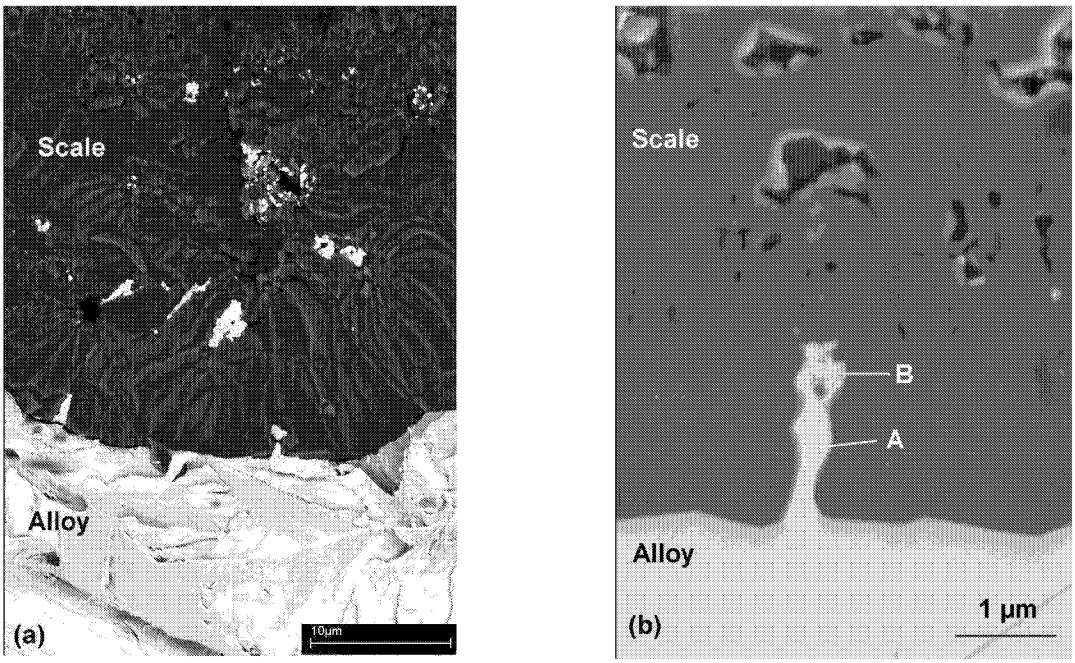

Figure 7.10. Oxide scale formed on Aluchrom YHf (Batch HDX) after 1000 h cyclic oxidation at 1200°C in air: (a) Fractured scale surface (SEM backscattered electron image); (b) High resolution SEM backscattered electron image of scale cross section;

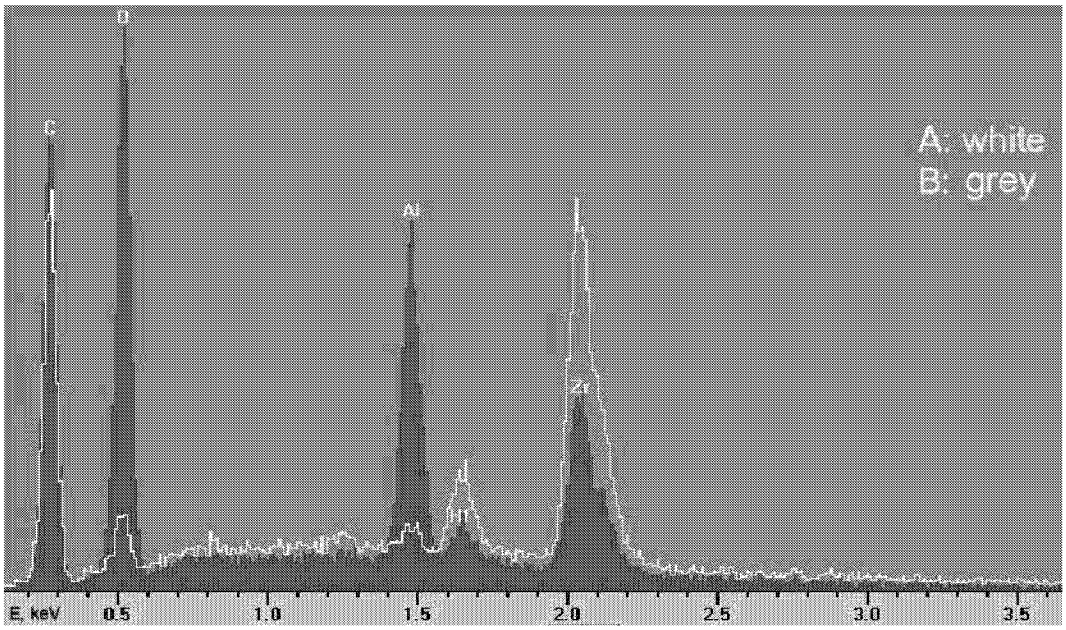

Figure 7.11. EDX spectra taken from points A and B in Figure 7.10-b

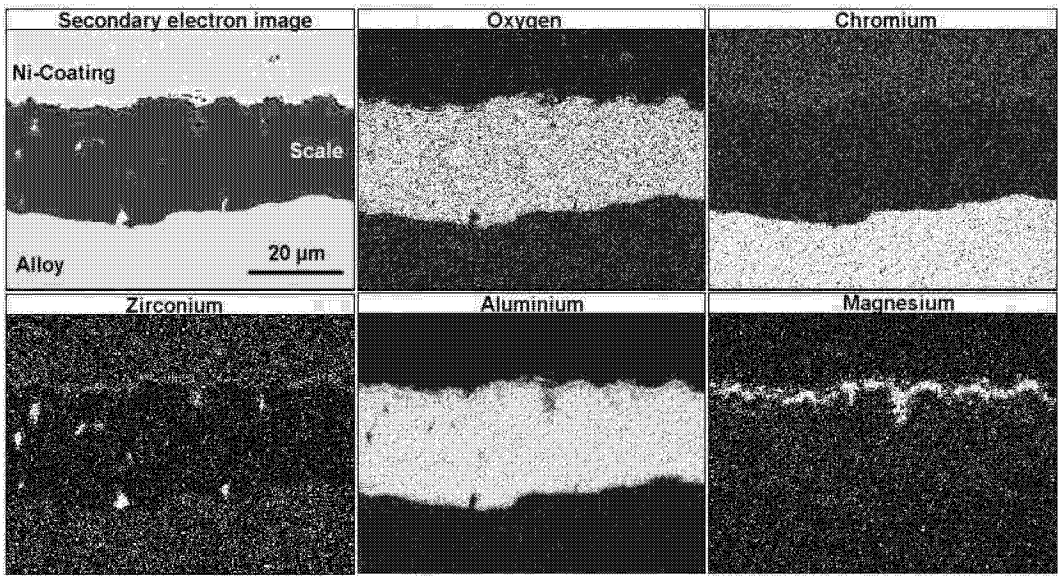

Figure 7.12. EDX element mapping of cross sectioned scale formed on Aluchrom YHf, batch HDX after 1000 h cyclic oxidation at 1200°C in air

7.1.3. Reasons for batch to batch variations in commercial wrought alloys

From studies performed on the batches of the commercial ODS and wrought FeCrAl materials it can be concluded that not only mere presence of a reactive element, e.g. yttrium, but also minor additions of the elements, such as Zr and Ti, which are able to tie up carbon and nitrogen into precipitates is an important factor affecting the scale growth rate and adhesion. In the case of the wrought alloy Aluchrom YHf, the formation of carbo-nitrides in the alloy matrix has no such drastic effect on the oxide growth rate as in the studied batches of the ODS alloy PM 2000. The chemical composition data for Aluchrom YHf (Table 2, Appendices) does not allow relation of the higher scale growth rate on batch HDX to its higher carbon and/or nitrogen contents. Thus, it is most probably the size and/or distribution of the Zr/Hf carbo-nitrides in HDX, which determines the enhanced oxidation kinetics of this batch.

In the commercial alloy systems the levels and distributions of minor elements and impurities are not easy to control. Hence, to better understand and unequivocally attribute the effects of minor elements on oxidation behaviour it is necessary to use high purity alloys with very well defined chemistry and microstructure. Therefore in the next Section 7.2. studies on high purity model wrought FeCrAl alloys with additions of typical carbide/nitride forming elements (Ti, Zr, V) are presented.

7.2 Study of high purity FeCrAlY model wrought alloys with additions of Ti, V and Zr

7.2.1. Effects of Ti, V and Zr additions to wrought Y-containing alloys on growth rate and adherence of alumina scale

The studied high purity model alloys on the base Fe20Cr5Al all contained ca 500 ppm yttrium. In addition to yttrium the alloys M+Ti, M+V and M+Zr were doped with 200 to 300 ppm of the respective carbide forming elements. The concentrations of common alloy impurities were at significantly lower levels, than those typically present in the commercial FeCrAl materials (Table 3 in Appendices). Similar to the studies made with the commercial alloys, long term 100 h cycles oxidation tests at 1200°C were performed with 1mm thick coupons of the model alloys. The results of these tests are presented in Figure 7.13.

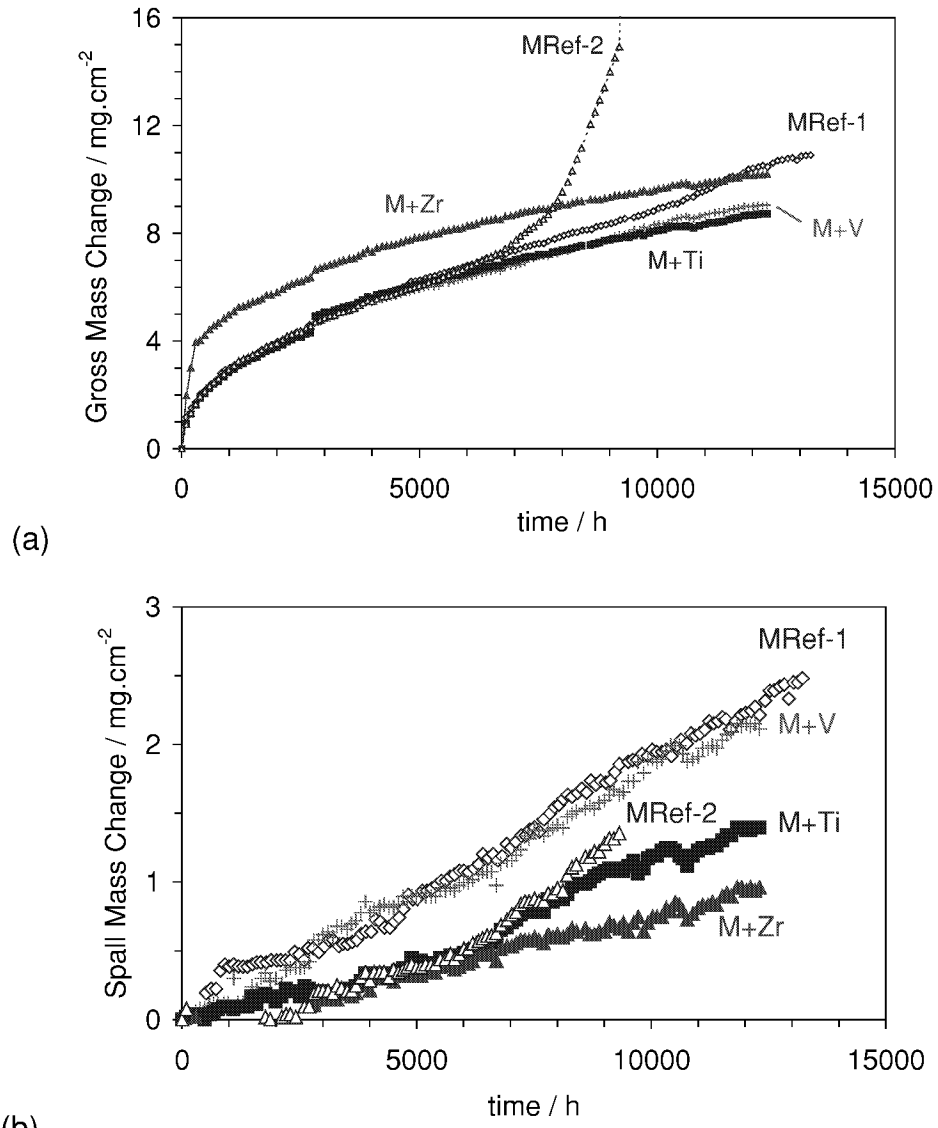

Figure 7.13: Mass change data of studied model wrought alloys during cyclic oxidation (100h cycles) at 1200°C in air: (a) Gross mass changes; (b) Mass change of spalled oxide

All the model alloys except the Zr-doped alloy "M+Zr" showed very similar oxidation behaviour up to several thousand hours exposure. Alloy "M+Zr" exhibited originally much higher oxidation rates than the other alloys, however, after relatively short time (ca 500 h) the oxidation rate dropped and the slopes of all mass change curves became virtually the same. Up to 13000 h exposure the only alloy which failed due to the breakaway oxidation was MRef-2 (Figure 7.13-a). The failure was not related to scale spalling (Figure 7.13-b), but apparently to an increased scale growth rate after ca 7000 h exposure. A comparison of the spallation resistance in Figure 7.13-b reveals that the best performance is shown up to 13000 h cyclic oxidation by alloy M+Zr. This is surprising since alloy M+Zr has the thickest scale amongst the alloys studied i.e.ca 50 µm, as can be concluded from the mass change data.

Macrographs of the studied model alloys after 8000 h cyclic oxidation at 1200°C are presented in Figure 7.14. No scale cracking was observed on M+Zr, and the small amounts of the spalled oxide (Figure 7.13-b) originated apparently from the specimen edges and corners. On the rest of the alloys the scale damage was similar to that observed on the wrought commercial alloys (see e.g. Aluchrom YHf in Figure 5.23-a).

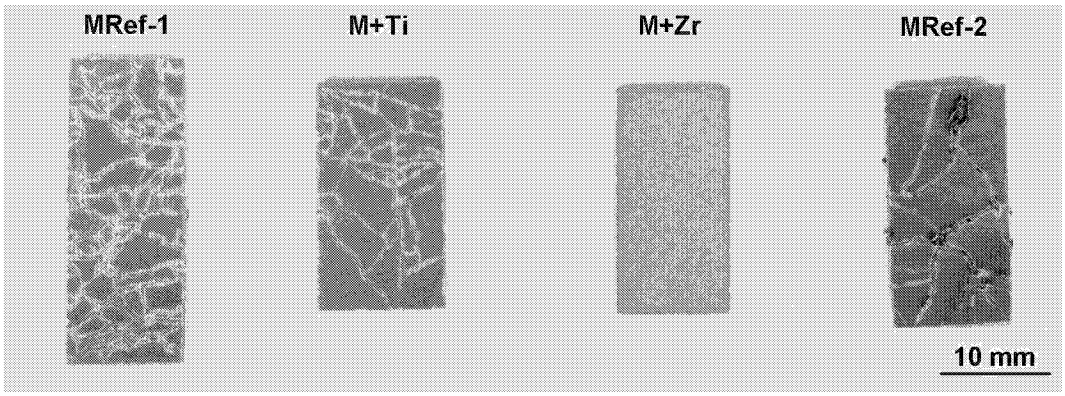

Figure 7.14: Macrographs of model wrought alloys after 8000 h cyclic oxidation (100 h cycles) at 1200°C in air

The alloys MRef-1 and M+V showed almost identical oxidation rates and masses of the spalled oxide. Somewhat lower masses of spalls after 5000 h oxidation were observed on MRef-2 and M+Ti. Visual examination of the model alloys during cooling and weighing at 100 h cycles revealed that after several thousand hours exposure on some of the specimens large brownish oxide nodules formed, growing with increasing the exposure time (Figure 7.14). These nodules most commonly emerged at the corners and edges of the specimens. In Table 6.1 times are listed at which these nodular "broccoli" oxides were observed for the first time. The only two alloys which did not show the broccoli-type oxide formation up to 13000

h oxidation were M+Ti and M+Zr. The macrograph of the specimen MRef-2, which went into breakaway after 9300 h accumulated exposure time is shown in Figure 7.15. Along with the adherent alumina scale in some parts of the specimen sub scale chromia formation occurred indicating, as it was explained in Chapter 5.1, the complete consumption of aluminium.

Table 7.1 Times of the first observation of outward growing nodules on FeCrAl model alloys

Alloy	MRef-1	M+V	M+Ti	M+Zr	MRef-2
First nodule observed after, h	8000	6100	Not Observed	Not Observed	5200

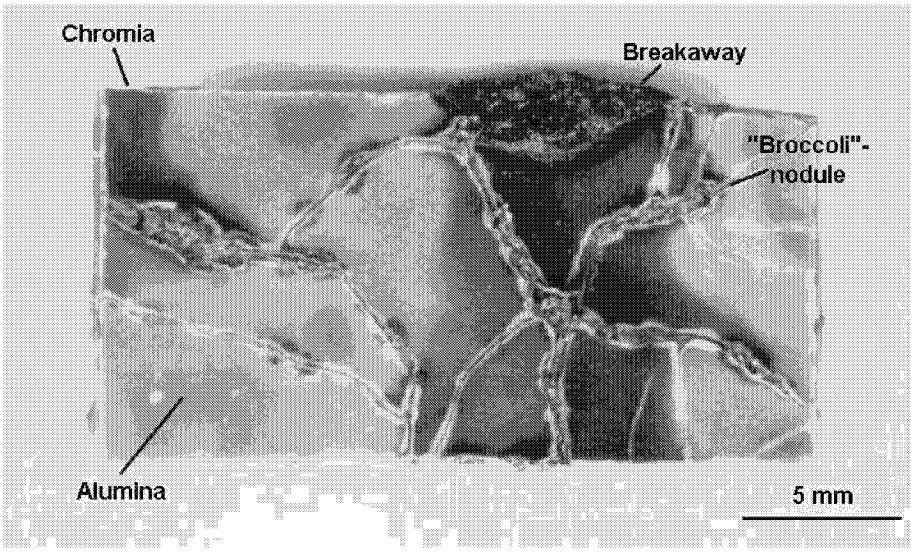

Figure 7.15: Alloy MRef-2 after cyclic oxidation till breakaway (9300 h accumulated exposure) at 1200°C in air

The results of isothermal oxidation testing of the model alloys at 1200°C in a microbalance are given in Figure 7.16-a. Very similar behaviour of the MRef-1, M+V and M+Ti with a mass change of ca 1 mg/cm^2 after 90h can be noted. MRef-2 showed after the same exposure times a little higher oxygen uptake of 1.1 mg/cm^2. Alloy M+Zr exhibited clearly higher growth rates, than the other materials, which is additionally confirmed by the plot of instanteneous parabolic parameter k_P in Figure 7.16-b. For comparison the 100 h cycles test data after the first cycle are also presented in Figure 7.16-a, showing a good agreement. All studied alloys demonstrated power law oxidation kinetics following eq-n 2.12. The values of the oxidation rate parameters k and n are given in Table 7.2. It is noteworthy that the value of the exponent n is 0.49 for M+Zr, whereas for the rest of the materials it varies between 0.35 to 0.38. No visible spalling of the oxide scale was detected on the specimens after 90 h isothermal oxidation at 1200°C and subsequent cooling down to room temperature.

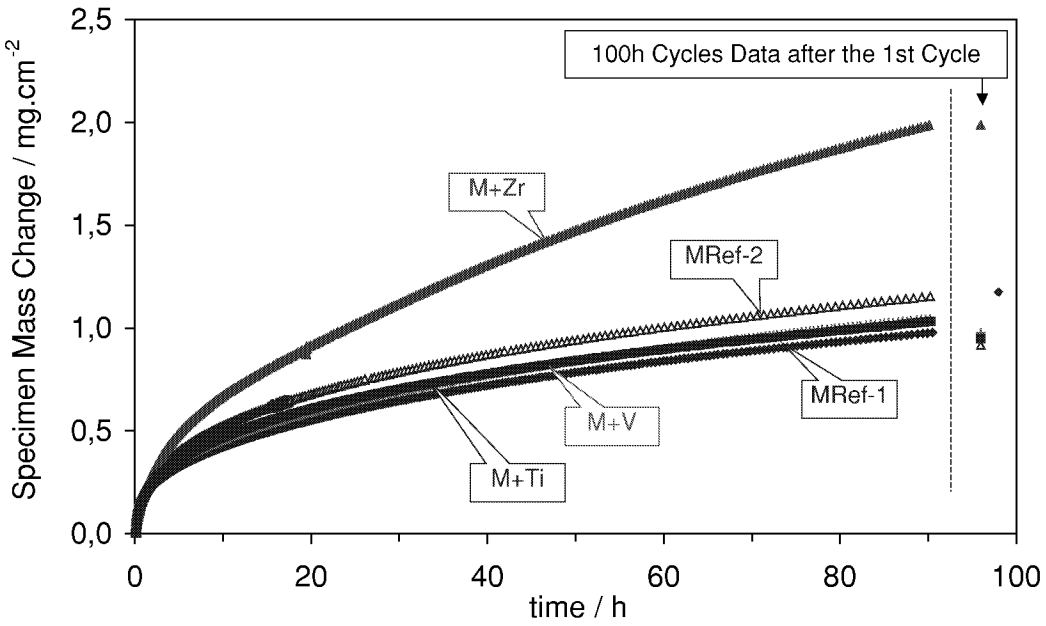

(a)

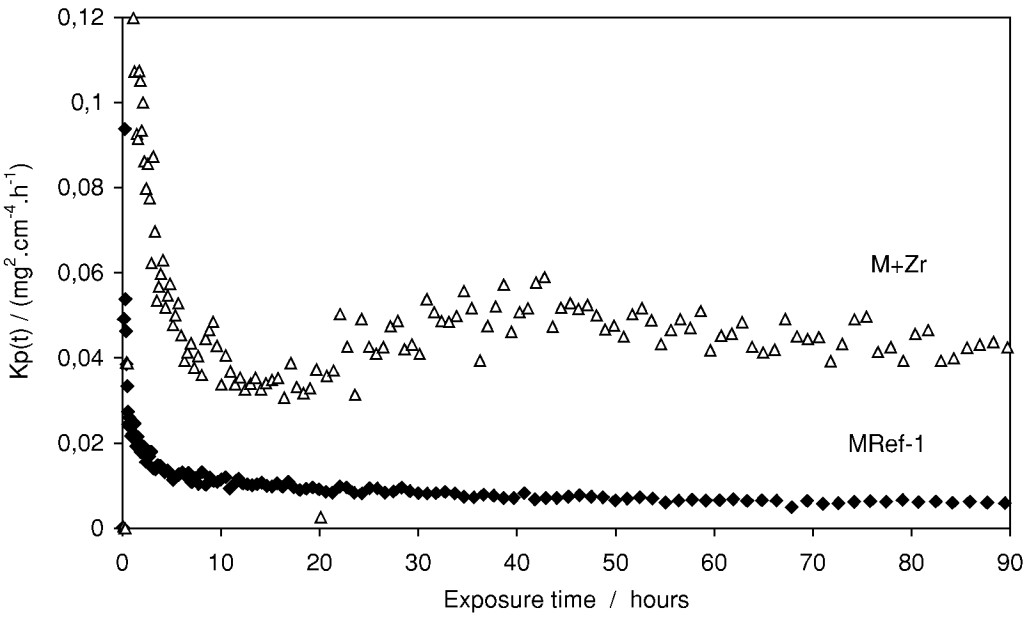

(b)

Figure 7.16: (a) Thermogravimetric data for model wrought alloys during 90 h isothermal oxidation at 1200°C in synthetic air; (b) Plot of instanteneous parabolic growth rate parameter k_P after eq-n (5.2) vs time for MRef-1 and M+Zr, calculated using data in (a)

Table 7.2: Oxide growth rate parameters calculated from isothermal mass change data in Figure 7.16-a, assuming the scale growth obeys the law $\Delta m = k.t^n$, where Δm – specific mass change in mg/cm^2 and t- time in hours

	MRef-1	M+V	M+Ti	M+Zr	MRef-2
k	0.17	0.19	0.20	0.22	0.22
n	0.38	0.38	0.37	0.49	0.37

7.2.2. Effects of Ti, V and Zr additions on microstructural features of alumina scale and substrate alloy

In Figure 7.17 SEM images of the surface scales formed after 100 h isothermal oxidation at 1200°C are presented. Noteworthy are the similarities in scale morphology of MRef-1 and MRef-2. Both alloys show small (ca 0.5 µm) alumina grains with large intragranular and intergranular voids. In contrast the scales formed on the alloys M+Ti and M+Zr are much more compact with only few, small intergranular voids. In addition Y-rich oxide precipitates of a size of 0.1 to 0.2 µm were found on alloy M+Ti and especially M+Zr (Figure 7.17-d).

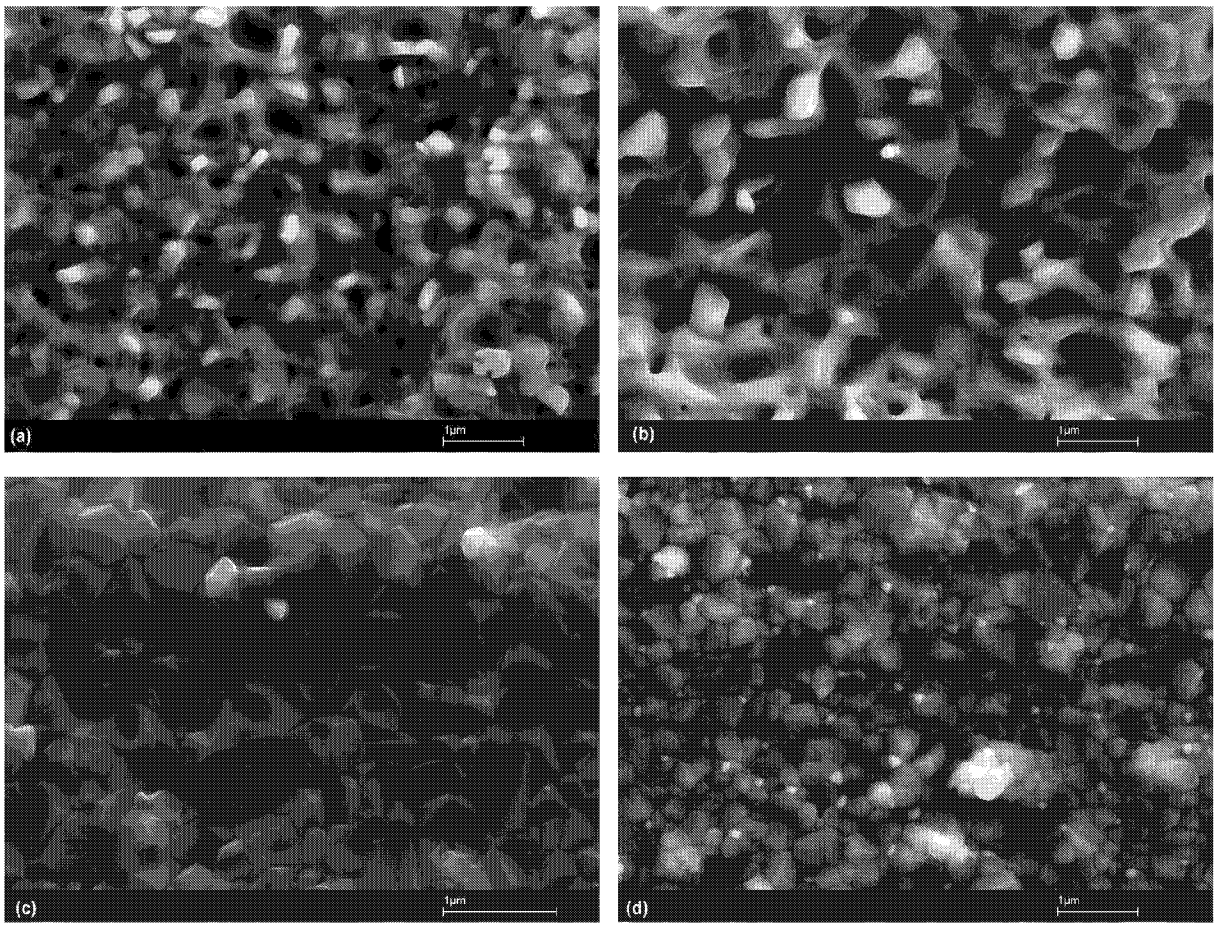

Figure 7.17: SEM images of surface scale morphologies on model wrought alloys after 100 h isothermal oxidation at 1200°C in air: (a) MRef-1; (b) MRef-2; (c) M+Ti; (d) M+Zr

Metallographic cross sections were prepared from the specimens of MRef-1, M+Ti and M+Zr isothermally oxidised for 100h as well as from the same materials in the as-received condition. Acid etching of the cross sections revealed that in the as-received state all alloys possessed a recrystallised equiaxed grain structure with a typical grain size of 150 µm (Figure 7.18). As received alloy M+Zr had a smaller average grain size of around 80 µm. During 100h exposure at 1200°C an obvious grain growth occurred in all studied cases, with alloy M+Zr having the largest extent of recrystallisation and consequently the biggest grain size (Figure 7.19).

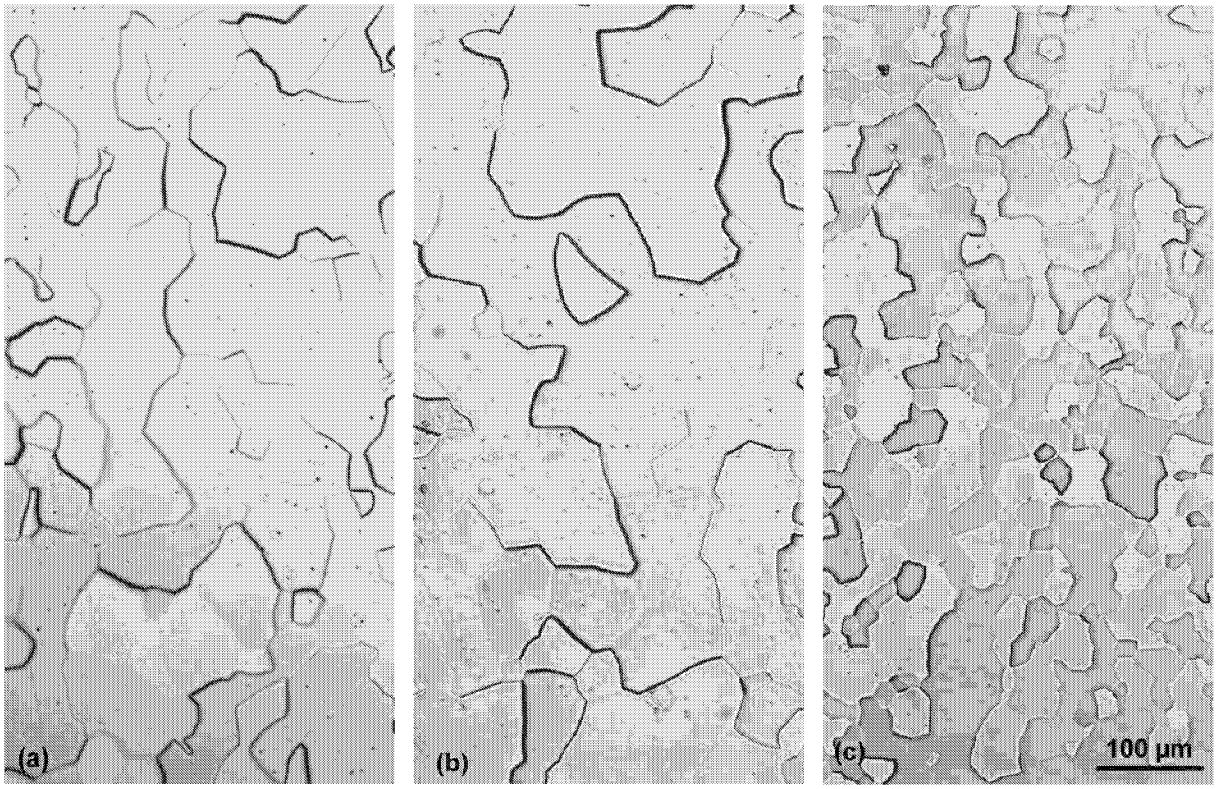

Figure 7.18: Etched metallographic cross sections of model wrought alloys showing microstructure of materials in as-received state: (a) MRef-1; (b) M+Ti; (c) M+Zr

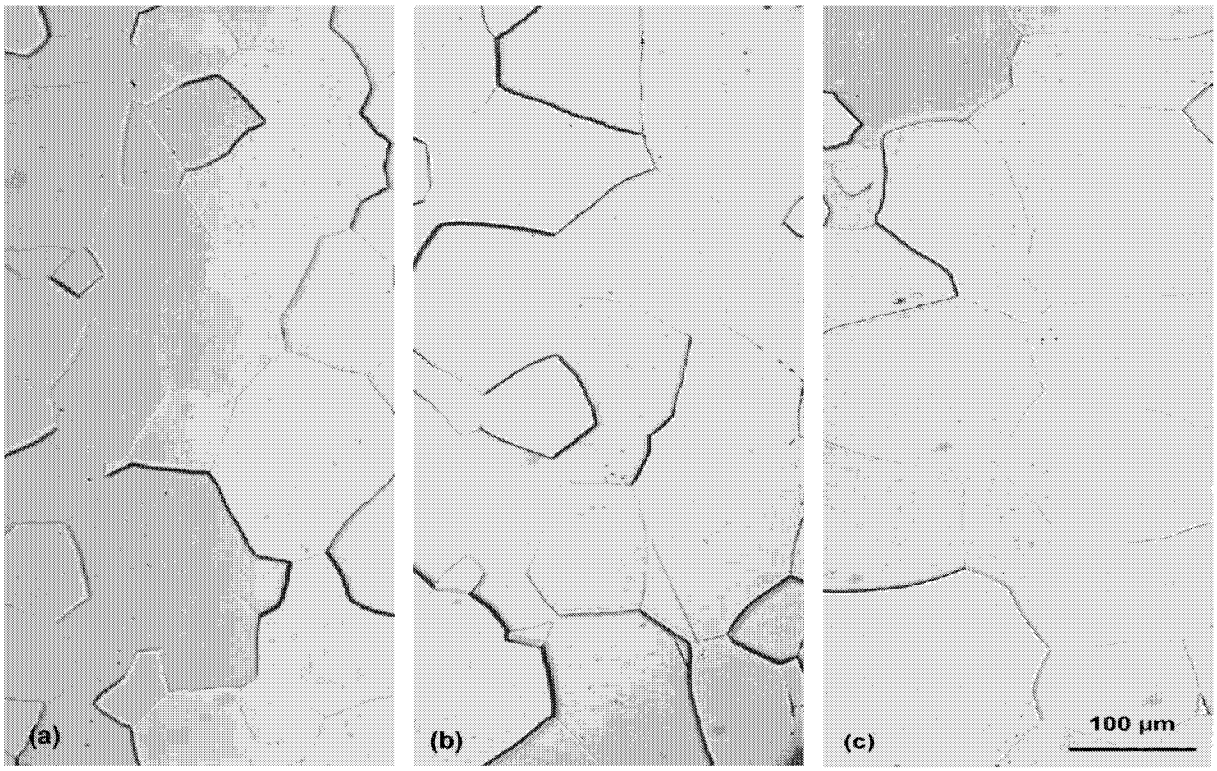

Figure 7.19: Etched metallographic cross section of model wrought alloys showing microstructure of materials after 100h exposure at 1200°C: (a) MRef-1; (b) M+Ti; (c) M+Zr

After 100h oxidation all alloys formed protective alumina scales. Additionally in the oxidised specimens internal oxide precipitates could be depicted in the alloy matrixes, with alloy M+Zr being the most susceptible to this effect (Figure 7.20).

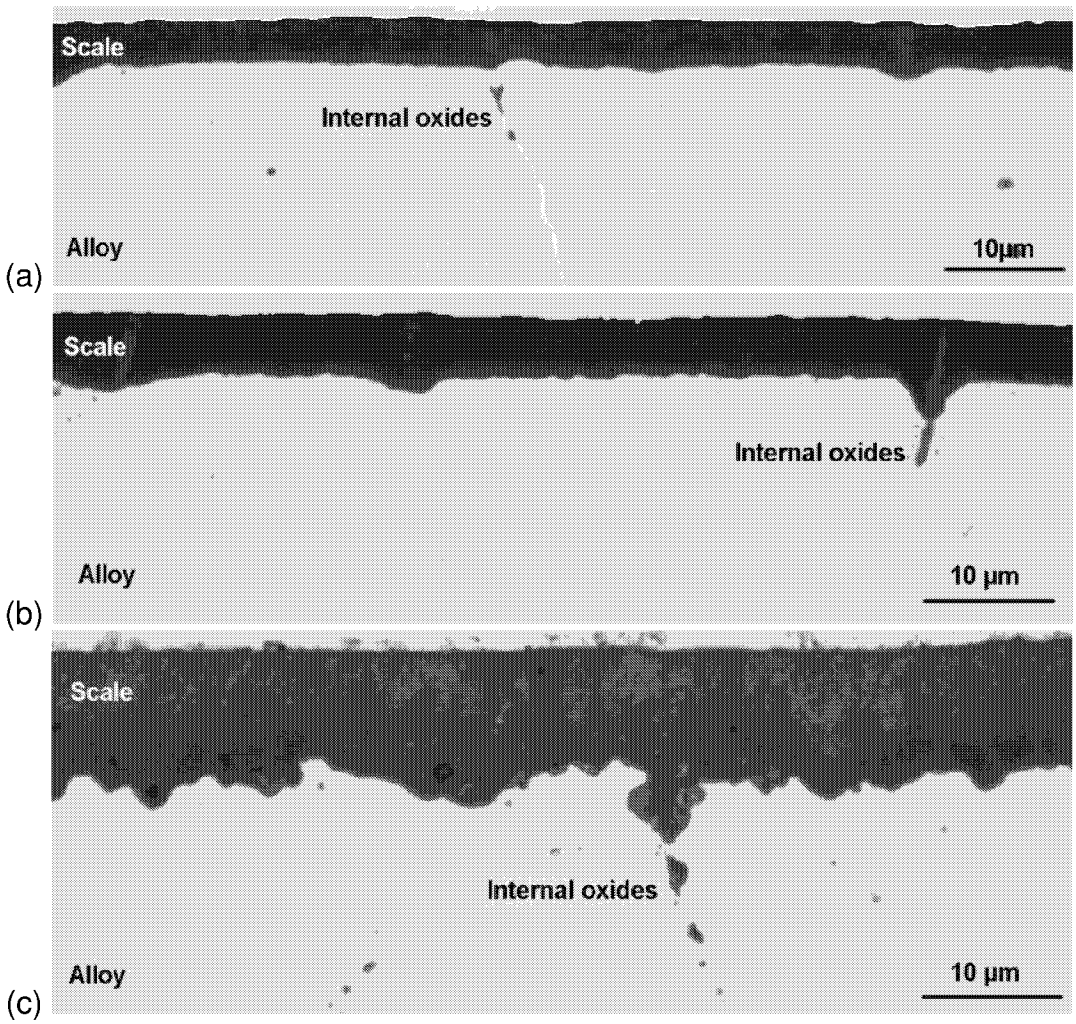

Figure 7.20: Metallographic cross sections of oxide scales formed on model wrought FeCrAl alloys after 100 h oxidation at 1200°C in air: (a) MRef-1; (b) M+Ti; (c) M+Zr

Figure 7.21 features the metallographic results with alloy MRef-2 after 9300 h exposure at 1200°C, i.e. when the specimen started to form breakaway Fe-based oxides. The alloy section was clearly affected by the broccoli oxides, which were found to possess a porous, sponge-like structure within the alloy matrix.

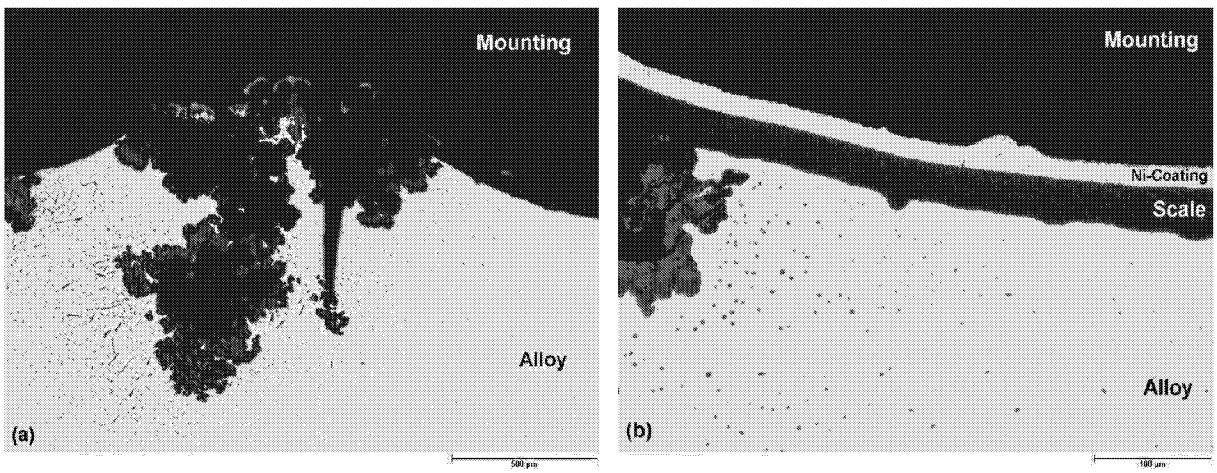

Figure 7.21: Metallographic cross sections of model wrought alloy MRef-2 after 9300 h cyclic oxidation at 1200°C in air: (a) internal oxidation attack; (b) uniform and adherent alumina scale in non-affected areas

Such a structure must lead to an increase in the effective surface area available for oxidation, which apparently explains the enhanced oxidation kinetics observed for this alloy after around 7000 h exposure with a consequence of an early breakaway failure (Figure 7.13-a). In the areas affected by the "broccoli effect" the substrate alloy is significantly deformed, which indicates that high mechanical stresses were imposed on the substrate by oxidation. However, in other parts of the specimens, no scale damage was observed and the alumina layer remained rather flat and adherent, which is in good agreement with mass change data in Figure 7.13-b.

7.2.3. Effect of carbide formation in alloy matrix on alumina scale integrity

The scale cross sections of the specimens exposed for 100 h were analysed using SEM/EDX. The scale on MRef-1 is a representative example of the structure and morphology, which is also typical for M+V and MRef-2 (Figure 7.22-a). Although generally dense and uniform, the scale on MRef-1 regularly featured some intrusions, which were apparently associated with the alloy grain boundaries. The EDX analysis of these inclusions in the alumina scale revealed that these are Y/Al-mixed oxides. EDX line scan analysis was used to study the chemical nature of the precipitates on the alloy grain boundaries deeper in the alloy matrix (Figure 7.22-a). The profiles of the elements of interest are shown in Figure 7.22-b. The respective data for chromium and carbon strongly indicate grain boundary precipitation of chromium carbides.

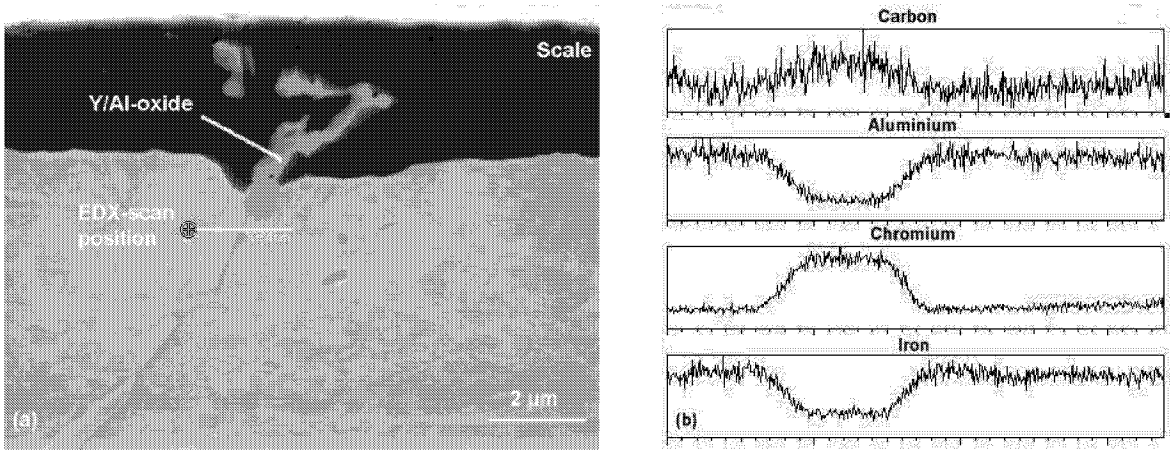

Figure 7.22: SEM studies of oxide scale cross section of model wrought alloy M Ref-1 after 100 h isothermal oxidation at 1200°C in air: (a) backscattered electron image, showing Y/Al-oxide peg and precipitates on alloy grain boundaries; (b) EDX scan data for line marked in (a)

After 2000 h exposure (Figure 7.23-a), alloy MRef-1 showed similar features to those after 100 h oxidation, i.e. Y/Al oxide pegs near the scale/metal interface and chromium carbides precipitates, decorating the alloy grain boundaries. Looking in detail at the Y-rich oxide intrusions, a feature to depict appeared to be initiation of cracks, which occurred within and in

the vicinity of these pegs. It must be noted that the scale cracking did not always occur at the Y-rich pegs, as can be seen in Figure 7.23-b. In the latter case, the alumina scale was successfully re-healed underneath the crack.

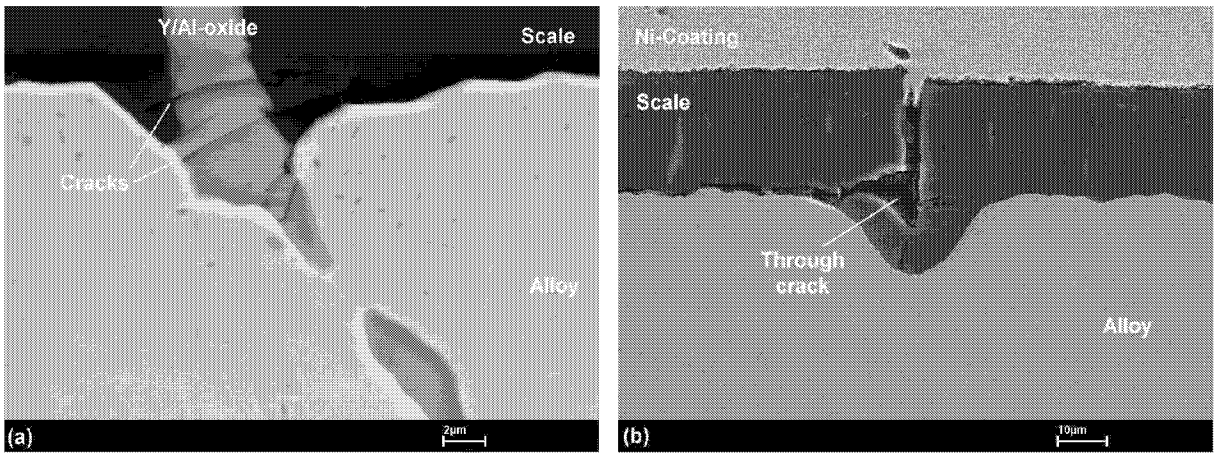

Figure 7.23: SEM backscattered electron images of the cross sectioned scale of MRef-1 after 2000 h cyclic oxidation at 1200°C in air: (a) Y/Al-oxide peg at the scale/metal interface; (b) re-healed crack in alumina scale

Following the question whether the Y and Cr-rich phases could also be observed in the non-exposed material, similar SEM/EDX analyses were performed on the as received alloy MRef-1. The large (up to 5µm) Y-rich precipitates identified as Y/Fe-intermetallics were distributed rather uniformly in the alloy matrix (Figure 7.24-a). Based on the EDX data yttrium was also present in the alloy matrix on random occasions as a compound other than the intermetallics Y_2Fe_{17} or YFe_9. These local enrichments could not be directly related to the common alloying elements, which have high Y-affinity. High resolution WDX spectra taken from these enrichments revealed the precipitating phase to be rich in Y and P, thus indicating presence of an yttrium phosphide (Figure 7.24-b). The analysis of the MRef-1 material additionally confirmed that the chromium carbide precipitates at the alloy grain boundaries were already present in the alloy prior to the oxidation exposure.

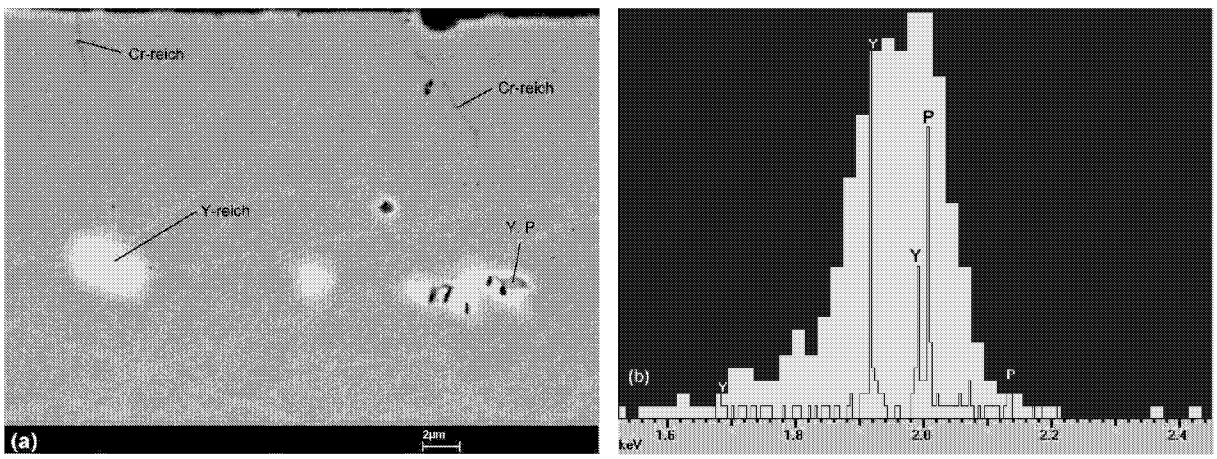

Figure 7.24: SEM microstructural studies of as-received model wrought alloy MRef-1: (a) backscattered electron image showing precipitates in alloy matrix; (b) EDX and WDX spectra taken from Y/P-rich particle in (a)

The SEM images of the cross-sectioned scale on M+Zr after 100 h oxidation is presented in Figure 7.25). Porosity (up to 0.2 µm in size pores) in the outer part of the scale on alloy M+Zr is obviously responsible for a faster oxide growth rate exhibited by this alloy during short term exposure. The observed pores could be often associated with the precipitates of Zr-rich oxides in the scale.

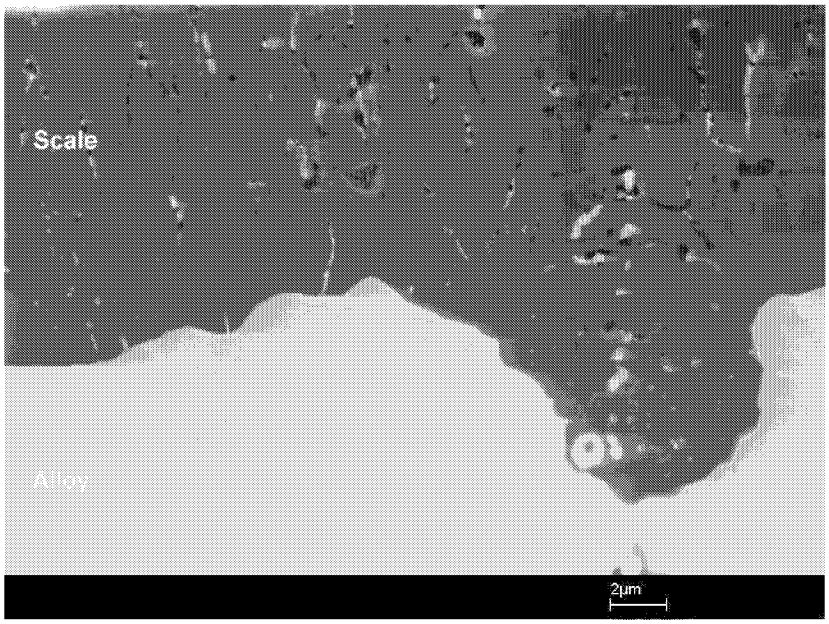

Figure 7.25: SEM images of scale cross section of model wrought alloy M+Zr after 100 h isothermal oxidation at 1200°C in air: alumina scale features pores and Zr-rich oxide precipitates (light phase)

7.2.4. Yttrium incorporation in alumina scale on wrought alloys: effect of Ti

After studying the Y-enrichment in the scales formed on the model FeCrAl ODS alloys with and without Ti-additions in Chapter 6.2 it appeared to be useful to check whether the same positive effect of Ti on yttrium mobility within the alumina scale occurs in the wrought FeCrAl alloys. The RBS spectra taken from the scales formed on MRef-1 and M+Ti after respective oxidation for 2h, 20h, 50h and 100h are shown in Figure 7.26.

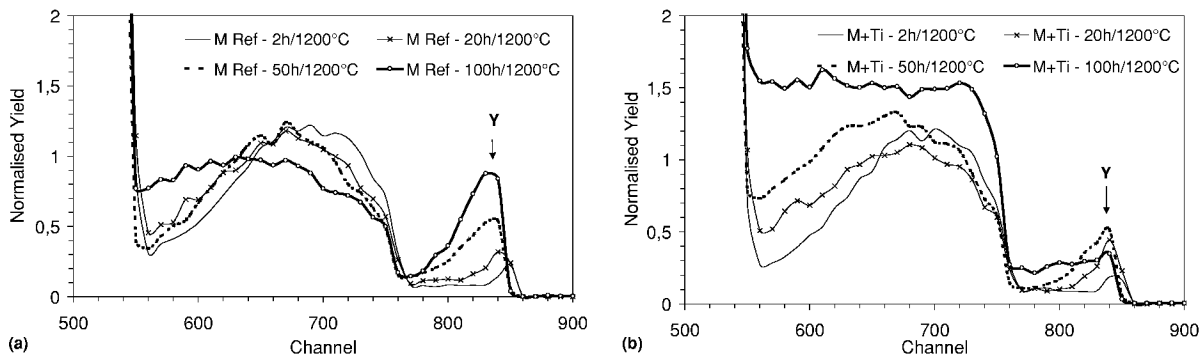

Figure 7.26. RBS spectra, showing yttrium enrichment, taken from surfaces of model wrought alloys after oxidation for different times at 1200°C in air: (a) MRef-1; (b) M+Ti

Contrary to the observations made with the ODS alloys, the effect of Ti additions in wrought Y-doped FeCrAl alloys seemed to be controversial. In the case of alloy M+Ti the yttrium concentration increases up to 50h exposure, however after 100h it seems to exhibit some decrease (Figure 7.26-b). In contrast, the yttrium enrichment in the outer part of the alumina scale on MRef-1 shows a definite positive trend with increasing the exposure time from 2h to 100h (Figure 7.26-a). Comparing the Y-enrichment after the same exposure time in the scales on MRef-1 and M+Ti it can be seen that already after 50h and especially after 100h oxidation more yttrium is concentrated in the outer part of the scale on MRef-1 than on M+Ti.

7.2.5. Significance of Ti and Zr additions for prevention of internal corrosion attack

As illustrated in Section 2.3, within the last two decades a plenty of literature data on the reactive element effect in wrought FeCrAl alloys has become available [15,17,34,36,72,74,75,76]. However, these data generally relates to the additions of one reactive element, mainly yttrium and the behaviour is compared in a standard way to that of an undoped FeCrAl alloy. In addition many authors have studied the RE-effect during short term (up to several tens of hours) isothermal oxidation. Hence, some of the important phenomena, occurring after quite long exposure times, which in this study were found to be a major life limiting factor, could not be observed in many of the earlier studies. The current work has been one of the first attempts to investigate the effects of the second reactive element additions, such as Ti and Zr on a model system during lifetime oxidation.

The five model alloys tested at 1200°C can be divided into two groups with respect to the scale properties (i.e. morphology, resistance to spallation, susceptibility to the "broccoli effect"). To the first group the alloys MRef-1, MRef-2, and M+V can be attributed, which all show a porous oxide structure of the scale/gas interface (Figure 7.17), similar scale spallation behaviour and, after longer exposure times, "broccoli"-oxides formation. In contrast M+Ti and M+Zr exhibited a compact scale/gas interface, better resistance to spalling (especially M+Zr) and absence of the "broccoli"-type oxides.

Prevention of the "broccoli effect" in FeCrAlY-wrought alloys seems to be the most obvious positive effects of Ti and Zr found in this study. As far as it is known to the author, under the prevailing experimental conditions the nodular oxide morphologies have not been typically observed on the commercial FeCrAl alloys, which contain Ti and/or Zr additions [8,46]. Since both Ti and Zr have a high affinity to carbon, no chromium carbide precipitates at the alloy grain boundaries of M+Ti and M+Zr were found. A plausible assumption then would be that

Ti and Zr tie up the carbon impurity in tiny Ti- or Zr-carbides. This is in a good agreement with literature on the microstructure of FeCrAl materials [26]. Hence, the "broccoli"-oxides which emerged on the model alloys without the carbon gettering elements can be related to the formation of chromium carbides on the alloy grain boundaries, especially in combination with the Y-rich phases also observed on the alloy grain boundaries. Taking into account the observed crack initiation in the vicinity of the alloy grain boundaries after long term cyclic oxidation (Figure 7.23-a), either tensile scale cracking during heating or, alternatively, the shear scale cracking on cooling may well happen in the Ti/Zr-free alloys. The alloy grain boundary decorated with the precipitated carbides becomes then exposed to the oxidant at high temperature. Oxidation of the carbides will apparently result in a rapid release of high pressure gaseous CO in a mechanically weak substrate at 1200°C. The gas evolution from the alloy depth is likely to be responsible for the observed substrate deformation and formation of the sponge-like porous oxide morphology (Figure 7.21-a). Thus the corrosion attack starts to affect large sub-scale zones of the alloy with the consequence of a fast depletion of the Al-reservoir. The latter in fact explains the much shorter lifetime of alloy MRef-2 compared to that of the other model alloys. If, however, the scale cracking occurs far away from the alloy grain boundary, then a successful scale re-healing is possible as illustrated in Figure 7.25. The formation of broccoli oxides on alloy MRef-1 occurs after longer exposure times, than on alloy MRef-2 (Table 7.1). This is surprising taking into account very similar chemical compositions of the two reference model alloys (Table 3, Appendices). However, a detailed look at minor constituents of MRef-1 and MRef-2 reveals, that the latter alloy contains a factor of 10 less phosphorous. Combining this with the observation of yttrium phosphide formation in the matrix of MRef-1 in the as received condition (Figure 7.24) leads to the conclusion that in MRef-1 a more regular yttrium distribution is achieved. Hence, the probability of scale failure due to the presence of the yttrium reach oxide phases at the scale/metal interface is lower for MRef-1 than for MRef-2. The V-additions appeared to be not as beneficial as those of Ti and Zr with respect to prevention of "broccoli"-oxides. This can be related to a lower V affinity to carbon, than those of Ti and Zr [5].

7.2.6. Importance of Ti and Zr additions for alumina scale adherence

The second positive effect of Ti and Zr observed in this study is the improved alumina scale adhesion. As can be seen in Figure 7.25-b, the spallation rates on M+Ti and especially on M+Zr are lower than those of the other alloys studied. The explanation may again, as in the case of the model ODS alloys with and without Ti (Chapter 6.2), lie in the modification of the scale grain boundaries with Ti and/or Zr containing oxide compounds. However, as the

microstructural SEM studies of the scale on M+Zr indicate, another important factor, namely scale porosity may play an important role. As it was shown for the high-nitrogen Batch CKT of the ODS alloy PM2000 (Section 6.1), the extremely porous alumina scale exhibited excellent resistance to spallation even after reaching a thickness of 50µm, i.e. far beyond typical critical value for this material to initiate the scale spalling [11]. Indeed, according to [57,79], the Young's Modulus of polycrystalline alumina is inversely proportional to the porosity. Thus, a decrease in the Young's Modulus for the porous alumina scales should result in much lower stresses on cooling, which are induced by thermal strains. This seems to be a good argument in clarifying why no visible scale cracking and spalling after 15 000h exposure, i.e. 150 cycles from 1200°C occurred on M+Zr, in spite of a large scale thickness.

The reason for the observed porosity in the scale of M+Zr is not completely understood and seems to the author being at least twofold. First, as rare earth elements have been known to stabilise θ-alumina even at high temperatures of 1100-1300°C [80,81], the formation of the metastable alumina might have initially happened. The subsequent transformation of the θ-alumina into α-modification is known to result in a volume change and formation of the observed small pores. This assumption can as well justify a faster scale growth on the Zr containing alloy during the first 500 h exposure. The formation of the pores can also be related to the mechanism described in this work for Batch CKT of the commercial ODS alloy PM2000 (Chapter 6.1), and Batch HDX of the wrought alloy Aluchrom YHf (Chapter 7.1), i.e. carbides and/or nitrides incorporation in the alumina scale and subsequent oxidation to Ti/Zr oxides. More detailed studies are necessary in order to clarify which one of the two above mentioned mechanisms actually prevails.

The results obtained with the ODS and wrought alloys in Sections 6 and 7 show that when considering the oxidation limited alloy life, one should take into account the RE-effects related to scale growth as well as those related to oxide adherence. Both effects are important, however, as found in this study, they often appear to oppose each other. For example, the porous scales formed on alloy M+Zr and on the high-nitrogen batch CKT of PM 2000 exhibited clearly higher oxidation kinetics than the dense scales on the other studied materials. At the same time the adherence of the porous scales on the former alloys was outstanding. In the next section the effects of different alloy and component properties and experimental parameters on the alumina growth rate and as a consequence on the oxidation limited life are summarised. In particular, the effects of the temperature cycle frequency and oxygen partial pressure on the oxide growth rate will be presented.

8. Significance of alumina growth kinetics for oxidation limited life

8.1. General remarks

A number of examples presented in the previous sections have indicated that, not only for thin sections, but also for relatively thick FeCrAl components the oxidation limited life is often determined by the consumption of the Al-reservoir due to the scale growth, rather than by scale spalling. Different from many earlier studies concerning this subject, in the present work the alumina scale growth rate has been shown not only to depend on the mere presence of one reactive element, but to a much larger extent, on its exact amount, distribution and especially on the interaction with other reactive elements and impurities. It has also been shown that the scale growth rate can be strongly affected by the component geometry and by temperature cycling. Especially for the industrial applications of the FeCrAl alloys, understanding of these effects is a necessary requirement for a reliable component operation, lifetime prediction and extension. In this section the results presented in Sections 5 to 7, complemented with the data, illustrating effects of service parameters will be briefly discussed in terms of the scale growth rate.

8.2. Effect of mechanical constraints on oxide growth rate

In Section 5.2 the model car catalyst body made of a 58µm thick foil was shown to have significantly higher oxidation rate, than that of a free hanging foil coupon from the same batch of material. This was attributed to the scale micro and macro cracking of the constrained catalyst body, which led to a lifetime decrease by roughly a factor of two (Figure 5.15). This means that if a FeCrAl component is to operate as a constrained part, the lifetime assessment must be made very carefully. Especially for thin walled components with a small aluminium reservoir a shorter life estimated from the model catalyst specimen must be taken into account.

8.3. Enhancement of scale growth rate due to alloy carbon and nitrogen impurities

It has been known for years that intrinsic alloy sulphur contamination leads to a significant deterioration of the scale adhesion [35,36]. Thus, nowadays in the modified compositions of the commercial FeCrAl alloys the sulphur impurity is kept at a level of around 20 ppm or lower (see Table 1 in Appendices). However, studying different batches of the commercial alloys PM2000 and Aluchrom YHf revealed that an important parameter which affects primarily the alumina scale growth rate is the alloy nitrogen and/or carbon content (Sections 6 and 7). Faster oxidation of the batches with high nitrogen and carbon content was observed

and related to the porosity and presence of microcracks within the scale. The proposed mechanism of the formation of such a defective scale structure has been given in Section 6.1. It has been shown that the porous scales form not simply due to the presence of C/N-impurities, but because of the interaction of these elements with the alloying additions of Ti/Zr and Hf. The studies on the high purity model alloys in Section 7.2 confirmed that if none of the above mentioned carbide forming elements is present within the alloy matrix, the carbon impurity is most likely to form chromium carbides on the alloy grain boundaries, which in turn can lead to a dramatic internal oxidation attack. Thus, generally a reduction of the oxidation rate is expected for the materials containing lower amounts of the above mentioned impurities.

8.4. Effect of temperature cycle frequency on scaling kinetics

In Figure 8.1 a comparison of the mass change data for two specimens of the same alloy batch CKT of PM 2000 is shown during oxidation at 1200°C at two cycle frequencies. It can be seen that after around 100h oxidation the specimen oxidised at 2h cycles started to exhibit a higher scale growth rate than that of the specimen at 100h cycles. This led to a faster Al-consumption and much earlier failure of the first mentioned specimen

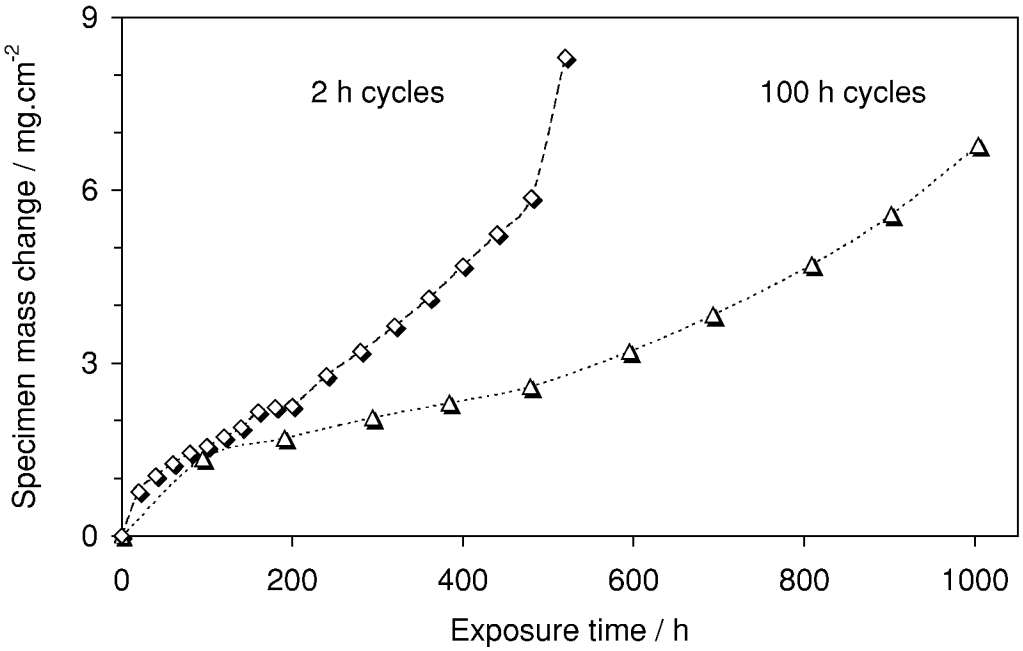

Figure 8.1: Mass change data for 0.5 mm thick specimens of commercial ODS alloy PM 2000 (Batch CKT) during cyclic oxidation at 1200°C in air

The macrographs of the specimens after finishing the oxidation tests (Figure 8.2) revealed significant deformation of the specimen oxidised at 2h cycles. Note that prior to the high temperature exposure both coupons had dimensions of 20x10 mm. No macroscopically visible scale spalling was observed on both tested specimens. The metallographic cross

sections in Figure 8.3 show that on the 2h cycles specimen the alumina scale is much more porous and cracked than that on the 100h cycles specimen, apparently due to a much higher number of cooling events. This observation explains the encountered faster oxidation kinetics of the material during 2h cycles exposures.

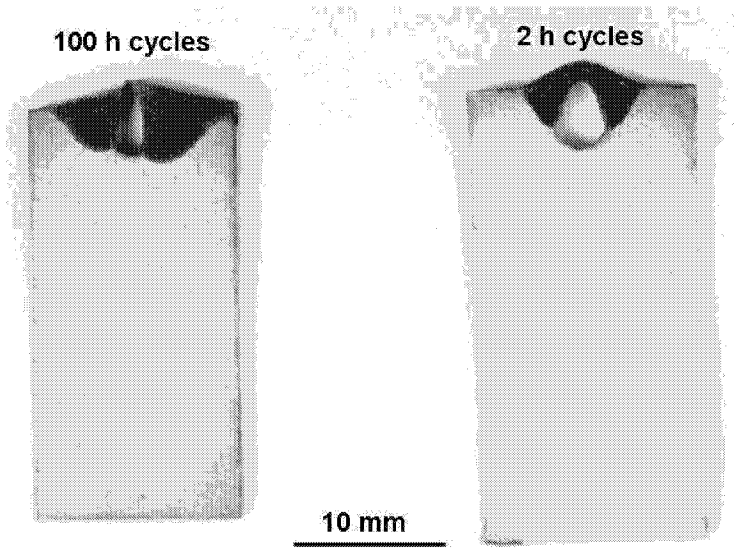

Figure 8.2: Macrographs of CKT specimens after cyclic oxidation till breakaway at 1200°C in air (compare with mass change data in Figure 8.1.)

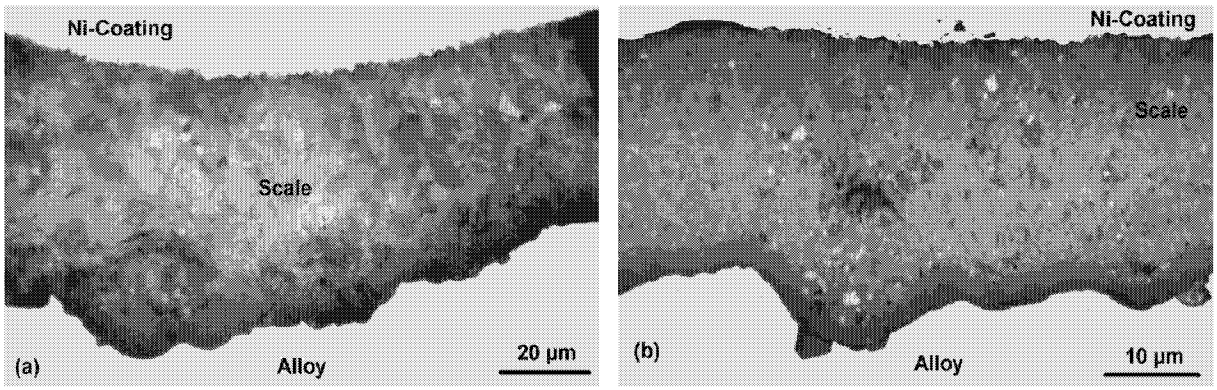

Figure 8.3: Metallographic cross sections of oxide scales formed on CKT specimens of PM 2000 after lifetime cyclic oxidation at 1200°C in air: (a) 2 h cycles test; (b) 100 h cycles test

As discussed above (Section 6.1) Batch CKT of the ODS alloy PM2000 exhibited non-typical for this material oxidation behaviour due to its high nitrogen content. In order to verify whether the same effect of cycling on the alumina scale growth occurs with a more "regular" alloy batch, 2 mm thick coupons of Batch HEQ were oxidised for 600 h at 1200°C in air. The isothermal exposures were compared to those at 2 h and 100 h cycles. The specimen mass change data during 600 h oxidation in Figure 8.4 clearly shows that also for this batch the scale growth rate is increased with increasing cycle frequency. The effect becomes apparent after around 100 h total exposure, i.e. when the scale reached a thickness of 5 to 6 µm. No significant scale spalling occurred apparently because the alumina scale had not reached a

critical thickness for the spall initiation. The scale appearance (Figure 8.5) and morphologies represented in the metallographic cross sections in Figure 8.6-b;c, look very similar for the specimens oxidised isothermally and at 100 h cycles. In contrast the scale on the specimen after 2 h cycles test appeared to be cracked, although still adherent (Figure 8.5, 8.6-a). The pieces of the scale between the cracks show a characteristic concave geometry. Such scale morphology indicates that the scale apparently failed by the shear cracking mechanism during cooling [42]. Heating up to the oxidation temperature during the next cycle resulted in greater expansion of the metal and the scale followed this deformation in order to maintain the adhesion. The alloy under the cracked region then started to oxidise forming inward oxide intrusions, which can also be seen in Figure 8.6-a. These intrusions, which occur at regular distances as a result of the shear cracks, can explain the observed increased scale growth of the 2 h cycles specimen. Schematically the process of scale deformation, induced by cyclic oxidation is illustrated in Figure 8.7.

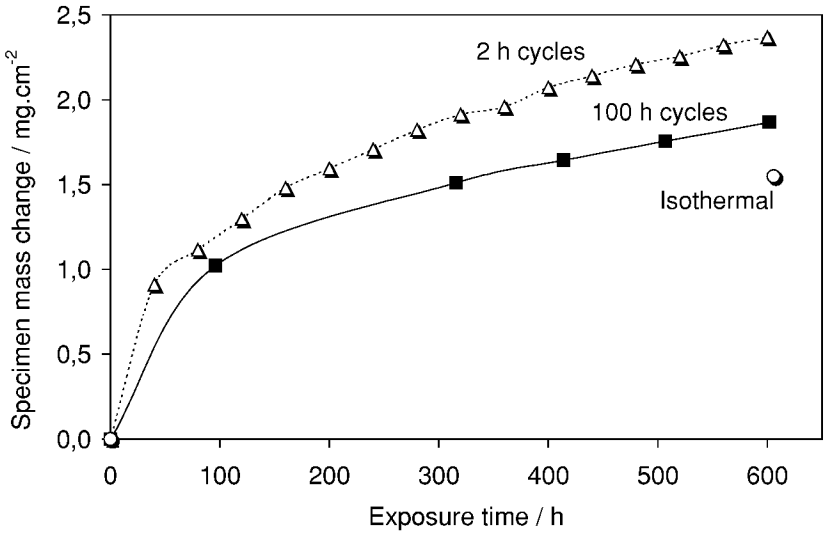

Figure 8.4: Specimen mass change data for 2 mm thick sheets of commercial ODS alloy PM 2000 (Batch HEQ) during oxidation at 1200°C in air

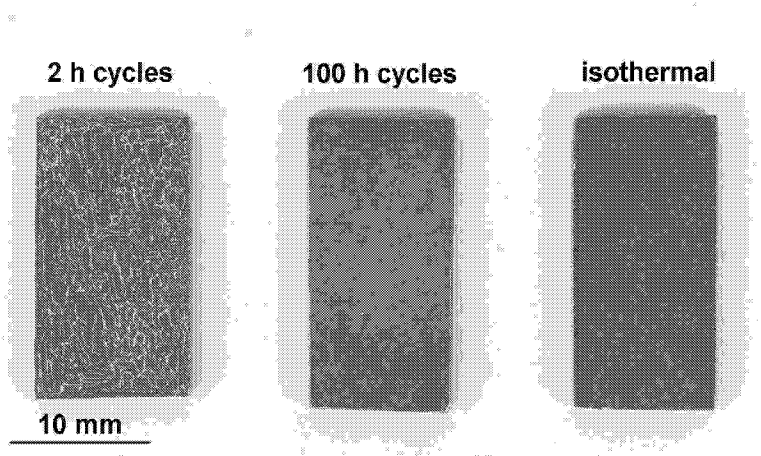

Figure 8.5. Macrocraphs of HEQ specimens (alloy PM 2000) after 600 h oxidation at 1200°C in air

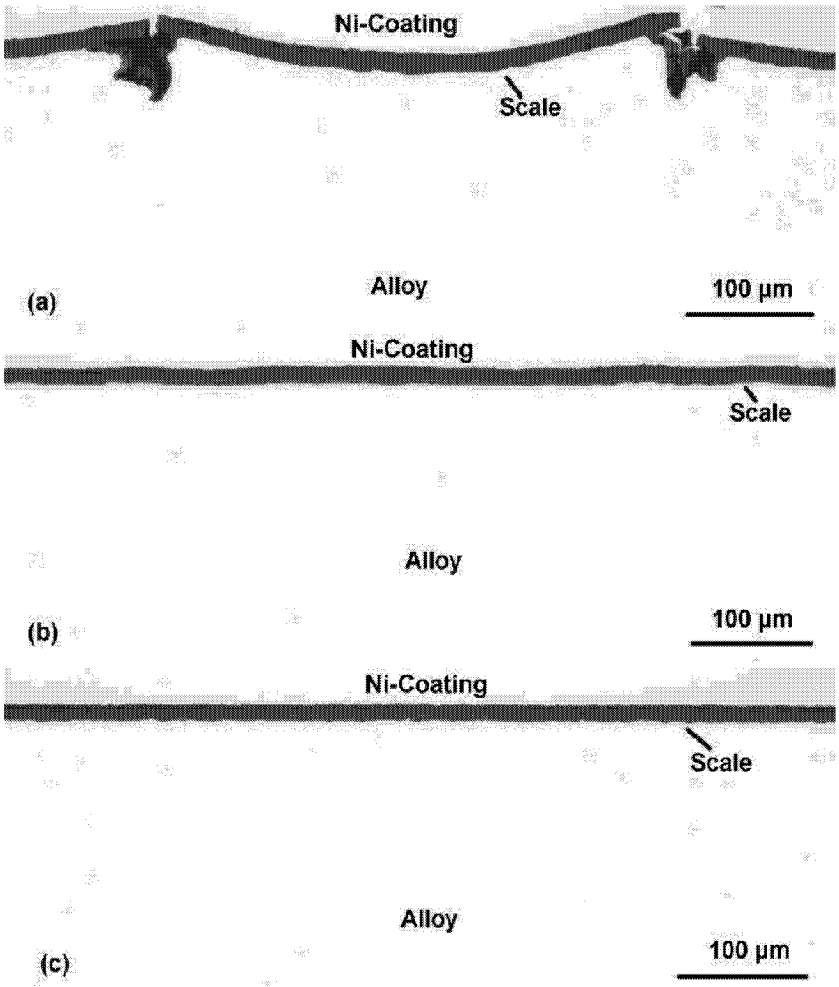

Figure 8.6: Metallographic cross sections of oxide scales formed on HEQ specimens after 600 h oxidation at 1200°C in air (compare with Figure 8.5.): (a) 2 h cycles test; (b) 100 h cycles test; (c) Isothermal

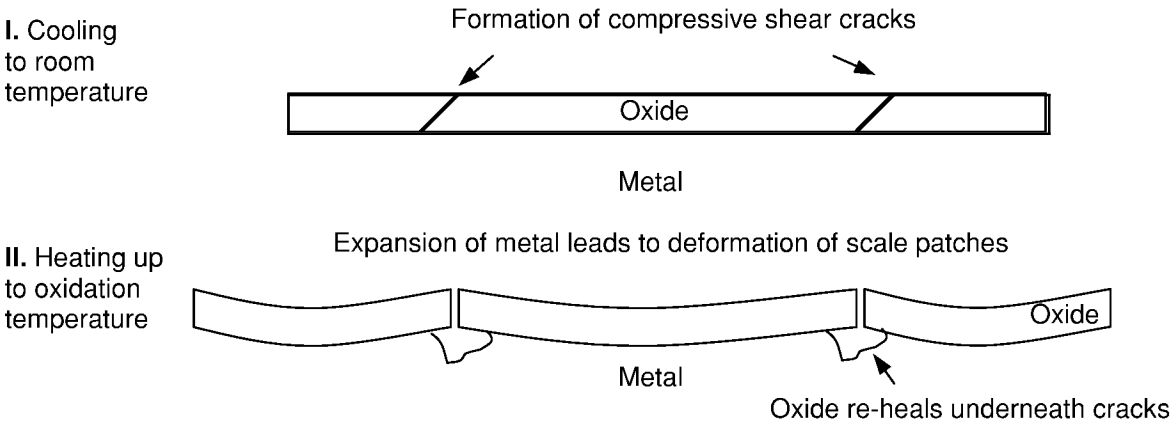

Figure 8.7: Schematic of scale deformation on PM 2000 induced by cyclic oxidation

Similar tests concerning the effect of temperature cycling on oxide growth rate were performed with 2 mm thick sheet of batch HDX (Aluchrom YHf). The mass change data for isothermal and 100 h cycles oxidation give very similar values after 600 h hours (Figure 8.8).

In contrast, at 2 h cycles an increased scale growth was observed after ca 200 h exposure, corresponding to a scale thickness of 12 to 13 µm. Based on the macrographs in Figure 8.9 it can be supposed that the enhanced oxidation kinetics, as in the case of the ODS alloy, is due to the scale cracking.

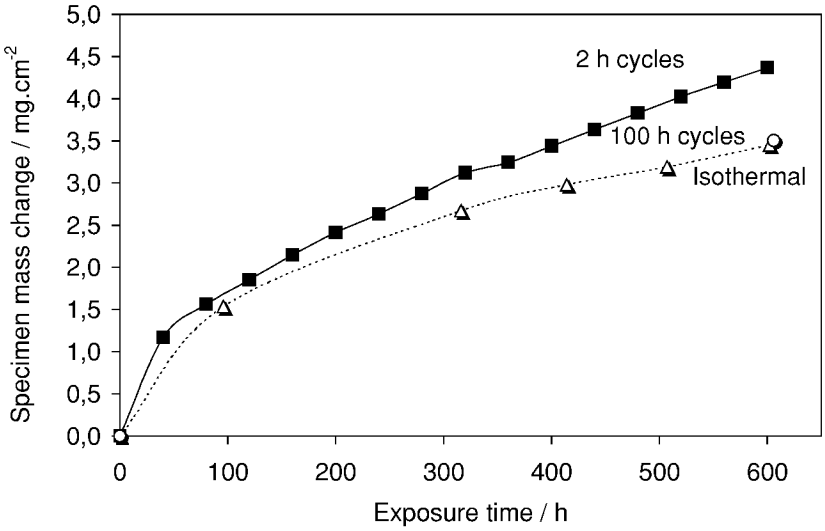

Figure 8.8: Specimen mass change data for 2 mm thick sheets of commercial wrought alloy Aluchrom YHf (Batch HDX) during oxidation at 1200°C in air

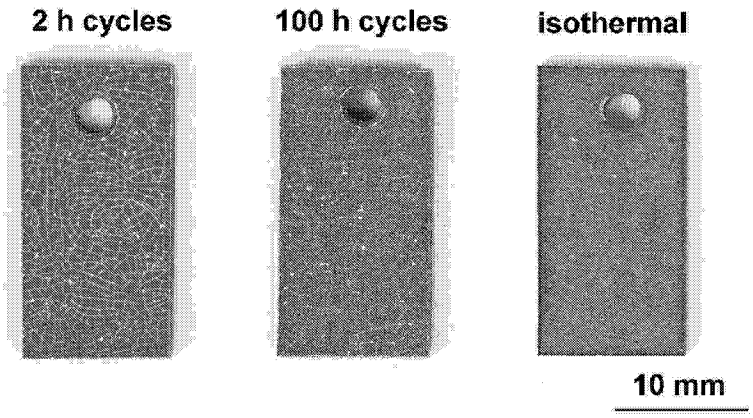

Figure 8.9: Macrographs of HDX specimens (alloy Aluchrom YHf) after 600 h oxidation at 1200°C (compare with mass changes in Figure 8.8.)

It has been well established in literature that temperature cycling can significantly affect the oxidation resistance of FeCrAl alloys by facilitating the scale spallation [82]. However, especially at short and medium oxidation times, before the alumina scale reached a critical thickness for spall initiation, cracking of the scale can occur. Although not as detrimental as the spallation of large scale patches, the scale cracking leads to a higher scale growth rates and thus to a faster consumption of Al for re-healing of the protective scale underneath the cracks. The temperature cycling obviously leads to changes in the scale morphology, which

can result in a faster spallation on the non uniform surfaces after the critical scale thickness has been reached [60].

8.5. Effect of atmosphere (oxygen partial pressure) on scale growth rate

The actual applications of the FeCrAl alloys are often such that the material is being oxidised in a gas mixture other than air. A good example of such application is the car catalyst systems, which in order to reduce the emission levels of CO, NO_x and hydrocarbons, operate at air/fuel ratios close to unit i.e. near to stoichiometric combustion condition. It can easily be shown, that very small changes in this ratio result in significant changes in the exhaust gas composition [84]. Thus, if a fuel rich combustion occurs, the oxygen partial pressure will be significantly lower that that in air.

Three foil materials, Kanthal AF, PM 2000 and Aluchrom YHf, tested previously in air (see Section 5.1) were studied in a synthetic car exhaust gas of a composition (vol.%): N_2-Base + 0.23% C_3H_8 + 4.2%CO + 9.2% H_2O + 10.2% CO_2, i.e. simulating a fuel-rich combustion. The oxygen partial pressure of this gas mixture was calculated using the computer software CHEMSAGE to be in the order of 1.10^{-12} bar at 1200°C. The results of the oxidation tests in the exhaust gas are presented in Figure 8.10 to 8.12 and compared to those obtained during air oxidation. Substantially decreased scale growth rates were observed in the exhaust gas mixture, which resulted in much longer times to failure than during air exposures. This retardation of the oxidation can be attributed to the very low oxygen partial pressure in the synthetic exhaust gas, using the following considerations.

As mentioned in Section 2, the oxidation studies using ^{18}O-Tracer have shown that gas tight alumina scales on RE-containing FeCrAl alloys grow mainly by oxygen grain boundary diffusion [22,23]. The sub-parabolic growth rates of the alumina scales was related to the increase of the average oxide grain size with increasing scale thickness (equations 2.21 and 2.22 in Section 2). For this case a cubic time dependence for the scale thickening is observed. Thus, the scale thickness x is proportional to $(\Delta\mu)^{1/3}$ and time to breakaway t_B is proportional to $(\Delta\mu)^{-1}$. The oxygen partial pressure at the scale metal interface for the temperature 1200°C can be calculated from the equilibrium reaction:

$$4Al + 3O_2 = 2Al_2O_3 \qquad (8.1)$$

Using the data for the Al activity in the alloy (non-depleted alloy $a_{Al} \cong 1.10^{-3}$ [85]) and standard thermodynamic data for alumina [5] the equilibrium oxygen partial pressure for

equation (8.1) is found to be around 1.10^{-22} bar. The oxygen partial pressure at the scale/gas interface equals 0.2 bar in case of the air exposed specimens and around 1.10^{-12} bar in the simulated exhaust gas. The ratio of the scale thickness formed in the two atmospheres after the same exposure time can be presented as:

$$\gamma = \frac{x_{exhaust}}{x_{air}} = \left[\frac{\Delta\mu_{exhaust}}{\Delta\mu_{air}} \right]^{1/3} \tag{8.2}$$

From eq-n (2.9) it follows that $\Delta\mu = RT[lnP(O_2)^{atm} - lnP(O_2)^{int}]$, where $P(O_2)^{atm}$ is the oxygen partial pressure in the oxidising atmosphere and $P(O_2)^{int}$ is the oxygen partial pressure at the scale/metal interface. Hence for the given above respective values of oxygen partial pressures:

$$\gamma = \frac{x_{exhaust}}{x_{air}} = (0.38)^{1/3} = 0.72 \tag{8.3}$$

In terms of the lifetime, this in the simulated exhaust gas comparing to that in air is extended by the factor ξ:

$$\xi = \frac{t_B^{exhaust}}{t_B^{air}} = \frac{\Delta\mu_{air}}{\Delta\mu_{exhaust}} = 2.63 \tag{8.4}$$

Figures 8.10 to 8.12 show calculated curves for the mass change data obtained during exposure in both atmospheres. The upper dashed line is a fit to the data points obtained in air assuming a cubic time dependence of scale thickening. The lower solid line was calculated from the upper one assuming the $P(O_2)$-dependence of scale thickness as given by eq-n (8.2).

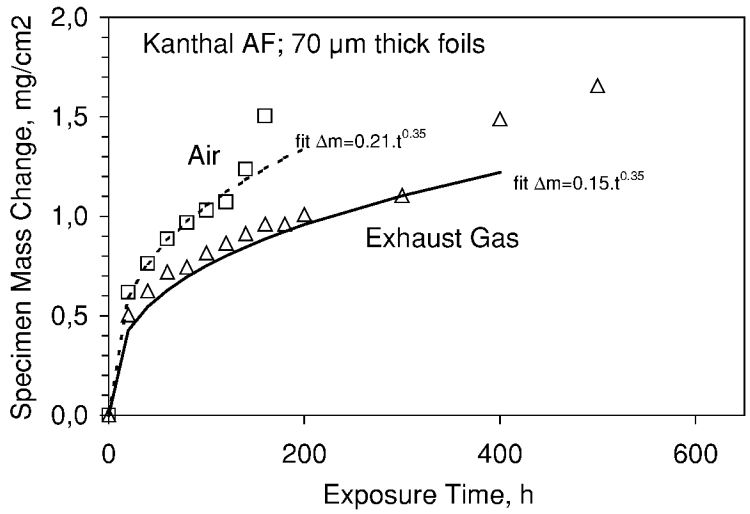

Figure 8.10: Mass change data compared to power law fitting for Kanthal AF 50µm thick foils during lifetime oxidation at 1200°C in air and simulated exhaust gas

The data show, that the calculated change in scale thickening rate (eq-n 8.2) and in time to breakaway (eq-n 8.4) upon changing the oxygen partial pressure are in reasonable agreement with the actually observed values.

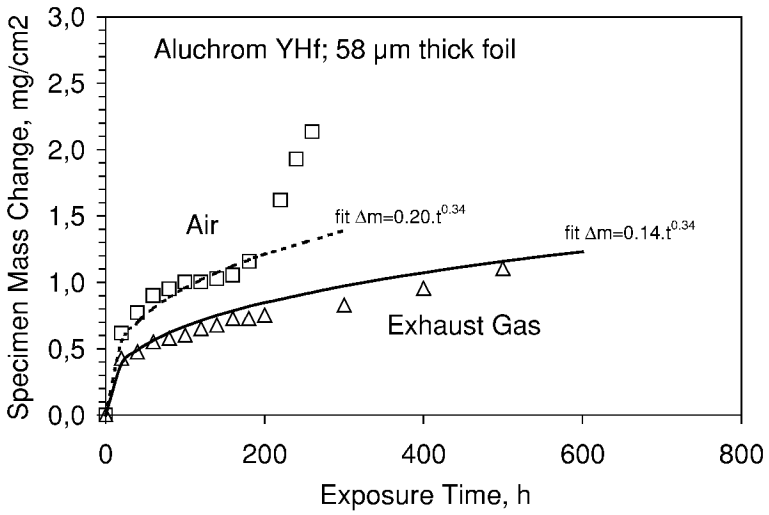

Figure 8.11: Mass change data compared to power law fitting for Aluchrom YHf, 58µm thick foils during lifetime oxidation at 1200°C in air and simulated exhaust gas

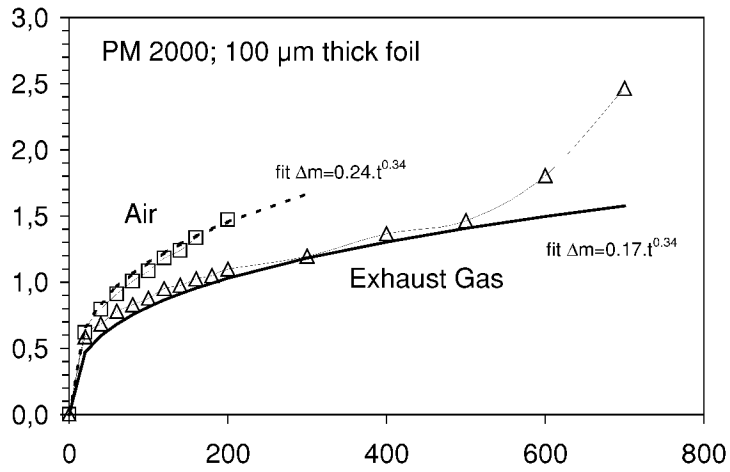

Figure 8.12: Mass change data compared to power law fitting for PM 2000 100µm thick foils during lifetime oxidation at 1200°C in air and simulated exhaust gas

In comparing prediction and experiment one should of course take into account that the calculated dependence can only be correct if the scale is solely growing by oxygen transport along grain boundaries. If e.g. molecular gas transport along micropores and microcracks substantially contributes to the scale growth process, the pO_2 dependence will of course be more complex, than assumed here. Microcracking can e.g. occur due to growth and/or thermally induced stresses as well as by oxidation of (carbo)nitrides as described earlier

(Section 6.1). In both mentioned cases the effect of microcracking on the oxidation, exhibited by a deviation from the ideal power law time dependence of scale thickening (Section 6.1 and reference [5]).

8.6. Effect of metastable alumina formation on scale growth rate

In the range of 1000 to 1300°C the rate of alumina scale thickening on FeCrAl alloys obviously increases with increasing the oxidation temperature. This can be easily explained in terms of the Arrenius' temperature dependence of the diffusion rates [5]. From the application point of view, however, often temperatures of 850 to 1000°C are of interest, as e.g. in the foil based car catalysts substrates, fibre based hot gas filters and burners etc. Having a wall thickness of 20 to 100 µm the above components are very sensitive to depletion of the Al-reservoir due to the scale growth, so that even relatively small increase in the scale growth rate might lead to breakaway oxidation within the estimated component lifetime.

In this study several batches of the commercial FeCrAl 50µm thick foils were tested at 100 h cycles at 900°C in air. Two important points can be noted, when analysing the mass change measurements presented in Figure 8.13. One is a rapid mass increase of the specimens during the first 100 h oxidation at 900°C, which indicates very high initial oxidation rates. In some cases mass gains of 0.60 mg/cm^2 (corresponding to an alumina scale thickness of approximately 3 µm) were reached during just 100h of exposure (Figure 8.13).

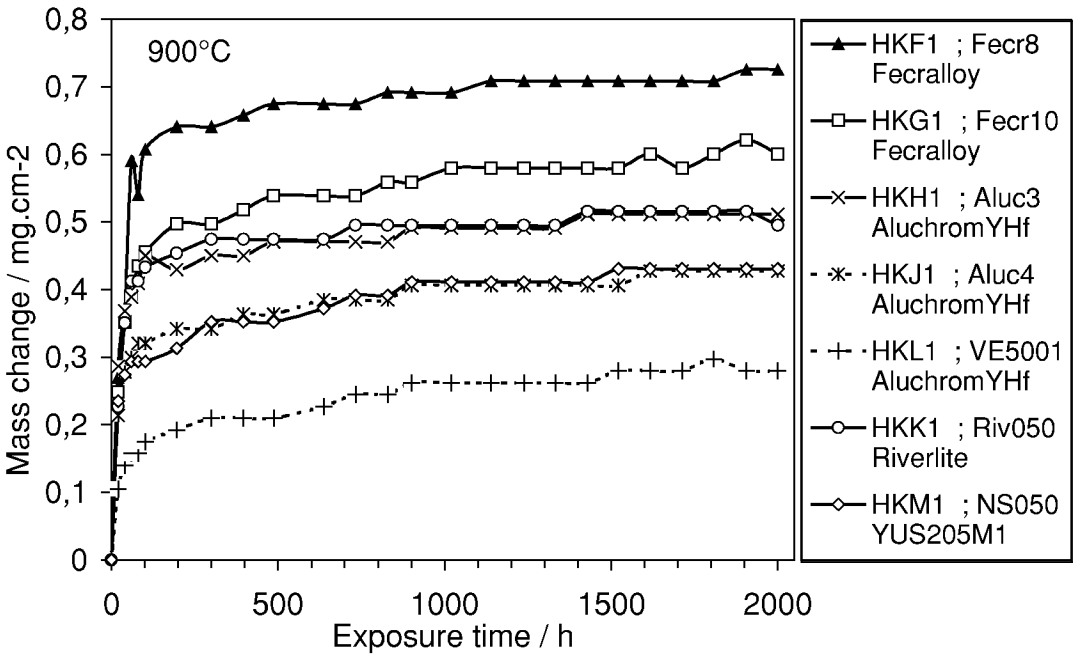

Figure 8.13: Mass change data during cyclic oxidation at 1200°C for 50 µm thick commercial foils during cyclic oxidation at 900°C in air

The second noteworthy point is a significant difference in the initial mass gains between different materials, e.g. 0.60 mg.cm^{-2} for the Resistalloy Batch HKF vs 0.15 mg.cm^{-2} for Aluchrom YHf Batch HKL. After ca 100h exposure the oxidation rates decreased drastically and become virtually the same for all foils, which can also be seen in the time dependence of the parabolic growth rate constant k_P for two selected materials in Figure 8.14. No catastrophic breakaway oxidation of the foils at 900°C occurred up to 2000 h.

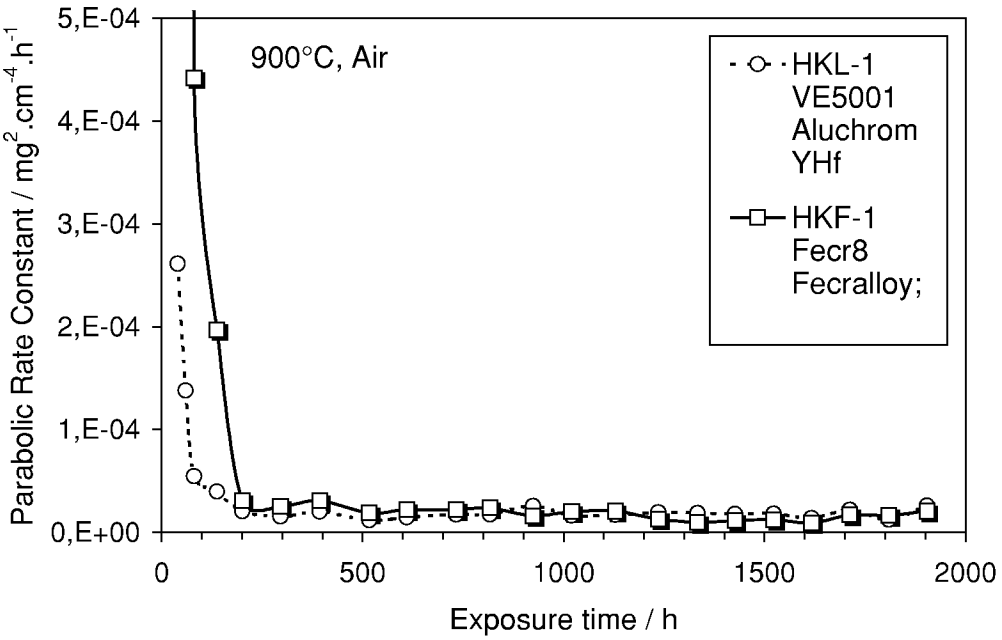

Figure 8.14: Instanteneous parabolic growth rate constant during cyclic oxidation at 900°C for two commercial foil materials showing large initial differences in oxidation kinetics which diminish after longer exposure time

From the above cyclic test data at 900°C two foil materials were selected for a more detailed investigation of the scale formation and growth during the initial stages of oxidation in lower temperature range. These were Fecralloy (Batch HKF) and Aluchrom YHf (Batch HKL) which showed the most extreme kinetics differences at 900°C. Isothermal tests in microbalance were performed at 875°C, 900°C and 925°C. The results are presented in Figure 8.15. At all three testing temperatures the Fecralloy batch HKF exhibited clearly higher initial growth rates than batch HKL. For alloy HKF the oxidation rates increased with raising the temperature from 875°C to 900°C. Further temperature raise to 925°C had resulted initially in higher oxidation rates, which, however, rapidly decreased after ca 20h exposure. For the alloy HKL the temperature raise from 875°C to 900°C led readily to lower oxidation rates. The mass change data of the two foil batches in Figure 8.15-a were used to calculate the time dependence of the parabolic rate constant in Figure 8.15-b.

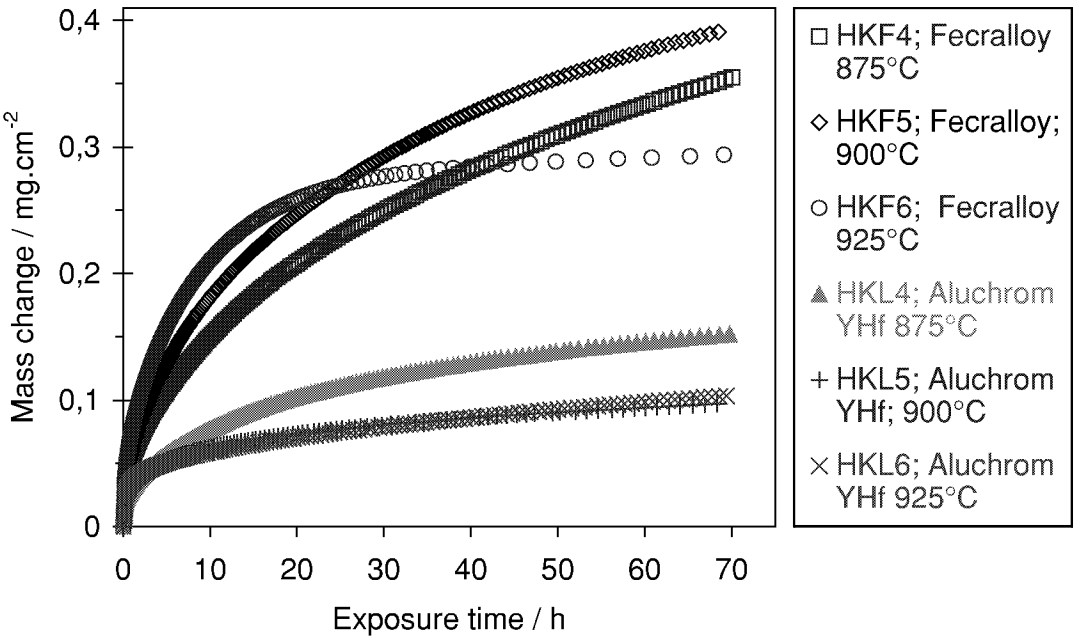

Figure 8.15: Thermogravimetry data obtained with HKF and HKL 50 µm thick foils during exposure at 875°C, 900°C and 925°C

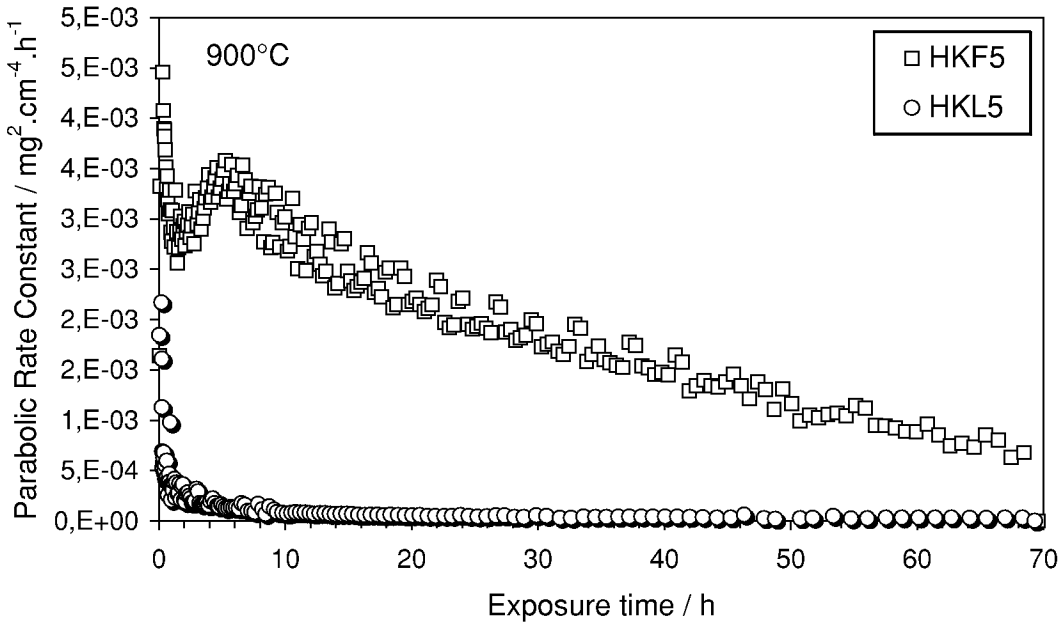

Figure 8.16: Plot of instanteneous parabolic rate parameter calculated after eq-n 5.2 from 900°C data in Figure 8.15

The macroscopically visible difference between the oxidised HKF and HKL materials can be seen in Figure 8.17. A light grey colour typical for transparent α-alumina can be seen for the HKL specimen. The dark grey colour of the HKF specimens combined with the oxidation kinetics in Figure 8.17 leads to the conclusion that the scale formed on this batch contains large amounts of other oxides than α-Al_2O_3. Cr^{3+}-fluorescence spectrum taken from the surfaces of the HKF specimens oxidised at 900°C (Figure 8.18) leaves no doubt about the

formation of θ–alumina, with the intensity of the characteristic peak for this metastable oxide phase being significantly higher than that for α-Al_2O_3.

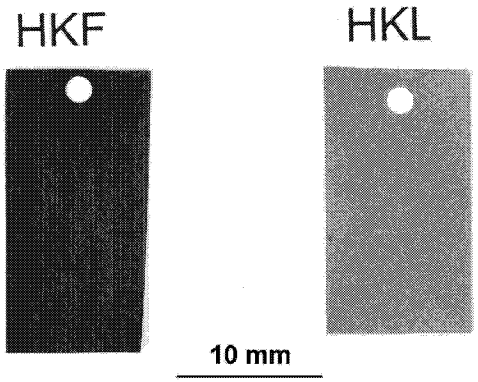

Figure 8.17: Macrographs of oxidised for 100 h at 900°C HKF and HKL foils

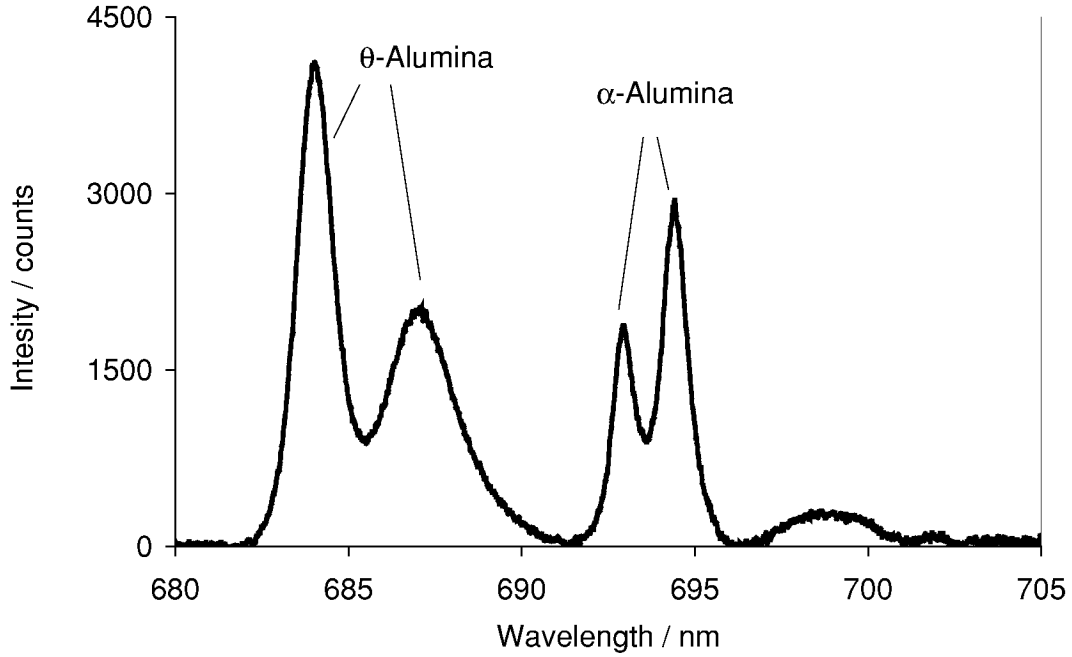

Figure 8.18: Cr^{3+}-fluorescence spectrum taken from specimen HKF after 10 h oxidation at 900°C, showing presence of *θ*-alumina within scale (Excitation by He-Ne Laser, λ=632.8 nm)

The results of metallographic studies on the specimens oxidised at 900°C are presented in Figure 8.19. Formation of metastable, outward growing alumina can be noted on both specimens. This effect, as well as formation of Fe-rich oxides in the regions of the spalled alumina scale appeared to be much stronger on HKF than on the other materials. In contrast, a much thinner scale with a lower amount of porosity was formed on HKL. No spalling or Fe-rich oxides could be found on the HKL-foil and the formation of the metastable Al_2O_3 was limited to local nodules rather than to a continuous layer. Both alloys exhibited no significant internal oxidation or breakaway features.

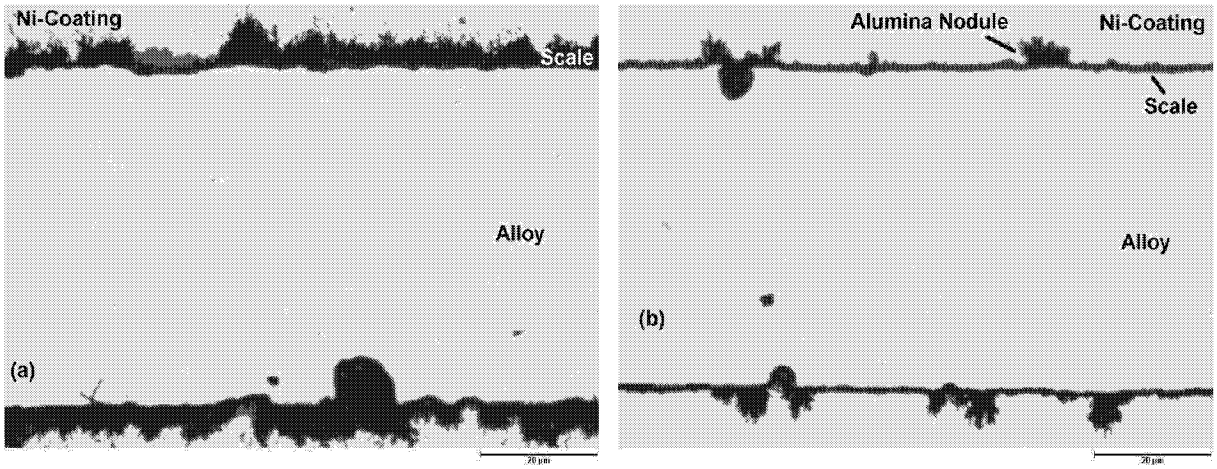

Figure 8.19: Metallographic cross sections of two commercial 50µm thick foil materials after 2000 h cyclic oxidation at 900°C in air: (a) HKF; (b) HKL

An important feature of the scale formed on HKF appeared to be porosity and presence of cracks (Figure 8.20-a). The metastable alumina nodules on HKL formed at 900°C appeared to be seldom and a 1µm thick scale covered most of the specimen surface (Figure 8.20-b), contrasting to that on the HKF specimen where a porous, 3-4µm thick, apparently outward growing scale was observed.

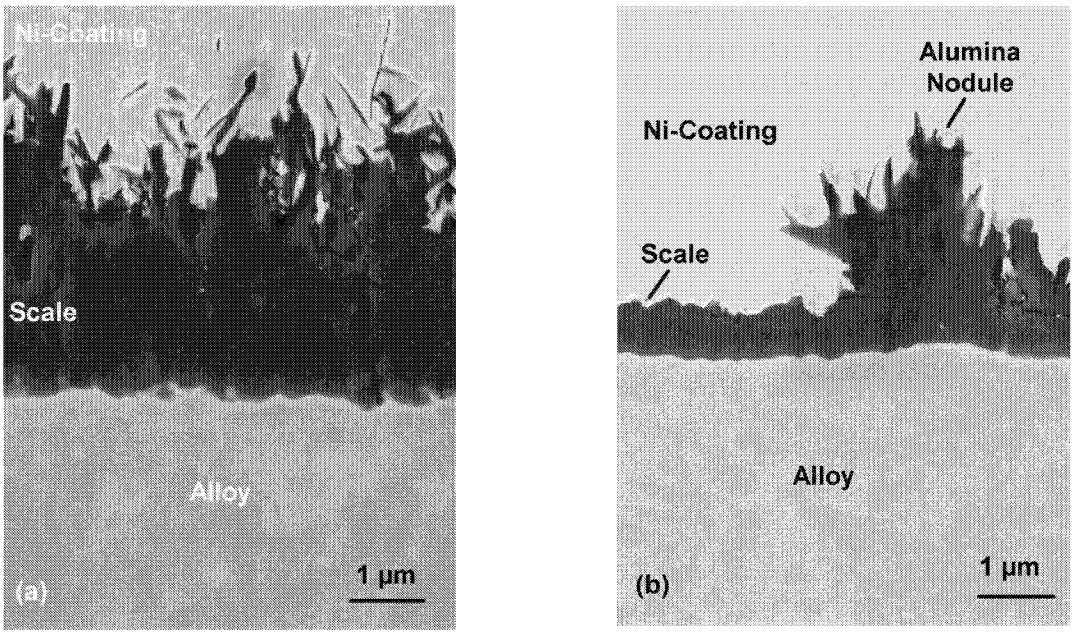

Figure 8.20: SEM images of cross sectioned foils after 2000 h cyclic oxidation at 900°C in air: (a) HKF; (b) HKL

At oxidation temperature of around 900°C, significant differences were observed in the scale growth kinetics between the studied alloys. The encountered variations in the oxidation behaviour were found to depend on the alloy susceptibility to form metastable θ-alumina based scale. At low temperatures such as 900°C, formation of a metastable, fast growing aluminium oxide can be a life limiting factor. This effect is of vital importance for thin walled FeCrAl components because of a rapid depletion of the Al-reservoir. For example, a 50 µm

thick foil HKF containing 5 mass % Al, shows after 100h at 900°C mass gains of 0.6 mg/cm^2 which means 80% loss of the Al-reservoir. Consequently, at the measured scale growth rate, for thinner components such depletion could already lead to a breakaway failure (Figure 8.21).

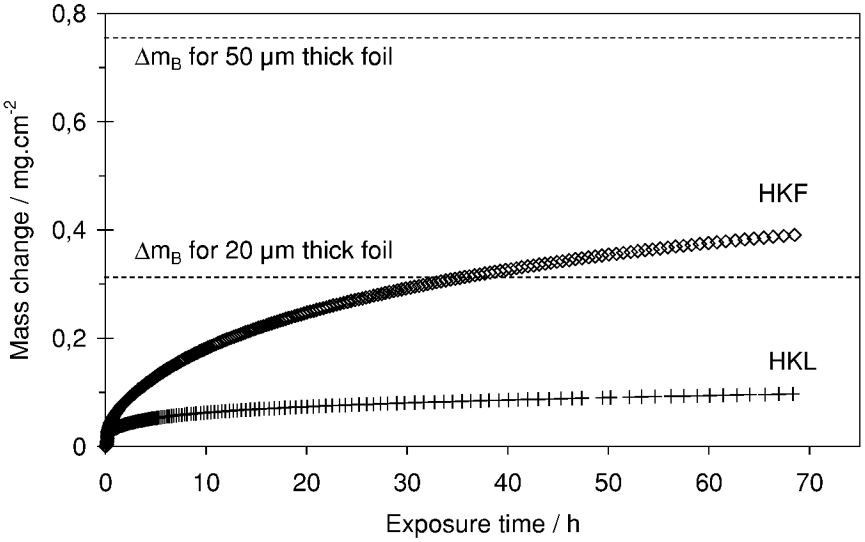

Figure 8.21: Effect of scale growth rate on depletion of Al-reservoir during isothermal oxidation at 900°C in air: critical mass gains for breakaway oxidation of 20µm and 50µm thick foils are shown as dashed horizontal lines

In the studied low temperature range, formation of the metastable alumina seems to be a less significant problem for the HKL material than for HKF and other studied alloys. The mass change data, the metallography and SEM studies indicate that this is because the transformation from metastable to stable alumina occurs on HKL faster and at lower temperatures than on HKF and on the other alloys (Figures 8.13, 8.15). The latter, in turn, can be related to the minor alloy chemistry. Comparison of the chemical compositions of the HKF and HKL materials (Table 1; Appendices) reveals that the first batch contains significantly higher amounts of the reactive elements Y, Zr and especially Ti. As discussed in Section 7.2, the literature data [80,81] indicates, that the elements with large atomic/ionic radii, such as La, Ti and Zr can stabilise the θ–alumina.

To stress this point once more, the preliminary results obtained with the model wrought alloys during thermogravimetry at 900°C are presented in Figure 8.22.

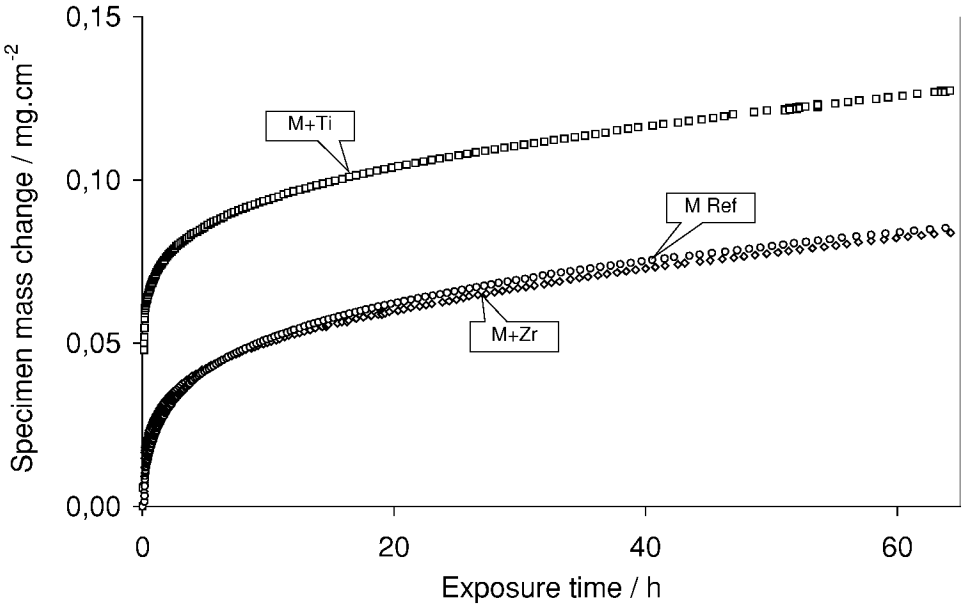

Figure 8.22: Thermogravimetry of model alloys during isothermal oxidation at 900°C in air

Alloy M+Ti demonstrates clearly higher oxidation rates than MRef-1 and M+Zr, which might be due to the stabilisation of θ–alumina by large Ti ions [80,81]. A practically important consequence of the metastable alumina formation at the low temperatures is that breakaway failure of thin walled FeCrAl components may unexpectedly occur within several tens hours exposure (Figure 8.21). This happens if no proper selection of the reactive elements is made and/or if the RE- and impurities contents are not adjusted to suitable levels.

9. Lifetime prediction of FeCrAl-components in view of obtained experimental results

9.1 General remarks

As has been explained in the previous Sections 5 to 8, a number of factors can influence the oxidation lifetime of a FeCrAl-component. These factors include metallurgical aspects, such as minor elements and impurity contents and component creep strength, as well as testing parameters during the oxidation exposure (temperature cycling, oxygen partial pressure etc.). The lifetime prediction model, developed in reference [11] gives values, which are in a reasonable agreement with the experimental results, when no changes in the scale growth mechanism and/or spallation resistance occur during long term oxidation. In the model the time to breakaway t_B depends on:

- the component aluminium reservoir, i.e. initial and breakaway Al-contents C_0 and C_B and thickness d;
- alumina scaling kinetics (parameters k and n);
- the critical mass change Δm^*, after which the alumina scale is prone to spalling

(see also Section 2 and reference [11]).

$$t_B = \left[4.4 \cdot 10^{-3} (C_0 - C_B) \frac{\rho \cdot d}{k} \right]^{\frac{1}{n}} \tag{2.18}$$

$$t_B = 4.4 \cdot 10^{-3} (C_0 - C_B) \cdot \rho \cdot d \cdot k^{-\frac{1}{n}} \cdot (\Delta m^*)^{\frac{1}{n}-1} \tag{2.19}$$

The general problem with lifetime modelling of FeCrAl alloys found in this study is that the above factors, incorporated in eq-ns 2.18 and 2.19 are specific for different alloy (batch) compositions, specimen geometry and exposure conditions (see Sections 5 to 8). Another problem is that under some particular exposure conditions the assumption made in (2.19), regarding the alloy spallation behaviour, i.e. linear spallation rate, is no longer valid. This section adopts the model in [11] as a basis and, taking into account the experimental data obtained in the present study, shows the possibilities for improvement of the model with respect to the observed effects.

9.2 Critical aluminium concentration for occurrence of breakaway (C_B)

The literature data give different values of the critical aluminium content at breakaway (C_B), which vary between values very near to zero and 2.5 mass%, depending on the material tested and exposure conditions applied [10,11,46,50]. The exact value of C_B is determined by a

number of factors. The most important one seems to be the protective properties of the oxide scale. If the alumina scale remains gas tight and adherent to the substrate, then the equilibrium oxygen concentration at the scale/metal interface is low, i.e. equals the dissociation pressure of alumina (eq-n 2.6 in Section 2). Consequently, the alloy aluminium can be depleted to a negligibly small value before intrinsic chemical failure occurs (Figure 5.13, [50]). If, however, the scale cracks and/or spalls and the depleted alloy is exposed to an oxidant with a high oxygen activity, then the value of C_B can be substantially higher, but in all studied cases not exceeding 2.5 mass% [4,10,11].

The parameters, which influence the gas tightness of the scale can primarily be related to the ability of a FeCrAl-component to relax the oxidation induced stresses (Section 5.1). The latter depends on the intrinsic creep strength of the material and the component wall thickness. Decreasing these two properties results in easier relaxation of the oxide stresses at temperature as well as during cooling and consequently in the lower values of C_B. Hence, in lifetime prediction of thin walled wrought alloy components the more suitable value of C_B would be a value close to zero, whereas for thin walled ODS components a more reliable prediction can be achieved when using 1.2 mass%, as proved experimentally [11,12] and confirmed by the present studies. As shown in reference [11], another important parameter, which can significantly increase the value of C_B is the alloy chromium content. If the chromium content is lower than 13 mass%, then the C_B value is expected to be in the order of 4 mass% [11].

9.3 Modification of thickness factor *d*

Equations 2.18 and 2.19 are based on the assumption of an infinite specimen length and width. In practice, however, the components have, of course, limited dimensions. Taking into account the fact, that the component thickness represents effectively the volume to surface ratio, namely:

$$d = \frac{2V}{A} \tag{9.1}$$

where V is the specimen volume and A is the total surface area, calculation of this ratio for different component geometry becomes possible [12]. For example, for a disc shaped specimen of diameter r and thickness d, the thickness in eq-ns 2.18 and 2.19 has to be replaced by a modification factor f, which is given by

$$fdisc = \frac{d}{(1 + 2d / r)} \tag{9.2}$$

For a cylindrical specimen of length L and diameter δ, the modification factor is

$$f_{cyl} = \frac{\delta}{(2 + \delta / L)} \tag{9.3}$$

From this equation, it is easy to verify that for a cylindrical specimen with quasi infinite length (L>>δ), such as is e.g. the case for a heating element wire, equation (9.3) changes to

$$f_{wire} = \frac{\delta}{2} \tag{9.4}$$

9.4 Modification of the alloy Al-reservoir with respect to aluminium depletion

In reference [11] it is assumed that the alloy density (ρ in eq-ns 2.18 and 2.19) and volume remains constant during the oxidation induced depletion of the Al-reservoir. In reality, however, the situation is different and e.g. the alloy density should change with changing the alloy Al-content from around 7.18 g/cm^3 for a Fe20Cr5Al alloy to 7.9 g/cm^3 for a completely Al-depleted FeCr-alloy. A simple calculation shows that considering this change, the alloy Al-reservoir is given by [86]:

$$Al(r) = f \cdot \rho \frac{(C_0 - C_B)}{(1 - C_B)} \tag{9.5}$$

It must be said that, according to eq-n (9.5) the actual Al-reservoir, considering the modified density factor, is expected to be not very different from that, used in eq-n (2.18), i.e. up to few percent difference.

9.5 Effects of changes in growth mechanism on scaling parameters k and n

As shown in Section 2 and proved by the thermogravimetrical experiments in Section 5, the growth of a compact alumina scale on FeCrAl, RE-doped alloys is well described by a sub-parabolic time dependence. This is because the oxide grain size has a tendency to increase with increasing scale thickness [8]. However, if a change in the scale growth mechanism occurs during oxidation, then the assumption of constant growth rate parameters k and n in equations 2.12, 2.18 and 2.19 is no longer valid. It has been found in this work, that the scale growth rate can be affected by alloy impurities of carbon and nitrogen (Sections 5 to 7), mechanical constraints of the FeCrAl-components, temperature cycling and, at low oxidation temperatures, by formation of a metastable alumina (Section 8).

The adverse effects of the carbon and/or nitrogen impurities on the oxidation kinetics of FeCrAl alloys is described in detail in Sections 6 and 7. These impurities form carbonitride precipitates in the alloy matrix due to reaction with the typical minor alloying additions of Ti, Zr and Hf. These precipitates are then incorporated into the inward growing alumina scale. Subsequent oxidation of these inclusions results in microcracking and formation of porosity. The scale growth mechanism then changes from scale grain boundary diffusion of oxygen to a combination of the former with the faster molecular oxygen transport through the pores and microcracks. The thermogravimetrical data, obtained during isothermal oxidation (Figures 6.3-b and 7.28-a) indicates that the scaling kinetics of the materials, which form porous scales are close to parabolic, rather then being sub-parabolic. The following mathematical considerations are proposed in order to explain the change in the growth rate exponent, due to contribution of the oxidant transport through the pores [87]. In these considerations it is assumed that:

1) The alumina scale growth rate is limited by oxygen diffusion on oxide grain boundaries (with a constant grain boundary width δ).
2) Diffusion through the bulk of an oxide grain is negligibly slow compared to that on oxide grain boundaries.
3) The oxide grain size increases with increasing distance x from oxide/gas interface towards the oxide/metal interface, according to the law $r(x)=ax$.
4) The intergranular porosity starts developing after the oxide scale reaches a thickness h_0.
5) The porous scale layer h_1 develops on the top of the dense layer h_0.
6) In the porous oxide layer h_1 macropores are developed, so the oxygen transport across such pores occurs via molecular diffusion i.e. it can be considered as infinitely fast compared to the solid state diffusion on the oxide grain boundaries;

After reaching a critical scale thickness h_0, the carbonitrides start to oxidise, producing pores. The assumption of a critical thickness of the compact layer is proved experimentally by the plots of the instanteneous parabolic rate parameter K_P in Figure 6.4, which shows a comparison for two batches of PM2000. The deviation in the K_P value of Batch CKT, which forms a porous scale from that of Batch CKS forming a compact scale, becomes apparent after approximately 10 h oxidation at 1300°C. The very similar oxidation rates up to 10 h exposure (corresponding to $h_0 \approx 5\mu m$) indicate that during this period the scale growth mechanism is the same for both materials, i.e. oxygen grain boundary diffusion. After the pore formation commences, the scale becomes essentially a double-layered structure, i.e. a

porous layer of thickness h_1 on the top of the compact layer of a constant thickness h_0. These two layers will definitely have different diffusion properties.

The effective diffusion coefficient for this double-layered structure is given as:

$$\frac{1}{D_{eff}} = \frac{h_0}{h_0 + h_1} \cdot \frac{1}{D_0} + \frac{h_1}{h_0 + h_1} \cdot \frac{1}{D_1} \tag{9.6}$$

The diffusion coefficients across layers h_1 and h_0 respectively are given as [87]:

$$\frac{1}{D_1} = \frac{1}{R} \cdot \frac{1}{h_1} \int_o^{h_1} \frac{dx}{\frac{2\delta}{ax} D_{gb}} \Rightarrow D_1 = 2D_{gb} \frac{2\delta}{ah_1} \cdot R \tag{9.7}$$

$$\frac{1}{D_0} = \frac{1}{h_0} \int_{h_1}^{h_1+h_0} \frac{dx}{\frac{2\delta}{ax} D_{gb}} \Rightarrow D_0 = 2D_{gb} \frac{2\delta}{a(2h_1 + h_0)} \tag{9.8}$$

R in equation (9.7) is an enhancement factor for the effective diffusion coefficient in a porous medium. In the model the pores are considered to be randomly distributed and occasionally they can agglomerate into chains (Figure 9.1). However, for any lateral cross section of the porous layer h_1, the area occupied by pores is supposed to be constant.

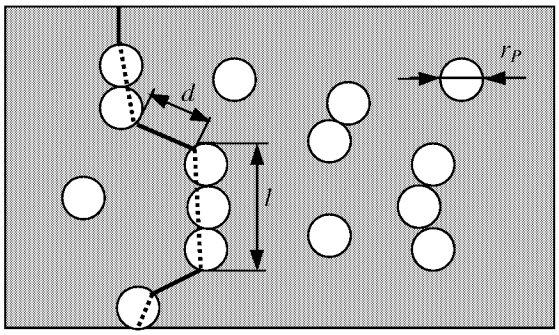

Figure 9.1: Schematic illustrating modelling of oxygen diffusion in porous alumina layer

The assumed infinitely fast oxygen diffusion through the pores results in a decrease of the effective diffusion path (Figure 9.1), or alternatively in an increase of the effective diffusion coefficient by the factor R, which is given by [87]:

$$R = \frac{d + l}{d} \tag{9.9}$$

where d is a typical interpore distance and l is a typical pore length. The enhancement factor R in eq-n (9.9), considering the pores are spheres of a constant radius r_P can be expressed in terms of porosity α. For sufficiently small porosity R can be expressed as [87]:

$$\frac{1}{R}=\frac{d}{d+l}\sim\frac{\frac{r_P}{\sqrt{\alpha}}}{\frac{r_P}{\sqrt{\alpha}}+\frac{2r_P}{(1-\alpha)^k}} \tag{9.10}$$

Since in the current model the pore radius r_P and the porosity α are assumed to be constant throughout the thickness of the layer h_1, the enhancement factor R is also constant. The value of k in (9.10) depends on the exact geometry of the problem and can be taken roughly between 3 to 8 [87].

Based on the Fick's first law of diffusion, the scale thickening rate can be expressed as:

$$\frac{dh}{dt}\equiv\frac{dh_1}{dt}=\frac{\Delta\mu}{RT}\cdot\frac{D_{eff}}{h_1+h_0}=\frac{\Delta\mu}{RT}\cdot 2D_{gb}\frac{2\delta}{a}\cdot\frac{1}{h_0(2h_1+h_0)+\frac{h_1^2}{R}} \tag{9.11}$$

where D_{eff} has been derived from eq-ns (9.6) to (9.8)

$$\left[h_0(2h_1+h_0)+\frac{h_1^2}{R}\right]dh_1=\frac{\Delta\mu}{RT}\cdot 2D_{gb}\frac{2\delta}{a}dt \tag{9.12}$$

Straightforward integration of (9.12) leads to:

$$h_1^2h_0+h_1h_0^2+\frac{h_1^3}{3R}+\frac{h_0^3}{3}\sim t \tag{9.13}$$

where $h_0^3/3$ is the integration constant, chosen so that $t=0$ corresponds to $h_0+h_1=0$.

If, as it is assumed, the scale growth obeys a power law time dependence, the effective instanteneous growth rate exponent n can be obtained by logarithmic differentiation of equation $h_0+h_1\sim t^n$, namely:

$$n=\frac{d\log(h_0+h_1)}{d\log t}=\frac{t}{(h_0+h_1)}\frac{dh_1}{dt}=\frac{\frac{1}{3}h_0^3+h_0^2h_1+h_0h_1^2+\frac{h_3^3}{3R}}{h_0^3+3h_0^2h_1+h_0h_1\left(2+\frac{1}{R}\right)+\frac{h_3^3}{R}} \tag{9.14}$$

Introducing the dimensionless ratio $y=h_1/h_0$ leads to:

$$n=\frac{\frac{1}{3}+y+y^2+\frac{y^3}{3R}}{1+3y+\left(2+\frac{1}{R}\right)y^2+\frac{y^3}{R}} \tag{9.15}$$

The analysis of the function in (9.15) reveals, that if $R=1$ (no pores have formed) n is reduced to 1/3. If $R>1$, then n changes during the scale growth process. In the beginning of oxidation, $y=h_1/h_0$ is small and the exponent n is close to 1/3 (Figure 9.2). At larger scale thickness n

increases to a value, which depends on the enhancement factor *R*, i.e. on the value of porosity (Figure 9.2). Further increase in scale thickness leads to a decrease in n, which proceeds, however, very slowly. It must be mentioned that from eq-n (9.10) the effect of porosity on the growth rate exponent becomes apparent only at relatively large values of α, i.e. when $\alpha \geq 10\%$.

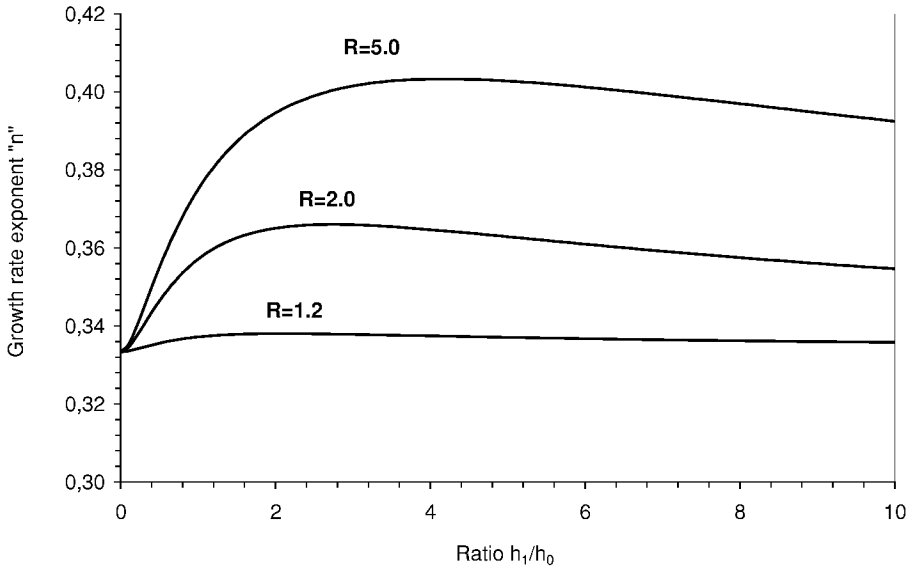

Figure 9.2: Growth rate exponent *n* in porous oxide as function of scale thickness, calculated from eq-n (9.15) for three values of diffusion enhancement factor R (eq-n 9.10)

As discussed in Section 8, not only the porosity, arising from the alloy impurities, can contribute to the change in the scale growth mechanism. In Section 8 several examples were given on the effects of exposure conditions on the growth rate of the alumina scales. One example shown in Section 8.4. was the effect of temperature cycling. It has been found that increasing the cycle frequency results in scale cracking and faster oxidation kinetics, because the scale re-heals underneath the cracks. In some cases (Figure 8.2) significant plastic deformation of the specimen occurs because of the stresses induced by temperature cycling. This deformation results in effective increase in the surface area available for oxidation, which can also account for the observed enhancement of the oxidation kinetics. Another example (Section 8.6) points out that at low oxidation temperatures, formation of a metastable alumina can lead to very high initial oxidation rates. As far as it is known to the author, the mentioned results in Section 8, showing the effects of oxidation conditions on the scaling rates of FeCrAl-alloys, have not been explicitly elucidated in literature. These few results, allow at the present time only a qualitative description of the observed effects and their physical backgrounds. Thus, it will be definitely the aim of future research to describe these effects in detail and incorporate them into a mathematical model for lifetime prediction.

9.6 Critical oxide thickness for scale spalling

It is a generally accepted concept that on FeCrAl, RE-doped alloys spallation of the protective scale occurs, after the scale reaches a critical thickness [11,42,43]. The critical thickness x* corresponding to a critical mass gain (Δm*) has been found to be alloy and component dependent [54, present study]. In equation (2.19) it is assumed that after reaching a critical thickness, the oxide scale spalls almost on the whole specimen surface. This is a plausible assumption, which is appeared to be valid in a number of cases [11]. However, especially on alloys with a low creep strength, due to the alloy plastic relaxation of the oxidation induced stresses, spallation of the scale during temperature cycling occurs only on part of the specimen surface. Therefore, direct application of eq-n (2.19) to such mechanically "weak" components can lead to significant underestimation of the lifetime. This issue can be accounted for in eq-ns (2.17 and 2.19) by introducing a spallation parameter β, which represents a statistical function, describing the ratio of the spalled oxide to the total oxygen uptake for a given time [88]:

$$\rho_m \frac{2V}{A}(C_0 - C_B) = \frac{2M_{Al}}{3M_0}\left[\beta\Delta m^{*\left(1-\frac{1}{n}\right)} k^{\frac{1}{n}} t_B + (1-\beta)k t_B^{\,n}\right] \qquad (9.16)$$

where M_{Al} and M_O are the molar masses of aluminium and oxygen respectively.

Unfortunately, with respect to the value of t_B eq-n (9.16) does not allow for a solution in terms of rational functions. As shown in Section 5, the resistance of the oxide scale to spalling, which determines the value of β, depends on a number of parameters. Amongst other factors, β is expected to depend on oxidation temperature, heating and cooling rates, specimen creep strength and thickness etc. Analysis of the cyclic oxidation data obtained on commercial alloys (Figure 5.17-5.19) reveals that the spallation rates can change significantly with exposure time. Hence, β becomes a function of exposure time, which makes its evaluation based on the presently available limited experimental data quite difficult. For practical application of eq-n (9.16) it appears to be necessary to establish a data base varying the mentioned above experimental parameters in order to get a reliable empirical β function for different FeCrAl alloys/components.

10. Conclusions

In the present work the lifetime oxidation behaviour of commercial and model FeCrAl alloys at elevated temperatures have been investigated. Full lifetime testing up to 15000 h exposure and extensive characterisation of the formed oxidation products as well as the substrate materials by a range of surface analyses techniques have been performed. The experimentally determined lifetimes were compared with prediction from the existing model.

The main life limitation, i.e. the rate of consumption of the component Al-reservoir have been found to depend on a number of factors.

For thin walled (up to 100 µm thickness) components, as e.g. for car catalyst substrates the main life limiting factor appears to be the scale growth rate, whereas scale spalling has hardly any effect. The scale growth and time to failure of these thin foil specimens seem to be unaffected by temperature cycling. On one hand this is because the alumina scales do not grow to a critical thickness for scale damage to occur and on the other hand, since the growth and/or thermal stresses, generated in the scale can be relieved by the substrate plastic deformation. However, a significant lifetime reduction (up to a factor of two) is possible if the foil-based component is constrained and thus not able to freely deform.

For 0.5 mm to 2 mm thick commercial sheets the scale cracking and spallation during cyclic oxidation undoubtedly contribute to the process of Al-depletion and lead to a reduction of lifetime. The propensity to the scale damage is increased with increasing specimen thickness (from 0.5 to 2 mm) as well as with increasing the alloy creep strength (from the wrought alloys Kanthal AF and Aluchrom YHf to the dispersion strengthened PM2000).

An important drawback for lifetime prediction is that significant batch to batch variations in oxidation resistance were observed for all studied commercial alloys. These variations were investigated in detail and could be mainly attributed to the interaction of minor alloying additions, such as Ti and Zr with typical alloy impurities, i.e. carbon and nitrogen. Ti and Zr were found to form carbo-nitride precipitates in the alloy matrix, which during high temperature exposure become incorporated into the inwardly growing alumina scale. Subsequent oxidation of these particles within the alumina scale results in volume change and release of gaseous reaction products, such as N_2 and/or CO. Both latter factors lead to formation of pores and microcracks in the scale, resulting in enhanced oxidation kinetics,

apparently due to the molecular diffusion of oxygen via these short circuits. It should be emphasised that this porosity occurs during isothermal as well as cyclic oxidation. An important observation made with the porous scales was their excellent adherence even under severe temperature cycling conditions. This finding offers big potentials for the improvement of the cyclic oxidation performance of alumina forming alloys and coatings (FeCrAl, NiCoCrAl, NiAl etc.) especially in applications, where the scaling kinetics is not the primary reason for the component failure.

Additions of a "second" reactive element, such as Ti and/or Zr to the base FeCrAl compositions, which already contain metallic yttrium or yttrium oxide dispersion, appears to be a necessary requirement for achieving optimum oxidation resistance.

In the ODS yttria-containing model alloys, the additions of Ti promote incorporation and mobility of yttrium on the scale grain boundaries. This results in improved adhesion of the alumina scale and consequently in a significantly increased lifetime of the Ti-containing alloy. In contrast, the Ti-free model alloy, despite a 0.5% yttria addition, exhibits scale features typically observed in undoped alumina scales.

In the wrought FeCrAl model alloys, additions of Ti and Zr prevent the internal oxidation attack of the alloy grain boundaries, apparently by tying up the alloy carbon impurity in small carbide precipitates. In the model alloys without Ti and/or Zr as carbon gettering elements, chromium carbides form on the alloy grain boundaries. Subsequent scale cracking in the vicinity of the alloy grain boundary leads to fast oxidation of the carbides with CO-evolution at temperature. This in turn results in the formation of porous sponge-like internal oxide morphologies and severe substrate deformation, which became macroscopically apparent as the "broccoli effect". After formation of the zones affected by internal oxidation attack, the effective surface area available for reaction with the atmosphere becomes greatly increased, which dramatically enhances the oxidation rate and thus significantly decreases the alloy life. Complementary to the carbon gettering effect, the Ti and Zr additions improve scale adhesion on the wrought alloys, probably in a similar way as described above for the ODS alloys.

At lower temperatures (such as 900°C), which are common service temperatures for FeCrAl-based car catalysts and hot gas filters, the formation of metastable fast growing θ-alumina was observed, which led to a rapid consumption of the alloy Al-reservoir within the first tens hours oxidation. Although the oxide growth rates change after relatively short times to very

low values, governed by the growth of α-alumina, the initial metastable oxide formation can lead to very early breakaway oxidation (e.g. 40 hours if 20 µm thick foils or fibres are considered). The effect of metastable alumina formation is clearly alloy dependent and a rough correlation of the observed variations with the minor alloy composition can be made. The alloys, containing a not well balanced combination of the reactive elements and high impurity levels are most susceptible to the metastable alumina formation. In contrast, on the alloys with moderate reactive element additions and lower impurities, the oxide transformation to the stable α-alumina occurs much faster and at lower temperatures

In addition to the metallurgical chemistry with respect to minor alloying additions, a number of other important factors have been shown to affect significantly the oxidation kinetics and lifetime of the FeCrAl alloys. Increasing the temperature cycling parameters (heating and cooling rates) and decreasing the dwell time at temperature results in accelerated oxidation kinetics due to the scale cracking. A decreased oxygen partial pressure, which is often encountered in industrially relevant environments, results in lower scaling rates due to a decreased driving force for diffusion across the protective oxide film.

The results presented in this work strongly indicate that for a significant extension of the oxidation limited life of a FeCrAl alloy a well balanced combination of the reactive elements, rather than just one reactive element addition is required. The reason for this is that for achieving optimum oxidation properties a number of requirements has to be fulfilled, including low scale growth rates, improved resistance against spallation etc. Therefore, it is not only the selected combination of the reactive elements e.g. Y+Zr or Y+Ti, which is important, but also the exact amount and distribution of the elements within the alloy matrix. The effects of the reactive elements also strongly depend on their interaction with common "harmless" alloy impurities, such as carbon and nitrogen.

In the present study the experimentally determined lifetimes were compared with mathematical prediction from the lifetime model known in literature. Although in many cases reasonable agreement between experiment and prediction was observed, the numerous experimental findings have shown that the parameters used in the modelling can strongly differ, depending on alloy purity, temperature cycling parameters, composition of gas atmosphere etc. Therefore, proposals were made how to modify the existing model in order to obtain more reliable lifetime prediction of FeCrAl-alloys.

11. References

[1] J.M.Herbelin, M.Mantel and J.Y.Cogne, Future trends of FeCrAl alloys for automotive catalytic converters to reach mass production, in Proc. Int. Conf. On Metal Supported Automotive Catalytic Converters (27-28 Oct. 1997, Wuppertal, Germany), p.79-92, (Edt. H.Bode), Werkstoff-Informationsgesselschaft mbH, Frankfurt, (1997)

[2] F.Starr, A.R.White, R.Kazimierzak, Pressurised heat exchangers for operation at 1100°C, Materials for advanced power engineering (1994)

[3] D.Sporer, O.Lang, Performance of alumina forming ferritic ODS alloys at temperatures in excess of 1200°C, in Proc. 3rd int. Charles Parsons Turbine Conf. (25-27 Apr. 1995, Newcastle upon Tyne, UK), p.631-641

[4] W.J. Quadakkers and M.J. Bennett, Oxidation induced lifetime limits of thin walled, iron based, alumina forming, oxide dispersion strengthened alloy components, Materials Science and Technology, Vol.10, p.126-131 (1994)

[5] P.Kofstad, High temperature corrosion, Elsevier (1988)

[6] N. Birks, G.H. Meier, Introduction to high temperature oxidation of metals, Edward Arnold Ltd., London, UK (1983)

[7] C.Wagner, Beitrag zur Theorie des Anlaufsvorganges; Zeitschrift für Physikalische Chemie, Abt. B., Band 21, Heft 1/2, S.25-41 (1933)

[8] W.J. Quadakkers, Growth mechanisms of oxide scales on ODS alloys in the temperature range 1000-1100°C, Werkstoffe und Korrosion 41, 659-668 (1990)

[9] J.C. Kuo, Oxidationsbedingte Lebensdauerngrenzen von Pkw-Katalysatorträgern auf FeCrAl-Basislegierungen (Diploma work), RWTH Aachen (2000)

[10] M.J. Bennett, R. Perkins, J.B. Price and F. Starr, in Proc Materials for Advanced Power Engineering, COST 501, Liege 3-6 October 1994, Edt. D. Coutsouradis et. al. Kluwer Academic Publishers, Part II, p.1553

[11] W.J. Quadakkers, K. Bongartz, The Prediction of Breakaway Oxidation for Alumina Forming ODS Alloys Using Oxidation Diagrams, Werkstoffe und Korrosion, 45, p. 232-241 (1994)

[12] I. Gurappa, S. Weinbruch, D. Naumenko and W.J. Quadakkers, Factors governing breakaway oxidation of FeCrAl-based alloys, Materials and Corrosion 51, 224-235 (2000)

[13] C. Wagner, Journal of Electrochemical Society 103, p.571 (1956)

[14] L.B. Pfeil, UK Patent no. 459848 (1937)

[15] D.P. Whittle, J. Stringer, Improvements in high temeperature oxidation resistance by additions of reactive elements or oxide dispersions, Philosophical Transactions of the Royal Society in London, A295, p309-329 (1980)

[16] G.C. Wood and F.H. Stott, The development and growth of protective α-Al_2O_3 scales on alloys, in Proc. Int. Conf. on High Temperature Corrosion NACE-6 (2-6 March, 1981, San Diego, California, USA) p.227-250 (1983)

[17] R. Prescott and M.J. Graham, The formation of aluminium oxide on high-temperature alloys, Oxidation of metals, Vol.38, Nos 3/4, p.233-254 (1992)

[18] J.D. Cawley, J.W. Halloran and A.R. Cooper, Oxygen tracer diffusion in single-crystal alumina, Journal of American Ceramic Society, 74 (9), p.2086-2092 (1991)

[19] C.R. Koripella and F.A. Kröger, Electrical conductivity of Al_2O_3: Fe+Y, Journal of American Ceramic Society, 69 (12), p.888-896 (1986)

[20] J.L. Smialek and R. Gibala, Diffusion Process in Al_2O_3 scales: void growth, grain growth and scale growth, in Proc. Int. Conf. on High Temperature Corrosion NACE-6 (2-6 March, 1981, San Diego, California, USA) p. 274-283 (1983)

[21] J. Philibert and A.M. Huntz, Microstructural and diffusional studies in α-aluminas and growth mechanism of alumina scales in Proc. 2nd Int. Conf. Microscopy of Oxidation, (29-31 March 1993, Cambridge, UK) Edt. S.B. Newcomb, M.J. Bennett, The Institute of Materials, London, p. 288-297 (1993)

[22] W.J. Quadakkers, A. Elschner, H. Holzbrecher, K. Schmidt, W. Speier and H. Nickel, Analysis of composition and growth mechanisms of oxide scales on high temperature alloys by SNMS, SIMS and RBS, Michrochimica Acta, 107, p. 197-206 (1992)

[23] J.P. Pfeifer, H. Holzbrecher, W.J. Quadakkers, W. Speier, Quantitative Analysis of Oxide Films on ODS-Alloys using MCs-SIMS and e-Beam SNMS, Fresenius Journal for Analytical Chemistry, 346, p. 186–191 (1993)

[24] J.Jedlinski and G. Borchardt, On the oxidation mechanism of alumina formers, Oxidation of metals, Vol. 36, Nos 3/4, p. 317-337 (1991)

[25] R.A. Versaci, D.Clemens, W.J. Quadakkers and R. Hussey, Distribution and Transport of Yttrium in Alumina Scales on Iron Base ODS Alloys, Solid State Ionics, 59, p. 235-242 (1993)

[26] A. Czyrska-Filemonowicz, R. Versaci, D. Clemens, W.J. Quadakkers, The Effect of Yttria Content on the Oxidation Resistance of ODS Alloys Studied by TEM; In Proc. of 2nd Int. Conf. Microscopy of Oxidation (29-31 March 1993, Cambridge, UK) proceedings, Edt. S.B. Newcomb, M.J. Bennett, The Institute of Materials, London, p. 288-297 (1993)

[27] B.A. Pint, A.J. Garratt-Reed and L.W. Hobbs, The reactive element effect in commercial ODS FeCrAl alloys, Materials at high temperatures, Vol.13, No. 1, p. 3-16 (1995)

[28] H. Nickel, W.J. Quadakkers, The Correlation between Growth Mechanisms and Technologically Relevant Protective Properties of Chromia and Alumina Scales on Oxide Dispersion Strengthened Alloys; First Int. Conf. on Heat Resistant Materials, (22-26.Sept. 1991, Wisconsin, USA) p. 87-94 (1992)

[29] Z. Liu, W. Gao and Y. He, Modelling of oxidation kinetics of Y-doped FeCrAl alloys, Oxidation of metals, Vol. 53, Nos 3/4, p. 341-350 (2000)

[30] K. Bongartz, W.J. Quadakkers, J.P. Pfeifer, J.S. Becker Mathematical Modelling of Oxide Growth Mechanisms Measured by 18O Tracer Experiments, Surface Science, 292, p.196-208 (1993)

[31] C.W.Li and W.D. Kingery, Solute segregation at grain boundaries in polycrystalline Al_2O_3, in Structure and properties of MgO and Al_2O_3 ceramics, Advanced ceramics, Vol. 10, American ceramic society, p. 368-378 (1984)

[32] B. Pieraggi and R.A. Rapp, Interfacial scaling reactions and the reactive element effect, Materials at high temperatures, Vol. 12, No. 2-3 p.229-235 (1994)

[33] W.J. Quadakkers, J. Jedlinski, K. Schmidt, M. Krasovec, G. Borchardt, H. Nickel The Effect of Implanted Yttrium on the Growth and Adherence of Alumina Scales on Fe-20Cr-5Al, Applied Surface Science, 47, p.261–272 (1991)

[34] B.A. Pint, Experimental observations in support of the dynamic segregation theory to explain the reactive element effect, Oxidation of metals, Vol.45, Nos ½, p.1-31 (1996)

[35] D.R. Siegler, Aluminium oxide adherence on Fe-Cr-Al alloys modified with Group IIIB, IVB, VB and VIB elements, Oxidation of metals, Vol. 32, Nos 5/6, p.337-355 (1989)

[36] P.Y. Hou and J.L. Smialek, The effect of H_2-anneal on the adhesion of Al_2O_3 scales on a Fe_3Al-based alloy, Microscopy of Oxidation-4, p.79-85 (2000)

[37] P.Y. Hou, K. Prüßner, D.H. Fairbrother, J.G. Roberts and K.B. Alexander, Sulphur segregation to deposited Al_2O_3 film/alloy interface at 1000°C, Scripta materialia, Vol. 40, No. 2, p.241-247 (1999)

[38] H.J. Grabke, D. Wiemer and H. Viefhaus, Segregation of sulphur during growth of oxide scales, Journal of applied surface science, 47, p.243-250 (1991)

[39] E. Schumann, J.C. Yang and M.J. Graham, Direct observation of the interaction of yttrium and sulphur in oxidised NiAl, Scripta Materialia, Vol. 34, No. 9, p.1365-1370 (1996)

[40] H.J. Grabke, M. Siegers and V.K. Tolpygo, Oxidation of Fe-Cr-Al and Fe-Cr-Al-Y single crystals, Zeitschrift für Naturforschung, 50a, p.217-227 (1995)

[41] A.B. Anderson, S.P. Mehandru and J. Smialek, Journal of electrochemical society, 132, p.1695-1708 (1985)

[42] H.E. Evans, Stress effects in high temperature oxidation of metals, International materials reviews, Vol. 40, No. 1, p.1-40 (1995)

[43] M. Schütze, Die Korrosionsschutzwirkung oxidischer Deckschichten unter thermisch-chemisch-mechanischer Werkstoffbeanspruchung, Publisher - Gebrüder Borntraeger, Berlin-Stuttgart, ISBN 3-443-23011-3 (1991)

[44] A. Rahmel and V. Kolarik, Metallography, Electron Microprobe and X-Ray Structure Analysis, in Proc. of EFC-Workshop "Methods and Testing in High Temperature Corrosion (20-21 Jan. 1994, Frankfurt, Germany) The Institute of Materials, p.147-157 (1995)

[45] W.J. Quadakkers, H.Viefhaus, The Application of Surface Analysis Techniques in High Temperature Corrosion Research, in Proc. of EFC-Workshop "Methods and Testing in High Temperature Corrosion (20-21 Jan. 1994, Frankfurt, Germany) The Institute of Materials, p.189-217 (1995)

[46] D. Naumenko, L. Singheiser and W.J. Quadakkers, Oxidation limited life of FeCrAl based alloys during thermal cycling, in Proc. of Int. Conf. on Cyclic Oxidation of High Temperature Materials, Feb. 1999, Frankfurt am Main, Germany), Editors M. Schütze and W.J. Quadakkers, p.287-306 (1999)

[47] W.J. Quadakkers, K. Schmidt, H. Grübmeier, E. Wallura, Composition, Structure and Protective Properties of Alumina Scales on Iron Based Oxide Dispersion Strengthened Alloys, Materials at High Temperatures, 10, p.23-32 (1992)

[48] K. Ishii, M. Kohno, S. Ishikawa and S. Satoh, Effect of rare earth elements on high temperature oxidation resistance of Fe-20Cr-5Al alloy foils, Materials transactions, JIM, Vol. 38, No. 9, p.787-792 (1997)

[49] F.H. Stott and N. Hiramatsu, Breakdown of protective scales during the oxidation of thin foils of Fe-20Cr-5Al alloys at high temperatures, Materials at high temperatures 17 (1), p.93-99 (2000)

[50] G. Strehl, D. Naumenko, H. Al-Badairy, L.M. Rodriguez-Lobo, G. Borchardt, G.J. Tatlock and W.J. Quadakkers, The effect of Al-depletion on the oxidation behaviour of FeCrAl foils, Materials at high temperatures 17 (1), p.87-92 (2000)

[51] N.B. Pilling and R.E. Bedworth, The oxidation of metals at high temperatures, Annual General Meeting in London p.529-582 (1923)

[52] U. v.d. Crone, M. Hänsel, W.J. Quadakkers, R. Vaßen, Oxidation behaviour of mechanically alloyed chromium based alloys, Fresenius Journal of Analytical Chemistry, 358, p.230-232 (1997)

[53] R. Herzog, Mikrostruktur und mechanische Eigenschaften der Eisenbasis-ODS-Legierung PM2000 (PhD Thesis), Berichte des Forschungszentrums Jülich; 3485, ISSN 0944-2952

[54] J.P. Wilber, M.J. Bennett and J.R. Nicholls, The effect of thermal cycling on the mechanical failure of alumina scales formed on commercial FeCrAl-RE alloys, in Proc. of Int. Conf. on Cyclic Oxidation of High Temperature Materials, Feb. 1999, Frankfurt am Main, Germany), Editors M. Schütze and W.J. Quadakkers, p.133-147 (1999)

[55] O.S. Heavens, Optical properties of thin solid films, Dover, New York, USA (1965)

[56] I.M. Lifshitz, V.V. Sliozov, The kinetics of precipitation from supersaturated solid solutions, Journal of Physical Chemistry of Solids, Vol. 19, Nos. 1/2, p.35-50 (1961)

[57] W.D. Kingery, Introduction to ceramics, J.Wiley and Sons, New York (1960)

[58] J.P. Wilber, J.R. Nicholls and M.J. Bennett, Assessment of defects in alumina scales formed on ferritic ODS alloys, in Proc. of 3rd International conference on Microscopy of Oxidation (16-18 Sept. 1996, Cambridge, UK) The Institute of Materials, Edts. S.B. Newcomb, J. A Little, p. 207-220 (1996)

[59] V.K. Tolpygo, D.R. Clarke, Spalling failure of α-alumina films grown by oxidation: I. Dependence on cooling rate and metal thickness, Materials science and engineering, A278 p.142-150 (2000)

[60] V. Guttmann, F. Hukelmann, P.A. Beaven and G. Borchardt, The influence of surface pre-treatment on the integrity of alumina scales on the ODS alloy MA 956, in Proc. of Int. Conf. on Cyclic Oxidation of High Temperature Materials, Feb. 1999, Frankfurt am Main, Germany), Editors M. Schütze and W.J. Quadakkers, p.17-37 (1999)

[61] M.Türker, The long term oxidation behaviour of ferritic ODS alloys at 1100-1200°C in air and nitrogen- 2% oxygen, Corrosion science, 41, p.1921-1935 (1999)

[62] G. Merceron, R.Molins and J-L Strudel, Oxidation behaviour and microstructural evolution of FeCrAl ODS alloys at high temperature, Materials at high temperatures 17 (1), p.149-157 (2000)

[63] B.A. Pint, A.J. Garratt-Reed and L.W. Hobbs, The effect of Y and Ti on FeCrAl oxidation at 1400°C, Journal de physique IV, Colloque C9, supplement au Journal de Physique III, Volume 3, decembre 1993, p.247-255 (1994)

[64] J. Klöwer, A. Kolb-Telieps, M. Brede, Effect of aluminium and reactive elements on the oxidation behaviour of thin Fe-Cr-Al foils, in Proc. Int. Conf. On Metal Supported Automotive Catalytic Converters (27-28 Oct. 1997, Wuppertal, Germany), p. 33-46, (Edt. H.Bode), Werkstoff-Informationsgesselschaft mbH, Frankfurt (1997)

[65] C.P. Jongenburger, R.F. Singer, Recristallization of ODS superalloys, in New materials by mechanical alloying techniques, Editors E. Arzt, L. Schultz, DGM Informationsgesellschaft Verlag, Oberursel, p.157-165 (1989)

[66] V.K. Tolpygo, D.R. Clarke, Wrinkling of a-alumina films grown by thermal oxidation – I. Quantitative studies on single crystals of Fe-Cr-Al alloy, Acta materialia, Vol. 46, No.14, p.5153-5166 (1998)

[67] V.K. Tolpygo, D.R. Clarke, Wrinkling of a-alumina films grown by thermal oxidation – II. Oxide separation and failure, Acta materialia, Vol. 46, No.14, p.5167-5174 (1998)

[68] C. Sariouglu, E. Schumann, J.R. Blachere, F.S. Pettit and G.H. Meier, X-Ray determination of stresses in alumina scales on high temperature alloys, Materials at high temperatures 17 (1), p.109-115 (2000)

[69] M. Groß, In situ Röntgenbeugungsuntresuchungen von Oxidschichten auf Hochtemperaturwerkstoffen (PhD Thesis at RWTH Aachen), Wissenschaftliche Schriftenreihe des Fraunhofer ICT; Bd. 18) ISBN 3-8167-5267-5 (1999)

[70] J.D. French, J. Zhao, M.P. Harmer, H.M. Chan and G.A. Miller, Journal of American Ceramic Society, 77, p.1013-1024 (1994)

[71] B.A. Pint, K.B. Alexander, foreign ion segregation on Al_2O_3 scale grain boundaries, in Proc. of 3rd International conference on Microscopy of Oxidation (16-18 Sept. 1996, Cambridge, UK) The Institute of Materials, Edts. S.B. Newcomb, J. A Little, p.153-165 (1996)

[72] M.C. Stasik, F.S. Pettit and G.H. Meier, Effects of reactive element additions and sulphur removal on the oxidation behavior of FeCrAl alloys, Scripta Metallurgica et Materialia, Vol. 31, No. 12, p.1645-1650 (1994)

[73] J. Quadakkers, L. Singheiser, Practical aspects of the reactive element effect, in Proc. of Int. Conf. on High Temperature Corrosion (22-26 May 2000, Les Embiez, France), in press

[74] J. Jedlinski, G. Borchardt, M. Konopka, M. Nocun, The effect of reactive elements on the oxidation behaviour of Fe23Cr5Al alloys at high temperatures, Solid state ionics, 101-103, p.1147-1155 (1997)

[75] F. Clemendot, J.M. Gras and J.C. van Duysen, Influence of yttrium on high temperature behaviour of Fe-Cr-Al-Y alloys, Journal de physique IV, Colloque C9, supplement au Journal de Physique III, Volume 3, decembre 1993, p.291-299 (1994)

[76] J.K. Tien and F.S. Pettit, Mechanism of oxide adherence on Fe-25Cr-4Al (Y or Sc) alloys, Metallurgical Transactions, Vol. 3, p.1587-1598 (1972)

[77] T. Amano, A. Hara, N. Sakai and K. Sasaki, Oxide adherence on Fe-20Cr-4Al alloys with small amounts of sulphur and reactive elements (Y, Hf), Materials at high temperatures 17 (1), p.117-124 (2000)

[78] G. C. Wood and J. Stringer, the adhesion of growing oxide scales to the substrate, Journal de physique IV, Colloque C9, supplement au Journal de Physique III, Volume 3, decembre 1993, p.65-73 (1994)

[79] K. Messaoudi, A.M. Huntz and L. Di Menza, Residual stresses in alumina scales. Experiments, modellíng and stress relaxation phenomena, Oxidation of metals, Vol. 53, Nos. 1/2, p.49- 75 (2000)

[80] B.A. Pint, J.R. Martin and L.W. Hobbs, The oxidation mechanism of θ-Al_2O_3 scales, Solid state ionics, 78, p.99-107 (1995)

[81] C.K. Loong, J.W. Richardson Jr., Masakuni Ozawa, Structural phase transformations of rare-earth modified transition alumina to corundum, Journal of Alloys and Compounds, 250, p.356-359 (1997)

[82] B.A. Pint, P.F. Tortorelli and I.G. Wright, Effect of cycle frequency on high temperature oxidation behaviour of alumina and chromia forming alloys, in Proc. of Int. Conf. on Cyclic Oxidation of High Temperature Materials, Feb. 1999, Frankfurt am Main, Germany), Editors M. Schütze and W.J. Quadakkers, p.111-132 (1999)

[83] W.J. Quadakkers, D. Naumenko, L. Singheiser, H.J. Penkalla, A.K. Tyagi and A. Czyrska-Filemonowicz, Batch to batch variations in the oxidation behaviour of alumina forming Fe-based alloys, Materials and corosion, 51, p.350-357 (2000)

[84] W.J. Quadakkers, R.J. Fordham and J.F. Norton, "Factors affecting long term performance of catalyst materials for automotive application, Part I: Review of catalyst degradation phenomena", Report on special activities, Commission of the European Communities, Joint Research Centre, Petten Site (1995)

[85] K. Hilpert and M. Miller, Zeitschrift der Metallkunde, 83, p.10-13 (1992)

[86] G. Strehl, D. Naumenko, A. Kolb-Telieps, J. Klöwer, B. Jönsson, V. Gutmann, R. Newton, J.R. Nicholls, M.J. Bennett, G. Borchardt and W.J. Quadakkers, The influence of sample geometry on the lifetime of FeCrAl-RE alloys, in Proc. Int. Workshop on Lifetime modelling of high temperature corrosion process, 22-23 Februar 2001, Frankfurt am Main, Germany, in press

[87] I. Ivanov, D. Naumenko, W.J. Quadakkers, to be published

[88] J.R. Nicholls, R. Newton, M.J. Bennett, H.E. Evans, H. Al-Badairy, G. Tatlock, D. Naumenko, W.J. Quadakkers, G. Strehl and G. Borchardt, Development of a life prediction model for the chemical failure of FeCrAl alloys in oxidising environments, in Proc. Int. Workshop on Lifetime modelling of high temperature corrosion process, 22-23 February 2001, Frankfurt am Main, Germany, in press

Appendices

Table 1. Chemical composition of studied commercial foils (mass%)*

Trade Name	Kanthal AF	PM 2000	Aluchrom YHf	Fecraloy	Fecraloy	Aluchrom YHf	Aluchrom YHf	Aluchrom YHf	Riverlite R205USR	YUS205M1
Supplier	Kanthal AB	Plansee AG	Krupp VDM	Resistalloy	Resistalloy	Krupp VDM	Krupp VDM	Krupp VDM	Kawasaki	Nippon Steel
Thickness	50µm	100µm	58µm	50µm	50µm	50µm	50µm	50µm	50µm	50µm
Batch	FSF	FSK	FTF	HKF	HKG	HKH	HKJ	HKL	HKK	HKM
Fe	Base	Base	Base	72.3	71.3	72.9	72	72	72.8	73.3
Cr	20.83	18.99	19.65	22	20.9	20.4	20.3	20.5	19.7	20.2
Al	5.23	4.18	5.53	5.1	5.03	5.55	5.52	5.39	6.07	4.86
Si	0.19	0.024	0.29	0.42	0.36	0.27	0.28	0.29	0.22	0.28
Ca	0.0001	0.0003	0.00012	<0.001	<0.001	<0.001	<0.001	<0.001	<0.001	<0.001
Ce	-	-	-	<0.005	<0.005	<0.005	<0.005	0.007	0.005	0.048
Hf	0.0003	0.00005	0.031	<0.01	<0.01	0.035	0.035	0.026	<0.01	<0.01
La	-	-	-	<0.01	<0.01	<0.01	<0.01	<0.01	0.032	0.019
Mg	0.0017	0.003	0.0078	0.003	0.003	0.013	0.013	0.008	0.002	0.002
Mn	0.061	0.0031	0.18	0.1	0.081	0.19	0.2	0.12	0.077	0.18
P	0.014	0.0024	0.013	<0.01	<0.01	0.011	0.011	<0.01	0.018	0.029
Ti	0.094	0.55	0.0098	0.051	0.054	<0.005	<0.005	0.005	0.011	0.05
Y	0.034	0.37	0.046	0.074	0.11	0.036	0.03	0.041	0.019	<0.005
Zr	0.058	0.0014	0.054	0.077	0.087	0.055	0.056	0.055	0.025	<0.005
C	-	-	0.023	0.048	0.03	0.039	0.039	0.035	0.023	0.053
S	0.0001	0.0028	0.0001	<0.001	<0.001	<0.001	<0.001	0.002	0.003	0.002
N	-	-	0.004	0.018	0.0067	0.0092	0.0063	0.0034	0.0049	0.0086
O	-	-	-	0.016	0.007	0.0066	0.0106	0.0086	0.0127	0.0451

*- The relative error δ=3% for absolute concentrations more than 1 mass% ,

δ=10% for concentrations between 1 and 0.1 mass%, and δ=25% for concentrations less than 0.1 mass%

Table 2. Chemical compositions of studied 0.5 to 2 mm thick sheets of commercial alloys (all values are given in mass% or mass ppm)*

Material Name	Aluchrom YHf	Kanthal AF	Kanthal APM	PM 2000	PM 2000	PM 2000	PM 2000	PM 2000	Aluchrom YHf	Aluchrom YHf	Aluchrom YHf	Aluchrom YHf	Aluchrom YHf
Supplier	Krupp VDM	Kanthal AB	Kanthal AB	Plansee AG	Plansee AG	Plansee AG	Plansee AG	Plansee AG	Krupp VDM	Krupp VDM	Krupp VDM	Krupp VDM	Krupp VDM
Thickness	1.0 mm	1.0 mm	1.0 mm	0.5 mm	1.0 mm	2.0 mm	0.5 mm	1.0 mm	2.0 mm	2.0 mm	2.0 mm	2.0 mm	2.0 mm
Batch	FVK	FVJ	FSG	FSK	HEP	HEQ	CKS	CKT	HDT	HDU	HDW	HDX	HDY
Fe, %	Base	Base	Base	73.8	72.3	71.2	72.6	73.2	73.1	72.8	72.8	72.9	73.3
Cr, %	19.65	20.83	21.00	20.0	19.6	20.9	19.9	19.8	20.2	20.2	20.3	20.1	20.1
Al, %	5.53	5.23	5.84	4.0	5.4	5.4	5.3	5.2	5.61	5.73	5.54	5.58	5.68
Si (ppm)	2900	1900	4000	20	32	21	200	600	560	340	380	1210	900
Ca (ppm)	10	-	-	20	20	20	210	59	8.5	7.5	6.0	6.0	10.0
Hf (ppm)	310	3.1	1.1	<50	<50	<50	-	-	220	370	130	85	340
Mg (ppm)	78	17	22	<20	<21	<22	-	-	100	95	85	100	80
Mn (ppm)	1800	610	800	400	430	400	2100	1200	1780	1940	1760	1010	2040
P (ppm)	130	140	170	<100	<100	<100	75	37	<100	<100	<100	<100	<100
Ti (ppm)	98	940	260	4700	4900	4200	4900	4900	80	65	50	75	35
Y (ppm)	500	340	0.19	3400	3400	3400	3700	3600	500	480	390	540	600
Zr (ppm)	100	580	110	<50	<50	<50	40	13	59	48	27	41	33
C (ppm)	-	-	-	240	580	250	240	290	250	250	280	220	230
S (ppm)	20	1.5	0.82	30	50	70	50	30	10	10	20	20	20
N (ppm)	-	-	-	101	273	72	143	316	28	26	38	23	21
O (ppm)	-	-	-	2842	3250	2426	4611	2582	83	<10	<10	36	81
V (ppm)	300	200	360	90	90	120	18	55	42	48	27	41	33
Cu (ppm)	200	330	240	70	100	90	2000	580	110	140	130	100	100
Nb (ppm)	<50	<50	<50	-	-	-	3.4	2.8	<10	<10	<10	<10	<10
Mo (ppm)	100	58	41	-	-	-	97	29	35	20	60	50	60
Co (ppm)	-	-	-	<4	35	8	210	99	230	230	230	220	210
Ni (ppm)	-	-	-	18	68	24	780	770	1360	1440	1630	1420	1550

*- The relative error δ=3% for absolute concentrations more than 1 mass% , δ=10% for concentrations between 1 and 0.1 mass%, and δ=25% for concentrations less than 0.1 mass%

Table 3. Chemical composition of studied model alloys;
all values are given in mass percents or mass parts per million

	Model ODS		Model Wrought				
Material name	Ti-free	0.4%Ti	MRef-1	MRef-2	M+V	M+Ti	M+Zr
Supplier	Plansee AG		Ecole de Mine, Saint Etienne				
As received Condition	∅6mm rod	∅6mm rod	1 mm sheet	1 mm sheet	1 mm sheet	1 mm sheet	1 mm sheet
Batch name	DAG	DAH	FSM	FST	FTG	FTH	FTJ
Fe (%)	76.2	75.1	Base	Base	Base	Base	Base
Cr (%)	15.9	16.6	19.9	19.8	19.7	19.7	19.7
Al (%)	6.56	6.33	5.00	4.90	4.88	4.91	4.86
Si (ppm)	120	150	20	17	*	*	18
Ca (ppm)	<10	<10	<0.05	<0.05	*	*	<0.05
Co (ppm)	110	120	-	-	-	-	-
Hf (ppm)	<50	<50	<0.005	<0.005	*	*	<0.005
Mg (ppm)	<10	<10	<0.005	<0.005	*	*	<0.005
Mn (ppm)	480	610	1.3	1.4	*	*	1.5
P (ppm)	<10	<10	86	2.4	83	78	78
Ti (ppm)	250	4000	15	15	*	220	12
Y (ppm)	3800	3800	510	500	500	480	490
Zr (ppm)	110	110	0.64	0.64	*	*	290
C (ppm)	260	200	92	74	98	90	90
S (ppm)	30	70	<10	<10	<10	<10	<10
N (ppm)	218	206	<10	<10	-	-	-
O (ppm)	2470	2620	<10	<10	-	-	-
V (ppm)	55	80	4.1	3.9	83	*	3.3
Cu (ppm)	16	13	4.7	4.5	*	*	5.0
Nb (ppm)	<50	<50	<50	<50	*	*	<50
Mo (ppm)	-	-	0.89	0.81	*	*	0.85

- Not measured;
* Not analysed, but should be same as MRef-1, M+Zr and MRef-2
Relative errors for concentrations less, than 0.1 mass% ± 30%;
for concentrations between 0.1 to 1 mass % ± 10 %,
for concentrations above 1 mass% ± 3%

Acknowledgements

The authors thank the following individuals in Forschungszentrum Jülich for their assistance in conducting the experiments as well as for helpful discussions:

Mr R Anton, Mr J Bartsch, Dr H L Bay, Dr D Clemens, Prof A Czyrska-Filemonowicz, Mr H Cosler, Mr P J Ennis, Dr J Ehlers, Mrs D Esser, Mrs M Felden, Dr W Fischer, Mr V Gutzeit, Mr I Ivanov, Mr J C Kuo, Mrs Ch Kraus, Mr P Lersch, Mr R Mahnke, Mr R Muñoz-Arroyo, Mr L Niewolak, Mr W Oberle, Mrs M Offermann, Mr R Olefs, Dr H J Penkalla, Mr J Pirron-Abellan, Dr V Shemet, Prof F Schubert, Prof L Singheiser, Dr E Wessel, Mr J Wosik.

The results presented in this work have been partly obtained in frame of the BRITE-EURAM program „LEAFA“ (Life Extension of Alumina Forming Alloys; Project No. BE-97-4491). The authors are grateful to the European Community for the financial support of the LEAFA Project as well as the following LEAFA project partners for their co-operation: Dr H Al-Badairy, Dr P Beaven, Dr M J Bennett, Prof G Borchardt, Prof J Le-Coze, Prof H Evans, Dr V Guttmann, Dr B Jönsson, Dr A Kolb-Telieps, Mr U Miller, Dr R Newton, Prof J R Nicholls, G Strehl, Dr G Tatlock, Mrs A Westerlund.